Sequentially linear modelling of combined tension/compression failure in masonry structures

J. Kraus

Master of Science Thesis

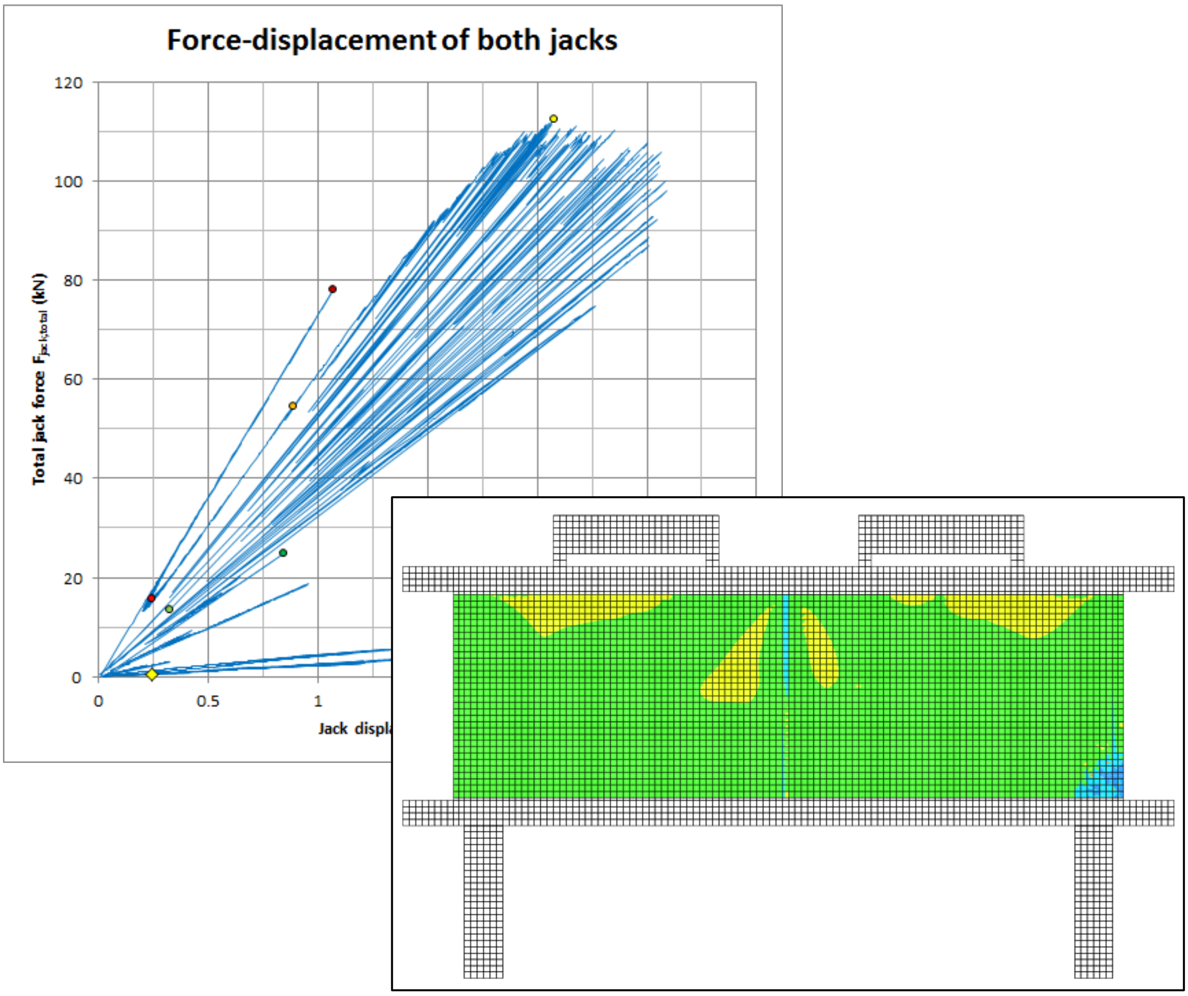

TU Delft
Delft University of Technology
Challenge the future

Sequentially linear modelling of combined tension/compression failure in masonry structures

Master of Science Thesis

For the degree of Master of Science in Structural Engineering
at Delft University of Technology

J. Kraus

May, 2014

Faculty of Civil Engineering and Geosciences · Delft University of Technology

Sequentially linear modelling of combined tension/compression failure in masonry structures

Johan Kraus
Section Structural Engineering – Structural Mechanics
Faculty of Civil Engineering and Geosciences
Delft University of Technology

Keywords
Finite elements, Sequentially linear analysis,
Deep wall-frame structure, Masonry,
Tension/compression failure, Brittle material behaviour.

Preface

This thesis is the product of several months of research to qualify for the degree of the Master Structural Engineering at Delft University of Technology (TU Delft). The work has been done at the section Structural Mechanics of TU Delft in the research fields of computational modelling and fracture mechanics. Due to the study taking place in multiple fields I was given the opportunity to contribute to the numerical method called the Sequentially Linear Analysis (SLA) method and apply it to a masonry structure, which is a fracture sensitive material.

The subject of improving the SLA method with the aid of a masonry structure as casus was proposed to me by Dr. Ir. M.A.N. Hendriks as well as by Prof. Dr. Ir. J.G. Rots. Both were active in studies supported by the calcium silicate industry and research into tunnelling induced settlement damage to masonry by modelling masonry structures numerically with nonlinear finite elements analysis (NLFEA). However, they concluded that the method was not sufficiently robust for very brittle materials and were positive that the recently created SLA, which is still in development, could bypass the limitations of NLFEA. This conclusion was responsible for the birth of my thesis and I gladly accepted to aid them in their work by carrying out this research.

For further guidance during my thesis two more researchers were invited to join the committee together with Dr. Ir. M.A.N. Hendriks and Prof. Dr. Ir. J.G. Rots. Ir. A.T. Slobbe, also from the section of Structural Mechanics, is actively involved with the newest form of SLA and continues to improve and complement the numerical method. Due to his expertise in this field he was asked to support the committee and support me during my research in SLA. Also Ir. S. Pasterkamp from the section Structural and Building Engineering of TUD joined the committee because of his experience with masonry structures in general. He is also familiar with the structure type used in the casus which makes him an great addition from the viewpoint of structural design.

I would like to thank all four people aforementioned for willing to be in the committee and supporting me during my thesis research. Another thanks goes out for TNO DIANA for providing the finite element software program DIANA, which was used extensively. I would also like to thank the continuous support from family, friends and the students I shared the office with during the research. Finally, I want to point out that I appreciate the pleasant atmosphere the whole section of Structural Mechanics provided for me to work in.

Constitution of the Committee:

Prof. Dr. Ir. J.G. Rots
Dr. Ir. M.A.N. Hendriks
Ir. A.T. Slobbe
Ir. S. Pasterkamp

Delft, May 2nd, 2014
Johan Kraus

Summary

The modelling of brittle fracture is essential for the assessment of structural safety. It remains a challenge due to sharp material softening after realization of the material strength. Standard nonlinear finite element analysis techniques using incremental-iterative solution procedures have been adapted to deal with the sharp softening curves associated with brittle materials, but convergence difficulties have stimulated the development of alternative modelling methods. The sequentially linear analysis method is an attractive alternative approach, since it is driven by increments of damage instead of increments of displacements, force or time. Consequently, this non-iterative procedure circumvents the aforementioned convergence difficulties. The goal of this thesis is to contribute to the sequentially linear analysis method by researching to what extent its most recent numerical framework improves on the numerical robustness and prediction of the post-peak behaviour with regard to combined tension/compression failure. Throughout the thesis a masonry deep wall-frame structure, tested by R. Sterrenburg and studied before using incremental-iterative procedures by J. Martens, is used as reference case for the research. This wall introduces the combined tensile, compression and shear failure modes, which makes it possible to improve the knowledge of masonry and masonry structures, providing data for validation and comparison for this thesis work.

This work starts with an exploratory analysis of the masonry deep wall-frame structure containing simple features in order to gain experience with the aforementioned standard nonlinear finite element analysis and the sequentially linear analysis method as presented in the literature. The results show that the obtained output of standard nonlinear finite element techniques are very dependent on many input parameters, such as step sizes and tolerances. Further it can be seen that where the standard nonlinear finite element analysis shows damage suddenly, and simultaneously if multiple instances of damage occur at the same time, the sequentially linear analysis method is able to show this in a more robust manner due to its event-by-event strategy introduced by the damage increments.

The most recent sequentially linear analysis framework, consisting of two different models for the coupling of the constitutive law of tension and compression, is then verified to make sure the numerical method works accordingly. One of the models is an uncoupled version only allowing different failure in the orthogonal directions, while the other model couples the constitutive law for tension and compression allowing a switch in damage state, but still has the limitation of not being able to reset the stiffness correctly in compression once previous tensile softening has occurred and vice versa. The numerical method is subjected to basic tests, such as tensile behaviour and the reversing of loading direction, confirming the correctness of the foundation of the numerical method. Also a biaxial tension-shear loading configuration is applied to a single element, verifying the elastic softening formulations used. It has been confirmed that the rotation of principal stresses after crack initiation is captured correctly by the sequentially linear analysis method. Finally, an experiment using a wall subjected to shear-compression loading has been tested, because this type of test has been adopted by the masonry community as the most common in-plane large tests and reassures the

effectiveness of the used event-by-event strategy. First erroneous results were found with very localized behaviour prematurely aborting the analyses. To solve this, an improved material representation of the softening curve was developed by extending the last ‘fictitious’ point of the diagram. And although both versions of the most recent sequentially linear analysis framework are imperfect with regard to the coupling of the constitutive laws, it is concluded that the influence of the limitations is negligible for the continuation of the thesis research, resulting in taking both versions further into account.

To reach the goal of the thesis combined tension/compression failure is re-enacted in a masonry deep wall-frame structure. The casus has been modelled with a homogeneous mesh of continuum elements and simplified orthotropic material relations, where only the masonry wall and the kicker joints had nonlinear material properties. A double load multiplier method is applied to handle non-proportional loading (constant) in combination with sequentially linear analysis. Firstly, a load is applied on the frame to ensure the separation of the frame with the deep wall and this load is kept constant as much as possible throughout the analysis. Afterwards, the top of the deep wall is subjected to a distributed load up until a new damage event is reached in every cycle. This resulted in a vertical crack in the centre followed by crushing of one of the two corners in the masonry deep wall. The analysis of both versions of the sequentially linear framework showed similar results and returned the full mechanical behaviour of the structure up until it reaches a point where failure is obviously inescapable. This is the moment where the numerical method is forced to reduce the initial load on the frame to achieve equilibrium and cannot reapply the full initial load anymore. Highly localized response finally causes abortion of the analysis after the structure can be considered to have failed.

These results of the masonry deep wall-frame study are validated with laboratory experiments in order to check if the sequentially linear analysis method is adequate to model combined tension/compression failure. It is also compared with results obtained with standard nonlinear finite element analysis. The crack formed in the centre of the masonry deep wall after the appearance of the separation crack are to be found in all experiments around the same magnitude of loading. After this, the standard nonlinear finite element analysis and the laboratory experiments first indicate that diagonal cracks have formed along the compressive strut from the points of loading to the support prior to the brittle compressive failure in the corner, where standard nonlinear finite element analysis immediately encounters numerical difficulties. The sequentially linear analysis method, however, continues by showing the gradual formation of crushing of the corner after the vertical crack in the centre of the wall. Both diagonal cracks and crushing of the corner are part of the same combined tension/compression failure, meaning that this difference found is a consequence of the modelling choice rather than being a consequence of the sequentially linear analysis not working properly. Thus the same failure mechanisms and response, crack formation in the centre of the deep wall and failure of the compressive strut, happen in the numerical experiments as well as in the laboratory experiments, indicating that the sequentially linear analysis method is a proper tool to model combined tension/compression failure in masonry structures.

It can be concluded that the sequentially linear analysis method improves the numerical robustness considerably in comparison to standard nonlinear finite element analysis. The post-peak behaviour of combined tension/compression failure can be successfully presented for quasi-brittle materials and the complete failure of structures can be simulated for the example of a masonry deep wall supported on a frame up until the initial constant load cannot be fully applied anymore in order to find equilibrium.

Table of contents

1. Introduction

Numerical models have been used for decades to predict structural behaviour, with the aid of validation provided by experimental laboratory results. A lot of research has gone into improving these numerical models to optimise the resemblance with reality. Those research results are for example used to understand and complement knowledge about the behaviour of masonry structures.

1.1. General thesis motive

The general background of the thesis can be described by several quotations made in research publications. The motivation for the research and the hypothesis of the research are globally represented in the first two quotations, whereas the last quotation indicates why a masonry structure came into the picture as casus to validate the numerical method. The quotations are from [1] and [2].

“Modelling the fracture of brittle materials is an essential requirement for assessing safety of structures through the prediction of failure, and remains a challenge due to sharp material ‘softening’ after realization of the material strength. Nonlinear finite element analysis techniques have been adapted to deal with the sharp softening curves associated with brittle materials, but convergence difficulties have stimulated alternate modelling methods.”
[Sequentially linear analysis of fracture under non-proportional loading; Matthew J. DeJong, Max A.N. Hendriks, Jan G. Rots; 2008]

“Modelling fracture through an event-by-event cracking procedure is an attractive alternative because modelling proceeds by imposing an increment of damage instead of an increment of displacement, force, or time. In this way, it is unnecessary to make large jumps in damage during a single load step or time step, which is usually the source of convergence problems and can influence results. In other words, while non-linear finite element analysis ‘skips over’ portions of the structural response when brittle behaviour occurs, and hopefully re-joins the response through iteration algorithms, event-by-event procedures avoid this by specifying damage directly.”
[Sequentially linear analysis of fracture under non-proportional loading; Matthew J. DeJong, Max A.N. Hendriks, Jan G. Rots; 2008]

“Application of structural masonry, however, is hindered by a lack of knowledge of the behaviour of materials and structures. Most of the present-day design and calculation rules are empirical and traditional by nature. These gaps in knowledge were recorded in 1987 by the CUR PC55 pre-advisory committee. Subsequently in 1989 the CUR PA33 pre-advisory committee outlined a new scientific approach to structural masonry with the integration of numerical mechanics and experimental techniques. This resulted in the research programme ‘Structural Masonry I’ in the period of 1989-1993.”
[Structural Masonry: An experimental/numerical basis for practical design rules ; Jan G. Rots; CUR]

1.2. Problem description

Structures are modelled numerically to design them safely. An important part of these computational efforts is the prediction of failure mechanisms. Commonly nonlinear finite element analysis is used to assess this peak and post-peak behaviour of structures, but the method has shown to be insufficiently robust and cumbersome with respect to quasi-brittle materials, as stated by the first quote.

As an alternative numerical model, as proposed by the second quote, sequentially linear analysis has been proposed as a robust technique for quasi-brittle post-peak behaviour. This method is in development and certain aspects of the numerical model still have to be verified and validated, in particular its applicability to tension-compression failure.

As indicated in the third quote, masonry is known to be a quasi-brittle material of which respectively little is known about. To improve masonry knowledge numerical analysis has been carried out with nonlinear finite element analysis, but from private communications with J.G. Rots and M.A.N. Hendriks it is clear that the method was not sufficiently robust to present the quasi-brittle tensile-compressive failure that occurred.

1.3. Problem definition

The objective of this thesis is to determine if the sequentially linear analysis method is sufficiently robust with regard to combined tension-compression failure and show that the solution procedure can provide more stable results than standard nonlinear finite element analysis. This objective is aimed to be reached by applying the method to a masonry wall supported on a frame, which has already been tested numerically with nonlinear finite element analysis and subjected to laboratory experiments. This can be translated in the following main question:

To what extent can the sequentially linear analysis method improve the numerical robustness and show stable post-peak behaviour with respect to combined tension/compression failure and be applied successfully to for example a masonry deep wall supported on a frame?

This main question is subdivided into research questions to build up an understanding of the question, the context of the research and the answer itself. They are split up in blocks that will encompass the *head*, *body* and *tail* of the report.

1. What computational method is used as foundation?
2. What is a nonlinear finite element analysis and why is it not robust enough?
3. What is a sequentially linear analysis and why is it an potential alternative?
4. What structural behaviour does masonry have and how is this translated numerically?
5. What structure is taken for the experiment and why is it connected to this research?

6. What experiences are gathered about NLFEA and SLA with exploratory analysis?
7. What is the state of the most recent SLA as concluded by element and wall tests?
8. How stable are the results of the casus with regards to tension-compression failure?
9. To what extent agree the casus results with laboratory and numerical experiments?

10. What are the conclusions and recommendations with respect to the presented work?

1.4. Scope of the research

The research aims to contribute to the ongoing research into sequentially linear analysis method. To achieve this goal, use has been made of a masonry wall supported by a frame as found in the Master thesis of Jasper Martens [3] and Rob Sterrenburg [4]. The scope of the research is to understand the numerical method and to make a next step by validating tension-compression failure.

It is noted that masonry experimental results show typically a wide scatter. This occurs in large structures as well as in small test models. The scope of this research is therefore to gain qualitative accordance and in a much lesser extent to reproduce precise quantitative results.

The numerical model is in development, which means there might be unfinished parts or bugs in the codes. It is not in the scope of the research to make the whole source-code of sequentially linear analysis error-free, but bugs will be cleared out and code is complemented if possible and necessary.

The research focusses on the numerical method and its potential to model quasi-brittle materials. A structure of masonry is used as a casus to achieve the proposed goal. Although results also corresponding to this casus are thus obtained, they are of lesser importance, but taken into consideration nevertheless if of value.

1.5. Research approach

The following part functions as a reading guide to understand what information can be found in which chapter. In order to answer the main question the following approach is taken:

Introduction

The first chapter, Chapter 1, provides the introduction into the subject of the thesis. The motive of the thesis is presented and the research problem is defined. Partial questions indicate the path taken and the scope of the research is stated. It also includes the research approach written as a reading guide.

Literature review

The *head* of the report consists of a literature review answering the first five question. In Chapter 2 an introduction is given to the finite element method which is the basis of the nonlinear finite element analysis procedure as well as the sequentially linear analysis procedure. Chapter 3 will discuss the nonlinear finite element analysis procedure as generally used throughout the research and presents current known limitations of the method. Chapter 4 will continue the numerical section of the literature review by discussing the sequentially linear analysis method research history as well as procedure and its promised potential. Chapter 5 introduces information about the casus by discussing the quasi-brittle material masonry. The material properties, constitutive models and computational applications are shown. Chapter 6 presents the masonry deep wall structure used and indicates the suitability of the casus.

Exploratory analyses, numerical verification and masonry deep wall validation

The *body* of the report treats questions 6-9 in order to answer the research question. Chapter 7 contains exploratory analyses which were carried by the author in order to experience the limitations of nonlinear finite element analysis and the potential of sequentially linear analysis method as presented in the literature, confirming the need of this thesis research. In Chapter 8 the sequentially linear models available and used are explained, verified and validated with the aid of elementary tests, a biaxial tension shear test and a shear compression test subsequently. The casus is then dealt with in Chapter 9. Herein, the structural as well as the control parameters are discussed and the results obtained are presented. Chapter 10 validates these results with laboratory and numerical experiments and explains the observed consistencies and differences.

Conclusion and recommendations

The *tail* of the report includes the final conclusions and recommendations. Conclusions are drawn with respect to all parts of the thesis research in Chapter 11. This chapter answers the research question and completes the circle. Recommendations on the improvement for the research itself as well as recommendations for future research are presented in Chapter 12.

HEAD

Literature review

2. The finite element method

The discussed finite element method is a displacement based formulation, the displacements are the fundamental unknowns. The method addresses the weak (variational form) of the governing equation and is hence known as a variational method. An equilibrium is always searched for between the known external forces **f** and the unknown displacements **u** by the use of a stiffness matrix **K** in the form **Ku** = **f** and by discretization of the problem into finite elements. The numerical results are retrieved from integration points and extrapolated to obtain a full structure response. Reference is made to [5], [6] and [7].

2.1. Formulation of the governing equations

For the governing partial differential equations of elastic continuum problems balance of linear momentum (translational equilibrium) as well as balance of angular momentum (rotational equilibrium) of a body $\Omega \subset \mathrm{R}^n$ with boundary $\Gamma = \partial\Omega$ should be guaranteed (see box 1). If translational equilibrium is satisfied then rotational equilibrium is also automatically satisfied if the stress tensor is symmetric, since $\boldsymbol{\mathcal{E}}\colon \boldsymbol{\sigma}^{\mathrm{T}} = 0$, if $\boldsymbol{\sigma}$ is symmetric. In those cases, as satisfied in this research, the governing equation in strong form is thus given by translational equilibrium (b1.3) only and balance of angular momentum (b1.5) will not be taken into further consideration due to the aforementioned reason. This governing equation is general of nature and does not only apply to elasticity.

The strong form of the governing equation (b1.3) has to be rewritten into a weak (variational) form. This reduces the order of the derivatives appearing in the governing equation and therefore becomes better edible for numerical applications. The strong form of the governing equation is multiplied by a virtual displacement $\delta\mathbf{u}$ (where δ stands for a variation of quantity) and integrated over the body Ω. This finally results in the virtual work equation:

$$\delta W_{\mathrm{int}} = \int_{\Omega} \delta\boldsymbol{\varepsilon}^{\mathrm{T}}\boldsymbol{\sigma}\,\mathrm{d}\Omega = \int_{\Omega} \delta\mathbf{u}^{\mathrm{T}}\boldsymbol{b}\,\mathrm{d}\Omega + \int_{\Gamma} \delta\mathbf{u}^{\mathrm{T}}\boldsymbol{t}\,\mathrm{d}\Gamma = \delta W_{\mathrm{ext}} \tag{2.1}$$

With:

With:	$\delta\mathbf{u}$	=	the virtual displacements
	$\delta\boldsymbol{\varepsilon}$	=	the virtual strains corresponding to $\delta\mathbf{u}$
	$\boldsymbol{t}$	=	traction forces on surface Γ
	$\boldsymbol{b}$	=	body forces on body Ω
	$\boldsymbol{\sigma}$	=	stress tensor

Box 1

Translational equilibrium is given by the following equation:

$$\int_{\partial\Omega} \boldsymbol{t}\,\mathrm{d}\Gamma + \int_{\Omega} \boldsymbol{b}\,\mathrm{d}\Omega = \int_{\partial\Omega} \boldsymbol{\sigma}\boldsymbol{n}\,\mathrm{d}\Gamma + \int_{\Omega} \boldsymbol{b}\,\mathrm{d}\Omega = 0 \qquad \text{(b1.1)}$$

With:	$\boldsymbol{t}$	=	traction forces on surface Γ
	$\boldsymbol{b}$	=	body forces on body Ω
	$\boldsymbol{\sigma}$	=	stress tensor

The divergence theorem can be applied over the integral $\partial\Omega$:

$$\int_{\Omega} \boldsymbol{\nabla}\cdot\boldsymbol{\sigma}\,\mathrm{d}\Omega + \int_{\Omega} \boldsymbol{b}\,\mathrm{d}\Omega = 0 \qquad \text{(b1.2)}$$

With:	$\boldsymbol{\nabla}$	=	the divergence operator

For every subdomain of Ω balance of linear momentum should hold.
This leaves the strong form for linear momentum:

$$\boldsymbol{\nabla}\cdot\boldsymbol{\sigma} + \boldsymbol{b} = 0 \qquad \text{in } \Omega \qquad \text{(b1.3)}$$

Rotational equilibrium is given by the following equation:

$$\int_{\partial\Omega} \boldsymbol{r}\times\boldsymbol{t}\,\mathrm{d}\Gamma + \int_{\Omega} \boldsymbol{r}\times\boldsymbol{b}\,\mathrm{d}\Omega = \int_{\partial\Omega} \boldsymbol{r}\times\boldsymbol{\sigma}\boldsymbol{n}\,\mathrm{d}\Gamma + \int_{\Omega} \boldsymbol{r}\times\boldsymbol{b}\,\mathrm{d}\Omega = 0 \qquad \text{(b1.4)}$$

With:	$\boldsymbol{t}$	=	traction forces on surface Γ
	$\boldsymbol{b}$	=	body forces on body Ω
	$\boldsymbol{\sigma}$	=	stress tensor
	$\boldsymbol{r}$	=	the position vector of a point on $\partial\Omega$

The divergence theorem can be applied over the integral $\partial\Omega$:

$$\int_{\Omega} \boldsymbol{r}\times(\boldsymbol{\nabla}\cdot\boldsymbol{\sigma})\,\mathrm{d}\Omega + \int_{\Omega} \boldsymbol{\mathcal{E}}:\boldsymbol{\sigma}^{\mathrm{T}}\,\mathrm{d}\Omega = 0 \qquad \text{(b1.5)}$$

With:	$\boldsymbol{\nabla}$	=	the divergence operator
	$\boldsymbol{\mathcal{E}}$	=	the permutation tensor

2.2. Discretization of the problem

Analogue continuous information has to be digitized, made discrete for further processing. The space is therefore spatially discretized by finite elements, consisting of nodes connected by element boundaries. The continuous unknown displacement field is lumped together onto the nodes of the finite element mesh with interpolation functions (shape functions). The shape functions are polynomials which are 1 at their respective nodes and 0 at other node's location. Elementwise it can be written as:

$$\mathbf{u} = \sum_{i=1}^{n} h_i(\xi,\eta,\zeta)\mathbf{a}_i \qquad \text{or more compact} \qquad \mathbf{u} = \mathbf{H}\mathbf{a}_{\boldsymbol{e}} \tag{2.2}$$

With:			
	$\mathbf{u}$	=	the continuous displacement field of an element
	h_i	=	the shape function of node i
	$\mathbf{H}$	=	$3\times3n$-matrix containing shape functions h_i
	$\mathbf{a}_i$	=	the displacement vector at node i containing a_{ix}, a_{iy} *and* a_{iz}
	$\mathbf{a}_{\boldsymbol{e}}$	=	$n\times1$-vector containing displacements $\mathbf{a}_i$

The displacements stored in the element-related vector $\mathbf{a}_e$ are related to the global displacement vector $\mathbf{a}$ through an incidence (or location) matrix $\mathbf{Z}_e$, which reflects the topology of the discretization. The spatial discretization (2.2) reworked into the weak form of the governing equation (2.1) will give:

$$\mathbf{f}_{\text{int}} = \sum_{e=1}^{n_e} \int_{\Omega_e} (\mathbf{B}\mathbf{Z}_{\boldsymbol{e}})^{\mathrm{T}} \boldsymbol{\sigma}\, d\Omega = \sum_{e=1}^{n_e} \int_{\Omega_e} (\mathbf{H}\mathbf{Z}_{\boldsymbol{e}})^{\mathrm{T}} \boldsymbol{b}\, d\Omega + \sum_{e=1}^{n_e} \int_{\partial\Omega_e} (\mathbf{H}\mathbf{Z}_{\boldsymbol{e}})^{\mathrm{T}} \boldsymbol{t}\, d\Gamma = \mathbf{f}_{\text{ext}} \tag{2.3}$$

With:			
	$\mathbf{B}$	=	matrix containing the derivative of the shape functions (**LH**)
	$\mathbf{H}$	=	$3\times3n$-matrix containing shape functions h_i
	$\mathbf{Z}$	=	Incidence matrix
	$\boldsymbol{t}$	=	traction forces on surface Γ
	$\boldsymbol{b}$	=	body forces on body Ω
	$\boldsymbol{\sigma}$	=	stress tensor

Using Hooke's Law as a constitutive model relating stresses σ with strains ε and the definition for the strains ε (2.4), while also assuming that the local and global coordinate systems coincide in axes directions (the matrix $\mathbf{Z}_e$ consists of ones and zeroes), gives (2.5).

$$\boldsymbol{\sigma} = \mathbf{D}\boldsymbol{\varepsilon} \qquad \boldsymbol{\varepsilon} = \mathbf{L}\mathbf{u} = \mathbf{L}\mathbf{H}\mathbf{a} = \mathbf{B}\mathbf{a} \tag{2.4}$$

$$\int_{\Omega_e} \mathbf{B}^{\mathrm{T}}\mathbf{D}\mathbf{B}\, d\Omega\, \mathbf{a} = \int_{\Omega_e} \mathbf{H}^{\mathrm{T}} \boldsymbol{b}\, d\Omega + \int_{\partial\Omega_e} \mathbf{H}^{\mathrm{T}} \boldsymbol{t}\, d\Gamma \qquad \text{or in short} \qquad \mathbf{K}\mathbf{a} = \mathbf{f} \tag{2.5}$$

2.3. Solving the element integrals

The integrals found are difficult to evaluate even for general geometries of the element. The elements are therefore mapped onto a parent element which is located in a natural coordinate system, the ξ, η, ζ –coordinate system. The shape functions of such isoparametric element type has to be evaluated only once and an integration scheme can be easily applied. Afterwards, the results are mapped backwards onto the original element. This mapping is represented by the jacobian j, which is the determinant of the Jacobian matrix $\mathbf{J}$.

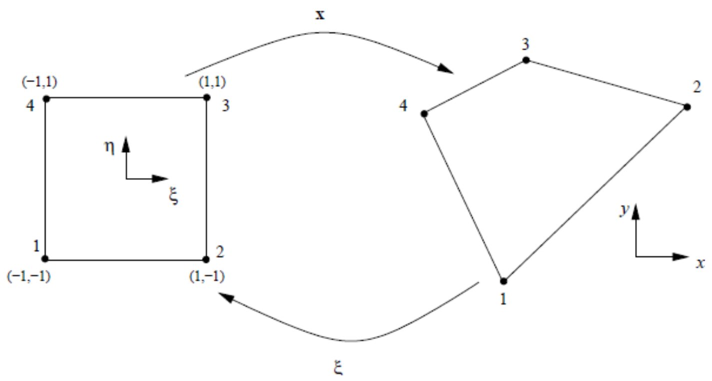

$$x = \sum_{i=1}^{n} h_n(\xi,\eta,\zeta)\, x_i \qquad y = \sum_{i=1}^{n} h_n(\xi,\eta,\zeta)\, y_i \qquad z = \sum_{i=1}^{n} h_n(\xi,\eta,\zeta)\, z_i$$

Figure 2.1: Mapping between cartesian and natural coordinate system and their relation. [6]

The space considered is now seen in a natural coordinate system making computing an easier task. This mapping changes for example the internal force vector from (2.3) in the following way:

$$\mathbf{f}_{\text{int}} = \sum_{e=1}^{n_e} \int_x \int_y \int_z \mathbf{B}^{\mathrm{T}} \boldsymbol{\sigma}\, dx\, dy\, dz = \sum_{e=1}^{n_e} \int_{\xi=-1}^{1} \int_{\eta=-1}^{1} \int_{\zeta=-1}^{1} j \mathbf{B}^{\mathrm{T}} \boldsymbol{\sigma}\, d\xi\, d\eta\, d\zeta \tag{2.6}$$

Numerical integration evaluates functions in a number of specific points. The evaluated values in these so called integration points are seen to be representative for their respective areas. Some integration points can cover larger volumes and so their weight, w_i, in the contribution are higher than other integration points. This last step takes care of the last integrals present in the governing equation (2.6) and makes the problem fully discrete in space.

$$\mathbf{f}_{\text{int}} = \sum_{e=1}^{n_e} \int_{\xi=-1}^{1} \int_{\eta=-1}^{1} \int_{\zeta=-1}^{1} j \mathbf{B}^{\mathrm{T}} \boldsymbol{\sigma}\, d\xi\, d\eta\, d\zeta = \sum_{e=1}^{n_e} \sum_{i=1}^{n_i} w_i\, j_i \mathbf{B}_i^{\mathrm{T}} \boldsymbol{\sigma}_i \tag{2.7}$$

3. Nonlinear finite element analysis

The finite element method makes the problem discrete in space and with it linear problems can be solved with it. However, in nonlinear analysis the relation between the known forces and the unknown displacements isn't linear anymore. The unknown displacements depend on previously determined displacements. It is therefore also necessary to make the problem discrete in 'time' with increments, creating a loading history, which can be solved by an iterative solution algorithm. Sadly, these solution procedures are not always sufficiently robust, especially in case of softening and brittle phenomena. Reference is made to [5], [7] and [8].

3.1. The incremental-iterative method

Nonlinearity in structural mechanics can present itself in three different forms. Firstly, in material nonlinearity the internal force vector usually depends nonlinearly on the displacements, as is the case for nonlinear elasticity. The same force vector can also depend on the displacements found in previous increments. This path dependency can be found for example in plasticity. Secondly, the external force vector can also be dependent on the displacements if geometric nonlinearity is present. In this type of nonlinearity the deformations are large enough to demand that equilibrium equations have to be rewritten, because loads can change direction or magnitude. In the governing equations these nonlinearities are found in $\boldsymbol{\sigma}$, being nonlinearly dependent on the strain $\boldsymbol{\varepsilon}$ through the constitutive matrix $\mathbf{D}$, and in the integral over the space Ω, being dependent on nodal displacements $\mathbf{a}$, respectively. Thirdly, contact nonlinearity can happen, which can be simplified by the use of interface elements in nonlinear finite element analysis.

To solve these nonlinearities a time discretization has to be performed, where "time" indicates a sequence of situations. In the procedure this results in starting with a known situation at time t, $\mathbf{u}^t$, and searching for the unknown state at time $t+\Delta t$, $\mathbf{u}^{t+\Delta t}$. To find the internal force vector $\mathbf{f}_{\text{int}}$ at the unknown state at time $t+\Delta t$, the previous state and the increments are thus used as the knowns. The external forces are only geometrically dependent for they are subjected to the applied increments. The used external force and found internal force have to be equal to each other, leaving no residual forces. These residual forces are gathered in the *out-of-balance* vector $\mathbf{g}$. The general flow of a nonlinear finite element analysis can be found in figure 3.1.

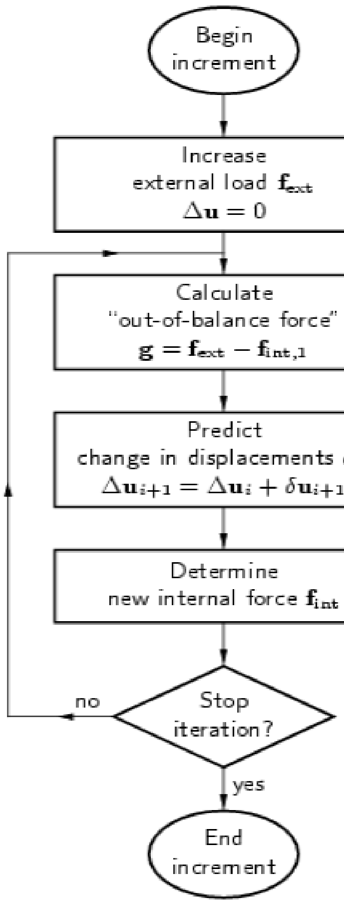

Figure 3.1: General flow of nonlinear finite element analysis. [5]

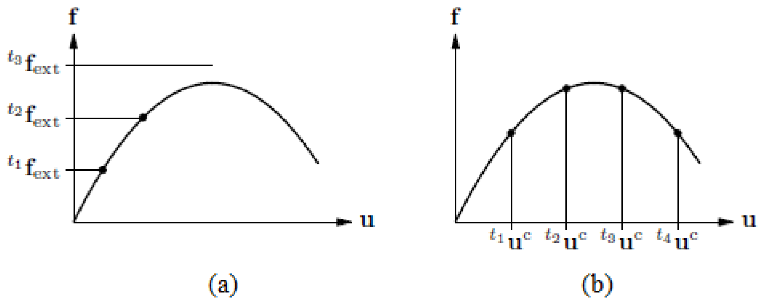

Figure 3.2: Control procedures force controlled (a) and displacement controlled (b). [5]

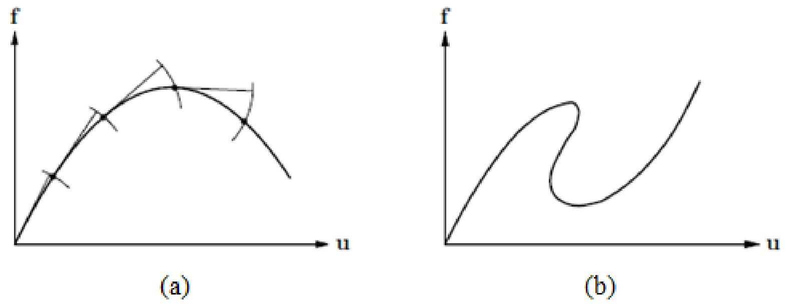

Figure 3.3: Arc-length control capable of visualising snap-through (a) and snap-back (b). [5]

The application of increments can be controlled in three different ways. Firstly, the external force vector can be increased directly at the start of every increment in a force controlled process. Force controlled analysis can result in erroneous predictions for the displacements if snap-through is occurring during the analysis, while snap-back behaviour is unseen. Secondly, using displacement control prescribed displacements are used as loading and the system of equations is then solved with the aid of partition, where the stiffness matrix and the force vector are split into a known part and an unknown part. Although this incremental procedure can handle snap-through, snap-back behaviour is still untraceable. Finally, arc-length control constrains the norm of the incremental displacements by simultaneously adapting the size of the increment itself within the iteration process. Although it is the most demanding method of the incremental procedures mentioned, it can trace both snap-through and snap-back if successful. Force control and displacement control are displayed in figure 3.2, whereas arc-length control and its possibilities are presented in figure 3.3.

During all applied increments equilibrium is approximated using iterations. A purely incremental method, an explicit procedure without iterations, gives inaccurate results. The obtained response drifts away from the true equilibrium path. The iterations are needed to reduce the errors successively, thus realising an implicit procedure. In these procedures the total displacement increment $\Delta\mathbf{u}$ is adjusted iteratively by a displacement $\delta\mathbf{u}$, which means that repeated linearization of the governing equation takes place. The linearization takes place with the use of a tangent stiffness matrix $\mathbf{K}$, which changes during iterations, and the out-of-balance force $\mathbf{g}$. The iterative methods available in DIANA, like the Newton-Raphson method, all use the same idea, but the updates of the tangent stiffness matrix used per iteration may differ.

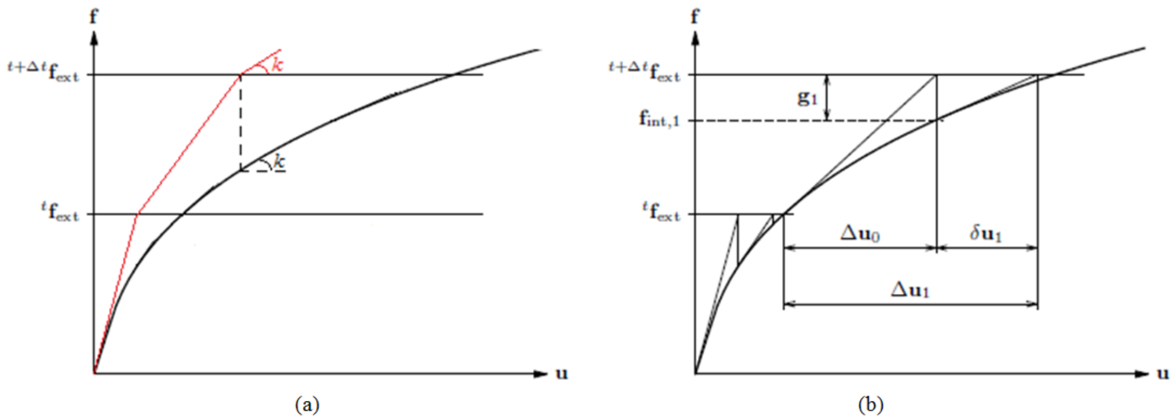

Figure 3.4: A purely incremental method (a) and a Regular Newton-Raphson method (b).

To stop the iteration loop and continue with the next increment the out-of-balance force **g** has to become as small as possible and a convergence criterion is required to control this. When this criterion is reached, it is assumed that the found solution of the latest iteration is sufficiently accurate and equilibrium is satisfied sufficiently. Different criteria can be used: force norm, displacement norm and energy norm. Firstly, the force norm is an Euclidian form of the out-of-balance vector **g**. Herein the unbalance of iteration *i* is checked against the initial unbalance. The remaining force imbalance should be a small fraction of the total applied force. This norm is, however, of little use when the structure can mostly deform freely. It will build up few internal forces in that case. Secondly, the displacement norm is an Euclidian form of the iterative displacement increment $\delta\mathbf{u}$. Herein, the iteratively adjusted displacement $\delta\mathbf{u}$ is compared to the displacement increment $\Delta\mathbf{u}$. The last update of the displacement increment should be a small fraction of the initial displacement increment. This norm in turn is, however, of little use when a lot of prescribed displacements are used. Thirdly, both criteria can be combined into an energy norm.

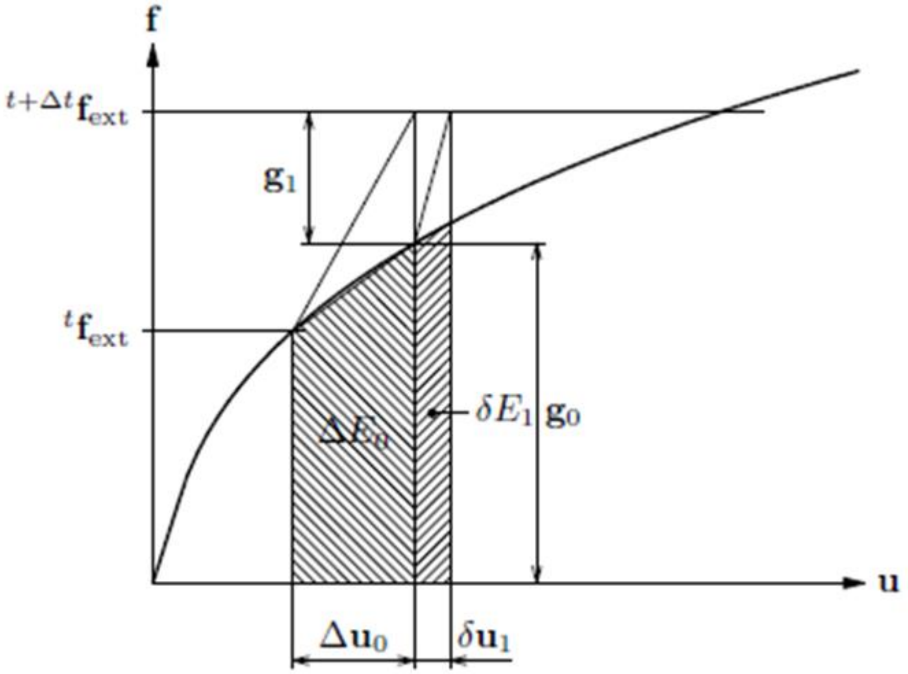

$$\text{Norm}_F = \frac{\sqrt{\mathbf{g}_i^{\mathrm{T}}\mathbf{g}_i}}{\sqrt{\mathbf{g}_0^{\mathrm{T}}\mathbf{g}_0}} \qquad \text{Norm}_u = \frac{\sqrt{\delta\mathbf{u}_i^{\mathrm{T}}\delta\mathbf{u}_i}}{\sqrt{\Delta\mathbf{u}_0^{\mathrm{T}}\Delta\mathbf{u}_0}} \qquad \text{Norm}_E = \left|\frac{\delta\mathbf{u}_i^{\mathrm{T}}\left(\mathbf{f}_{\text{int},i+1} + \mathbf{f}_{\text{int},i}\right)}{\Delta\mathbf{u}_0^{\mathrm{T}}\left(\mathbf{f}_{\text{int},1} + \mathbf{f}_{\text{int},0}\right)}\right|$$

Figure 3.5: Representation of norm items with their respective formula. [5]

3.2. The limitation of the analysis type

Nonlinear finite element analysis has shown to be a successful application in many fields. Nevertheless, limitations and the lack of robustness have become noticeable throughout the years. The limitations are most noticeable for applications involving quasi-brittle materials like concrete and masonry. The local stiffness in for example cracked integration points switches from a positive to a negative tangent stiffness. Due to the ability in nonlinear finite element analysis for multiple integration points to enter such a state simultaneously the system of equations can become ill-conditioned, losing its uniqueness, causing bifurcations and divergence.

The explosive behaviour of structural failure for quasi-brittle materials is difficult to trace with nonlinear finite element analysis. The method does provide enhancements like arc-length control and additional feedback mechanisms like crack mouth opening displacement (CMOD) for cracking behaviour, but even with these options it is still very difficult to stay on track and obtaining the desired response cannot be guaranteed. A clear example is found in the second shear wall test modelled by Lourenço [9], wall W2. The analysis was successfully able to find with much effort values after where normally the computation diverged. This final point is in agreement with the laboratoral experiment found in [10] qualitatively, indicating explosive failure. However, this sudden drop in the graph only shows that explosive failure has taken place, but it does not show the explosive failure itself.

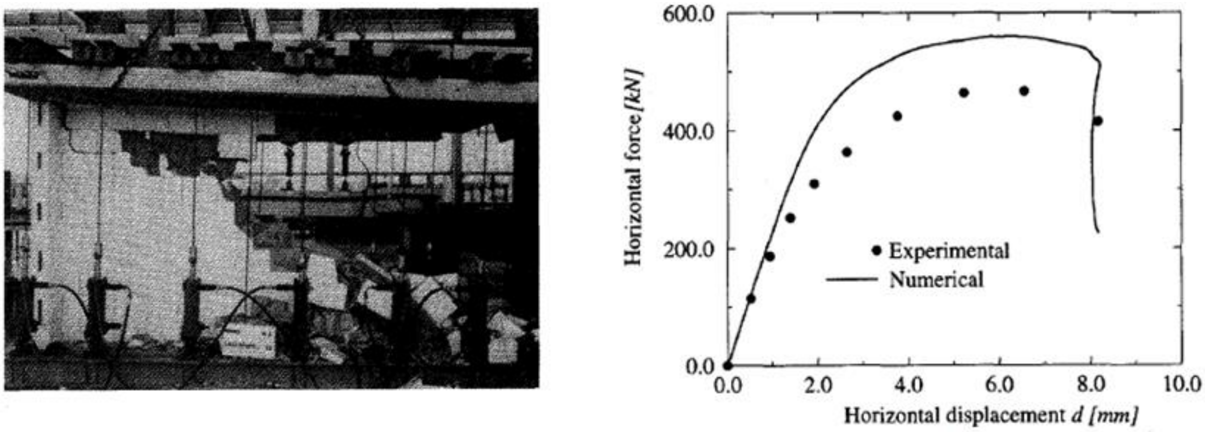

(a) (b)

Figure 3.6: The experimental failure pattern at the end stage of wall W2 as presented by [10] (a) and the load-displacement graph found from the numerical simulation as presented by [9] (b).

Another example of convergence problems are bifurcations, alternative equilibrium states, e.g. found in symmetric tests [11]. After reaching the bifurcation point, here peak-load, the structure can fail symmetrically or non-symmetrically. The non-symmetrical result is the correct behaviour, because nature is imperfect. With nonlinear finite element analysis the symmetric solution may be found, because the specimen is implemented perfectly symmetrical into the numerical model and multiple integration points can enter a same state simultaneously. In the results [12] presented in the paper (figure 3.7), a slight imperfection in fracture energy has been made for both sides of the specimen, on forcing the non-symmetrical behaviour and thus avoiding the alternative equilibrium state.

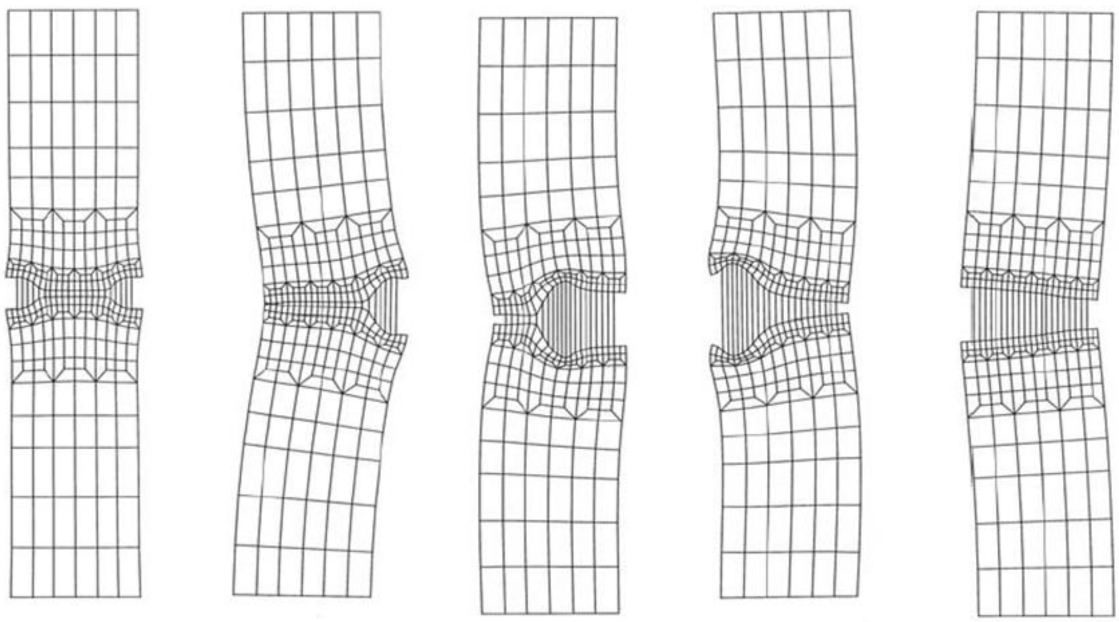

Figure 3.7: Computed incremental deformations. Left to right: pre-peak, at-peak and three post-peak states. [11]

However, the selection of imperfections, the selection of increment sizes and the selection of arc-length options is a delicate issue and often the numerical process diverges, follows an incorrect path or neglects snap-backs. Not only extra procedures like CMOD have to be followed, but also smaller adjustments like adding small deviations in fracture energy and increments have to be made to steer the analysis into the correct directions. Such intervention is not user-friendly and poses demands to the analyst, causing it to be cumbersome and often inadequate for practising engineers when the structures becomes more complex and the limitations more present.

4. The sequentially linear analysis method

An alternative method was born for cases where nonlinear finite element analysis was insufficiently robust. Its development has known a long road and it is still unfinished for commercial use. The basis has been laid via a sequence of linear analyses and contrary to nonlinear analysis always a positive tangent stiffness is present during each analysis step. The method is still in development and improved up till this day. For further reading reference is made to [1], [13], [14], [15] and [16].

4.1. The origin of SLA

At increasing loading, materials show two different types of behaviour. Before reaching the strength, the material behaves linear elastically in this pre-peak phase, for nothing in the structure has failed yet. After that and in post-peak behaviour the material is succumbing to the applied loading and does not behave linear elastically anymore. This leads to two different numerical approaches frequently used, simply put the linear elastic analysis and the nonlinear analysis.

Linear analysis is used preliminary to check if the basic input parameters are correctly implemented and/or if the finite element program produce the correct linear elastic material response. Results can be easily verified manually with hand calculations. This analysis type also gives the possibility to be able to assess weaknesses in structures in a short time by locating the maximum presented stresses. The structure has not failed yet, but the critical areas in the structure can easily and quickly be identified. For more in-depth calculations of structures, the structures can also be modelled after finishing its linearly elastic region. Therefore nonlinear analysis is commonly used, for it is well suited to follow the nonlinear behaviour of materials, such as yielding and hardening.

However, a nonlinear analysis is not always stable or shows the desired results. These problems arise for quasi-brittle materials, for which it is a challenge to model their behaviour after realising the material strength due to their sharp softening behaviour. This softening behaviour is caused by the difference between the fracture energy used and the stored elastic energy. The negative tangent stiffness, which is not present at yielding or hardening of the material, is the reason for the convergence difficulties arising, resulting in numerical instabilities and divergence.

A linear analysis always has a positive tangent stiffness and users can still find out what the critical areas are of the structure. In sequentially linear analysis a sequence of linear analysis are carried out with each subsequent analysis containing a damage increment instead of a force, displacement or time increment. The critical integration point will be assigned a reduced Young's Modulus and strength parameters to simulate damage in that particular area for the next linear analysis, while maintaining a positive tangent stiffness.

4.2. Previous developed work

The main idea of SLA is similar to the fracture analysis on lattices, where little beam elements are removed. Every time a beam element reaches its maximum capacity, it is considered completely damaged and removed from the model's mesh, instead of being given reduced properties. This lattice model can be seen as a saw-tooth curve with only one tooth. After reaching the maximum capacity, the properties are then reduced to zero, as if being removed. The lattice model only contains one damage increment, whereas SLA uses multiple damage increments, i.e. the stiffness and strength are reduced in a stepwise manner, turning the continuous softening curve into a saw-tooth curve. For the procedure of fracture analysis on lattices, reference is made to [17] and [18] as referenced by [13].

During the development of the method much attention has been given to the translation of the material behaviour into a sequence of Secant branches. One way is to reduce the stiffness by a certain factor after every cycle. Another way is to reduce the strength by a certain factor after every cycle. These models are shown in figure 4.1. Their fracture energy was not invariant and the models where mesh dependent [13]. The energy consumption is underestimated in these models.

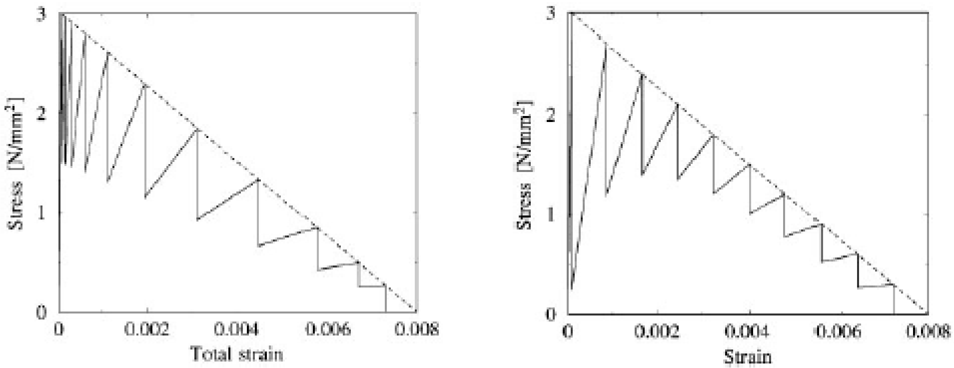

Figure 4.1: Graphical representations of damage increments with stiffness (left) and strength reduction (right). [13]

In the same paper a solution has been worked out for this issue to achieve a mesh-objective model with an invariant fracture energy. One way to improve the model is to increase the allowable stress or to increase the maximum ultimate strain. But the best improvement seemed to be applying both. These improved models are shown in figure 4.2 as model A, with a constant decreasing stiffness, and model B, with a constant decreasing strength.

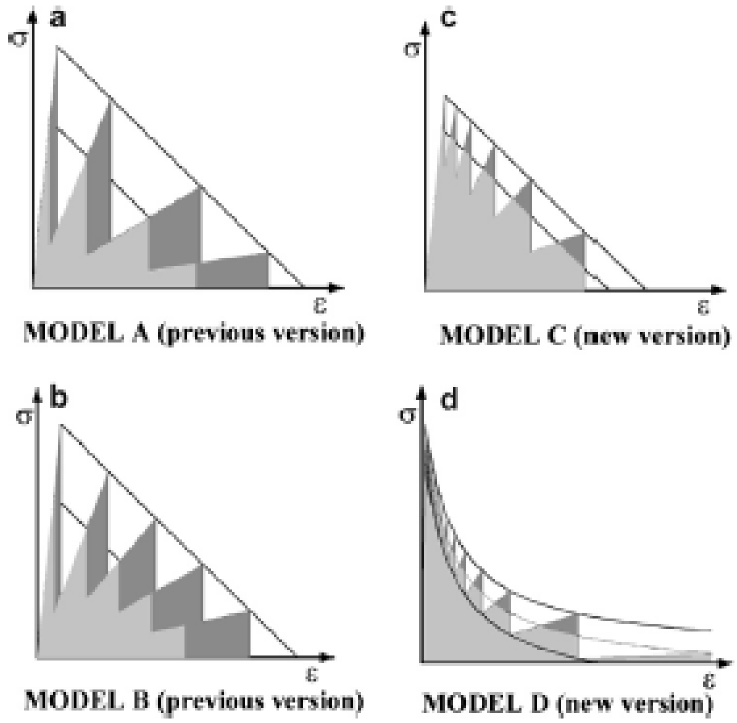

Figure 4.2: [14] MODEL A: Reduction of Young's modulus by a fixed factor.
MODEL B: Division of the softening line into equidistant portions.
MODEL C: Fixed strength range at either side of the linear softening curve.
MODEL D: Fixed strength range at either side of the nonlinear softening curve.

Although these models, model A and B, do not present the same issues as their predecessors shown in figure 4.1, it is stated that the results were not accurate enough for fine meshes with a small number of teeth [16]. Herein an improvement to these models, model C in figure 4.2, has been made by introducing a strength range. This means a strip is placed on the softening diagram delimited by two curves parallel at a constant strength distance. This new formulation of the linear tension softening diagram also keeps the fracture energy invariant and the additional mesh-size objectivity measures are not needed anymore. With the new model extensions have been made to other softening diagrams, like nonlinear behaviours as seen in model D.

Not only the sequentially linear analysis translation of the material properties have been under development, but also the procedure itself. The addition of non-proportional loading has recently been introduced and discussed by inter alia DeJong [1].

4.3. A sequence of linear analyses

The brittle behaviour of materials can thus be modelled using a sequence of linear analyses, where the softening behaviour is presented with a secant approximation of multiple branches. These branches together show a saw-tooth curve, which is a characteristic feature of the sequentially linear analysis. The procedure is described in many papers concerning this subject. Every subsequent paper implements a new subroutine or expands on an existing routine as the research on sequentially linear analysis progresses. The global flow of the most recent process, which also includes non-proportional loading, is as follows [1]:

- Apply only non-proportional load *A* with its full value.
- Perform a linear analysis.

- Apply only proportional load *B* as a unit load
- Perform a linear analysis.

- Determine the load multipliers $\lambda_{1,2}$, at which the maximum principal stress resulting from the combination of loads A and B ($\sigma_A + \lambda_{1,2} \cdot \sigma_B$) equals the current tensile strength, f_{ti}^{+}.
- Determine the critical integration point and calculate λ_{crit}.
- Apply the critical load combination by scaling the reference load *B* with the critical load multiplier, $\sigma_A + \lambda_{crit} \cdot \sigma_B$, and obtain the current stress-strain state.

- Remove all loads and update the stiffness and strength properties of the critical integration point according to the saw-tooth constitutive model.

- Go back to the first step with the updated material properties.
- Repeat until whole structure is completely damaged.

The difficulty of the SLA is mainly in finding and selecting the correct load multiplier λ_{crit}. When the material is still undamaged, thus the first step of the analysis, finding the critical load multiplier does not come with difficulties if the non-proportional load does not produce stresses that exceed the strength of the material. The minimum load multiplier can be selected as a result. It becomes more complicated, however, when the material is damaged and/or the proportional load is allowed to reverse direction, in the latter case λ is allowed to become negative. A procedure to determine the correct load multiplier for prestressed beams subjected to bending is shown in figure 4.3 [1], where γ is the principal stress direction corresponding to λ, the load multiplier, needed to determine the orientation of the crack.

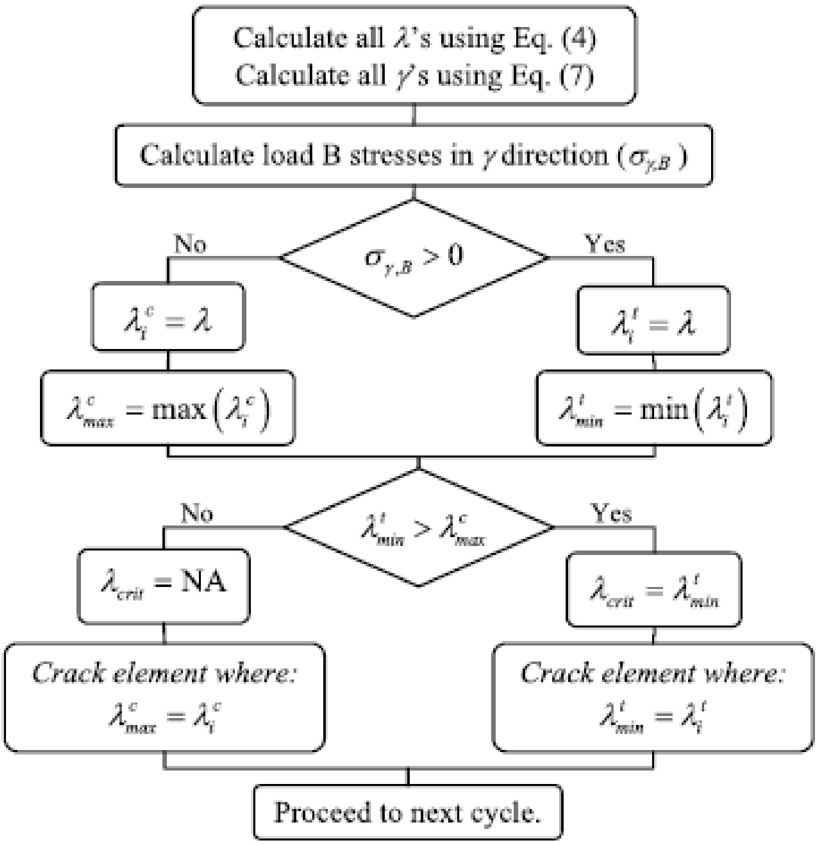

Figure 4.3: Flowchart for selection of the critical integration point and the critical load multiplier, λ_{crit}. [1]

This procedure can sometimes not find a suitable critical load multiplier for any situation. Every load multiplier available will result in exceeding the ultimate state somewhere in the structure. In these cases the latest successful total load, proportional and non-proportional together, is scaled with an overall multiplier until equilibrium is reached. This means that temporarily less non-proportional load is applied to fulfil the requirements as shown in figure 4.4. [19]

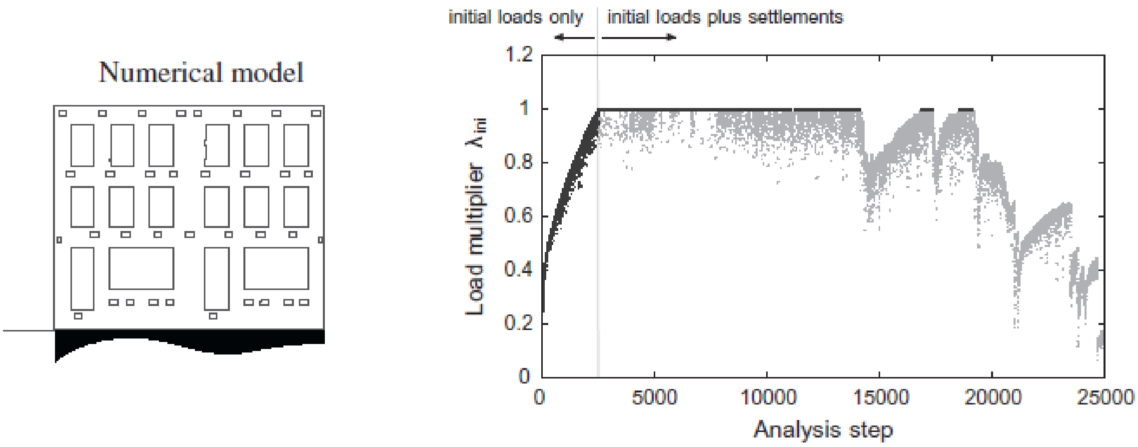

Figure 4.4: Evolution of the initial load multiplier λ_{ini} throughout the simulation with SLA on a masonry structure subjected to tunnelling-induced settlements. [19]

4.4. Material representation

In this section there will be globally explained how the saw-tooth curves are constructed for constant, linear (figure 4.2: model C) and nonlinear (figure 4.2: model D) softening. Although the SLA version used also supports more complex softening curves such as a Hordijk and a Moelands & Reinhardt tension softening, they will not be used in this research. The new method uses a total strain, orthotropic fixed crack model that decreases the stiffness and strength after reaching the maximum capacity in an integration point. For more detailed explanation on each individual softening curve, reference is made to [16].

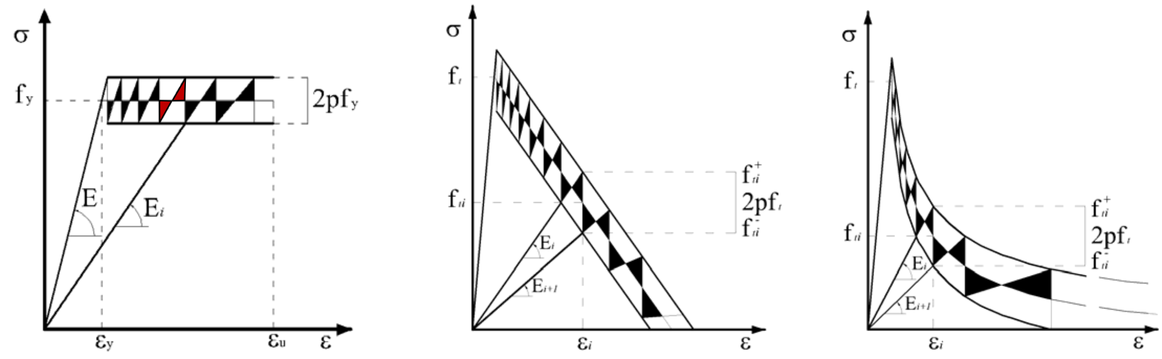

Figure 4.5: Saw-tooth curves for constant (left), linear (centre) and nonlinear (right) softening diagrams.

On the base diagram a strip is made with a width of $2pf_t$, with p representing a percentage and pf_t a fraction of the maximum allowable strength. The maximum allowable stress is now enlarged to f_{t1}^+. With each damage increment, maximum stress reached, the stiffness and strength reduces. This results in a new upper and lower bound values, f_{ti}^+ and f_{ti}^- respectively, where f_{ti}^+ becomes the new maximum allowable stress. A new piece of the saw-tooth curve can be constructed with these values. This is repeated until the material is totally damaged.

As can be seen in the figures, the fracture energy is indeed invariant. Every upper triangle has a lower triangle of the same magnitude. This has been indicated with two red triangles in the left picture of figure 4.5. So, every overestimated area is cancelled out, leading to the same area under the ripple diagram as under the original base diagram if the ultimate strain of the ripple diagram is the same as of the base curve.

The method to construct the saw-tooth curve for nonlinear softening curves is more complex. An approximation method is used following the bilinear Model Code 90 curve [16]. Figure 4.6 shows this idea. The construction is not as straight forward as the other two models, but for further detail on the bilinear Model Code 90 reference is made to [20] as referred in [16].

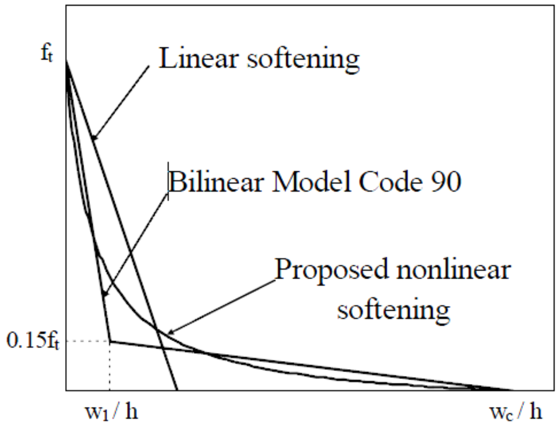

Figure 4.6: Nonlinear softening curve stress-crack strain, approximating the bilinear Model Code 90 curve.

In comparison to NLFEA the material properties are damage dependent. This is thus also the case for Poisson's ratio and the shear modulus. In NLFEA the shear modulus can be made dependent on a shear retention function β. This shear retention function is not used anymore in SLA for the shear modulus is dependent on the damaged Young's modulus and reduced Poisson's ratio as well as on the initial values of these parameters in the following way [21]:

$$G_{red} = \frac{E_{min}}{2(1+\nu_{red})} \qquad E_{min} = \min(E_n, E_t) \qquad \nu_{red} = \nu_0 \frac{E_{min}}{E_0}$$

Figure 4.7: Damaged material parameters for SLA.

4.5. The potential of the method

It is mentioned that in NLFEA analysis the load is incremented in finite steps. The use of these finite steps ends up in multiple integration points being able to enter a damaged state simultaneously, obtaining symmetrical results, a so called bifurcation. In SLA a damage increment is applied, meaning that in each step only one integration point can enter a damaged state. This results in always obtaining an asymmetrical result and circumventing the symmetrical bifurcation.

A negative tangent stiffness can also not be obtained anymore. SLA makes use of a sequence of linear analysis, meaning that the softening behaviour is replaced by a sequence of positive secant branches, instead of following the softening branch with a negative tangent stiffness. The matrices obtained will never be ill-defined, resulting in always gaining results, even if the material behaves very explosive.

It also mentioned that with cumbersome procedures positive results can be obtained with NLFEA if snap-back and divergence are not becoming huge problems. This issue is overcome by the use of damage increments. This makes SLA present a subsequent damaged state instead of skipping a lot of damaged states, due to the application of for example a displacement increment. With this ability to see subsequent damaged states snap-back and snap through behaviour can always be monitored with SLA and the full behaviour visualised.

4.6. Method in development

As stated before the method is still in development. The goal of this thesis is to confirm that sequentially linear analysis is a sufficiently robust method to model brittle structures with respect to combined tension-compression failure. Meanwhile, other researchers have been playing a part too in improving the numerical method.

M. Kabos [22] added a compression failure criterion to the existing SLA source code to model shear-compression failure in concrete beams. For this a parabolic compression softening model was used, with a fracture energy regulated by a bandwidth parameter called the “crush bandwidth”. Based on results the crush band model was adjusted for numerical localization and crack orientation.

Others, such as A.T. Slobbe, are focussing on improving crack bandwidth estimators and crack propagation algorithms. A. van de Graaf studies the addition of non-proportional loading on structures and the implementation of material models for interface elements in the sequentially linear analysis method.

5. Masonry behaviour and modelling options

Masonry has an aesthetic appearance, is a durable material and is handled easily on site. It is a composite material with brittle characteristics. Its inhomogeneous nature gives rise to different failure mechanics. To implement this versatile material behaviour different approaches and material models are used to achieve this goal, such as micro-modelling and Rankine-Hill plasticity. Reference for an overall idea about masonry is made to e.g. [2], [9] and [23].

5.1. Constituent parts of masonry

Masonry consists of typical three parts: the solid units, the mortar joints (head and bed joints) and the unit-mortar interface. Each of these individual parts have their own non-linear behaviour. The solid units and the mortar can be considered to have brittle characteristics for they both are stone-like materials. The connection between the two, the unit-mortar interface, can often be seen as the weakest link in the structures. Cracks often appear alongside these interfaces. While the units and mortar are mostly responsible for the compressive behaviour, this interface between the two is mostly responsible for the tensile and slipping behaviour in masonry structures.

Being a very brittle material, masonry reacts sensitively to unevenness. This effect is most noticeably at masonry buildings subjected to tunnel induced settlements, where the ground continuously provides the unevenness, or at highly changing temperatures, making the structure crack due to repeated expansion and contraction. For situations like placing a masonry wall on a concrete floor, a kicker joint levels out the tolerances in the surface of the foundation. The kicker joint can be seen as the first big bed joint of the construction. This provides a smooth layer, which is subjected to compression, providing an optimal starting position for the masonry wall. The effect of the thickness of a kicker layer has a negative effect when the strength of the units are considerably higher than of the mortar of the joint itself [24].

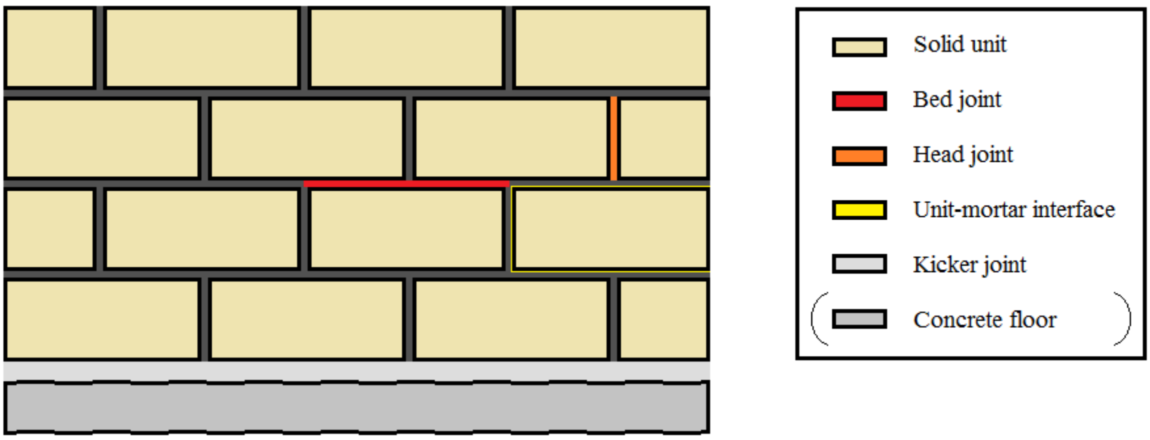

Figure 5.1: Constituent parts of masonry.

5.2. General characteristics

Masonry is dependent on the composition of the units and the mortar and the treatment of the unit-mortar interface. Masonry is known to be commonly seen as a material with orthotropic elastic characteristics. In the direction parallel and perpendicular to the bed joints different values are assigned to the material properties. The material can be seen as a laminated material with units and mortar, where the unit-mortar interface acts as a type of glue holding the layers of units together. This makes the material well suited for compressive loading, but ill-suited if it is loaded in tension or shear. Masonry acts very stiff in linear elastic conditions, making post-peak behaviour seem very explosive.

5.2.1. Units and mortar

As mentioned before, the units and the mortar are stone-like materials, which are, like concrete, very dependent on their mixtures. This means their softening behaviour will follow the typical post-peak path for these kind of materials, as presented in figure 5.2. Softening is a gradual decrease of mechanical resistance under a continuous increase of deformation forced upon a material specimen or structure. It is a salient feature of these quasi-brittle materials which fail due to a progress of progressive internal crack growth. Initially there are micro-cracks in the material which are stable. They only grow when the load is increased. After reaching the peak load an acceleration of crack formation occurs, however, and unstable macro-cracks appear. Unstable means that the load has to decrease in order to avoid an uncontrolled growth of cracks. This is the softening behaviour that is perceived during experiments [25].

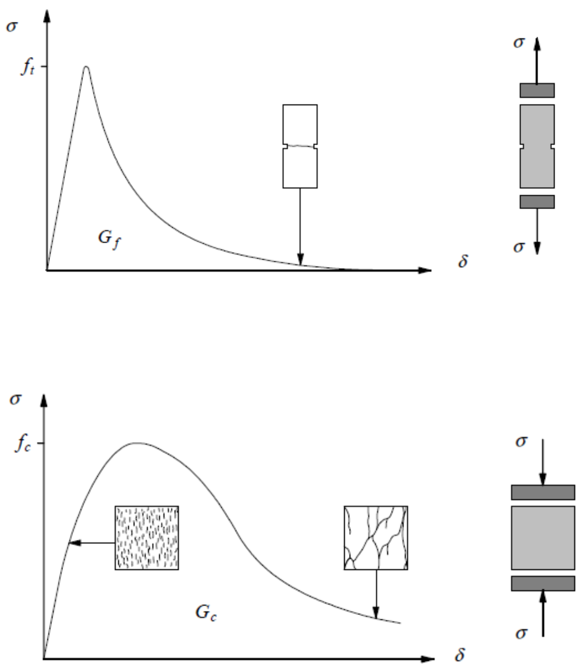

Figure 5.2: Uniaxial material behaviour of stone-like materials. [2]

5.2.2. Unit-mortar interface

The properties of the unit-mortar interface are dependent on the composition of the mortar and unit as well as the real bonding surface. Water plays an important role in the bonding of these two elements [26]. During the building process water of the mortar is sucked into the pores of the units. This water carries cement particles from the said mortar and these particles are spread along the surface of the units, creating a bond between mortar and units by small cement arms hooked into the face of the units. A lack of water results into a lack of this transmission, resulting in a lower strength bond. It also results into a lack of spreading, making the area of adhesion of the masonry specimens after fracture considerably smaller than the full area of the specimen. An extensive use of water will liquefy the mortar, making hardening of the specie a long time procedure. The net bonding is determined by “looking” and experimental results showed that indeed not the full area is used for bonding after cracking [2,26]. These resulted in the tensile behaviour as seen in figure 5.3. The interface tension failure softens exponentially, like the behaviour of the units and the mortar.

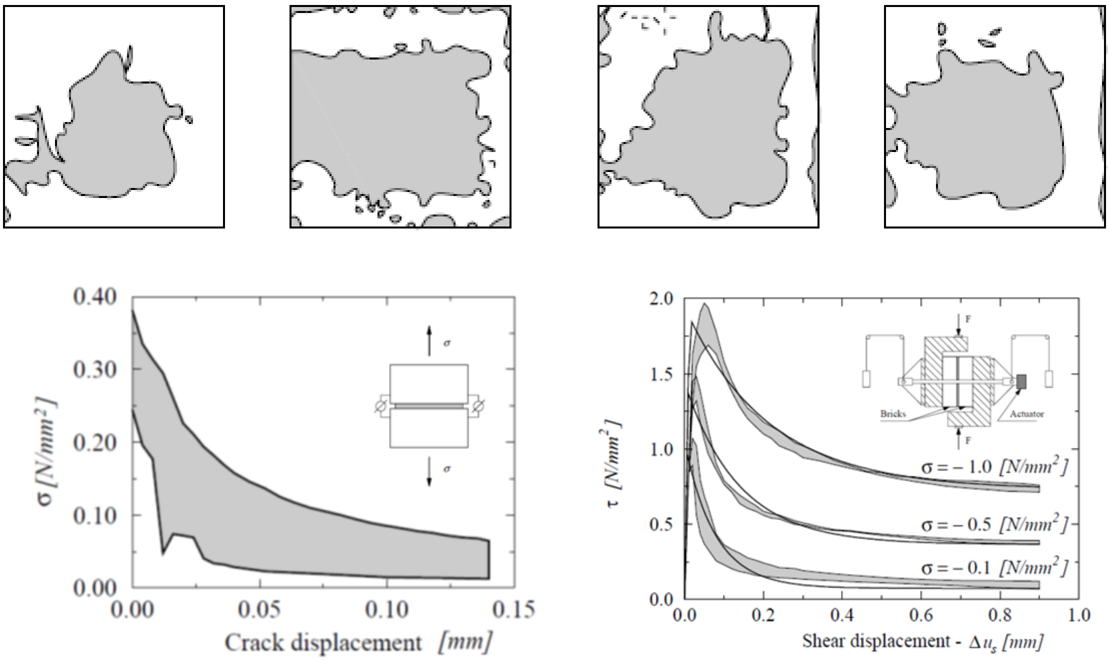

Figure 5.3: Bonding surface of different specimen (top) and unit-mortar interface behaviour (bottom). [23]

The shear behaviour of the unit-mortar interface also showed exponential softening. The limit point of the shear is however dependent on the compressive strength applied on the specimen. This is expected, because after slipping has fully developed there is still, due to the compressive loading, contact between both sides of the cracked interface. This roughness results in some cohesion between the unit and mortar resulting in the possibility to still transfer shear stresses.

5.2.3. Masonry

The ratio in tensile strength between the mortar and the units is dependent for the type of post-peak behaviour. Most of the time the units can sustain much more loading than the mortar, resulting in cracks between the units. However, when this is not the case the cracks can run through the units itself. In the case of tensile loading parallel to the bed joints this results in different outcomes as shown in figure 5.4. For loading perpendicular to the bed joints tensile softening for the mortar bed joints can be assumed.

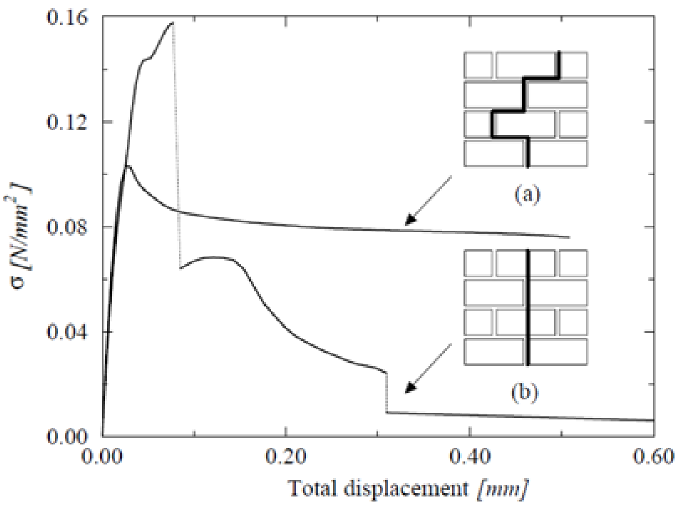

Figure 5.4: Masonry behaviour when units are considerably stronger (a) and when the mortar is (b). [23]

Masonry loaded under compression perpendicular to the bed joints has been tested and it was noticed that difference strength in mortar influenced the behaviour of masonry [27]. If a stiffer kind of mortar is used a stiffer response and more brittle response is seen as masonry behaviour. In most cases the mortar has lower compressive strength than the solid units, but a higher Poisson's ratio. This results in "squeezing out" of the mortar between the units, resulting in extra tensile stresses parallel to the joint direction. This gives a larger crack than when the mortar is lower in strength, thus reducing the maximum stress the specimen can sustain. This phenomena is researched and found to be true in practice [28], see figure 5.5. Loading parallel to the bed joints is not researched considerably, for the aim is to have the bed joints under the main compression and not the head joints.

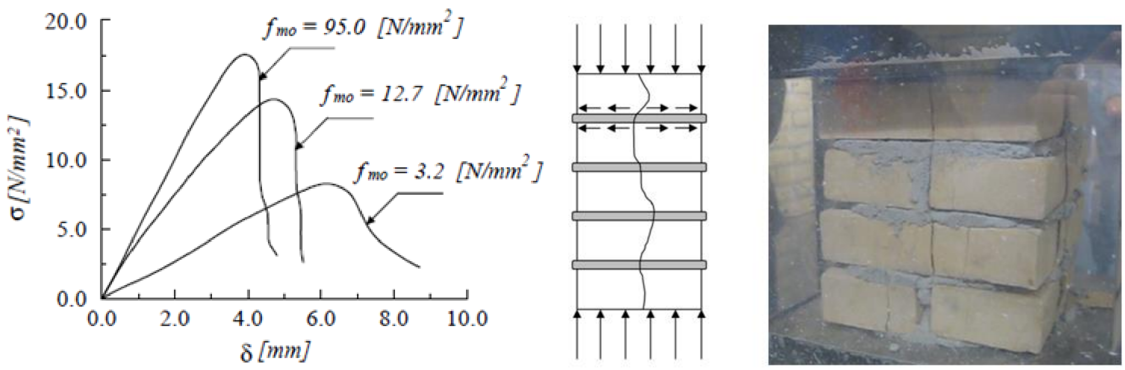

Figure 5.5: Effect of "squeezing out" of the mortar. [23]

Masonry subjected to biaxial loading can result in different failure mechanisms, depending on the properties of the individual parts of masonry. For a two dimensional problem, where the out-of-plane loading and out-of-plane failure is not considered, the possible failure loads are threefold according: Slipping of mortar joints, cracking of elements and splitting of mortar joints, and crushing of the elements [29]. These failure modes can be combined and further scrutinized to for example the nine failure modes [30], but the basis of tensile, compression and shear failure remains the same. A.W. Page [31,32] carried biaxial tests out to present a failure surface, thus a situation up to peak-stress, with different directions of the principal directions (figure 5.6 and figure 5.7) and is often use to validate models. Both the orientation of the principal directions to the axes of the material and the ratio of the principal stresses considerably influence the failure modes observed and strength recorded.

As a sidenote to biaxial material properties, it has to be stated that limited is known compared to the other properties of masonry. There are no experimental results available for example for the influence of lateral tensile stress in the tensile strength [9]. It is further unknown if the failure surface developed by A.W. Page [31,32] is independent of the loading path, as is the case with concrete [33]. Moreover, although the basic idea is the same, the failure surface has to be adjusted for other applications of masonry due to the difference in failure modes occurring and strength envelopes found for different masonry materials, unit shapes and geometry. For the latter studies have been carried out in Switzerland for example for hollow clay units masonry and for concrete units masonry.

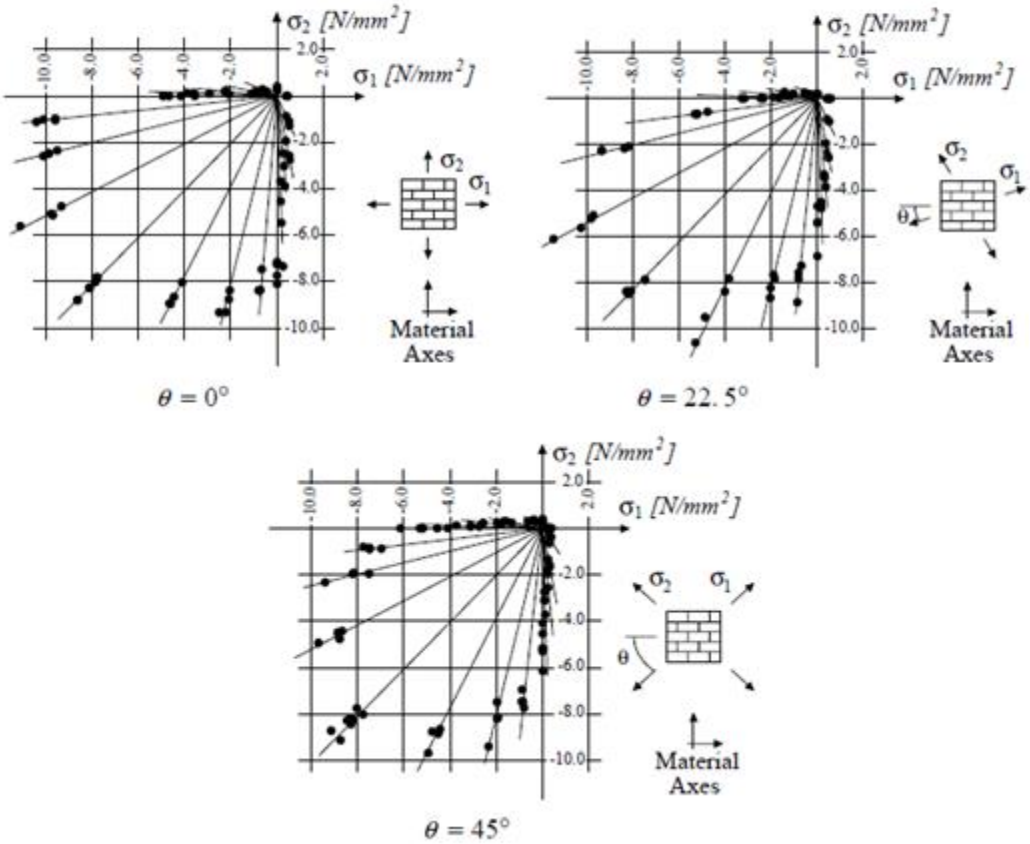

Figure 5.6: Different failure surface for different loading directions. [23]

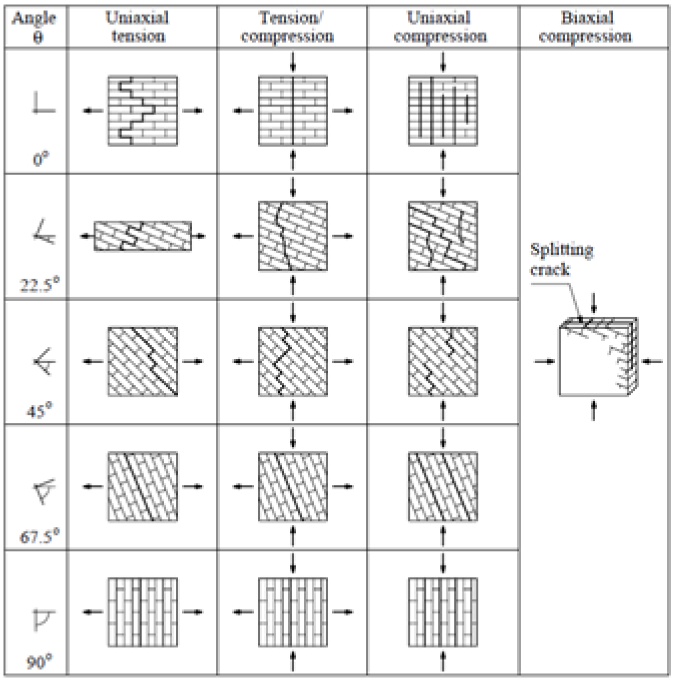

Figure 5.7: Different failure mechanisms. [23]

5.3. Numerical modelling of masonry

Masonry is a quasi-brittle material. The constitutive behaviour of masonry is, like other brittle and quasi-brittle materials, characterized by tensile cracking and compressive crushing. Furthermore, long-term effect like shrinkage play a part. However, the latter will be left out of the research. The cracking is an important phenomena in masonry structures and good care has to be taken to implement the most correct cracking model.

5.3.1. Cracking models

There are in total three major crack models available to simulate cracking in continuum elements and in total two crack models to simulate cracking with interface elements in DIANA, see figure 5.8. Used in the models are Multi-Directional Fixed Cracking, as recommended by the DIANA manual, and Total Strain Cracking Model. Both are combined with the Discrete Cracking Model for the interface element. Details about the respective crack models can be found in [5, 34].

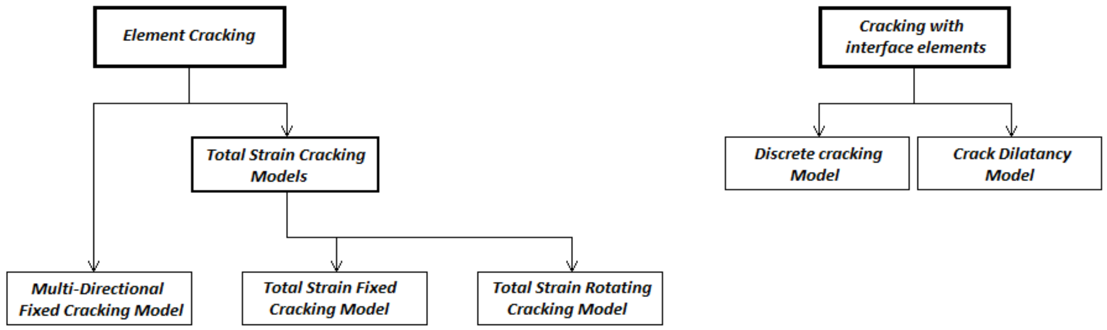

Figure 5.8: Cracking models.

In the multi directional fixed cracking model only cracking is considered with a tension cut-off, tension softening curve and a shear retention function. The model is rather limited with input possibilities and applications. This model can be combined with other constitutive models. This means that the lacking parameters can be augmented with other plasticity models. Multiple cracks can occur in an element, each having their own respective *nt*-coordinate system.

Total strain cracking models are based on total strains, while the previous one divided the strains in an elastic and cracked component. Both tension and compression are described with one stress-strain relationship. Because it encompasses the whole constitutive model, it cannot be combined with other models. The Total Strain Rotating Crack Model, also known as the coaxial stress-strain concept, is part of the orthogonal crack models. The model is mostly applied for reinforced concrete. The axis of the coordinate system rotate continuously with the principal stresses. The Total Strain Fixed Crack Model is more suitable for the use to research the physical nature of cracking. Here the stress-strain relationships are evaluated in a fixed coordinate system.

5.3.2. Methods of modelling

Masonry is mostly modelled in three ways as can be found in literature [2,9,35]:

1. *Micro-level*; where the material is modelled in detail, with interface thicknesses.
2. *Meso-level*; where the whole material is taken as a heterogeneous model, with interface thicknesses of zero. All the information is thus lumped into the units.
3. *Macro-level*; where the whole material is taken as one homogeneous material.

All models can be found in figure 5.9.

In the first case (figure 5.9.b) a comprehensive analysis of masonry shows the full model interaction of the masonry with continuum elements for the units and mortar, while the unit-mortar interface is represented by discontinuous elements. The Young's modulus, Poisson's ratio and, optionally, inelastic properties of both unit and mortar are taken into account, while the interface represents a potential crack/slip plane. Such a detailed representation of masonry demands a highly defined mesh, especially where perpendicular and longitudinal joints cross each other, and a large amount of memory, resulting in long computational time required for the calculation. However, micro-modelling approaches are well suited for small structural elements with strong heterogeneous states of stress and strain. Nevertheless, it is not used often due to the aforementioned limitation.

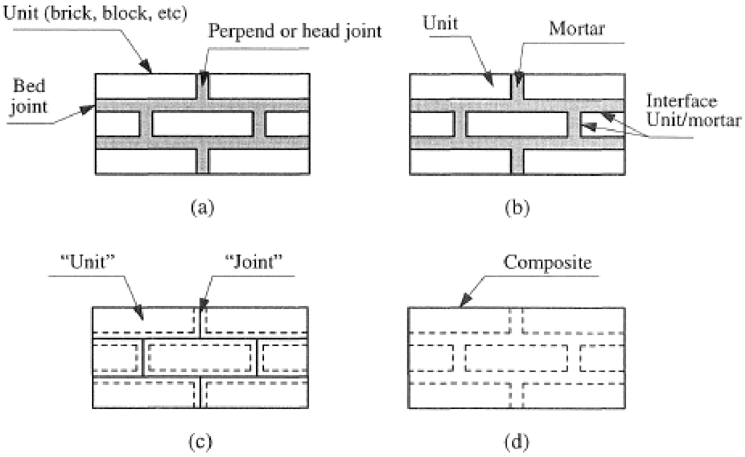

Figure 5.9: Methods of modelling with masonry sample (a), micro-modelling (b), meso-modelling (c) and macro-modelling (d). [23]

In a simplified micro-model the interface element is used for the joints, including both areas of adhesion, so that considerable fewer elements are necessary, reducing the computational effort. However, a disadvantage is that the effect of transverse contraction is now neglected and this scheme does not meet the requirements of rotational equilibrium. Corrections are needed with regards to the thickness of the interface elements, because interface elements only function properly when the thickness is zero.

In the meso-level of masonry modelling (figure 5.9.c) the interface element's thickness is zero. However, this means that the mortar is not modelled anymore and the information of the mortar is lumped together with the solid units. These "blown-up" units have adjusted values to facilitate the mortar-unit interaction. Therefore a translation is needed to attach these new adjusted mechanical properties to the blown-up units. This translation is pictured below in figure 5.10 [2].

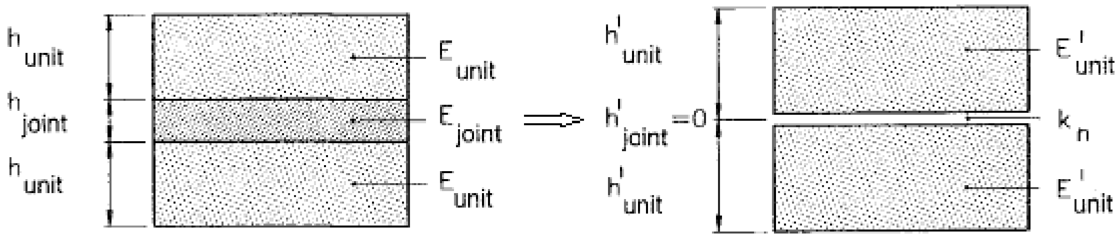

Figure 5.10: Scheme to determine the stiffness k_n. [2]

The macro-level (figure 5.9.d) considers the masonry as a whole anisotropic or isotropic homogeneous material. This model is mostly used in large and practice-oriented analysis and in these analysis the distinction between individual units and joints is not made. Although this type of modelling demands the least computational effort, it must be clear that the results are average and global. Local failure mechanisms of joint and units cannot be found. The method is however especially suitable where a detailed simulation of the crack propagation is neither possible nor desirable [2], like in the building modelled and shown in figure 5.11.

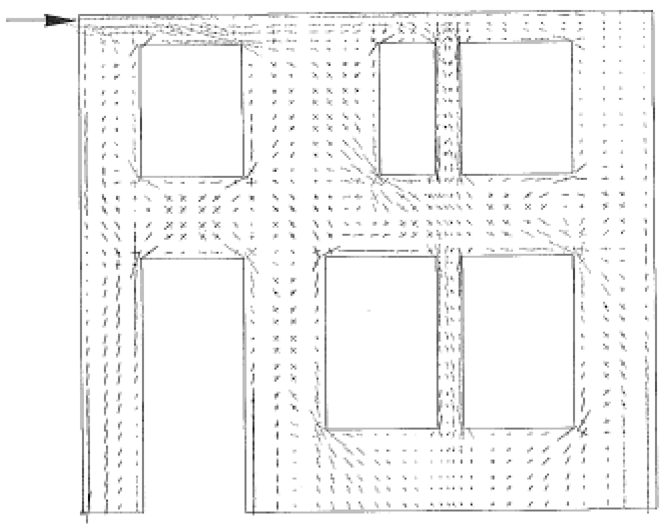

Figure 5.11: Example of global continuum modelling of masonry as a composite. [2]

5.3.3. Material models for continuum masonry

The most commonly used material model as a base for masonry structures is the Rankine-Hill model. This model was created, alongside other models, to describe the masonry behaviour as presented by A.W. Page [31,32]. This plasticity model consists out of an anisotropic Rankine yield criterion for the tensile and tensile-compressive region, while an anisotropic Hill criterion is used for the compressive region. This makes the whole model anisotropic, which means that masonry is thus overall modelled with parameters in both x- and y-direction. Post-peak behaviour is then commonly modelled by exponential softening in tension and parabolic hardening followed by a parabolic and exponential softening branch in compression. The model can be simplified to more general concepts such as isotropic models for homogeneously simulated structures.

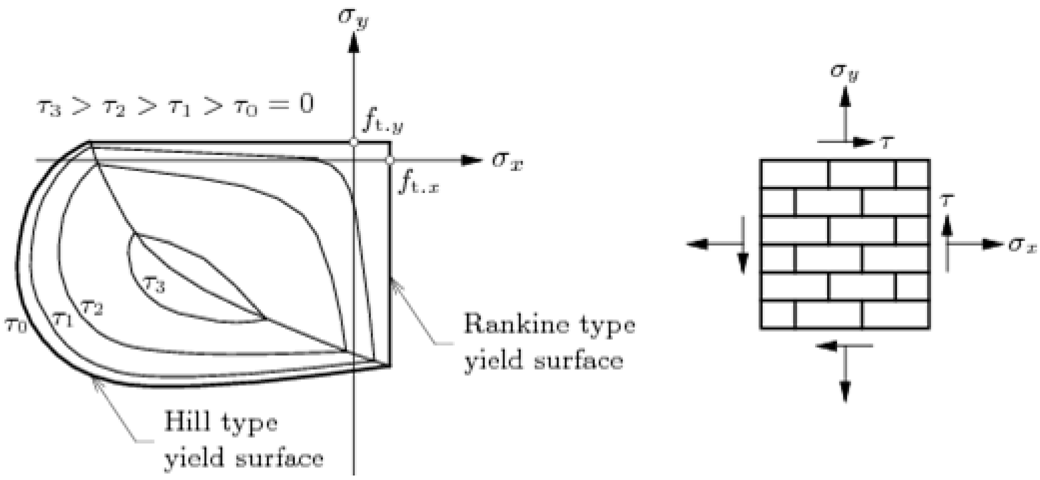

Figure 5.12: Rankine-Hill plasticity model. [9]

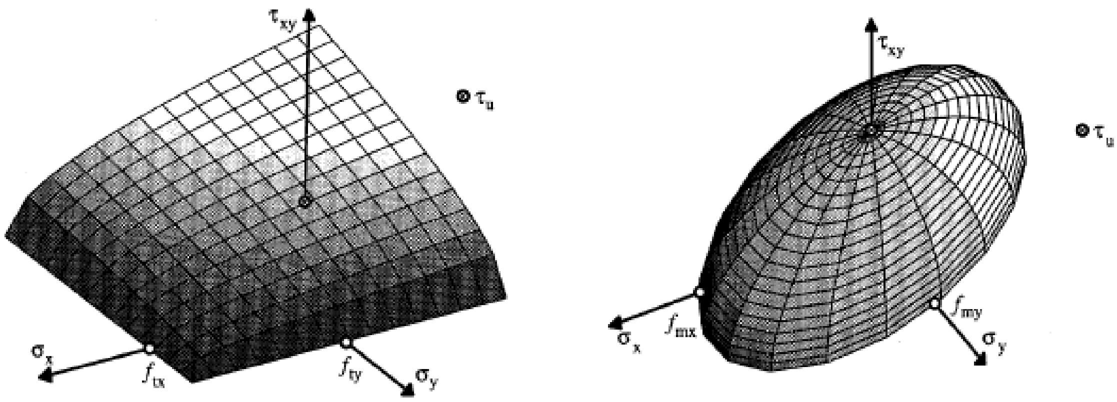

Figure 5.13: 3-D representation of Rankine-criterion (left) and Hill-criterion (right). [9]

5.3.4. Material model for discontinuum masonry

Discontinuum masonry must include all the basic types of failure mechanisms. Commonly the approach followed [2,9] is to concentrate all the damage in the weak joints, and if necessary in the centre of the units as pure tensile cracks. The interface elements of the joints have to account for a combined failure of crack formation and slipping. The discrete cracking of the interface is dealt with a tension cut-off accompanied by some sort of softening behaviour if the maximum allowable stress has been reached. The shear stresses and combinations with compressive stresses is dealt with a coulomb friction model, a failure envelope. This model is also accompanied by some kind of softening behaviour if the shear stress, dependent on the cohesion and internal friction, exceeds its maximum. To account for compressive criteria a compressive cap can be placed on the combination of these models.
hfhgh

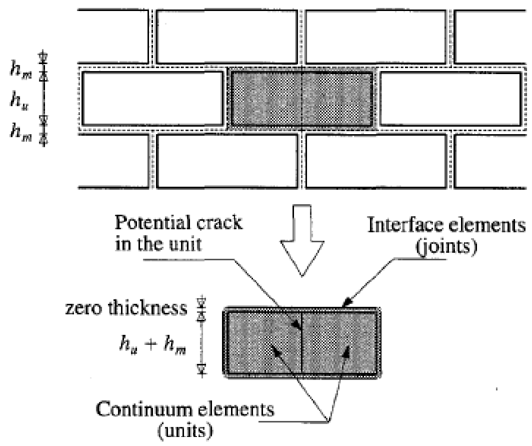

Figure 5.14: Commonly used discontinuum model for masonry structures. [9]

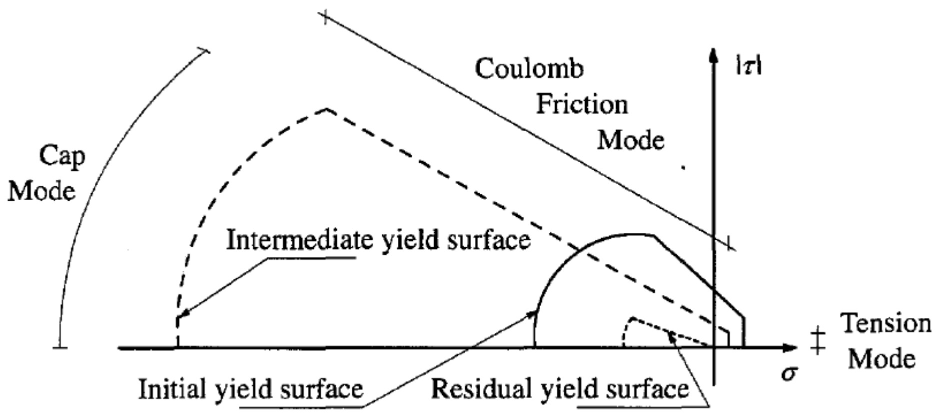

Figure 5.13: The composite interface model, the Coulomb-friction model. [9]

6. Masonry deep wall on a frame

The casus used to test the sequentially linear analysis on combined tension-compression failure is a calcium silicate wall supported by concrete beams lain on steel columns as shown in figure 6.1. This casus is applied in a lot of buildings, in which the lower storey contains for example commercial spaces and the upper storeys are reserved for residential use. The relevance of masonry research as well as the research performed with respect to masonry and the casus is discussed in this chapter. The casus is described and lastly the general loadpath is shown as presented by predecessors.

6.1. Relevance of masonry research

Throughout the years, natural sandstone (aside from other solids used for masonry, like rock) has always been popular way to construct housing, temples and it was even used for artistic purposes in ancient Rome, like the construction of statues. The natural sandstone can be found for example in rivers and lakes, making its availability plentiful and thus cheap. It also is relatively soft, making it easy to handle and work with. In those times construction knowledge was empirical and traditional [2,9].

In the 19th century the material could be made artificially in fabrics. In the beginning the production of these bricks were cumbersome. The bricks had to dry first, lasting several weeks. Afterwards they were heated at high temperature, which does not come cheap. But in 1894 it was possible to produce calcium silicate bricks on an industrial scale by using a rotating press. Further development in manufacturing techniques took place to make buildings more labour-saving. Nevertheless, due to this contribution of the Industrial Revolution, in countries where there was a lot of sand available, like the Netherlands, the calcium silicate brick became an important structural material. Masonry was more common, but it did not lose its empirical nature of construction.

Nowadays calcium silicate elements can compete with in-situ concrete constructions for relatively small projects. It is mostly used for the construction of load bearing walls. The material requires less space on the construction site for it can be stacked easily and the elements are more adaptive to the demands of the builder. However, for bigger projects, like multi-storey buildings, concrete and steel still remain the preferable construction material.

The masonry branch wants to be allowed to make structures out of masonry for high rise residential buildings up to fifteen storeys and increase its market share, but according to the building codes it is not possible to construct these structures if the load bearing capacity is interrupted by free space, like a garage or commercial space. The shear stresses would exceed the limits in the standards. However, it is believed that the structure can withstand larger forces and that the building codes are on the safe side. But the lack of knowledge prevented the branch to expand.

6.2. Previous research on the casus

In 1987 these gaps in knowledge of masonry were recorded by the CUR PC55 pre-advisory committee, confirming the safe nature of the design codes. The technical-scientific development of design rules has lagged behind compared to concrete and steel, resulting in decrease of market share. In 1989 the CUR PA33 pre-advisory committee outlined a new scientific approach to structural masonry with the integration of numerical mechanics and experimental techniques. This resulted in the research programme “Structural Masonry I”, which was carried out by TNO Building and Construction Research, Eindhoven University of Technology and Delft University of Technology. This research was started by the Royal Dutch Association of Brick Manufacturers and supported by the calcium silicate industry for it would give more knowledge about their material. Its main objective was to create a basis for general approach towards structural masonry. Results are beneficial for the widening of the usage of calcium silicate elements in other applications, like a multi-storey masonry buildings. Results of the research “Structural Masonry I” can be found in CUR-Report 171 [2].

The latter research did not discuss a multi-storey building. Therefore, a subresearch was carried out with the same research design as the original one. In Eindhoven University of Technology laboratory experiments have been carried out by R. Sterrenburg [4] to obtain experimental data to be used in numerical models. This data, alongside with other data found by other researchers has been taken into account in the numerical modelling of J. Martens [3] at Delft University of Technology. The aim of both works were to obtain mechanical behaviour of a masonry wall supported by a frame.

However, J. Martens [3] modelled the brittle structure with standard nonlinear analysis techniques. This analysis type can become unsuitable for quasi-brittle materials like concrete and masonry due to ill-defined stiffness matrices created by negative tangent stiffnesses. Therefore, difficulties were encountered during the process, such as the explosive tension-compression behaviour in the lower corners of the wall, that limit the progress of the research into modelling the behaviour of brittle materials. When such limitations are encountered one can seek to improve the existing method, creating a variant, or make a new alternative method and bypass the limitations.

Such an alternative is sequentially linear analysis. This analysis type does not use a negative stiffness to describe post-peak behaviour, but a sequence of positive tangent stiffnesses. Although the analysis type can potentially bypass the limitations of nonlinear analysis, it is still in development. For example, checks have to be carried out if the structure behaves accordingly using the SLA under combined tension-compression failure. Being that in this casus the structure is heavily subjected to combined tension-compression failure at the supports (between wall edge and lower beam) it is an excellent casus to not only answer this research question and compare it with previous obtained data, but also simultaneously continue the research of the casus itself.

6.3. Description of the structure

The casus used to test the sequentially linear analysis on combined tension-compression failure is a deep wall on a column-beam system as shown in figure 6.1. This casus is applied a lot in buildings in which the lower storey contains for example commercial spaces and the upper storeys are reserved for residential use. The loadbearing wall is thus interrupted by free space and the forces of the wall have to be transmitted to the columns underneath.

The whole casus is scaled for laboratory use. The wall is made of masonry consisting out of calcium silicate bricks. On top and under the wall concrete beams are placed. These beams have slightly different properties and dimensions and its influence was one of the research purposes of predecessors [3,4]. These beams were reinforced in the laboratory experiments. The ensemble is placed on two steel profiles representing the columns. Between the columns there exists free space, simulating the non-bearing area used for e.g. commercial use.

Loading is applied twofold. During the experiments first the lower concrete beam is pushed downward as if floor loading is present. After fully applying the non-proportional (constant) floor load, two jacks apply a deformation proportionally. These two loads are spread out by steel profiles creating four points of loading on the top concrete beam. This roughly simulates loading of higher storeys that are placed above the first level.

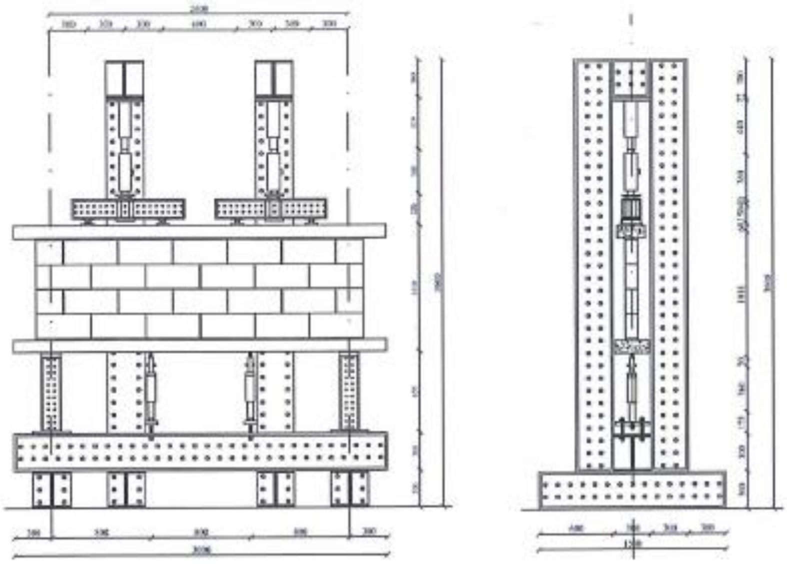

Figure 6.1: The structure used as casus. [4]

6.4. General loadpath

From experiments performed by J. Martens and R. Sterrenburg [3,4] the general loadpath in the construction can be determined. The construction fails in four steps during the application of the total load. Firstly, during the application of the non-proportional (constant) floor load, the kicker joint is damaged and the lower concrete beam separates itself form the masonry wall (figure 6.2.a). In total around 40 kN were needed to make the separation happen.

Starting with the proportional load applied by the jack forces, the structure will develop compressive struts from the points where the load is applied directly to the supports, the steel beams. This creates a large tensile band through the lower part of the masonry wall and the lower concrete beam, while creating a compressive zone in the top part of the construction. This is comparable with a classic bending test and because the tensile strength is lower than the compressive strength of the masonry wall, secondly, a vertical crack in the centre of the masonry wall starting from the bottom appears after applying around 100 kN (figure 6.2.b).

The compressive struts remain, but the tensile band is now interrupted. The tensile stresses need to find an adjusted path which results in spalling cracks as compression increases. In the experiments these spalling cracks appeared as diagonal cracks throughout the construction after applying around 230 kN (figure 6.2.c). Apparently, these cracks were to happen earlier than crushing of the compressive struts in the corners according to [3,4]. The corners are starting to crush however, for part of the load is carried through the lower concrete beam.

Lastly, also the lower corners are succumbing to crushing, according to private communications with the supervisors (figure 6.2.d). It was also stated that the spalling cracks and crushing are mechanisms with their point of occurrence close to each other for both are part of the failure of the compressive struts. However, this crushing has not been found by [3,4].

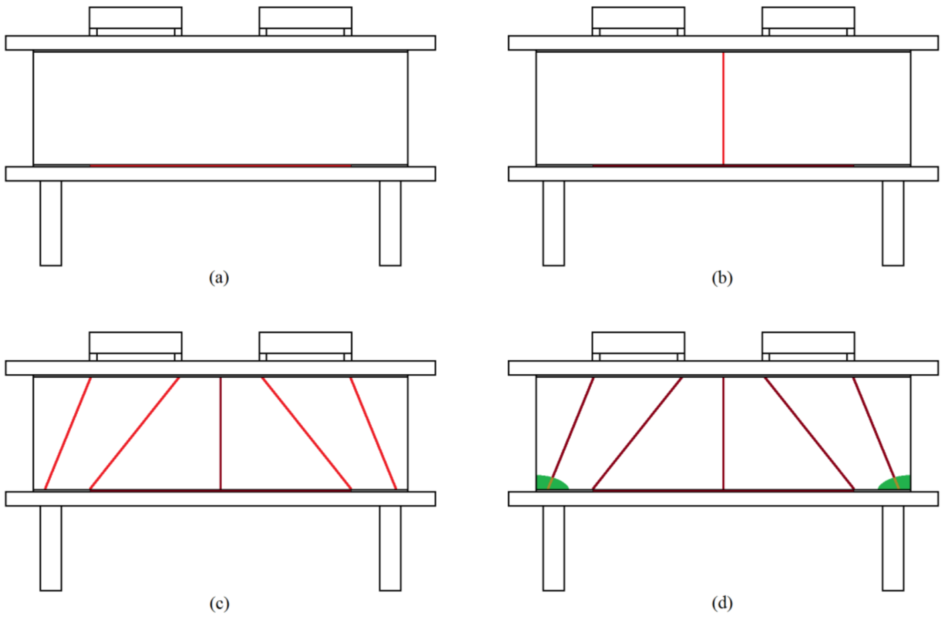

Figure 6.2: Order of failure as found in literature [3,4] and private communications.

BODY

Exploratory analyses, numerical verification and masonry deep wall-frame validation

7. Exploratory analyses

At the start of the research a look has been taken into using NLFEA to obtain post-peak behaviour of masonry structures. The aim was to get a feel of the arising difficulties accompanied with the numerical method as stated in many literature. To achieve this goal, the calculations done by J. Martens [3] to obtain a fully functional homogeneous nonlinear numerical model were remade.

The same has been done for sequentially linear analysis to confirm the potential as presented in literature. An older, simpler model of sequentially linear analysis was then applied on the same structure to experience the positive outcome of this alternative method by comparing it to its nonlinear finite element counterpart.

Both exploratory analysis are found in this chapter. Both models show simplified implementations of the structure as well as the numerical models. However, this is enough to get an understanding for it is not the goal of this exploratory analysis to scrutinize the behaviour of masonry.

For these nonlinear finite element analyses the same masonry wall supported by concrete beams lain on steel columns is used as discussed in Chapter 6. The material properties and the behaviour of this structure are added in steps or are partially used to reach the aimed goals.

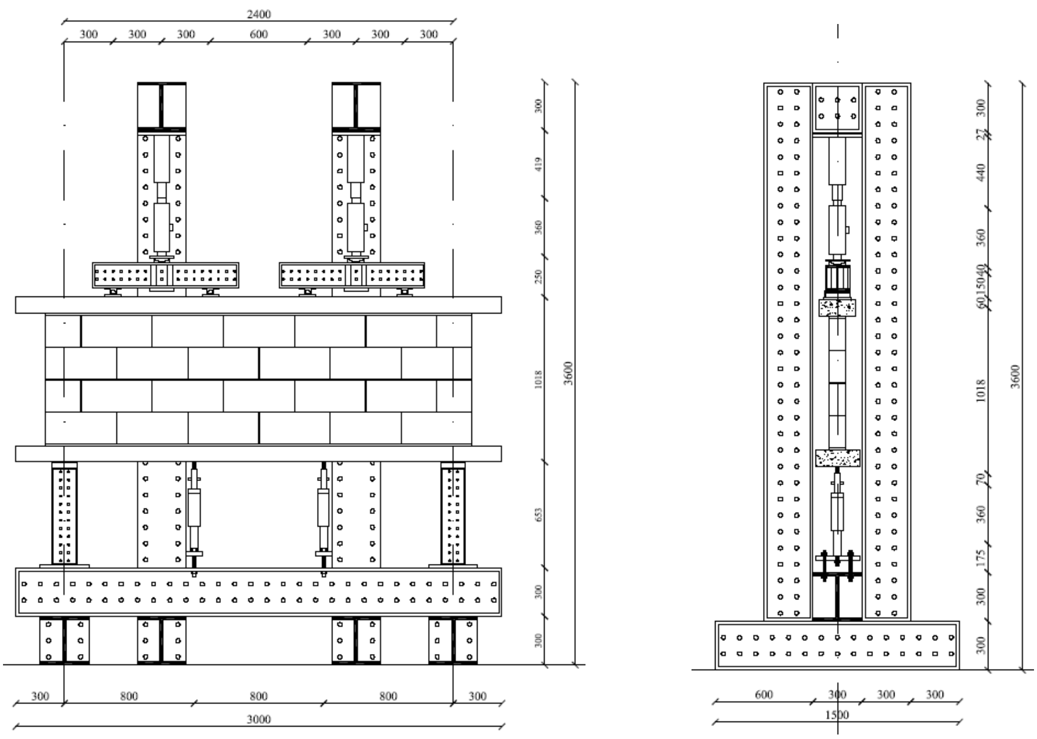

Figure 7.1: The structure used as casus. [4]

7.1. Finite element model

The input used for both exploratory analyses is shown in the following figures. In figure 7.2 the geometry used is shown and in table 7.1 the geometrical parameters are presented. In figure 7.3 the used mesh is shown with each colour indicating a material and boundary condition. The mesh spacing of the elements used in the model is 25 mm. Both columns are clamped, but one of the two columns can displace in horizontal direction. The displacement are applied as proportional loading (scaled during the analysis) whereas the forces are applied non-proportional (constant during the analysis). Lastly in table 7.2 the material parameters are given. These parameters are used throughout the exploratory analysis if not stated elsewise.

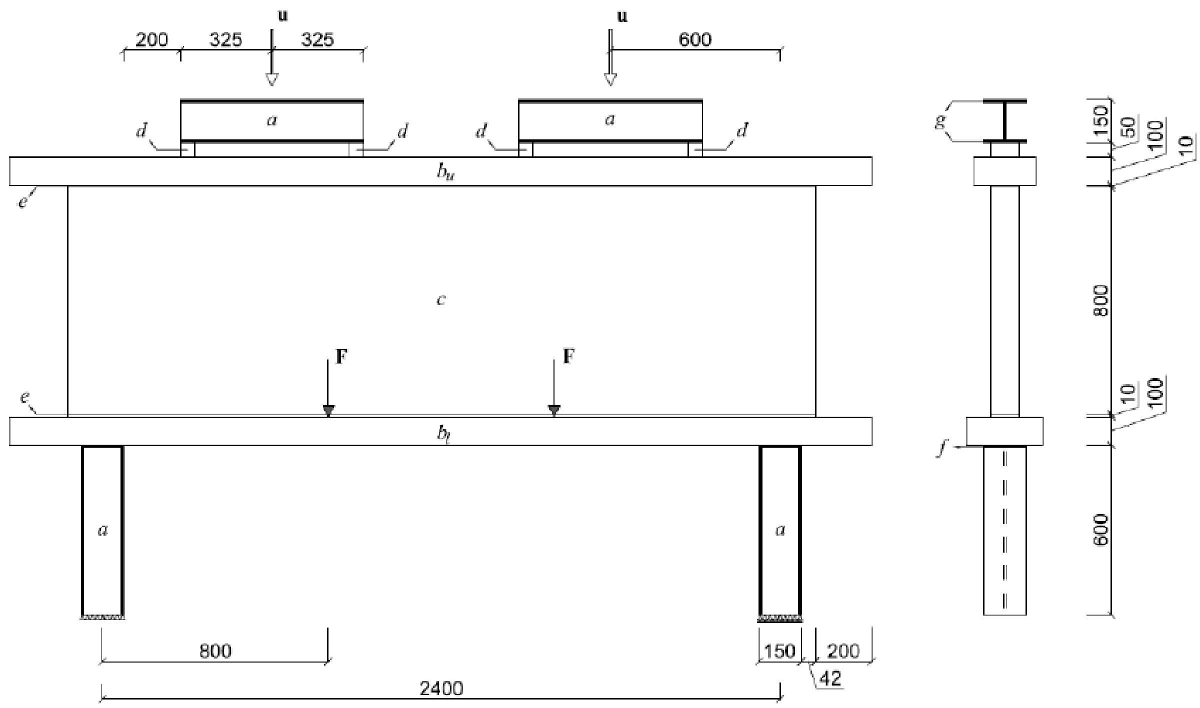

Dimensions in mm

Figure 7.2: Geometry of the casus used for computational input. [3]

.

Table 7.1: Geometric values of the casus.

Symbol	Representation	Geometry		Elements	Integration
a	Steel HE150A web	*t*	6 mm	CQ16M	2 × 2-point Gauss
b_l	Concrete lower beam	*t*	270 mm	CQ16M	2 × 2-point Gauss
b_u	Concrete upper beam	*t*	220 mm	CQ16M	2 × 2-point Gauss
c	Masonry wall	*t*	100 mm	CQ16M	2 × 2-point Gauss
d	Rubber hinge	*t*	100 mm	CQ16M	2 × 2-point Gauss
e	Mortar kicker joint	*t*	100 mm	CL12I	2-point Gauss
f	Steel plate	*A*	150 × 30 mm	L6BEN	2-point Gauss
g	Steel HE150A flange	*A*	150 × 9 mm	L6BEN	2-point Gauss

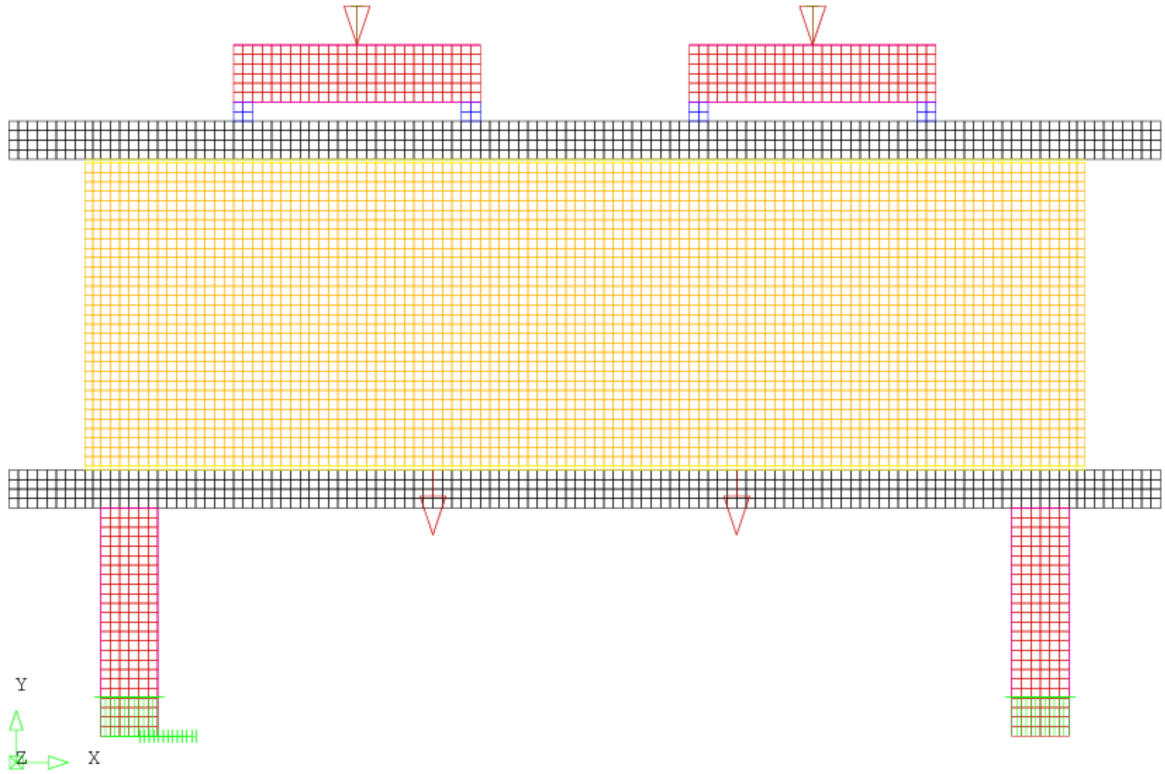

Figure 7.3: Mesh of the structure used for computational input.

Table 7.2: Material properties of the casus.

Components	Parameter	Symbol	Value	Dimension
Concrete beams (plane stress elements)	Modulus of Elasticity	$E_{concrete}$	25.400,00	N/mm^2
	Poisson's ratio	$\nu_{concrete}$	0,20	-
Mortar kicker joints (interface elements)	Normal stiffness	k_n	100,00	N/mm^3
	Shear stiffness	k_t	41,67	N/mm^3
	Tensile strength	f_t	0,01	N/mm^2
	Softening diagram	-	Linear	-
	Fracture energy	G_f	$2{,}5\cdot10^{-3}$	N/mm
Masonry wall (plane stress elements)	Modulus of elasticity	$E_{masonry}$	4.000,00	N/mm^2
	Poisson's ratio	$\nu_{masonry}$	0,20	-
	Tensile strength	f_t	0,80	N/mm^2
	Softening diagram	-	Linear	-
	Fracture energy	G_f	0,01	N/mm
	Crack bandwidth	h	25,00	mm
	Shear retention function	-	Linear	-
	Shear retention factor	β	0,20	-
Rubber hinges (plane stress elements)	Modulus of elasticity	E_{rubber}	1.000,00	N/mm^2
	Poisson's ratio	ν_{rubber}	0,30	-
Steel profiles (Line & plane stress elements)	Modulus of elasticity	E_{steel}	210.000,00	N/mm^2
	Poisson's ratio	ν_{steel}	0,30	-

7.2. Standard nonlinear finite element analyses

This paragraph summarizes the exploration into the use of nonlinear finite element analysis for masonry structures and the accompanying cumbersome routines. Herein, focus lies on the nonlinear analysis of the casus as done by J. Martens [3]. He made his thesis concerning multi-storey masonry buildings and tried to model the casus with nonlinear analysis, but not with sequential linear methods. Like Jasper Martens, step by step the nonlinear model will be made. In the first experiment the implementation of crack models has been taken into consideration. Also, a quick look has been made to step sizes and tolerances. In the second numerical experiment phased analysis will be considered, considering the combination of non-proportional loading and proportional loading. The third numerical experiment will include compression softening and lastly a few words will be spend on interface sliding. For every step a maximum of 99 iterations are used and the force-displacement graphs are of one jack only.

7.2.1. Tensile behaviour

In the first experiment two crack models are compared: the total strain rotating crack model and the multi-directional fixed crack model. Results are shown in figure 7.4. Firstly the influences of the step sizes are presented in figure 7.4.a, secondly the influence of the convergence tolerances in figure 7.4.b and the influence of the material parameter β in figure 7.4.c. Finally an example of a deformed mesh is shown in figure 7.4.d. For the fracture energy of the interface element a value of $2{,}5 \cdot 10^{-6}$ Nmm is used.

In figure 7.4.a it is shown that qualitatively the same output is obtained. An example of deformed mesh of such a the rotating crack model is shown in figure 7.4.d. The step sizes influence the moment of apparition of the cracks. Smaller step sizes also have more difficulties to convergence as can be seen for the used step size of 0,01 mm in figure 7.4.a.

In figure 7.4.b the influence of convergence tolerances is shown. Logically, the computation can convergence easier if the tolerance is less strict. However, less strict tolerances may result following wrong paths. The most lenient tolerance used of 0,1 does not show any clear drops and smears them out in the graph of figure 7.4.b. Such a tolerance is thus not desired for it is the goal to model this kind of brittle behaviour. Whereas the most strict tolerance used clearly shows a path with difficulties found as non-convergence, resulting in unnecessary longer computation times.

Figure 7.4.c also shows that if a fixed crack model is used, in this case a multi-directional fixed crack model, the material parameter β also greatly influences the outcome in such an extent it can result it divergence. A relatively large β-value could result in ‘stress-locking’, while a relatively low β-value can lead to convergence problems [1]. In this same figure the rotating crack model is plotted as a reference for the fixed crack calculations. It is clear that a fixed crack model reacts more stiff than their rotating crack counterpart.

In figure 7.4.d a deformed mesh at 5 mm jack displacement is shown for a rotating crack model. It can be seen that first the masonry wall is separated from the lower concrete beam followed by the consecutive appearance of the diagonal cracks. The first drop spotted in the graphs represents the separation crack with the inner diagonal cracks and the second drop is due to the outer diagonal cracks. Overall, the basis output is the same with a separation crack and diagonal cracks as shown in figure 7.4.d, but slight deviations in deformations are present. An asymmetric response is even obtained with the multi-directional fixed crack model for the crack directions isn’t allowed to rotate with the principal directions.

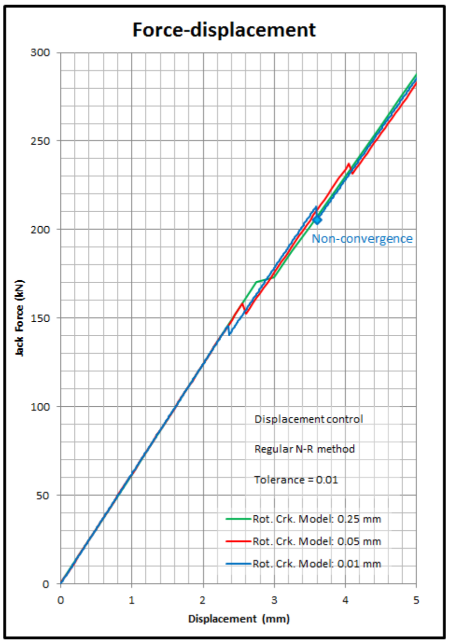

(a)

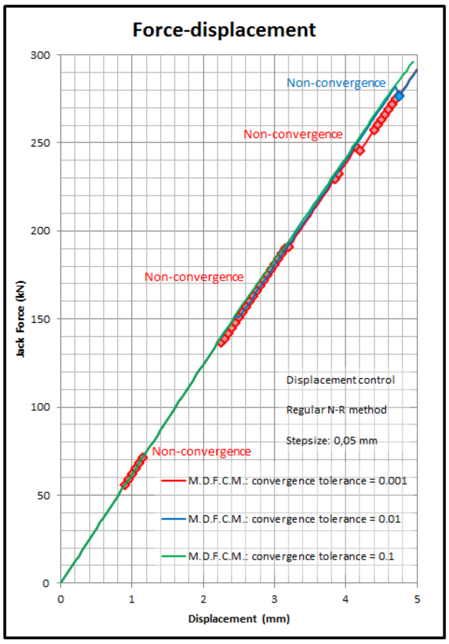

(b)

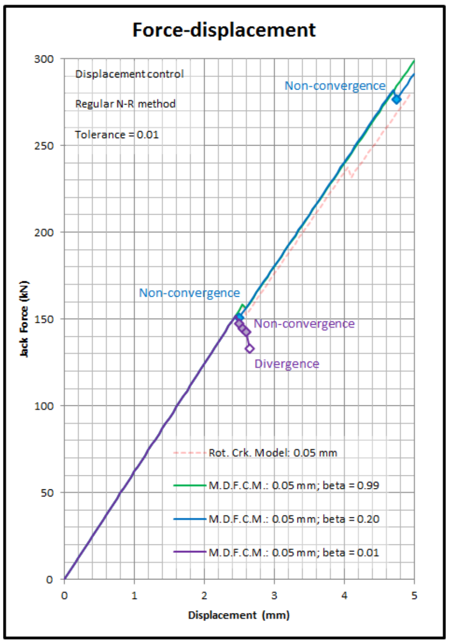

(c)

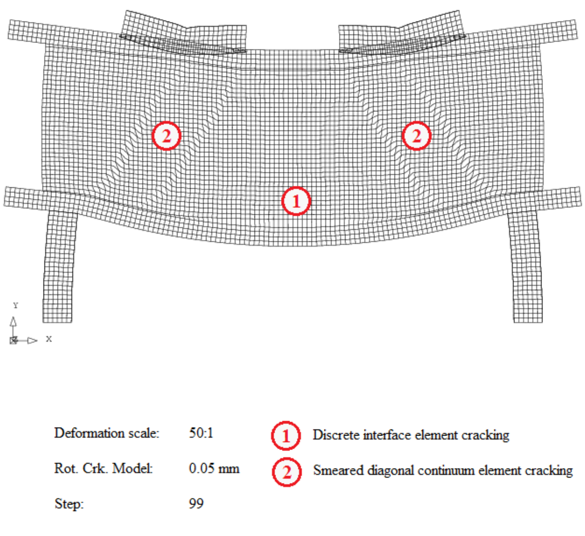

(d)

Figure 7.4: Results of tensile tests containing the influence of step sizes (a), the influence of convergence tolerance (b), the influence of the shear retention factor β and the deformed mesh (d).

7.2.2. Phased analysis

The second numerical experiment discusses the implementation of phased analysis. It is needed to consequently simulate the vertical crack in the centre of the masonry wall. The analysis is split up in two phases. The first phase is force controlled and uses the two point loads on the lower beam, loading of the first floor, to separate the masonry wall from the concrete floor. This results in the separation crack. The second phase is displacement controlled and displaces the jacks on top of the masonry walls, loading of the second floor. Due to the fact that the forces are applied by different control procedures, phased analysis is needed. Like in the previous experiment, self-weight of the structure is not considered. The second phase is presented below in a graph. Keep in mind that the separation crack is not present in this graph, for it is part of the first phase.

Now the vertical crack also appears in the results, which is in figure 7.5.a represented by the first, but small, drop in the force-displacement diagram indicated by the arrow. The separation crack is not present in the graph, as stated before for figure 7.5 shows results from the second phase only. However, its influence can be found at the start, where the graph does not start at the origin. The second drop in the graph is representing the diagonal cracks, who appear simultaneously. Both the rotating crack model and multi-directional fixed crack model show similar results with phased analysis. But ultimately the multi-directional fixed crack model is reacting again stiffer than the other model. After the presented 5 mm the analysis can be continued, but it will diverge.

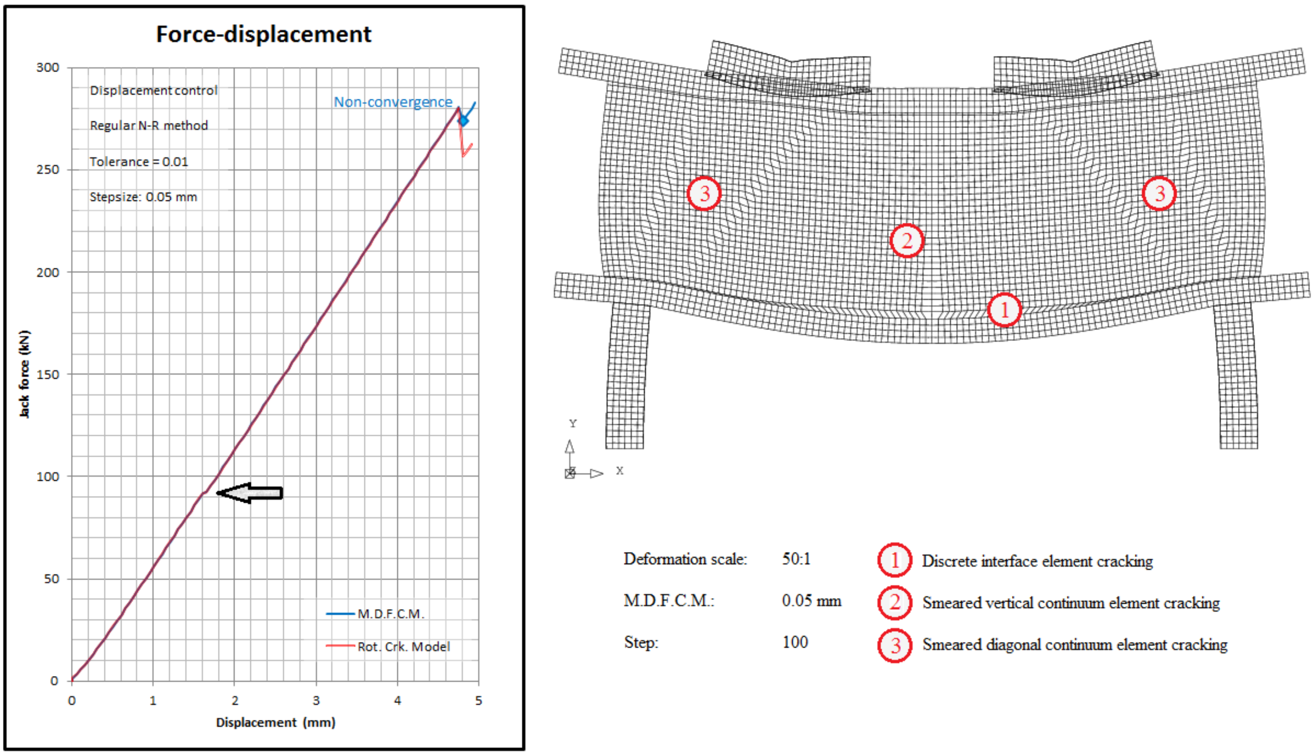

(a) (b)

Figure 7.5: Results of phased tests containing a load-displacement graph (a) and a deformed mesh (b).

7.2.3. Compressive behaviour

Up until now the experiments were to get the cracks appear at the right location in the right order. However, the material might also fail due to crushing. Therefore, compressive criteria have to be implemented.

There are a handful ways to implement compression softening, as shown in the figure 7.6 taken from the DIANA manual [5]. In the previous experiments the compressive model of the masonry has been elastic (7.6.a). In this experiment focus will lie on three softening curves. The first one being a constant plasticity, using thus a plateau (7.6.b). The second one is mostly used for concrete, a similar material to masonry, and is developed by Thorenfeldt (7.6.c). The last considers a parabolic curve, the generalisation of Thorenfeldt (7.6.g). Hardening will not take place and for that reason the other curves are left aside.

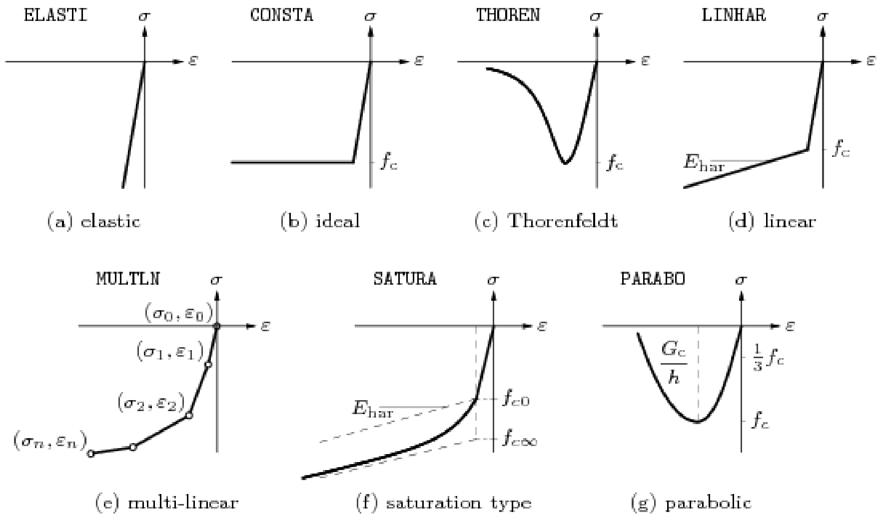

Figure 7.6: Compression softening models as presented in DIANA manual. [5]

In figure 7.7 it can be seen that there are almost no differences between the three compressive constitutive models. For the multi-directional fixed crack model there is even no difference to be found at all, which is unexpected. The ideal model reaches the highest failure load in the rotating crack model, for it actually does not soften at all. The parabolic version clearly falls short to the others for the associated strains are much lower due to the shape of the softening curve. The Thorenfeldt curve seems to be able to stay on track with a lot of effort, actually being able to survive through the major part of crushing. For further analysis a parabolic (generalized Thorenfeldt) compression softening curve is chosen, however, because generalized material properties are used.

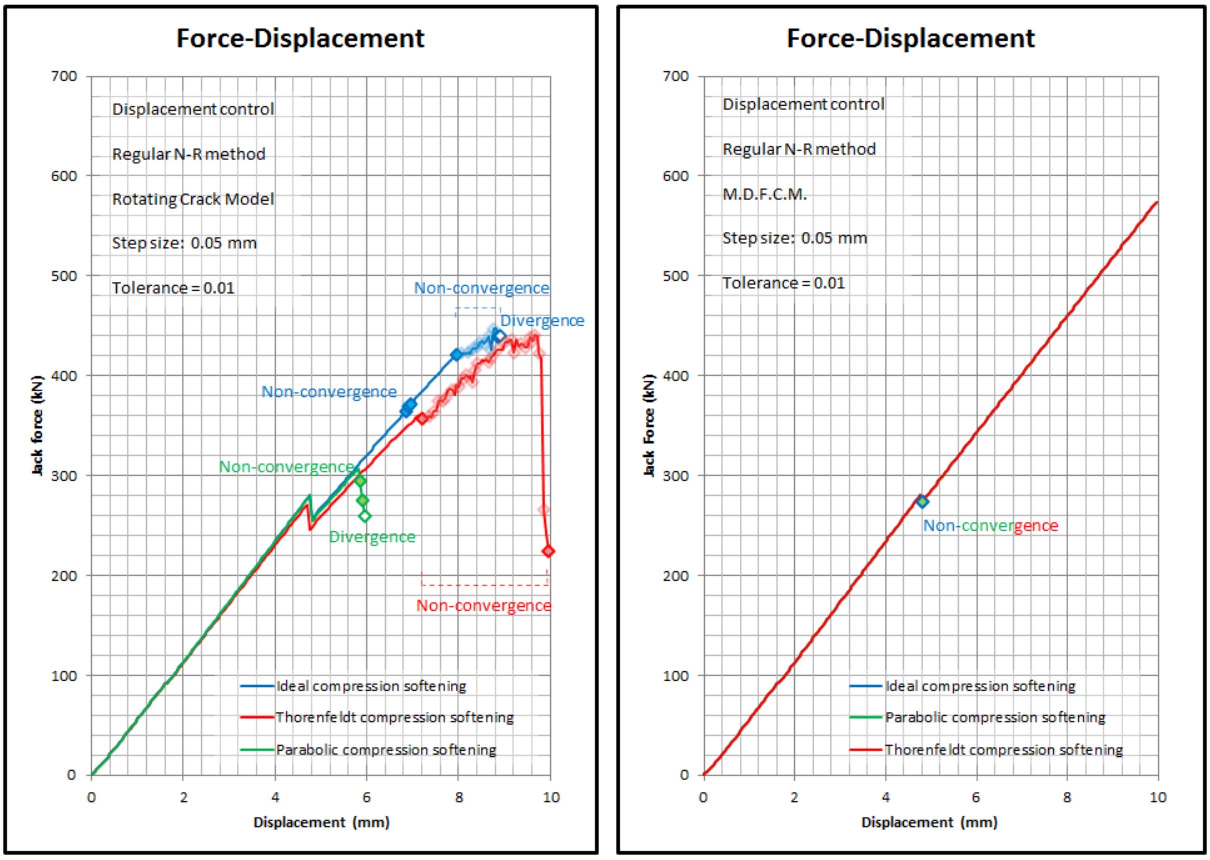

(a) (b)

Figure 7.7: Results of the compressive tests showing the rotating crack model (a) and the multi-directional fixed crack model (b).

New to these graphs is the addition of crushing and to illustrate this the parabolic compression softening model of the rotating crack model will be taken as an example. With the aid of the strains, it can be proven that crushing has taken place, but that it apparently is a too difficult behaviour to follow with nonlinear finite element analysis without further addition of other control procedures. Softening laws are shown in figure 7.8, crack patterns and deformations have been illustrated in figure 7.9, principal strains in figure 7.10 and crushing in figure 7.11.

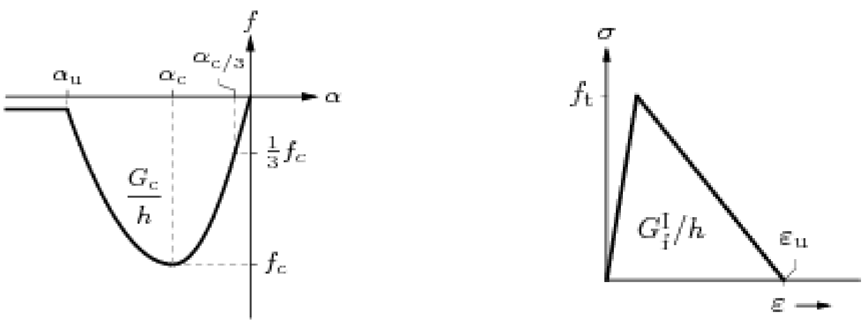

Figure 7.8: The used softening curves in compression and tension. [5]

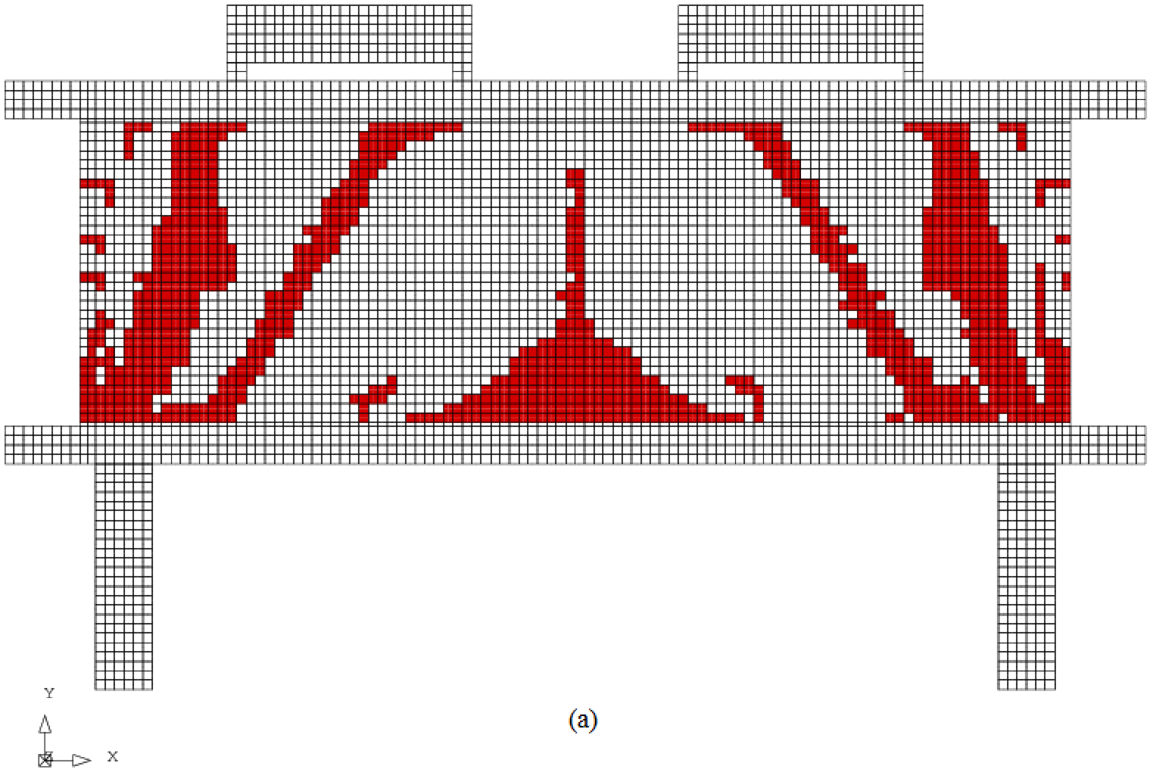

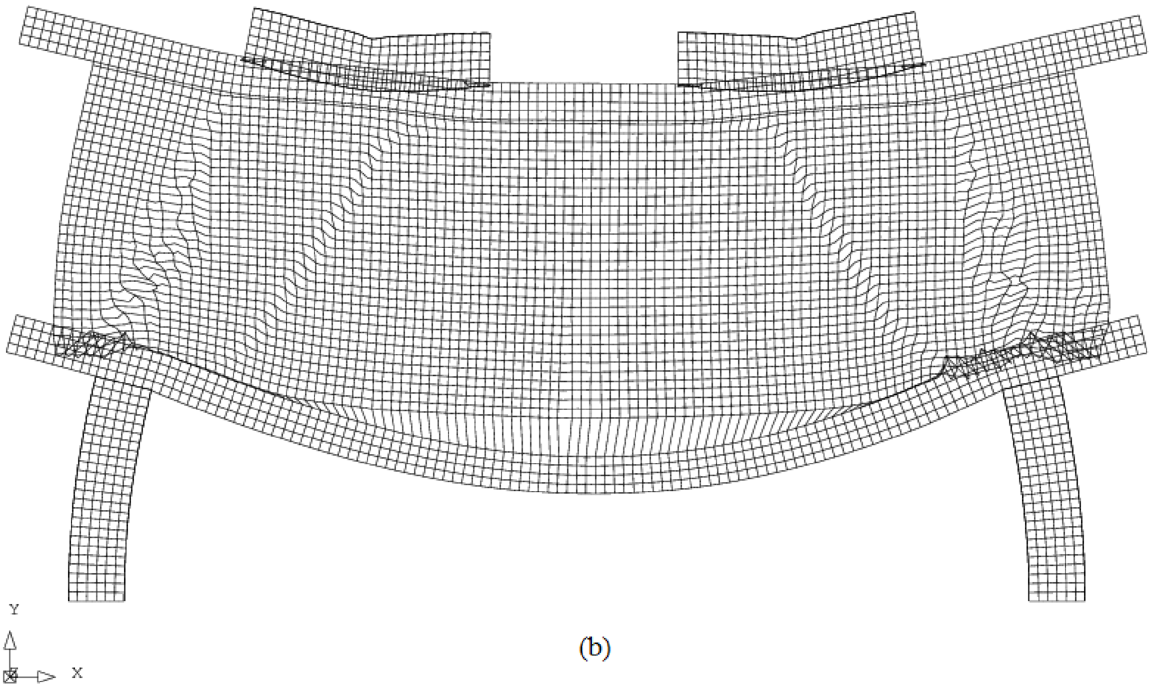

Figure 7.9: Cracked elements (a) and deformation 50:1 (b) at the last step.

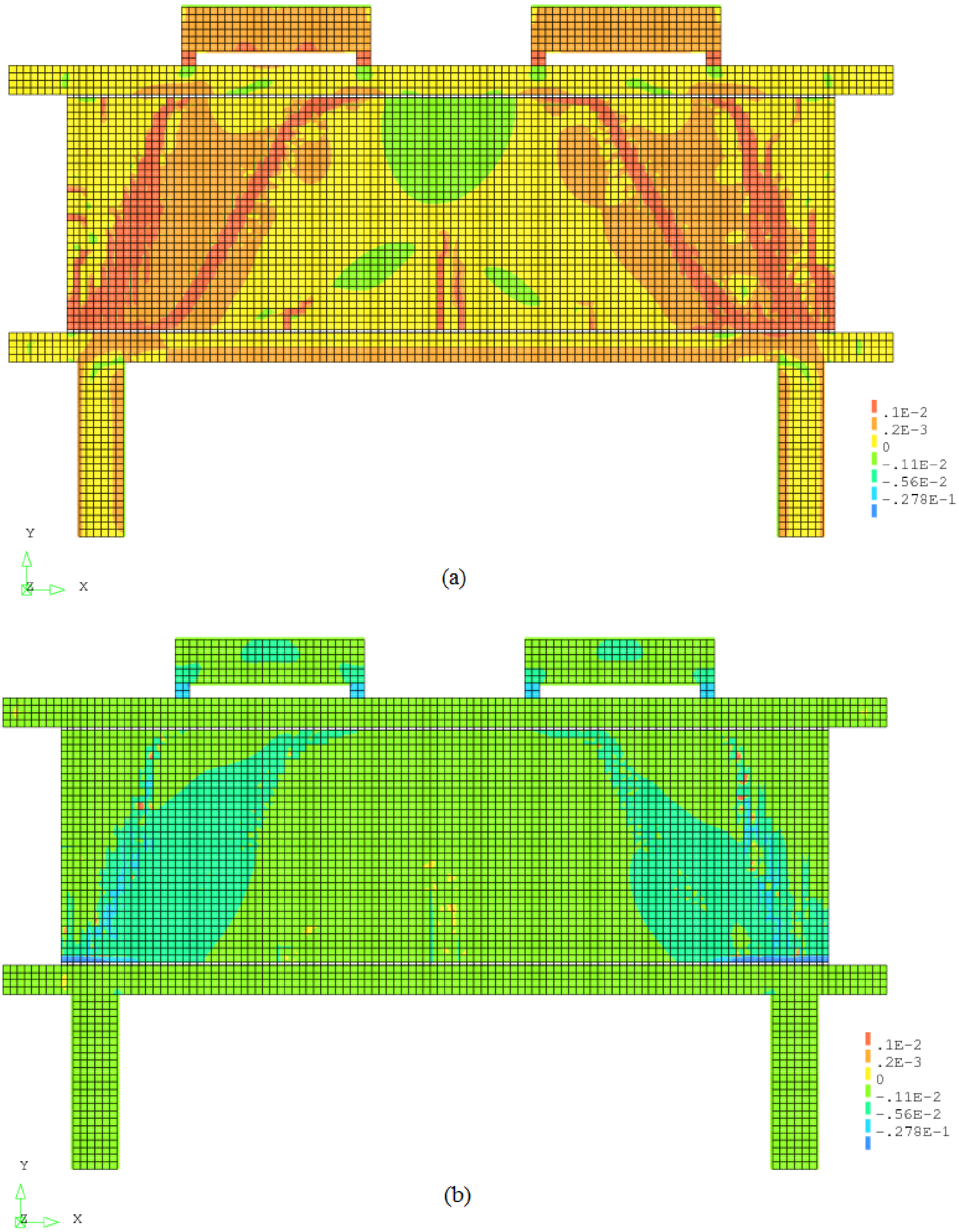

Figure 7.10: First principal strain ε_1 (a) and second principal strain ε_2 (b) at the last step.

The tensile strains are a result from a linear tension softening model. Following the background theory in the DIANA manual, the following strains define the softening curves, α being the strains in compression and ε the strains in tension.

<u>Box 2</u>

The strains for the linear tensile softening are according to the following formulae:

$$\varepsilon_c = \frac{f_t}{E} = 0{,}0002 \tag{b2.1}$$

$$\varepsilon_u = 2 \cdot \frac{G_f}{f_t \cdot h} = 0{,}001 \tag{b2.2}$$

The strains for the parabolic compression softening are according the following formulae:

$$\alpha_{c/3} = -\frac{1}{3} \cdot \frac{|f_c|}{E} = -0{,}0011 \tag{b2.3}$$

$$\alpha_c = -\frac{5}{3} \cdot \frac{|f_c|}{E} = -0{,}0056 \tag{b2.4}$$

$$\alpha_u = \alpha_c - \frac{3}{2} \cdot \frac{G_c}{|f_c| \cdot h} = -0{,}0278 \tag{b2.5}$$

Looking at figure 7.9 and 7.10 all the cracks (separation crack, mid-crack and diagonal cracks) are clearly visible. In figure 7.9.b and 7.10.b it can also be seen that the structure was crushing. The right bottom corner of the masonry wall of these figures have been amplified and shown in figure 7.11. The deformation, 7.11.a, clearly shows the crushing behaviour, showing the elements wanting to "go through each other". In figure 7.11.b it is also shown that these elements are crushed completely, presenting a dark blue colour indicating it exceeded the ultimate allowable compressive strain as calculated in box 2.

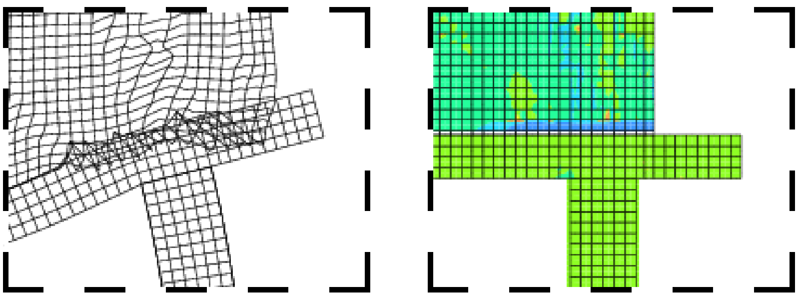

(a) (b)

Figure 7.11: Cut-out image of figure 7.9.b (a) and 7.10.b (b).

7.2.4. Interface sliding

The overall structure has been overestimating the failure load, according to J. Martens. Therefore interface sliding has to be included. Sliding is a mechanisms that, according to the DIANA manual, goes better with the multi-directional fixed crack model than with the total strain rotating crack model. Sliding can't even be included in the latter itself.

The multi-directional fixed crack model could calculate a response. However, it did not drop like in the previous numerical experiment. The rotating crack model did not end up well. Errors occurred and the calculations aborted prematurely. The calculations are made with the parabolic compression softening curve and the following values: c = 0.01, tan(ϕ) = 0.75 and tan(ψ) = 0.1. The result is shown in figure 7.12.

A downside, however, is that this sliding model replaces the discrete cracking model which uses fracture energy. The augmentation of this model is therefore not more useful in this setup. The only interface element found in the mesh is the kicker joint, while the model is more useful if it was a heterogeneous model with head and bed joints. This exploration does not and, even if the errors would be bypassed for the rotating crack model, would not give any useful additional information for that reason.

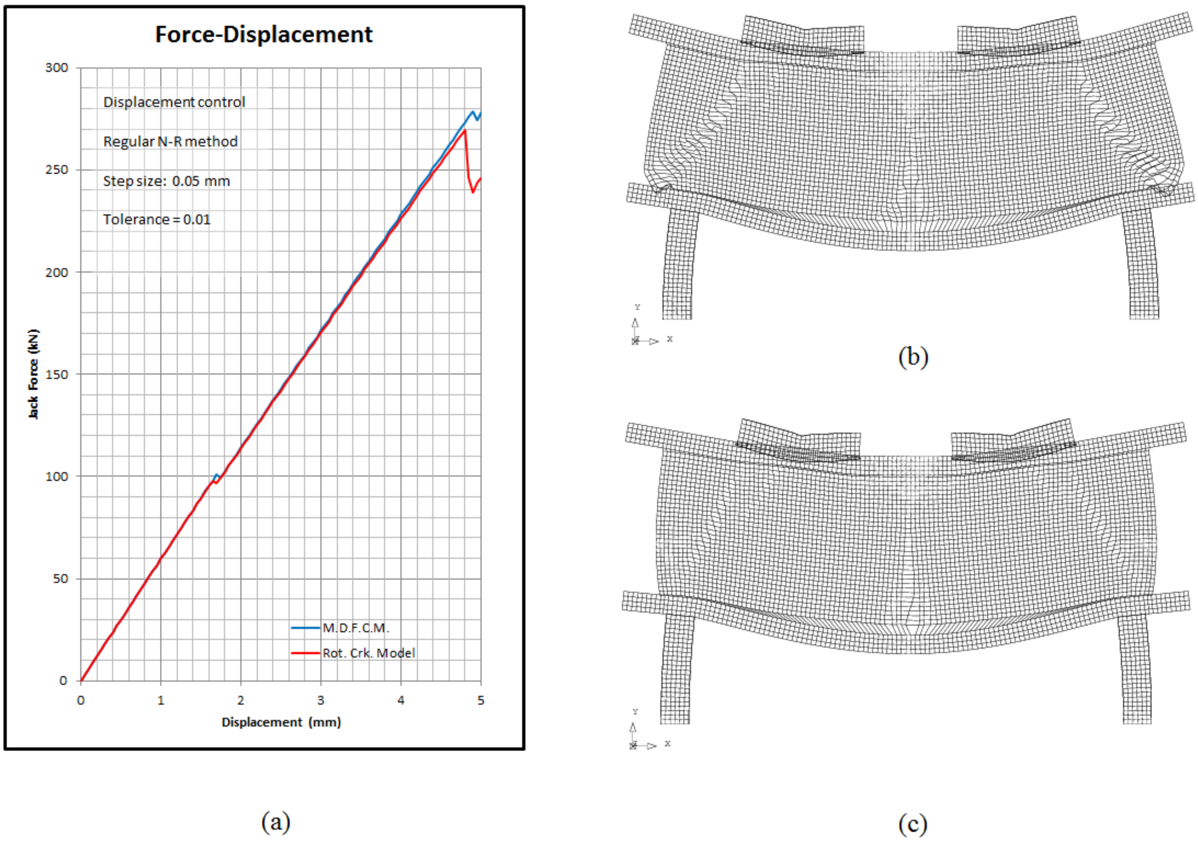

Figure 7.12: Results of the sliding interface exploratory test with a force-displacement diagram (a), deformed mesh of the Rot. Crk. Model (b) and deformed mesh of the M.D.F.C.M. (c) at 5 mm applied displacement.

7.3. Sequentially linear analysis

To get used to sequentially linear analysis a test run has been made with the whole structure as used in the nonlinear analysis. The used method of SLA was an old version where it was only possible to implement a saw-tooth curve in tension for plane stress elements. For this reason only the plane stress elements of the wall were taken as nonlinear, everything else, even the interface elements, behaved linearly. With the results a first impression has been retrieved and the results are compared with a parallel nonlinear analysis to confirm the potential of SLA.

7.3.1. Displacements

For both the analysis the force-displacement diagram has been plotted below in figure 7.13. In it, the softening behaviour can be seen for both analysis. For the NLFEA a decreasing branch can be found twice, both corresponding to the formation of the cracks. The SLA shows considerably more data points, each point corresponding to a state where in one of the integration points, the critical integration point, the maximum allowable tensile stress is reached. Here the stiffness and strength of the structure is reduced with each step, which means that decreasing branches are not clearly, or not at all, visible due to its visually crowded nature. SLA has significantly more damage increments than NLFEA has in displacement increments. Furthermore, both analysis showed that the structure did not fail, which is due to the ability to carry the loads to the supports through compression linear elastically.

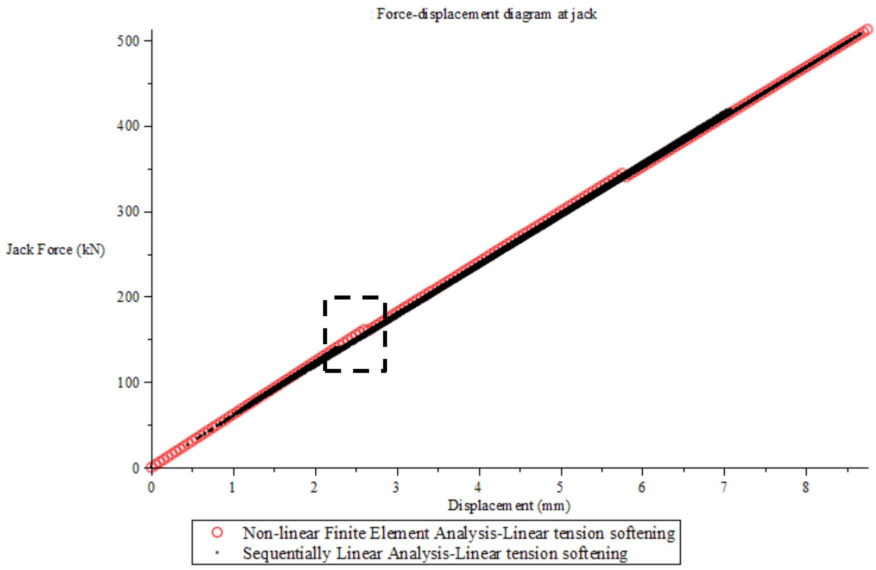

Figure 7.13: Jack force-displacement diagram of both analysis types with the box being figure 7.14.

7.3.2. Crack formation

Qualitatively the graphs look almost the same, but the crack apparition are different for both methods. Where the nonlinear analysis shows the apparition of cracks simultaneously and spontaneously, the sequentially linear analysis shows the formation of these cracks separate and slowly. The NLFEA skips a lot of information, while SLA, which uses damage increments, is naturally able to obtain this information. As stated earlier, it is difficult to pin-point exactly in the sequentially linear analysis where the cracks appeared. However, looking at the two first drops of SLA a lot can already be told, see figures 17.13, 17.14 and table 17.3.

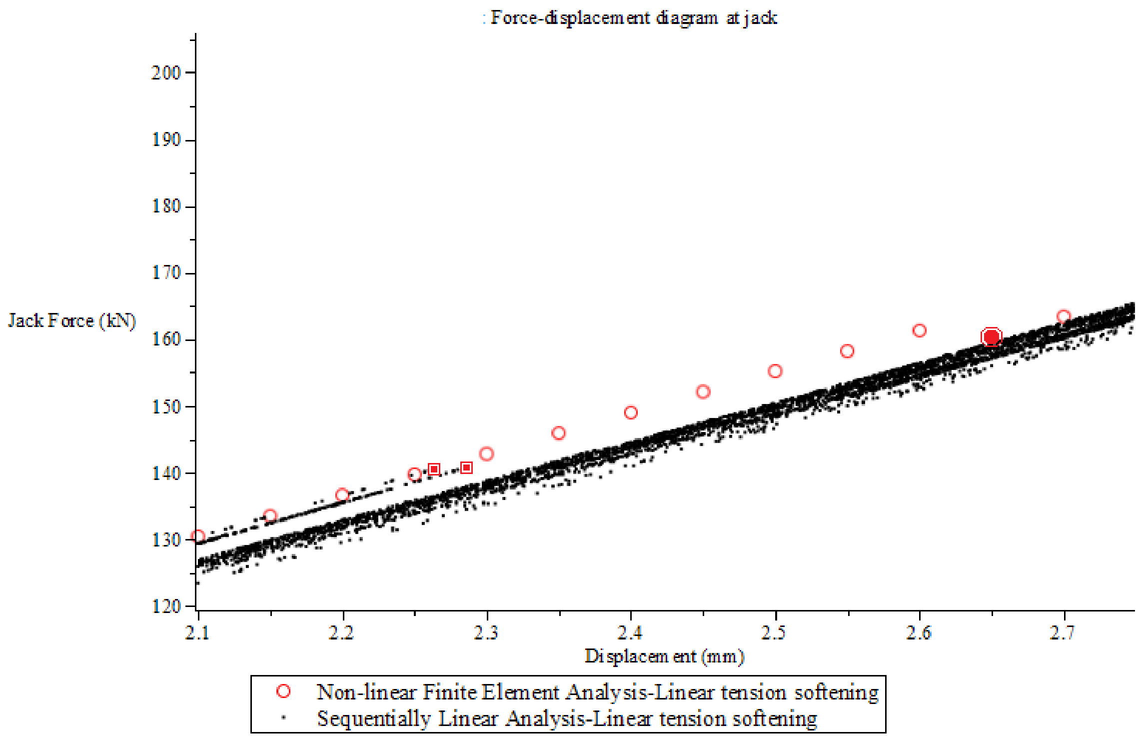

Figure 7.14: Close-up view of the jack force-displacement diagram (box in figure 7.12).

Table 7.3: Crack apparition for both methods.

Analysis type	Crack	Jack Displacement [mm]	Jack Force [kN]
NLFEA	Internal diagonal cracks	2,60	161,3
SLA	Internal left diagonal crack start	2,26	140,5
	Internal right diagonal crack start	2,29	140,8

The first drop of the nonlinear analysis, shown with the enlarged red circle, displays both internal cracks at the same time. The SLA drops, shown with the enlarged red squares, shows the starts of the internal diagonal cracks of the structure. The other pair of diagonal cracks happen much later for SLA around 7 millimetres, while for NLFEA this happens around 6 millimetres. The SLA shows extreme snap-back behaviour for each crack and it shows that both internal cracks happen at almost the same moment. Because of its close nature and the fact that NLFEA used simple displacement step procedures in this analysis, it cannot show the cracks individually growing, for the step taken is too big and cannot be reversed. Instead it shows the sudden apparition of the cracks simultaneously, whereas SLA can show the grow of the cracks without further control parameters, figure 7.15.

It might be possible to actually follow this snap-back with other procedure parameters like step sizes and tolerances or arc-length control. However, the results of NLFEA are dependent on these parameters quantitatively as seen in paragraph 7.2. Furthermore, it cannot guarantee stable analysis, prevention of bifurcation or zero-energy modes as concluded out of literature in paragraph 3.3.

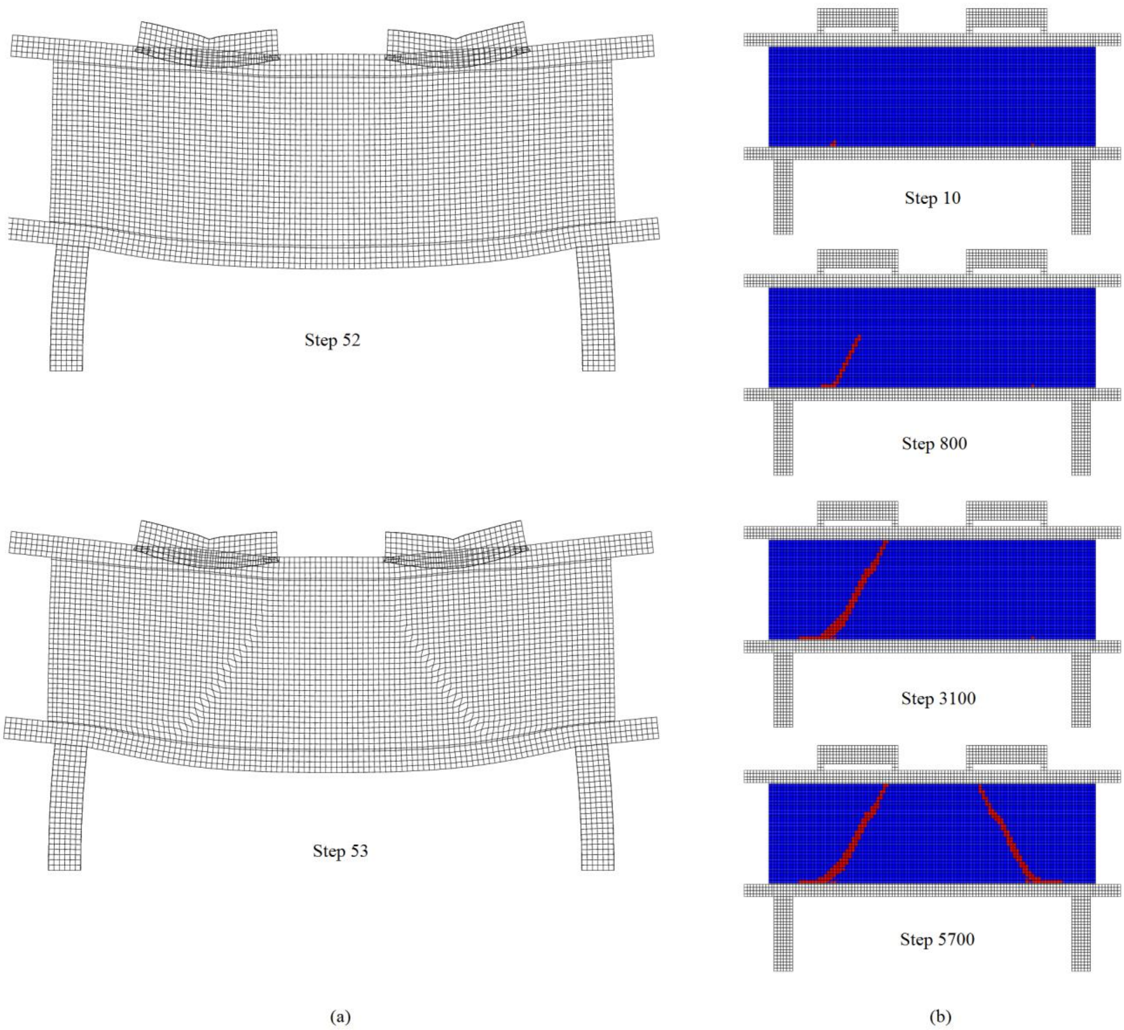

Figure 7.15: Crack patters of the first cracks for NLFEA (a) and SLA (b).

7.3.4. Jack forces

The cracks were formed separate and gradually in the SLA calculation, because only one integration point is allowed to be the critical integration point. This will make any problem in SLA asymmetric, even when the problem starts symmetric. This theory suggest that the jack forces applied on the steel beams on top of the wall are very different from each other in SLA. This is especially expected to be the case when one side of the structure contains a crack, while the other side remains uncracked. The analysis was displacement controlled, so the jack displacements, where the loads were applied, are the same for both sides.

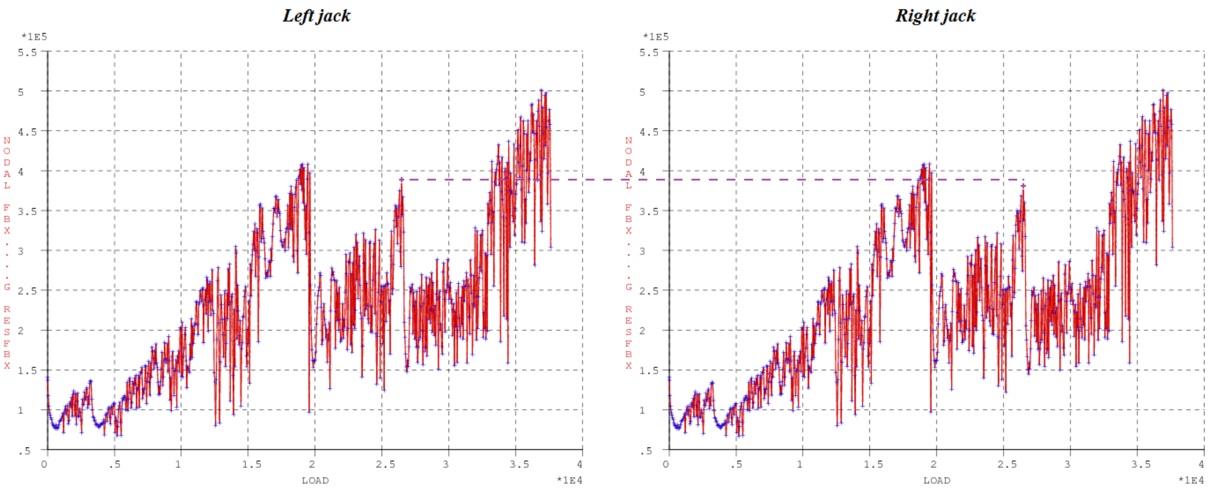

Figure 7.16: Force-displacement diagrams of the left and right jack.

A difference can be spotted in figure 7.16. However, the difference is small. The reason for this reduced asymmetric behaviour is the concrete beams that engulf the masonry wall. They spread out all effects in the same way a point load is spread out into a “line load” if introduced by a lath.

This slight difference is also spotted in NLFEA, which means that it might as well be from the fact that the structure is slightly asymmetric from the start. One column is clamped and the other is also given the ability to move horizontally. This boundary condition also gives a slight difference in jack forces during the analysis.

7.3.5. Post-peak behaviour

The more load there is applied in NLFEA, the more the structure deforms and the more the cracks open. In SLA however, these cracks seems to spread over neighbouring elements, see figure 7.17.a, widening the band of cracked elements, instead of increasing the strain of the already cracked elements. The structure has already failed completely, meaning it already finished its path along the implemented ripple diagram used as constitutive law for tension. If an integration point is completely damaged it is forced to choose another integration point in the next step. The bands of cracked elements are thus higher at the same amount of computational steps if less secant branches are used in the ripple diagrams as seen in figure 7.17.b.

The fact that the elements do not reach very high strains like in NLFEA is because the elements will always have a certain amount of stiffness in this configuration, for the last implemented secant branch of the ripple diagram is a “dummy branch”. This branch is not taken quantitatively into the calculation, meaning a small stiffness of 0,0065 N/mm^2 remains for “completely” broken elements in tension as seen in figure 7.17.a. This results in some resistance and strains to be carried over by neighbouring elements.

The strains obtained in the neighbouring elements as seen in figure 7.18 are significant, meaning the SLA calculation will theoretically proceed until all integration points are completely damaged. And that is possible in this scenario. Although in figure 7.17 it looks like the elements at the support are completely cracked, the forces are still carried through these same elements through compression as shown in figure 7.19. Because there is no compressive criterion in this analysis, it is possible for SLA to continue selecting critical integration points until no viable options are left.

The crack in the middle also gets attention secondly. This is because the wall wants to create a vertical crack in the centre and separate itself from the interface element. The latter is not possible due to the material implementations used and therefore the vertical crack will not appear. However, the tension still exists in this section of the wall. As a work-around, the structure behaves in such a way that a upper half ellipsoid is made as a crack, relieving itself from all the tension stresses in that way and to be able to deform accordingly. This crack band is the same kind of separation as a combined separation crack with an interface mechanic and the vertical crack.

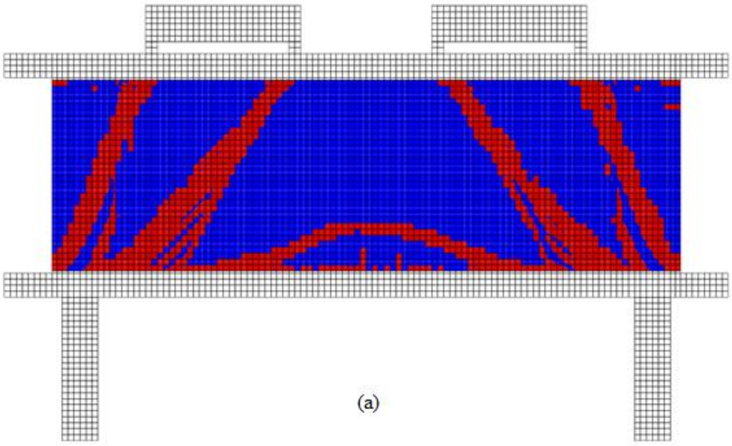

(a)

```
'MATERIALS'
4      HARDIA  4000.0000000   0.866236828
               3259.2592590   0.828574357
               2628.2578870   0.784361891
               2090.7382000   0.732460301
               1632.8510590   0.671532348
               1242.7990500   0.600008228
               910.53252410   0.516045131
               627.49066870   0.417479756
               386.38093990   0.301772578
               180.99117110   0.165942411
               6.0295161140   0.006489607
               0.0001000000   0.000000000
```

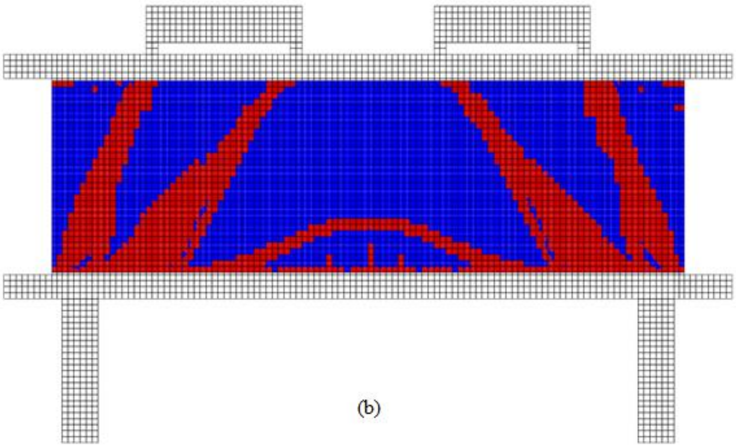

(b)

```
'MATERIALS'
4      HARDIA  4000.0000000   0.866236828
               3259.2592590   0.828574357
               2628.2578870   0.784361891
               2090.7382000   0.732460301
               1632.8510590   0.671532348
               1242.7990500   0.600008228
               910.53252410   0.516045131
               627.49066870   0.417479756
               386.38093990   0.301772578
               180.99117110   0.165942411
               6.0295161140   0.006489607
```

Figure 7.17: Crack pattern of structure with dummy branch (a) and removing last secant branch (b).

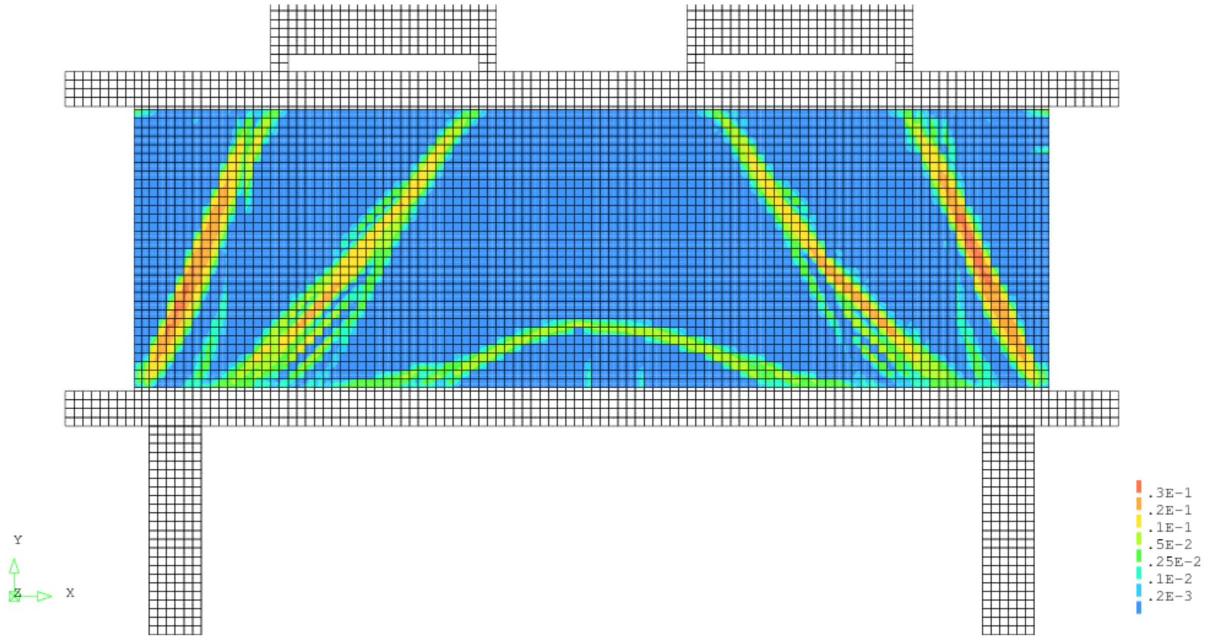

Figure 7.18: Crack strains of figure 7.15.a.

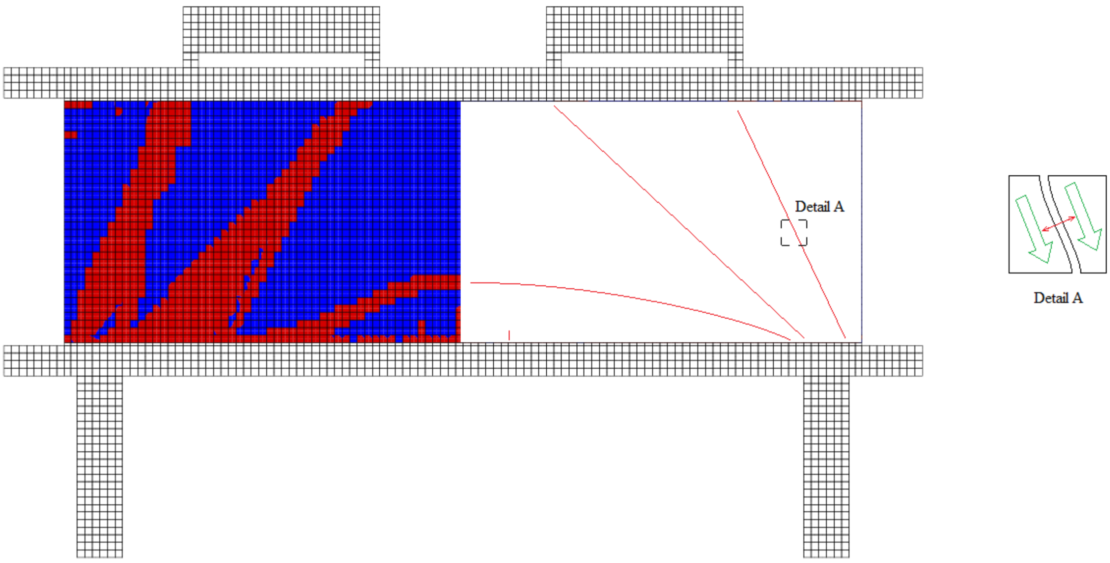

Figure 7.19: Structure carries the load through compression

7.4. Final remarks

Taking both these exploratory analyses and the available literature into account, it can be said that for NLFEA the output is very much dependent on the analysis parameters you implement. High tolerances will skip problems, while strict tolerances will not be able to find an equilibrium path. Low step sizes show earlier crack apparitions, though the chances on non-convergence or even divergence are higher. The casus can be modelled homogeneously with a nonlinear analysis. However, much depends on the choice of the researcher. This means that global conclusions can be drawn with this analysis type, but the exact behaviour cannot, due to the sensitivity to most of the parameters. Even with more difficult to implement models the results are quantitatively heavily dependent on the implemented parameters. This dependency, or lack of robustness, is certainly unwanted in further research into masonry and other brittle materials. It is therefore clear an alternative more robust method is needed.

With the literature and with the short inventarisation into the application of a simple version of the SLA method it is clear that the brittle behaviour can be followed. SLA is easy to implement and use to obtain the desired results. This shows SLA has a lot of potential if one wants to follow crack formation and other brittle failure mechanisms step by step for quasi-brittle materials. The computation time also is multiple times higher than for nonlinear analysis, but nevertheless it shows why SLA is an promising alternative to the nonlinear analysis.

8. Single-element and shear-wall verifications

A SLA model in development is provided and is used to answer the research question. The model has to be verified. Therefore the state of the current SLA models is scrutinized and this is followed up by single-element tests. A biaxial tension-shear test is used to verify the elastic softening formulation and finally a shear-compression wall is used as a test on a full mesh.

8.1. On the coupling of tensile and compressive behaviour

In Chapter 7 an old version of SLA has been used to experience the potential of SLA. For the verification of the sequentially linear model the newest available model is used. However, there are two numerical models of SLA available at the time the research was performed. One model uses a decoupled constitutive law for the compressive and tensile behaviour while the other model couples these aspects into one total constitutive behaviour. Both models are explained and used in further analysis for neither one of them is seen as better than the other, for both are situational models. Afterwards theoretical improvements are proposed to further enhance the numerical model.

8.1.1. Coupled saw-tooth law

The first model, which will be named from now on the “coupled model”, uses an ordinary constitutive law. The stress-strain relation is one relation with a compressive part and a tensile part. The elements can switch from cracking to crushing and back again. An arbitrary visualisation of the coupled saw-tooth law is presented in figure 8.1.

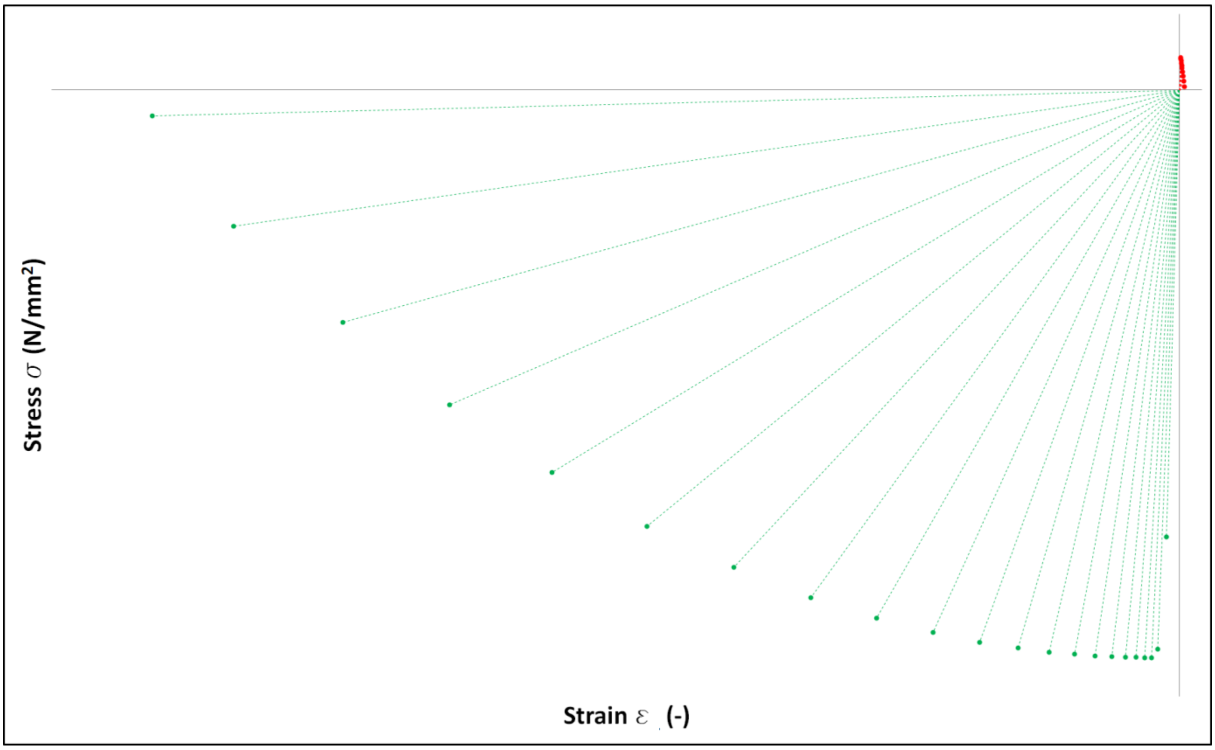

Figure 8.1: Coupled saw-tooth law

Although it is thus theoretically possible for an element to switch from cracking to crushing during the sequentially linear procedure, it is noticed that this phenomena is not formulated correctly yet in the source-code of the method. If the element for example has been damaged in tension, resulting in having its material properties reduced already a few times, and starts to crush, it carries over the damage history of cracking ending in the skipping of compressive teeth.

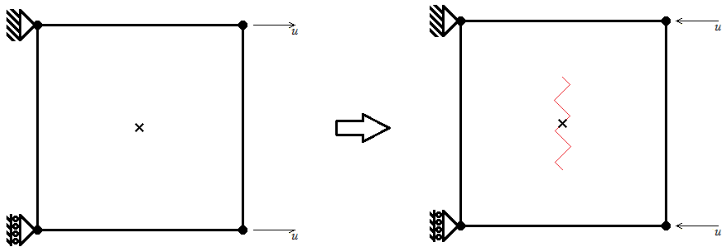

Figure 8.2: Setup for verifying the behaviour of switching from cracking behaviour to crushing behaviour.

In figure 8.2 the issue is presented visually. Here a linear quadrilateral element with one integration point has been loaded in tension for four steps, before reversing the loading direction. The new situation will ensure that the element is subjected to compression, resulting in entering the compressive saw-tooth relationship. The results are presented in figure 8.3 and with these results the limitation is proven.

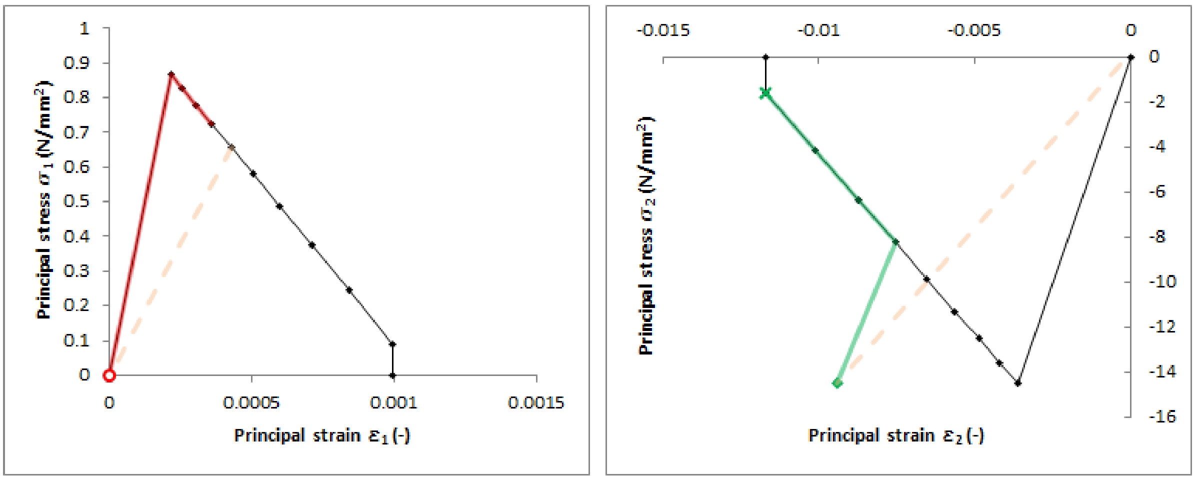

(a) (b)

Figure 8.3: Cracking until step 4 (a) after which it crushes starting from step 5 (b).

After four steps, (damage +4) the load is reversed and the procedure will find that the integration point will reach its criteria for crushing. The integration point has to reach the maximum allowable stress, but finds it with the given softened tensile Young's modulus ($E_{t,4}$), resulting in a different strain than implemented in the input files. Instead of following the first crushing secant branch and continuing with second branch, it follows the last calculated tensile secant branch for the fifth damage (damage -5) and continues thereafter with the sixth crushing secant branch. The material thus jumps to crushing behaviour, while having tensile behaviour as compressive history.

8.1.2. Decoupled saw-tooth law

The decoupled saw-tooth law separates the saw-tooth law in two separate saw-tooth laws, one compressive and one tensile law. The interaction between both saw-tooth curves are lost and once an element entered tensile cracking it cannot enter compressive crushing behaviour in the same direction. Furthermore, the implementation was made for reinforced concrete where compressive struts and orthogonally cracking occurs. Therefore, as a simplification elements cannot simultaneously be cracked or crushed in both orthogonal directions forcing the appearance of a compressive strut in the structure. If the first direction is crushed, the second direction must become cracked or keep behaving linear elastically. This situation are present in reinforced concrete structures. An arbitrary visualisation of the coupled saw-tooth law is presented in figure 8.4.

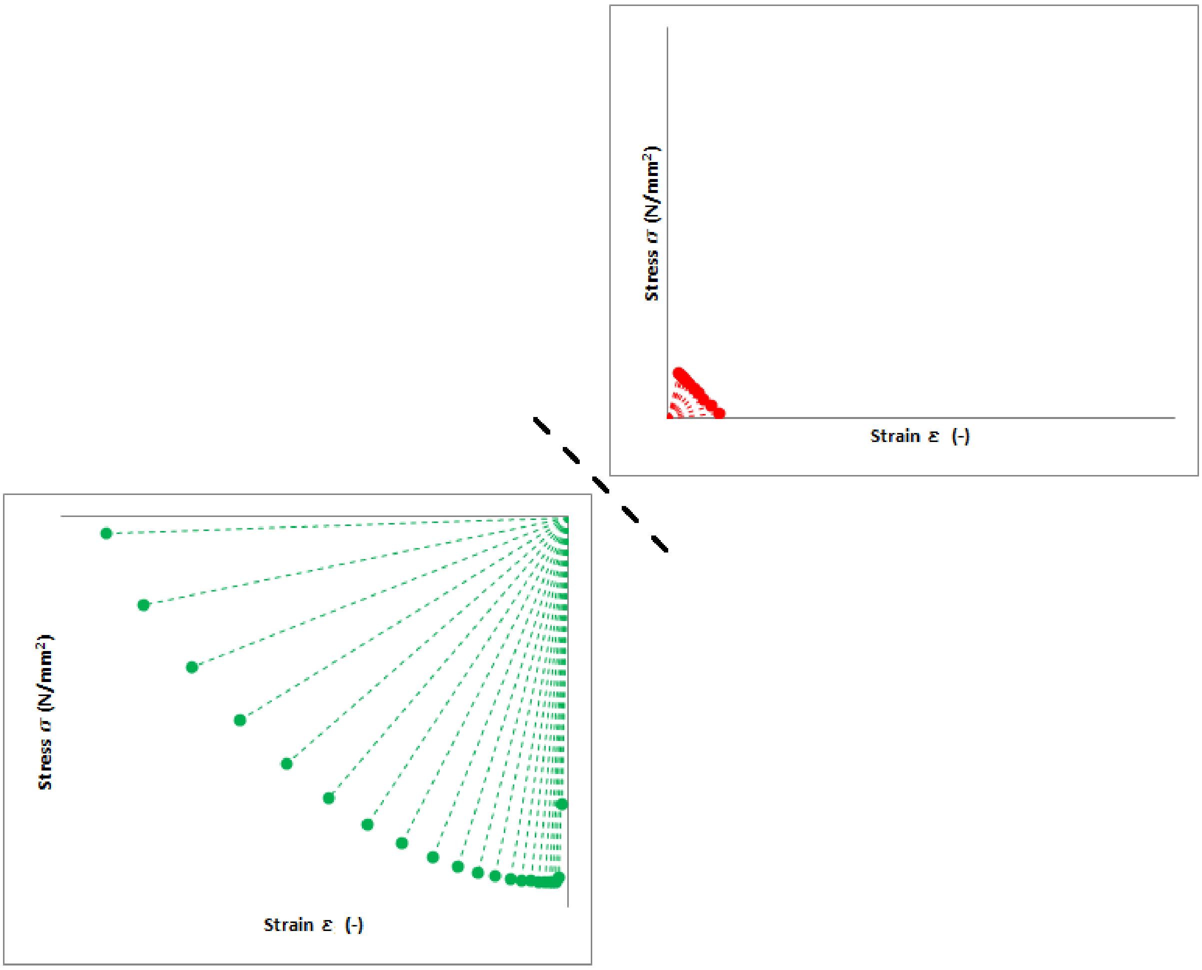

Figure 8.4: Decoupled saw-tooth law.

The decoupled saw-tooth law doesn't allow an element to crack in the same direction, when it started to crush and vice versa, because the saw-tooth laws for compression and tension have no interaction. A direction is assigned either the one or the other and sticks with that assignment for the rest of the calculation. Consequentially, if the stress state in the element switches from tension to compression, the procedure will not find that the supposed critical integration point is indeed the critical integration point. The procedure will chose another point in the structure and continue the calculation.

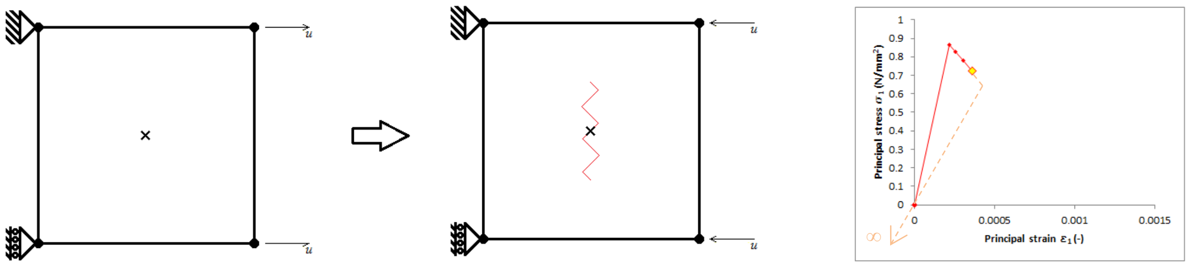

Figure 8.5: Setup for verifying the behaviour of switching from cracking to crushing behaviour with result.

This phenomena is illustrated in figure 8.5. First the element is subjected to tension. After a few steps the loading is reversed. The element is now subjected to compression and should therefore start to crush. However, the element does not crush at all. Instead, in its first step of compressive loading the numerical procedure returns the statement that it cannot find a critical integration point anymore. The integration point is behaving linear elastically, using the latest tensile Young's modulus, in compression, because cracking has already been assigned to this integration point in this same direction. It can still continue cracking if the elements is again loaded in tension and damaged.

This situational model also does not allow the second direction to be of the same failure as the first direction. It must be a combined tension-compression failure or the second failure direction will not be a failure direction at all and thus will continue to behave linear elastically. This can cause unrealistic high stresses in the construction that can influence the outcome of the calculation. The elements can sustain more force than actually allowed.

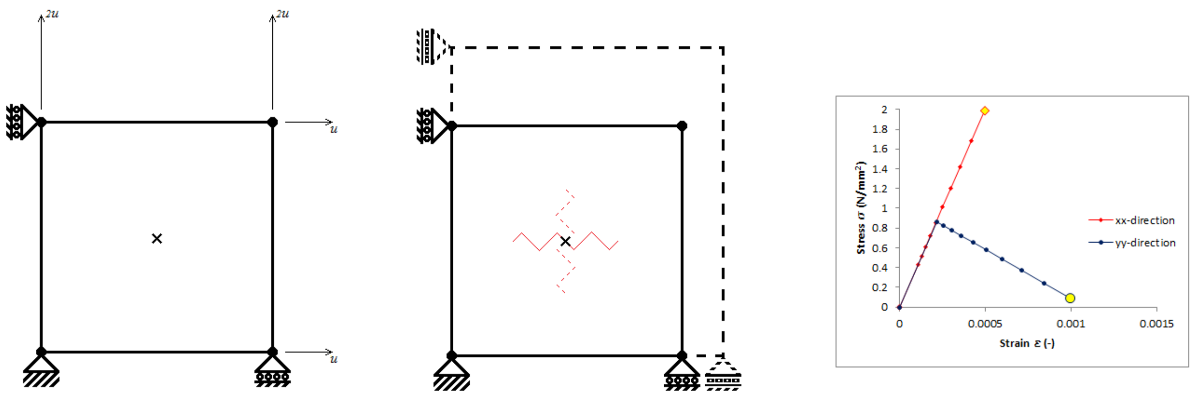

Figure 8.6: Setup for verifying the behaviour of double failure with results.

This situation is illustrated in figure 8.6. The element is subjected to tension in both directions. It is thus to be expected that this element cracks in both directions. However, with the model used and the theory explained above, this is not possible. The first failure direction will return the softening behaviour as expected, but the second failure direction does not exist at all. As long as it will not crush, it will continue to behave linear elastically. Even if the strains are bigger than the crack strain and the stresses become bigger than the maximum allowable stress.

8.1.3. Notes regarding the casus

Both variants have limitations and neither can represent the behaviour of crack closure and reopening. The limitations of both influence the results obtained and the question remains which is recommended for usage with respect to the casus. As will be explained in the following section, both models are taken into further consideration.

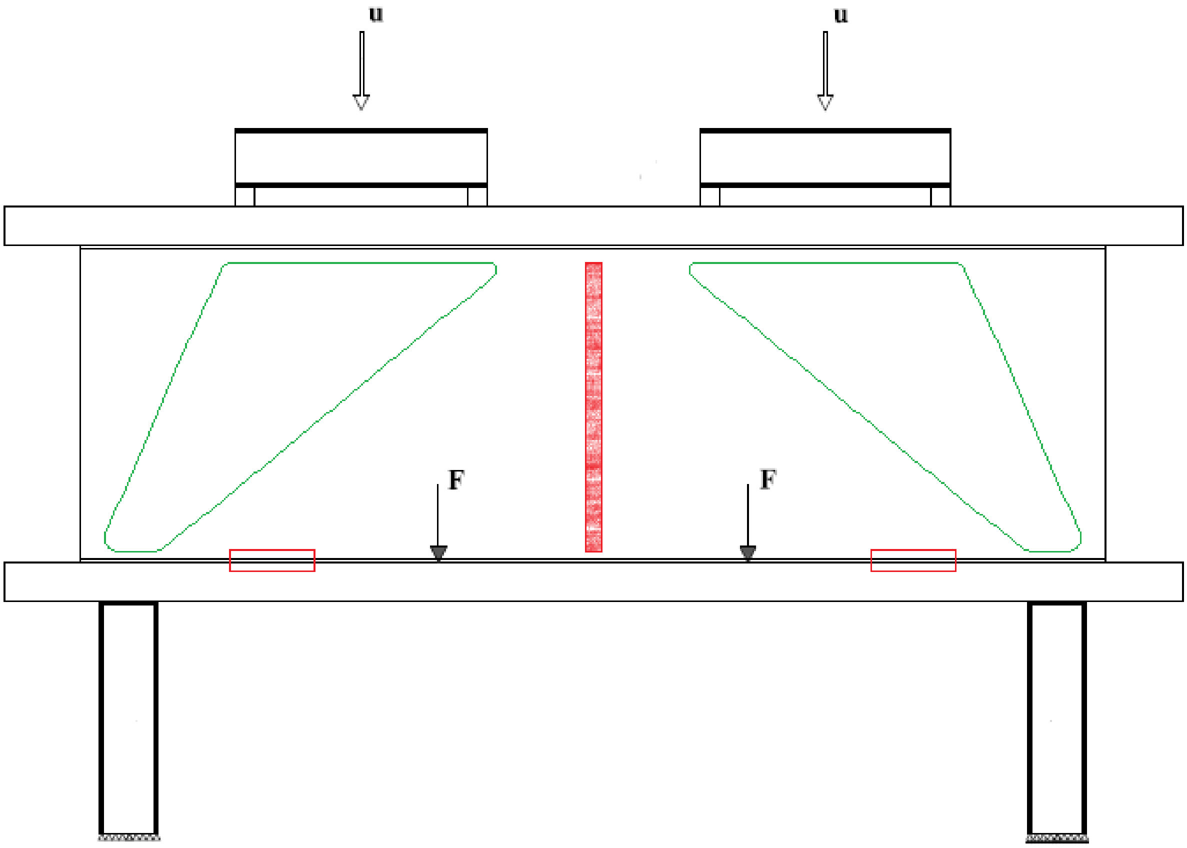

Figure 8.7: Notes regarding the casus.

The version which uses a coupled saw-tooth law does not correctly model crack closure and crack reopening as proven by the single-element example. The phenomena of crack closure and crack reopening is not expected to happen significantly or at all in the masonry wall itself, but only noticeably in the interface elements. In the non-proportional phase where point loads are used to separate the lower concrete beam from the masonry wall the interface elements will crack. After loading of the proportional displacement loading from the jacks, the masonry wall itself is also pushed downwards to such an extent that the edges of this separation crack, red rectangles in figure 8.7, will experience crack closure.

The version which uses a decoupled saw-tooth law also does not allow the same type of failure in both orthotropic directions in a integration point. This seemed to mostly only happen in the region around the crack appearing in the centre of the masonry wall, the shaded red rectangle in figure 8.7. The crack in the centre can reach in the second direction unreasonable high stresses and strains for they continue to behave linear elastically and they will be skipped as critical integration points in the process.

Both might affect the behaviour in those areas, but the region of interest in this research is the green area in figure 8.7. Herein combined tension-compression failure will clearly be the most important failure mechanism and the most represented failure mechanism. This means that crack closure and crack reopening as well as same type of failure in both orthotropic direction of an integration point will not be present in a large extent. This means that although the SLA process is not perfect yet, resulting in two imperfect versions, it is expected that both versions of SLA will give results that are globally very alike. The limitations of both versions will have a negligible effect on the total response of the structure.

8.1.4. Proposed improvement

Now two damage indicators are used for SLA, one for *n*-direction and one for *t*-direction. A positive damage indicator indicates tensile damage while a negative damage indicator represents compressive damage. At the moment of failure it is now decided if the integration point will be damaged in tension or compression and sticks with this choice throughout the whole analysis for the decoupled saw-tooth law model. It does not allow the damage state to be reversed. The coupled saw-tooth law model, however, uses a wrong loading history if the stress state is switched.

As an improvement for this orthogonal damage model four damage indicators are proposed. Two indicators have to be used for each direction. This means that each integration point contains in each possible failure direction a tensile saw tooth diagram and a compressive saw tooth diagram, instead of one or the other depending on the moment of first damage.

By introducing more damage indicators than there are in directions, parallel calculations are created. This will significantly enlarge the computation time needed for multiple calculations have to be carried out at the same step. Normally, the stiffness in a failure direction is updated after an increment and this same stiffness is used in the next step. However, each failure direction now has two possible stiffnesses. In the case of first cracking in the first step, the direction has a damaged tensile stiffness or an undamaged compressive stiffness. This means that a damaged integration point gives four scenarios to calculate. The scenario with the lowest applied load, is the decisive scenario. The integration point is updated and the procedural loop is run again. One can imagine that with a full structure and many integration points the computational effort becomes unrealistically high.

To prevent the propagation of number of scenarios the saw-tooth laws have to be coupled somehow. This means there has to be unloading and reloading in the model, while going through the origin of the stress-strain diagram during the process each time. A status indicator is probably needed to determine the previous state of the integration point.

8.2. Verifications using element tests

In this section tests have been carried out in order to find out if the basics of the code works accordingly. All sorts of simple single-element tests are used to verify the source code. Special cases are treated as well for uncommon situations and options are discussed to solve or bypass the found inconsistencies. For a full-fledged report of this part the reader is directed to Appendix A.

8.2.1. Basic tests

A number of simple tests have been carried out and are shown in figure 8.9 to demonstrate that the model functions properly with the common loading schemes. Tension, compression, shear and a combination of all three together is used and the constitutive results are obtained to the implement ripple-diagrams and hand calculations.

A side not has to be made for the element subjected to tension in both orthogonal directions. As discussed before in Chapter 7, this gives different results for both versions used in this research. The decoupled saw-tooth law model will continue to behave linear elastically, while the coupled saw-tooth law model is able to crack in both orthogonal directions. These results, which are obviously very different, and possible impact on the global behaviour of structures are already discussed in the previous chapter.

8.2.2. Rotated axes

In the basic tests the local axes of the element and the global axes coincided. Here a look will be taken into the situation where this is not the case. The local axes can be changed in two different ways. The first options is to rotate the element as a whole and to put it under an angle of α degrees. The second options is overriding the local axes with a newly defined axes.

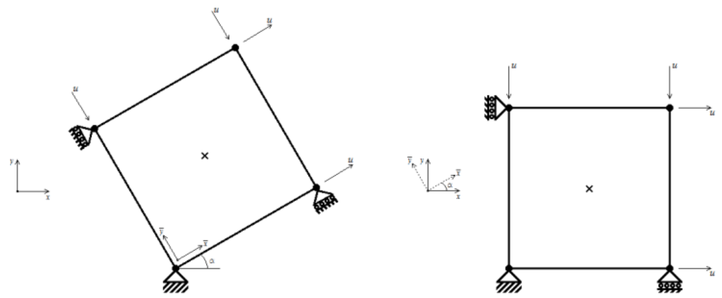

Figure 8.8: Rotated element (left) and rotated local axes (right).

The test should give insight into the way results, like stresses, are transformed from one coordinate system to another coordinate system. In this test both ways of coordinate rotation, figure 8.8, result in correct transformation of the stresses. The output is checked and transformed with hand calculations concluding that the transformation procedures are correctly implemented in the code.

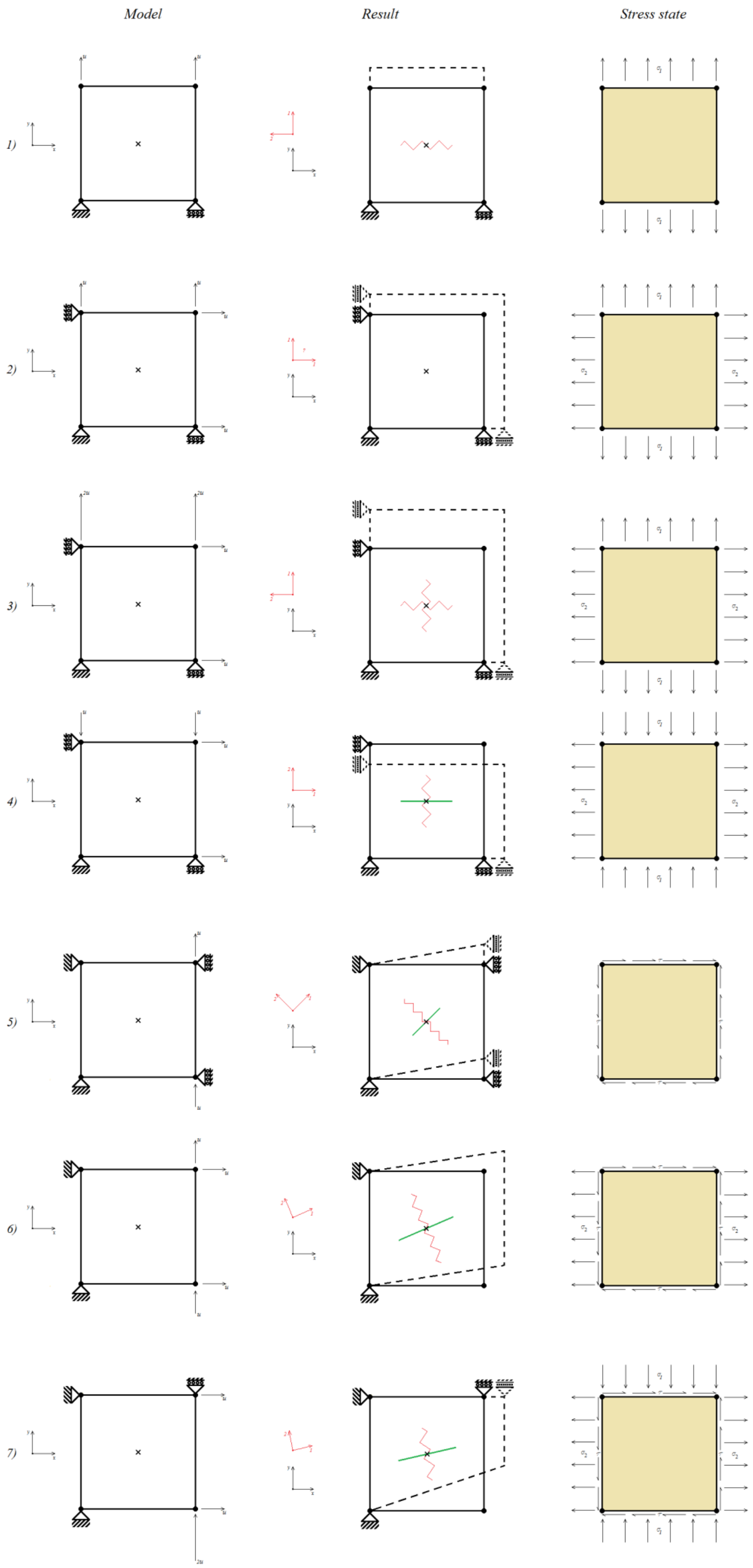

Figure 8.9: Basic tests.

8.2.3. Non-proportional loading

Non-proportional loading is a loading scheme recently added in SLA code to represent forces working on the structure which are present, but not dependent on the applied proportional loading. These loads remain the same magnitude throughout the analysis, like self-weight. These loads have to be implemented manually and replaced by the standard loading at the moment however, for the loading types as self-weight are not available yet in the code.

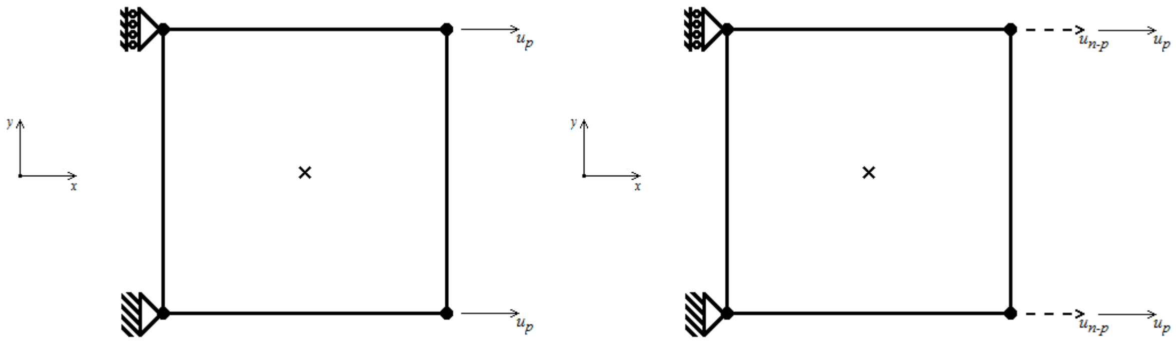

Figure 8.10: Proportional loading only (left) and combined proportional and non-proportional loading (right).

A small test has been carried out and pictured in figure 8.10 to check if the implementation of non-proportional loading goes well. The results indicate this loading scheme is correctly taken into account. When the non-proportional load does not generate significant stresses causing the integration point to reach its maximum allowable stress in the first Secant branch, then the load is applied in one step. And when the non-proportional load creates bigger stresses than allowed, it will be dealt with proportionally until the full load can be applied. After this the reduced material properties will be taken into the proportional loading phase and the calculation continues until the element is completely damaged.

However, this combination of loading does not work the same as phased analysis as used in NLFEA. Although two "phases" are used to put on the loading, it is not possible to apply more than those two phases and the two phases are always applied in the same order. The load is either assigned to the proportional (load case 1) or non-proportional load class (all other load cases) and all the loads are applied simultaneously during the active part of their loading class. It is thus not possible to let one direction to be fully proportionally be cracked by proportional loading after having applied a non-proportional load, beforehand another direction is loaded in the same way.

The addition of non-proportional loading adds a second phase to the analysis, but must not be confused with phased analysis. It works accordingly, but if multiple phases are used during the experiment, it is also needed to make multiple models.

8.2.4. Multiple integration points

The same linear element can contain multiple integration points. This still returns the input as the output. All the cracks are in the same direction and afterwards all the integration points are crushed orthogonally to the crack direction as shown in figure 8.11. The fact that it's a linear element, which describes the displacement field linearly in *x*- and *y*-direction, is the reason the results are as expected.

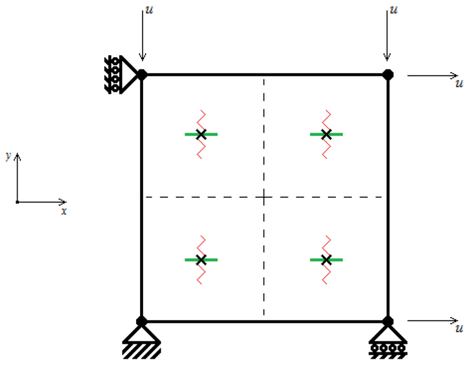

Figure 8.11: Linear element with multiple integration points.

However, using a quadratic element of the same type and geometry does not result in the same results. The displacement field isn't described linearly anymore in the orthogonal directions, but quadratic. This results in an uneven displacement creating unwanted results, as can be seen in the left picture of figure 8.12.

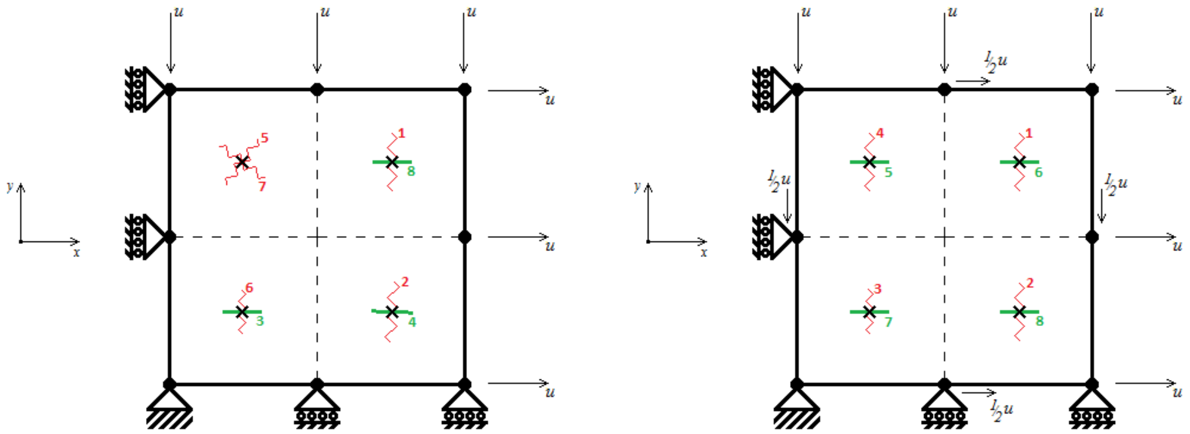

Figure 8.12: Quadratic element with multiple integration points unjustly loaded (left) and justly loaded (right).

In the left figure not all degrees of freedom are described with imposed deformations, while in the right figure this is the case. The correct results were retrieved with the right figure, for the centre nodes of the bottom and left side were not equally displaced as the center nodes from the top and right side respectively. Due to the loose behaviour of the nodes, unrealistic results are obtained with in particular integration point 1 and 2.

The left model is thus also used in NLFEA to see if the same happens in this analysis type or if it is a strange phenomenon of the SLA. It does not happen in the nonlinear analysis. These results are due to the traits of both analysis types as discussed in Chapter 7. Nonlinear analysis shows the crack apparition spontaneous and simultaneous. So integration point 3 and 4 both reach their maximum tensile strength at the same time and this means they crack at the same time. This simultaneous cracking makes sure the computation is symmetric of nature and can be seen as a bifurcation as seen in paragraph 3.3 [11]. However, normally structures contain more than one element and neighbouring elements will ensure this free behaviour of the nodes are constraint.

8.2.5. Influence of Poisson's ratio

The same linear element will now be subjected to tension and compression. The same tension softening and compression softening is used, but now a Poisson's ratio of ν = 0.2 is added to the material properties of the element. Before, the ripple diagram implemented was retrieved in the output results. Now these results, with respect to the strains, are larger.

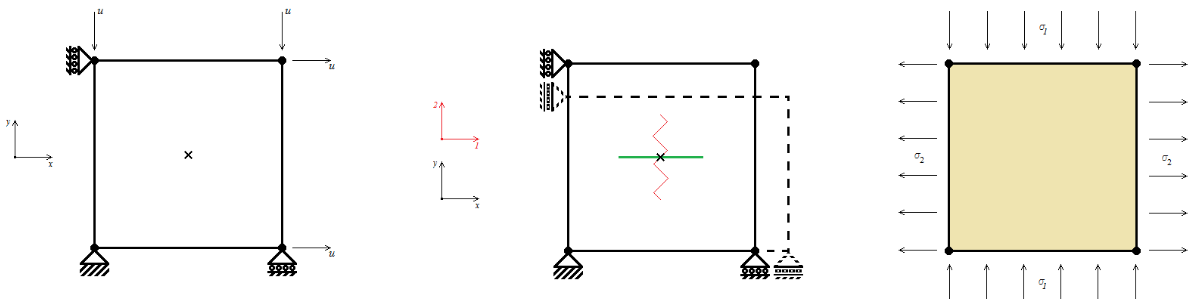

Figure 8.13: Model (left), displacements (centre) and stress state (right) of the test with ν = 0,2.

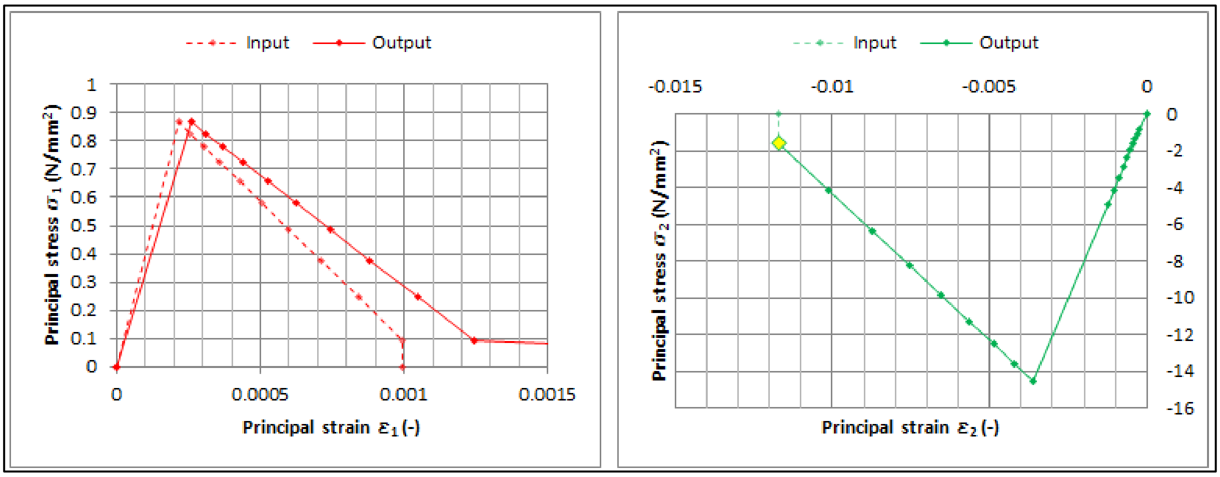

Figure 8.14: Graphical results of the influence of Poisson's Ratio.

The stresses are returned exactly the same, but the tensile strains are not equal to the strains of the ripple diagram implemented. This is due Poisson's ratio. When the stresses are implemented in the orthotropic constitutive law the strains received are indeed larger than the strains implemented. When $\nu = 0$, then the strains returned are equal to the strains implemented, because the constitutive matrix is decoupled. When the material is fully cracked, the interaction between the two orthogonal directions is completely reduced to zero. The tensile stresses are not present anymore in the first principle direction, for it failed. This reduces the constitutive matrix to a 2×2-matrix, for the first column and row can be removed from the system. Poisson's ratio has then no further effect for the second principal direction, as can be seen in the results. The compressive strains are the same as the strains implemented.

Poisson's ratio seemingly effects the origin of the secant branch obtained from the output, meaning they do not cross the origin anymore. This is clearly visible in a double compression test as shown in figure 8.15 and 8.16. The test used a linear softening diagram for compression it was run twice, one with a Poisson's ratio of $\nu = 0{,}0$ and the other with a Poisson's ratio of $\nu = 0{,}2$. The actual Young's Modulus obtained from the results is still the same as the input, but like in figure 8.14, Poisson's ratio constantly shifts the points in the graph a bit more in every step.

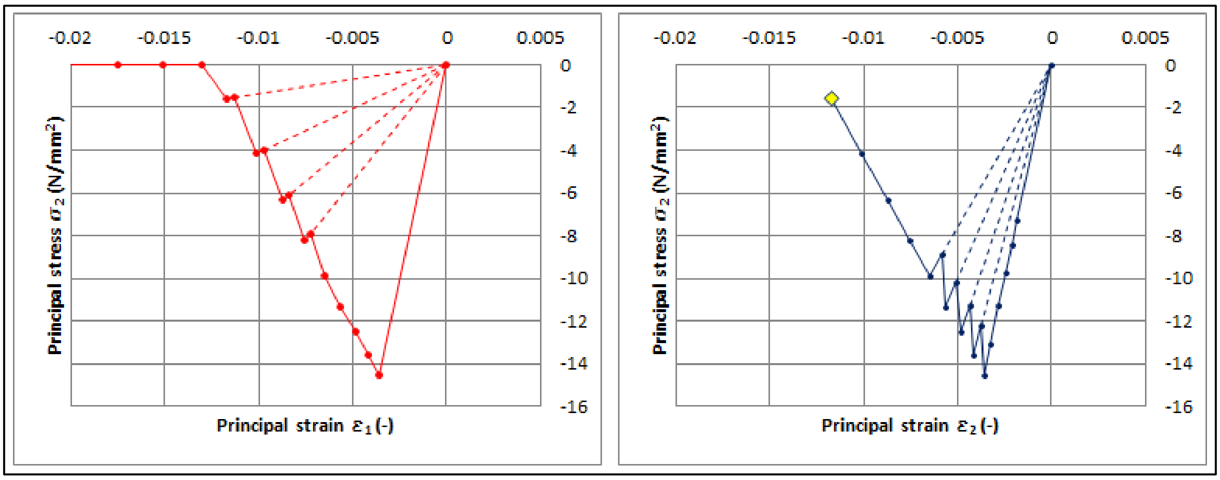

Figure 8.15: Results of double compression test with ν = 0,0.

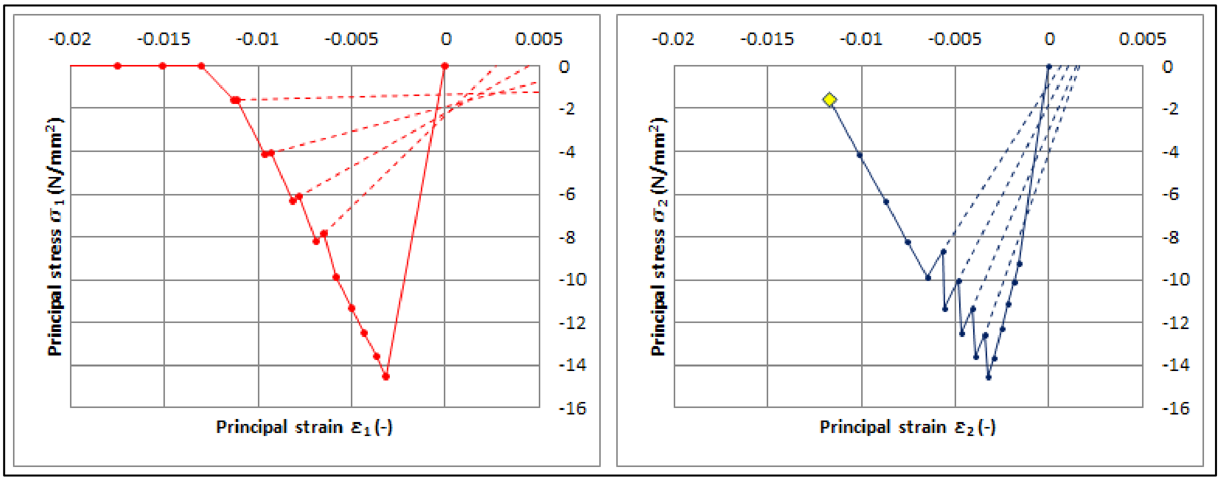

Figure 8.16: Results of double compression test with ν = 0,2.

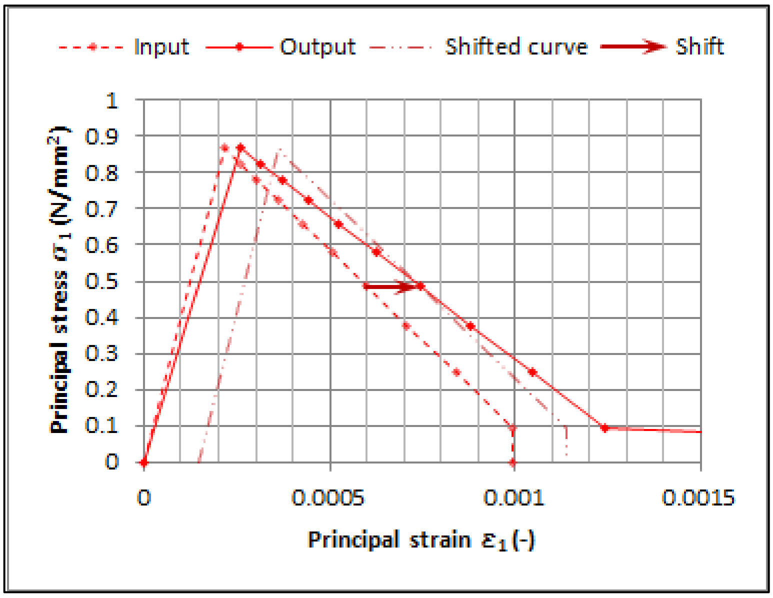

Figure 8.17: Constant shifting of the graph.

This shifting is visible and can be easily shown with the results found in figure 8.14. The explanation is presented in figure 8.17 presenting one shifted curve. In this figure it is clearly visible that with each step the curve shifts a bit to the right. Only one point of these shifted curves is taken into consideration each step for the formation of the complete curve representing the output. This means that the output is a combination of points from multiple shifted curves, making it look like the Secant branches are different. But each point has still the correct Secant branch in its own shifted curve.

8.2.6. Extreme localisation

All tests were made for one element only. To be sure everything works accordingly, multiple elements will be subjected to an overall combination of combined tension and compression. The tested model is found in figure 8.18. All elements should be able to fully crack in one direction while being fully crushed orthogonally. For this test a parabolic compression softening with 22 teeth and the same linear tension softening of 10 teeth as before has been used. The results are shown below in figure 8.19.

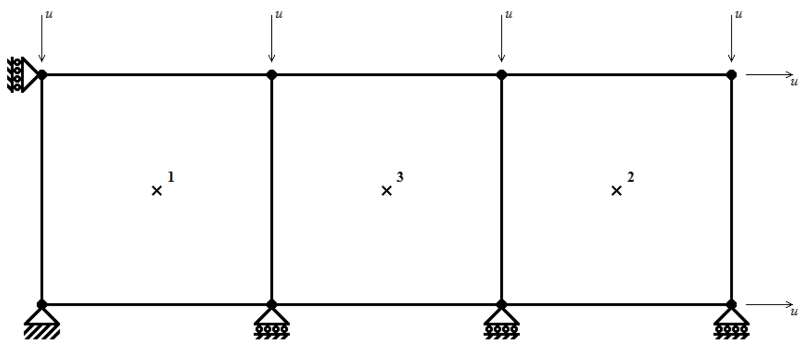

Figure 8.18: Model of multiple elements.

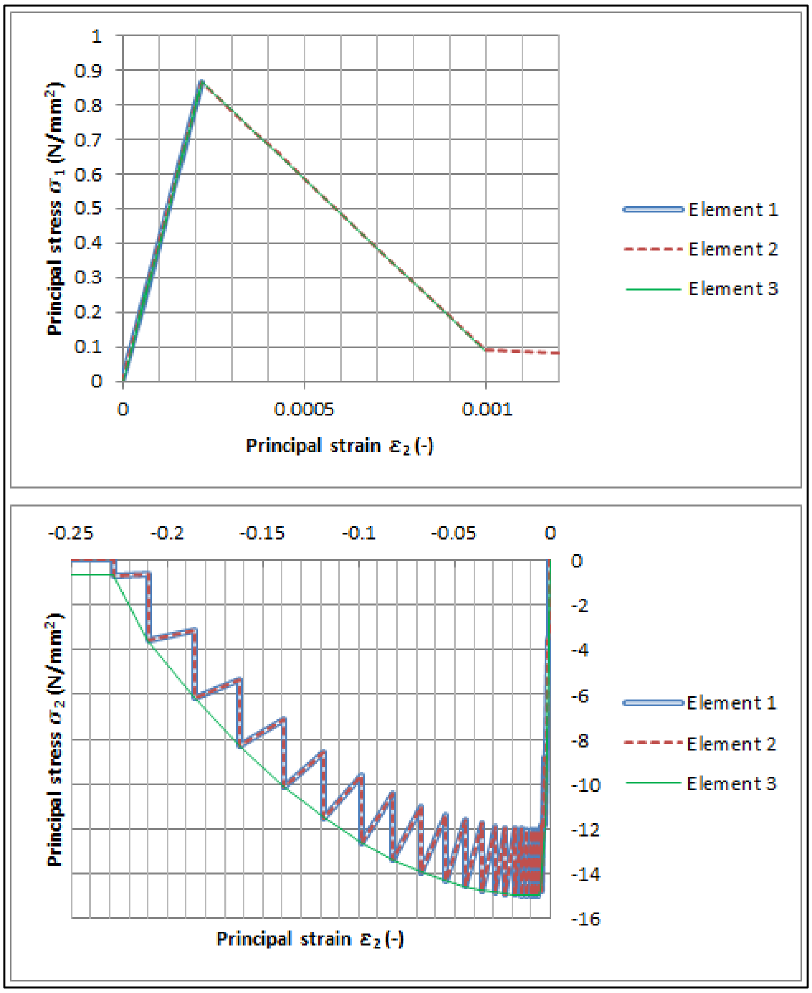

Figure 8.19: Results of principal stress-strain for the test of multiple elements.

At first glance, the results are as expected. Both tensile and compressive softening are retrieved in the same shape as implemented as input. Visually, the deformations and stresses are accordingly. However, element 1 did not crack at all. The computation stopped prematurely, preventing the element from cracking.

What happens is that after element 3 has been completely damaged, as well as in compression as in tension, the procedure selects element 3 anew in the next step as critical element. This is not possible theoretically, for the element was completely damaged and it should thus have picked element 1, which was the only element left not damaged in tension.

It actually indicates that unrealistic behaviour is occurring. After 10 steps, 10 teeth of tensile linear softening diagram, element number 2 is completely damages in tension. This means that tensile reactions should not be transferred anymore to the other elements and interaction is lost. Nevertheless, the structure continues to let the elements crush up until step 76 (10 + 3 × 22). In step 77 the calculation should stop. However, the SLA procedure still has more teeth to follow and continues the calculation by letting the remaining elements fail in cracking. As aforementioned, the element where the load is applied on is completely damaged. This results in an unrealistic high results in step 77 and onwards. After element 3, the middle element, also is fully cracked in step 86, the calculation is stopped due to the mentioned error.

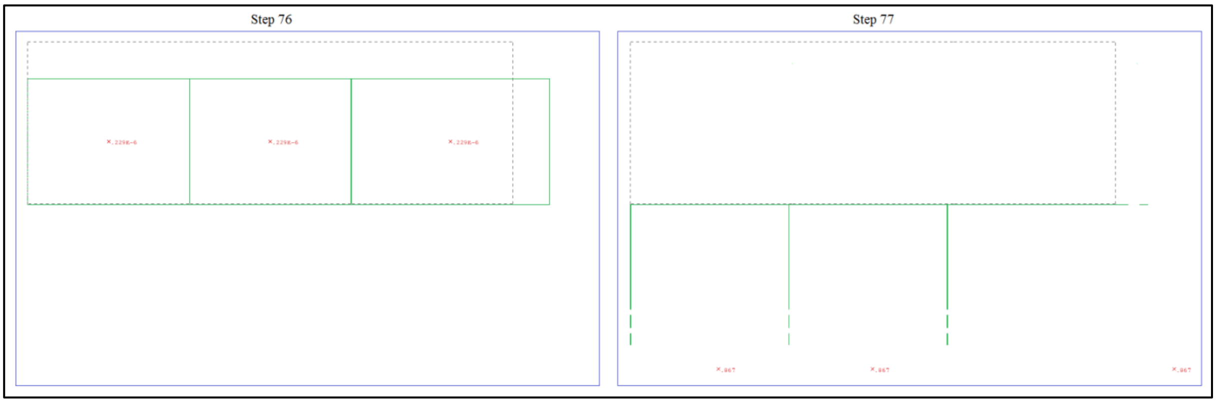

Figure 8.20: Step 76 and step 77 of the calculation. Step 77 returns unrealistic deformations.

Element 3 is reselected by the procedure, because very localised behaviour arises. It is even so big, that the end point of the dummy tooth is reached. Although next results may be unusable as shown in figure 8.20, the end point of the dummy tooth should never be reached. Therefore the following change in the ripple diagram is made.

Previously, the strain of the dummy tooth is kept the same as the previous tooth, ultimate strain, while adding a very low stress. This represents a negligible stiffness and indicates that the integration point is thus completely damaged. However, for very localized behaviour this dummy tooth can reach its peak and be the critical point. By enlarging the strain of the dummy tooth enormously as shown in figure 8.21, this problem is postponed. The goal is to make sure the element is not critical anymore and the dummy tooth should thus approach linear elastic behaviour, which is achieved by this measure.

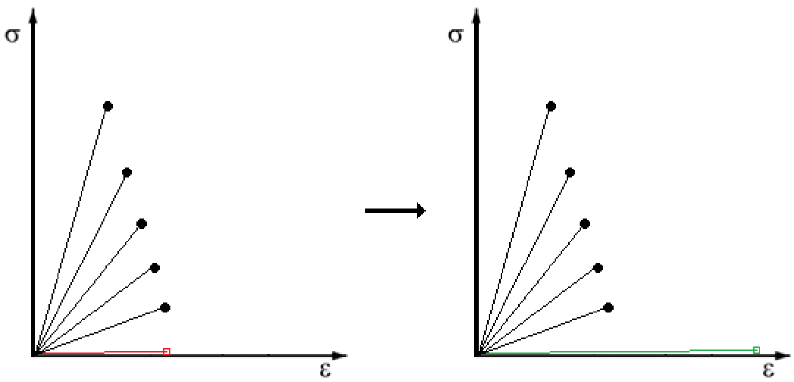

Figure 8.21: Previous definition (left) and newly used definition of the dummy tooth (right).

8.3. Biaxial tension-shear element test

To further scrutinize the combination of load types and to verify the elastic softening formulation the test made in paragraph 3.4. of [12], see figure 8.22, has been remade with SLA. The results have been plotted against the results found in [12]. Comparison has been made with the branch of 90°, which stands for a single orthogonal cracking. This was only possible to test with the coupled saw-tooth law for cracking in both directions had to be allowed.

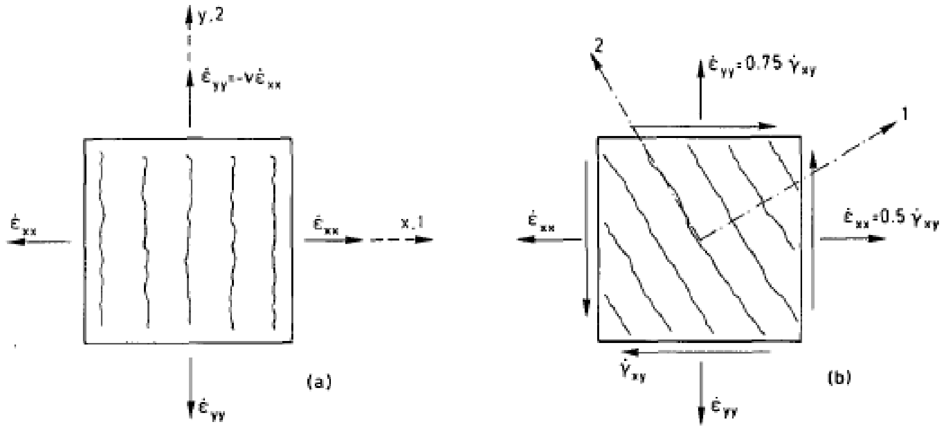

Figure 8.22: Lay-out of the problem with tension up to cracking (a) and biaxial tension-shear scheme. [12]

8.3.1. Input

The model used with SLA slightly differs from the model used in NLFEA as seen in NLFEA. In the first phase, figure 8.22.a, there will be a compressive strain due to Poisson's ratio. However, this respective strain is not present in this SLA calculation. In NLFEA it is possible to change the model during phases of the analysis, like boundary conditions. In SLA it is only possible to change the loading during the two phases of non-proportional loading (8.22.a) and proportional loading (8.22.b). As it is needed in 8.22.b to have all nodes prescribed and thus "supported", it was also needed to have this configuration in 8.22.a for SLA. This inability to change the mesh during the analysis in SLA will give small deviations in the results compared to NLFEA.

Almost all the material properties have been taken as in the referenced report. These material properties have been gathered in table 8.1. The only difference is found in the reduced shear modulus G_{red}. Where J.G. Rots [12] used a parabolic formulation for β to determine the reduced shear modulus, this test uses a damaged stepwise reduction as shown in Chapter 4.

Table 8.1: Material properties for biaxial tension-shear test in SLA.

Components	Parameter	Symbol	Value	Dimension
Element	Modulus of elasticity	$E_{element}$	10.000,00	N/mm^2
	Poisson's ratio	$\nu_{element}$	0,20	-
	Tensile strength	f_t	1,00	N/mm^2
	Softening diagram	-	Linear	-
	Fracture energy	G_f	$1{,}5 \cdot 10^{-4}$	N/mm
	Crack bandwidth	h	1,00	mm
	Shear retention function	-	Damage	-

8.3.2. Output

The whole SLA calculation was run until no critical integration points where left to be selected, meaning that the element has been completely damaged. Matching results are qualitatively obtained and can be found in figure 8.23 and 8.24, where the blue lines are results from SLA and the red lines are the results from NLFEA used for comparison. The results of SLA are slightly higher, because a ripple diagram slightly overestimates the tensile strength. Also, the SLA results deviates from the NLFEA in the right figure of 8.24, because the element cracks anew orthogonally in SLA, while in NLFEA only one crack was applied. The most clear difference can be found in the shear stresses, but this is due to the different definition of the reduced shear modulus.

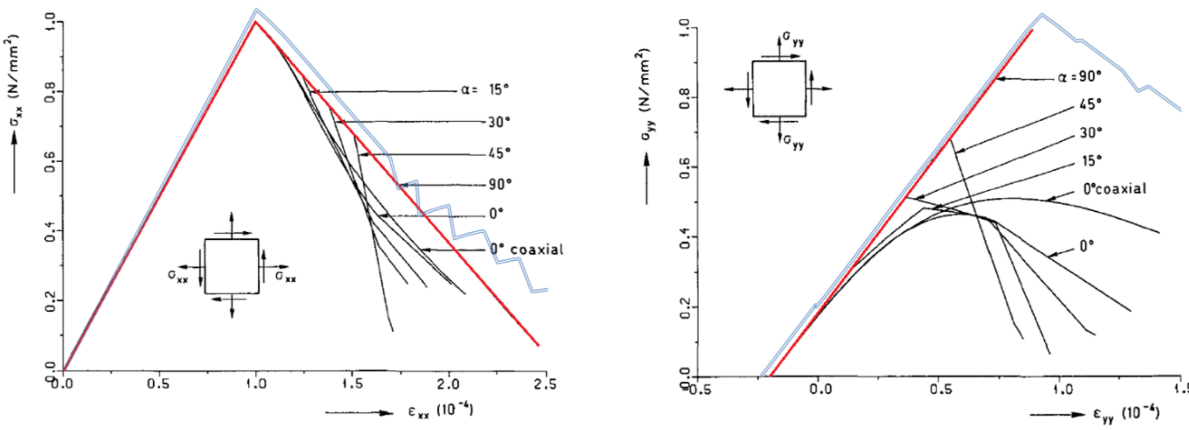

Figure 8.23: Results for x-direction (left) and y-direction (right) where the blue line indicates SLA results with orthogonal cracking and the red line indicates NLFEA results with only one crack.

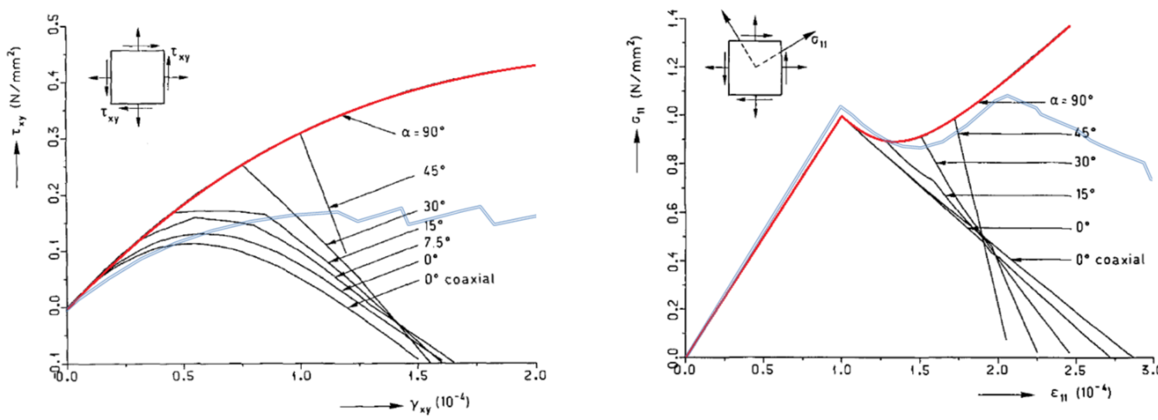

Figure 8.24: Results for shear (left) and the first principal direction (right). where the blue line indicates SLA results with orthogonal cracking and the red line indicates NLFEA results with only one crack.

While the NLFEA used a β-factor depending on the crack strains (ε_{cr}), the SLA used a "β-factor" that depends on damage increments and their reduced properties (E_{min}). The development of both reduced shear modulus are shown in figure 8.25. In this figure it can be concluded that the graphs used by J.G. Rots [12] looks a lot like the graph used by the SLA code. However, they are not the same, for example, the descending branch of SLA is steeper than of the NLFA, almost two times steeper. This phenomena is reflected in the obtained results in the left graph of figure 8.24, where can be seen that the shear stresses of the NLFEA almost increase twice as much as the SLA at the start.

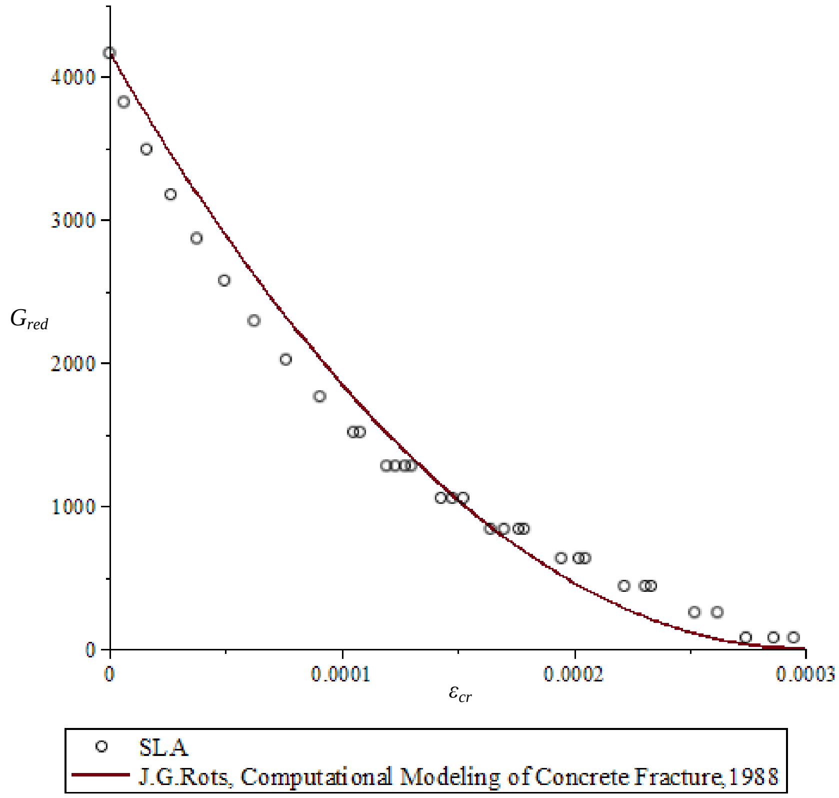

Figure 8.25: The reduced shear modulus G_{red} during both analyses.

8.3.3. Concluding remarks

The output of SLA is consistent with the found results by J.G. Rots [12]. No inexplicable results are obtained and the used formulation and shape for the reduced shear modulus is comparable with the one proposed by J.G. Rots. The SLA model works fine with regard to the elastic softening formulation and the transition from both loading phases also goes well. The rotation of principal stresses after crack initiation is captured correctly by the sequentially linear analysis method.

8.4. Shear-compression wall test

Experiments in shear walls have been adopted by the masonry community as the most common in-plane large tests. Still little knowledge exists about this type of structure. In this chapter a shear wall of the same form as tested in ETH Zurich [10] and numerically modelled with nonlinear analysis [9] is modelled with SLA. The behaviour is compared with the nonlinear and laboratory experiments.

8.4.1. Input

In total there were four shear walls tested. Only the geometry of one arbitrary shear wall of the three modelled by Lourenco has been taken into consideration. The wall consists of a masonry panel of 3600×2000×150 mm^3 and two flanges of 150×2000×600 mm^3. Two additional concrete slabs are placed at the bottom and top of the masonry wall. The geometry of shear wall W2 is found in figure 8.26.

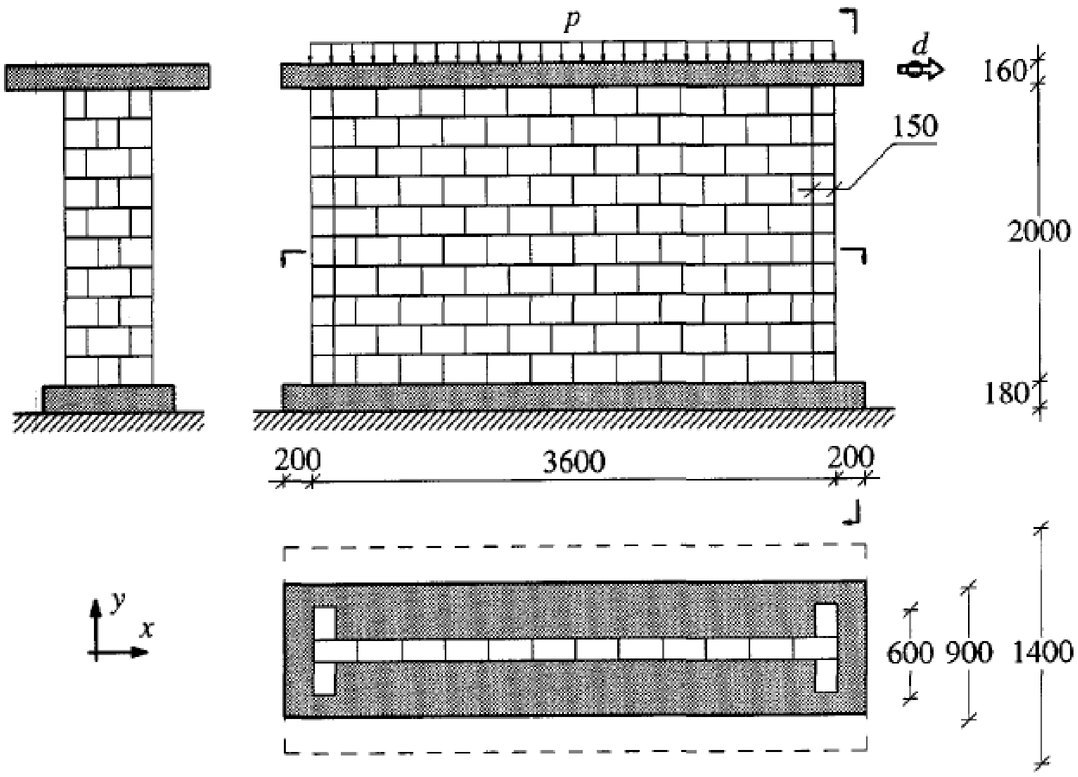

Figure 8.26: Geometry and loads for ETH Zurich shear walls. [9]

A homogeneous mesh is used in this variant of the model with orthotropic properties, which is different form the anisotropic properties in the nonlinear and laboratory variant. The mesh consist of 24×15 4-noded linear Q8MEM quadrilaterals for the masonry panel and 2×15 division also for each flange, which differs from the cross diagonal patches of 3-noded triangles for the flanges as used by P.B. Lourenço [9]. The concrete slabs consisted of the same division and elements as the masonry panel. All elements used a 2×2-Guass integration scheme. Other geometrical properties are taken from figure 8.25.

The structure is firstly pre-loaded by a distributed surface load p = 1,91 N/mm^2. After full application of the compressive prestress the top slab is prevented to move vertically and an increasing horizontal deformation loading d is applied at the edge of the top concrete slab to push the whole slab in horizontal direction. The self-weight had to be applied as line-loads placed in levels over constant heights for SLA does not have self-weight incorporated as a valuable load yet. And while the nonlinear analysis can compute this structure with one phased analysis, it is necessary in SLA to perform two analysis. One analysis applies the non-proportional loads implemented as forces and the second analysis applies both loading types where the non-proportional load is placed on the structure as a deformation load, which are the displacement results of the first analysis. This has to be done, for the model (here: the boundary conditions) cannot be changed during phases in SLA.

While the nonlinear analysis as well as the laboratory experiments do not use orthotropic properties, it will mean implemented material properties are different. Both x- and y-directions will have the same properties in this sequentially linear test while in the other tests [9,10] this is not the case. The material properties used are intermediate values used by P.B. Lourenço [9] and found in table 8.2.

Table 8.2: Material properties for shear compression wall in SLA.

Components	Parameter	Symbol	Value	Dimension
Masonry wall (plane stress elements)	Modulus of elasticity	$E_{element}$	4000,00	N/mm^2
	Poisson's ratio	$\nu_{element}$	0,20	-
	Tensile strength	f_t	0,35	N/mm^2
	Softening diagram	-	Linear	-
	Fracture energy	G_f	0,02	N/mm
	Crack bandwidth	h	25,00	mm
	Shear retention function	-	Damage	-
	Compressive strength	f_c	4,00	N/mm^2
	Softening diagram	-	Parabolic	-
	Fracture energy		6,00	N/mm
Concrete slabs (plane stress elements)	Modulus of Elasticity	$E_{concrete}$	25.400,00	N/mm^2
	Poisson's ratio	$\nu_{concrete}$	0,20	-

8.4.2. Output

The results for the coupled saw-tooth law calculation are shown in graphically in figure 8.27 as a force-displacement diagram and a non-proportional load diagram. They indicate the load path the structure has taken. The results regarding the principal strains and deformed mesh is presented in figure 8.28. This figure indicates the damage propagation throughout the structure. The same figures can be found for the decoupled saw-tooth law in figure 8.29 and 8.30 respectively.

The figures indicate crack formations at the red and orange dots. Sharp snap-backs are observed and the strains indicate complete damage from certain integration points, forming lines of completely cracked elements. The structure is pulled apart along that line, which is visible in the deformed mesh.

Up until the maximum peak load, which is represented by the yellow dot, the structure keeps to mainly crack until a complete diagonal line of complete damaged elements in tension is formed from the top to the bottom slab. The structure is cracked in half and is two parts are separating as seen in the deformed mesh.

From this point crushing will take a significant role and it is noticed that integration points are being completely damaged in compression. The bottom elements are succumbing to this explosive behaviour. This extreme quasi-brittle representation is found clearly with the initial load multiplier λ_{ini}. It is not possible anymore to find equilibrium with the full non-proportional loading applied. As stated in Chapter 4, the complete load consisting of both loading types will be scaled as a whole until equilibrium is reached. The initial load multiplier, thus the non-proportional load as well, will need to decrease in this case to satisfy the conditions. During crushing this seems to be an often occurring problem and sometimes equilibrium is reached with initial load multipliers lower than λ_{ini} = 0,2, which means it was almost impossible to load the structure at all. Two moments during crushing are represented by the green dots.

Finally also a complete crushed band is visible. At this point certain integration points are completely damaged, meaning they contain negligible stiffness. If a node is surrounded by only complete damaged integration points, these nodes theoretically fly away from the structure. These part of the structure will explode out of the specimen in laboratory experiments. Numerically, these parts can achieve strains high enough to make their dummy tooth the next critical Secant branch. The computation is stopped after 34567 steps for the coupled saw-tooth law formulation and after 32303 for the decoupled saw-tooth law formulation for this reason.

The traits of both saw-tooth law formulations are visible in the output. In the coupled saw-tooth law formulation it can for example be seen that certain integration points failed in both orthogonal directions in tension. The decoupled saw-tooth law formulation does not allow this phenomena. When an integration points should fail in the second orthogonal direction in the same way as the first, the integration point is not selected. Instead, the process ignores this and continues with a situation where damage is allowed. The constitutive behaviour of the second direction of the ignored integration point keeps behaving linearly. The damage in that integration point is skipped, resulting in less total amount of analysis steps.

For the coupled saw-tooth law it can also be spotted in the output files that a switch from tensile to compressive damage is made, while carrying over the damage history of the other. A warning message is returned indicating this occurrence. This happens quite regularly like the skipping of integration points occurring in the decoupled saw-tooth law. Both give overall the same result and neither of the limitation seem to have a huge impact on the qualitative outcome.

One step in the decoupled saw-tooth law formulation requires a negative load multiplier to reach equilibrium. This situation is found at step 20653 for the decoupled saw-tooth law formulation and is absent for the coupled saw-tooth law formulation. In the load-displacement graph it can be seen that a line goes through the y-axis, meaning it's data point is found in the negative values.

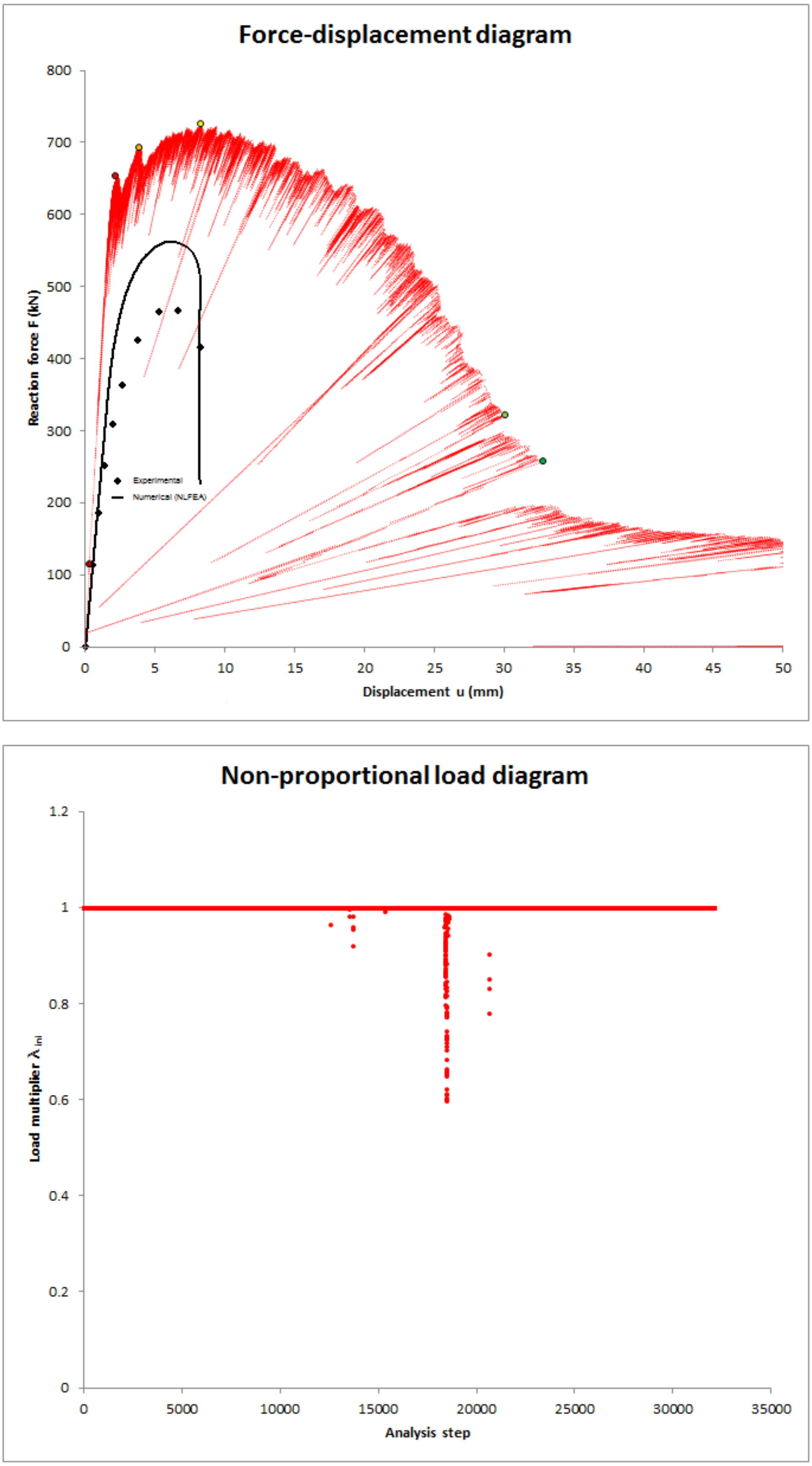

Figure 8.27: Force-displacement at load application (top) and initial load multiplier during analysis (bottom) for the coupled saw-tooth law formulation.

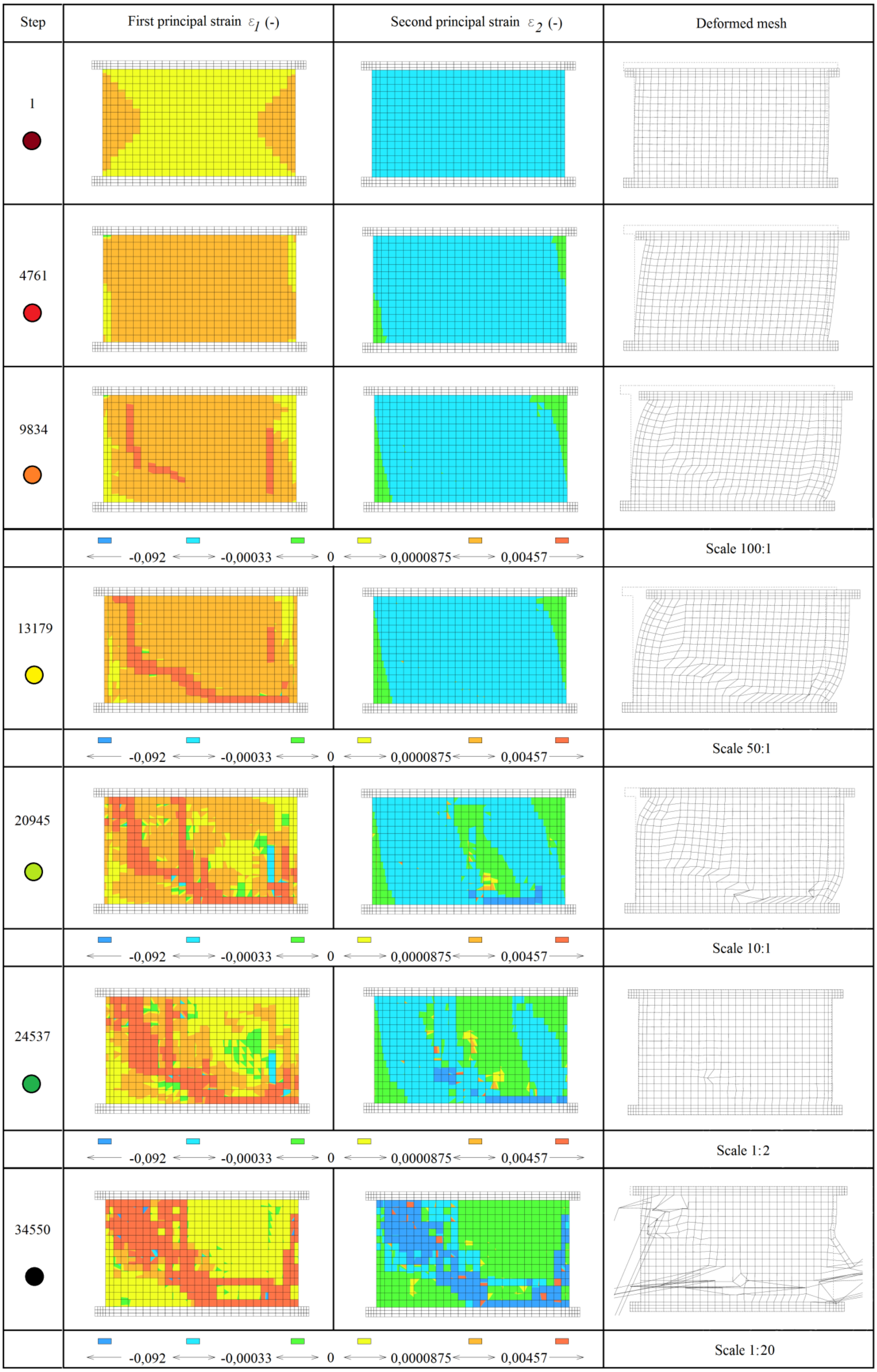

Figure 8.28: Principal strains and deformed mesh of the structure for the coupled saw-tooth law formulation.

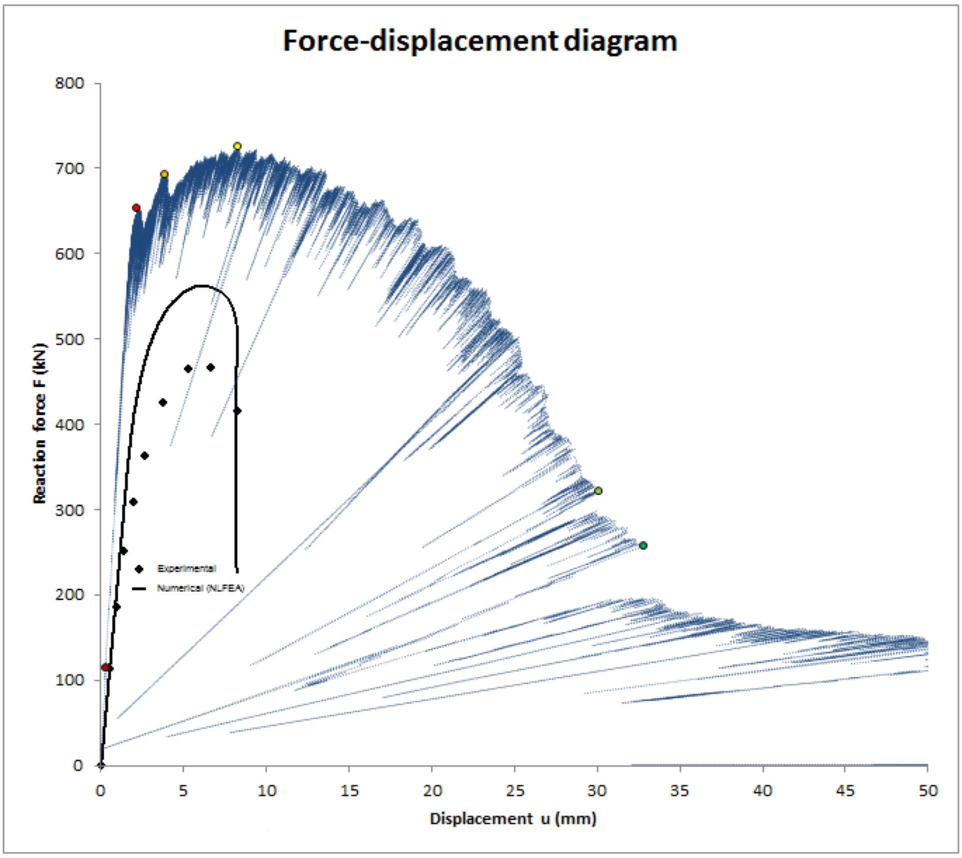

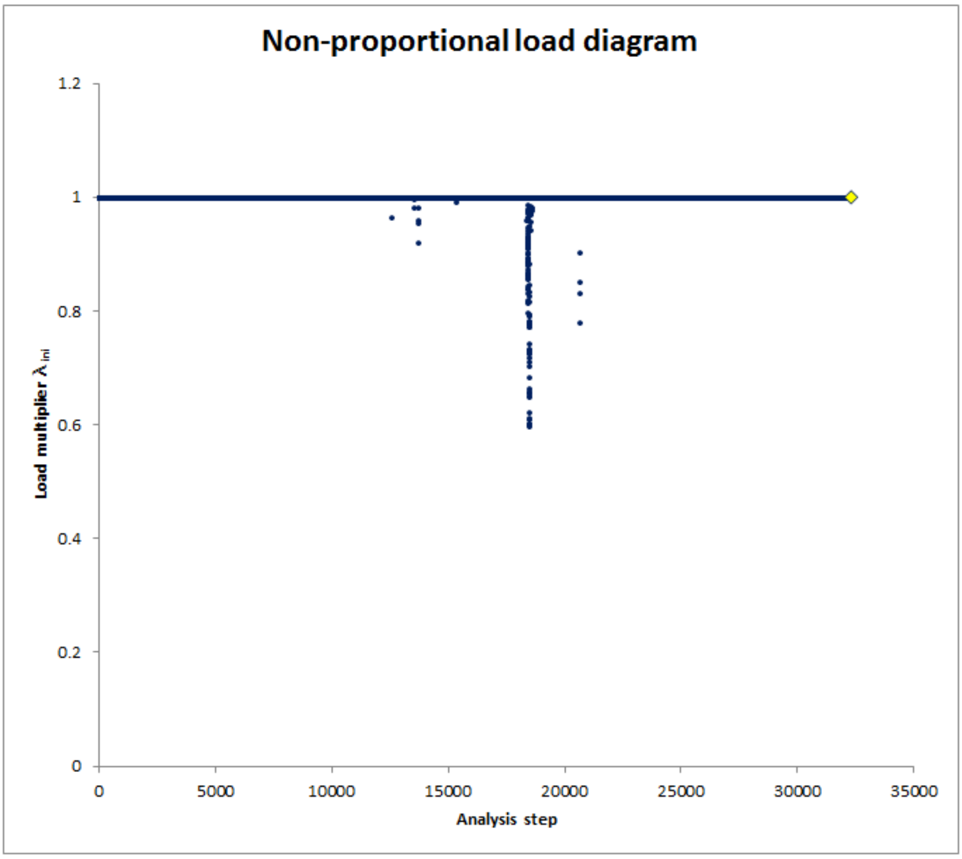

Figure 8.29: Force-displacement at load application (top) and initial load multiplier during analysis (bottom) for the decoupled saw-tooth law formulation.

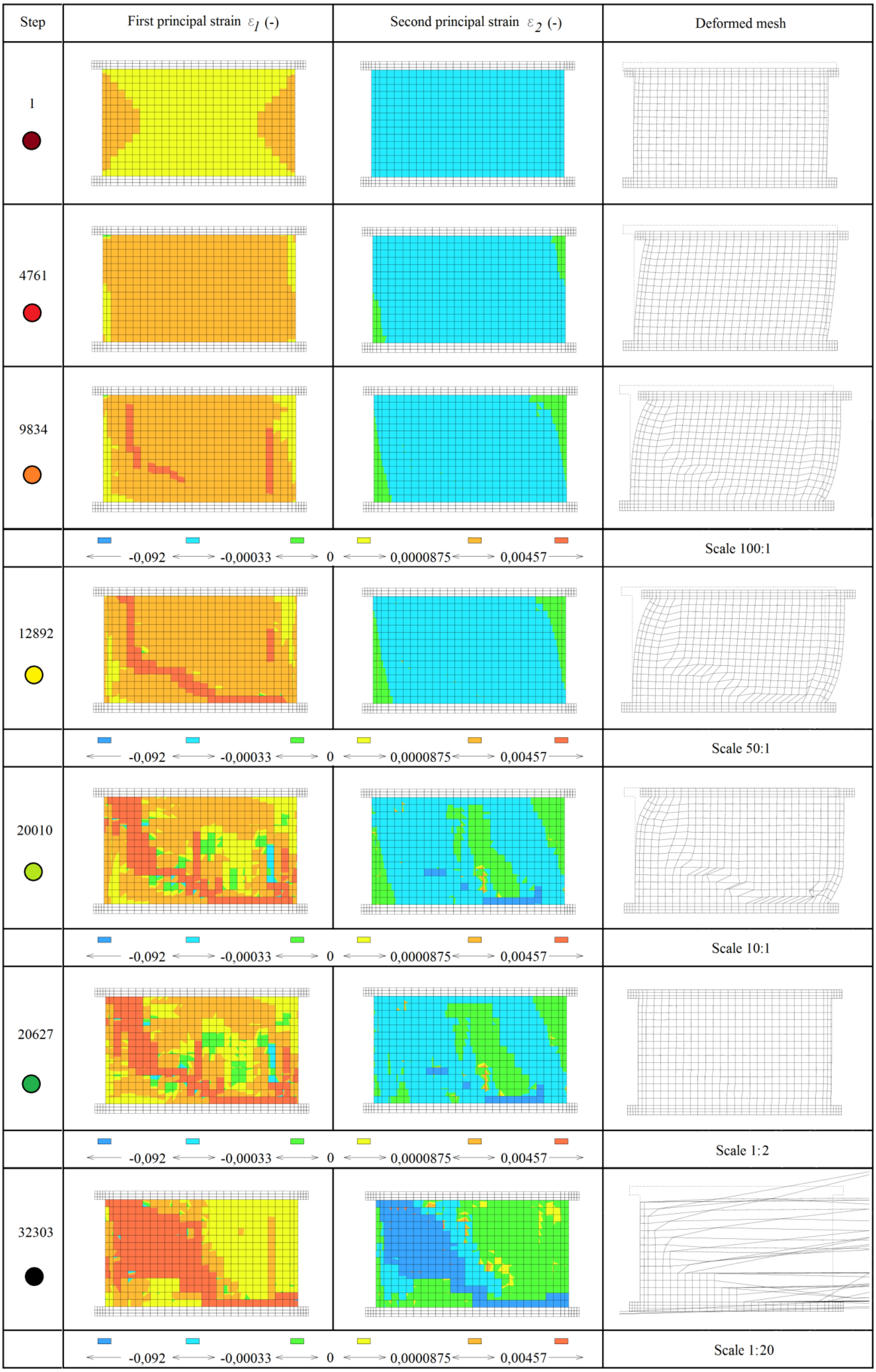

Figure 8.30: Principal strains and deformed mesh of the structure for the decoupled saw-tooth law formulation.

8.4.3. Discussion

The parameters did not contain the exact same values as the experiment performed in the lab [10] as well as the numerical calculation [9]. Quantitative results are not the same, but they are close to each other, meaning that qualitatively the same response is obtained. The load slightly increases, reaches its peak load and starts to crush, like in the other experiments. The other experiments are found in figure 3.6 or presented anew in figure 8.31.

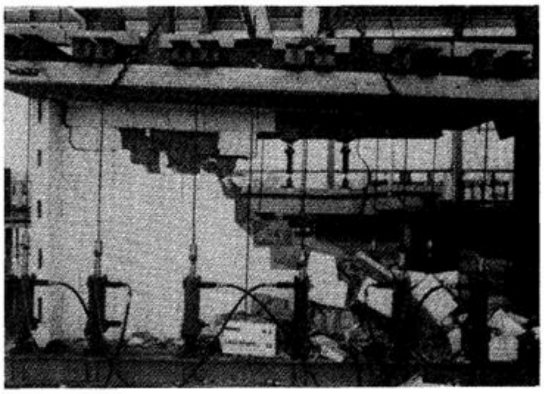

(a)

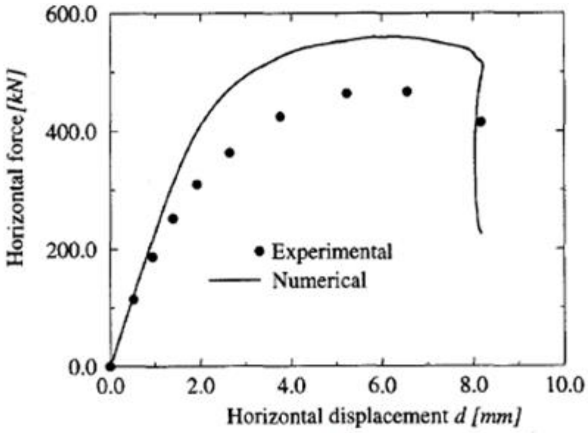

(b)

Figure 8.31: The experimental failure pattern at the end stage of wall W2 as presented by [10] (a) and the load-displacement graph found from the numerical simulation as presented by [9] (b)

With regard to the visual comparison, figure 8.31.a, it is clear the crack is not in the exact location. The top slab is moved as a whole in the laboratory experiment, making the wall split in two almost identical halves. One half is still in its place, where the other upper triangle has fallen out. In the SLA calculation the slab was pushed from the left, making this line of division shift slightly to the left. Whereas if the wall is pulled from the right this will shift to the right. But in all cases it is clear that a line develops that makes the wall separate in two parts. The bottom part has also a crushed line of masonry at the right, this is also clearly visible in the SLA calculations performed.

With regard to the graphical comparison, figure 8.31.b, it was stated in Chapter 3 that after much effort a successful stable point was found during the phase where compressive behaviour is the most important failure mechanism to be found at that moment. After this step equilibrium was very hard to find with NLFEA even after applying cumbersome procedures and computational effort. This moment is also visible in the SLA calculations. Right when the load-displacement graphs reached their peak load and started to curb downwards again while crushing significantly increased in importance, difficulties arised in finding equilibrium. The SLA can bypass this problem temporarily by lowering the initial load multiplier λ_{ini} as shown in the figures and continue the calculation. SLA can thus successful continue the calculation after this point with ease, but at this same point NLFEA diverged.

8.5. Final remarks

The SLA is a numerical model which is still in development and has to be constantly verified with each version. At this moment two versions are available to apply on structures. One model uses a coupled formulation for the constitutive law of tension and compression, which is basically the standard model. The second model uses a decoupled formulation and is a simplified model for application to certain situations, mainly compressive strut formation in concrete-like materials.

Both models have been tested with basic tests on elements to verify the foundation of these models. The model show differences, but that is due to their known characteristics and limitations. Influences of other types of situations are scrutinised to ensure no future behaviour is conceived as weird or incorrect.

A single element verification has been made using the biaxial-tension shear test as performed by [12]. This test could only be done with the coupled saw-tooth law formulation. A minor change in the model is made to make it edible for SLA. The results are the same and the difference in how the reduced shear modulus is represented is clearly visible in the results.

A shear compression wall verification as performed by [9] is redone to see SLA in action on a system of multiple elements, a structure. Also in these tests the results obtained are the same as presented by [9] and [10], the obtained failure mechanism and load path are comparable. It is also clear why the NLFEA diverged. This has been shown by the path SLA had to take.

The method works accordingly and can bypass brittle behaviour as found in the last verification. In the next chapter it is applied to the casus, a masonry wall supported by a frame. In it, arguments will be provided to answer the research question.

9. Deep wall-frame study

In this chapter tension-compression failure in SLA is simulated using a deep wall-frame structure. After presenting the implementation of this casus into the numerical environment results of both SLA versions are presented. The output is discussed with regards to each other. The overall goal is presenting that the qualitative results obtained can show that the numerical model is robust enough to show post-peak behaviour.

9.1. Finite element model of the casus structure

The deep wall-frame structure is shown in figure 9.1 as used in laboratory experiments [4]. Figure 9.2 shows the deep wall-frame structure converted and as used in the analyses with dimensions, boundary conditions and loading. The mesh of the structure can be found in figure 9.3 and is enhanced in Appendix C, both also containing boundary conditions and loading. Mesh properties are found in table 9.1 and the mesh elements used are presented in figure 9.4. Material properties used in both versions of the SLA calculation is shown in table 9.2. The used saw tooth curves are given in figure 9.5. The tables and figures are followed by a textual explanation. Simplified modelling options are taken into consideration, for it is the goal to validate tension-compression failure in SLA and not to exactly numerically model masonry structures.

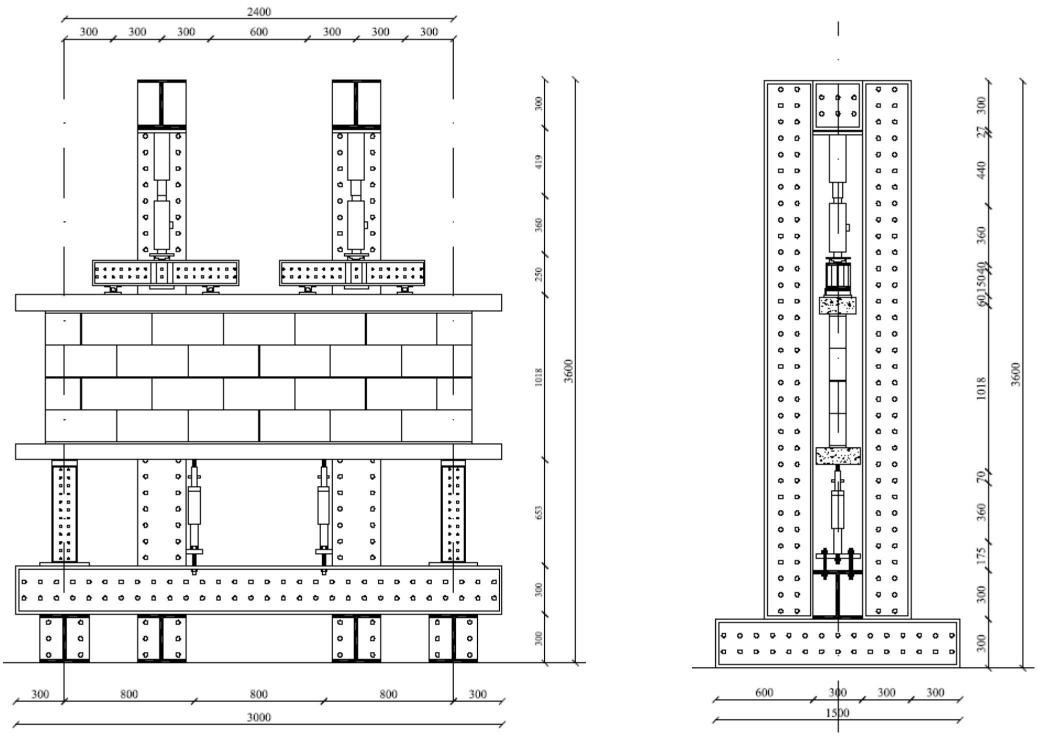

Figure 9.1: The structure used as casus. [4]

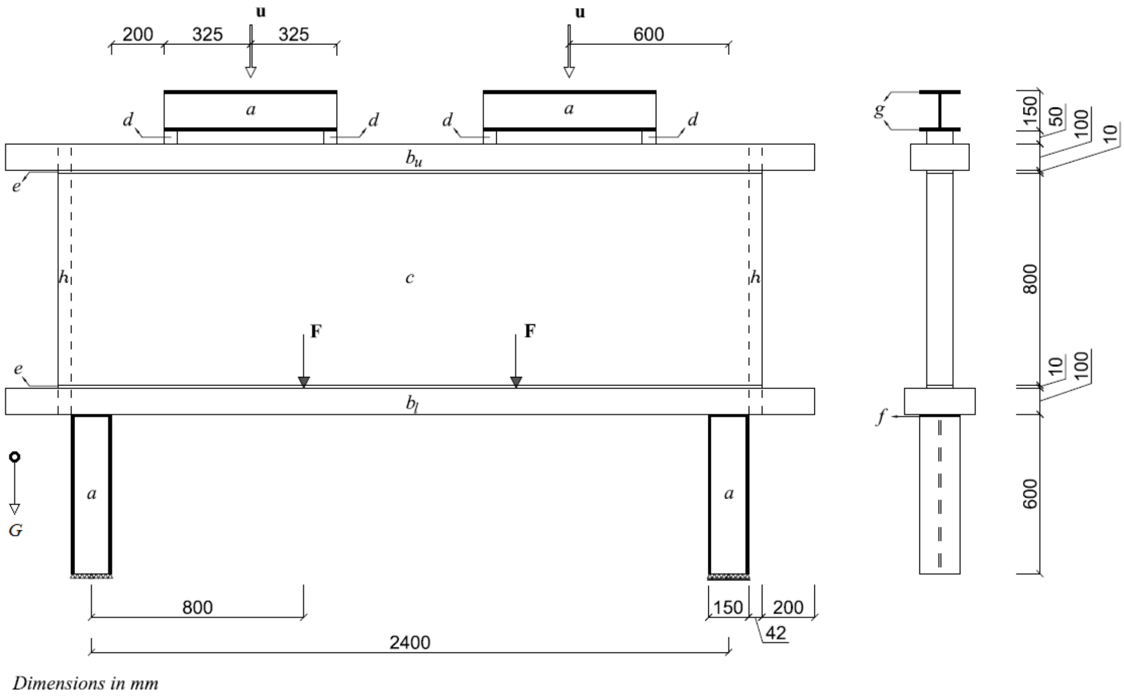

Figure 9.2: Geometry of the casus used for computational input

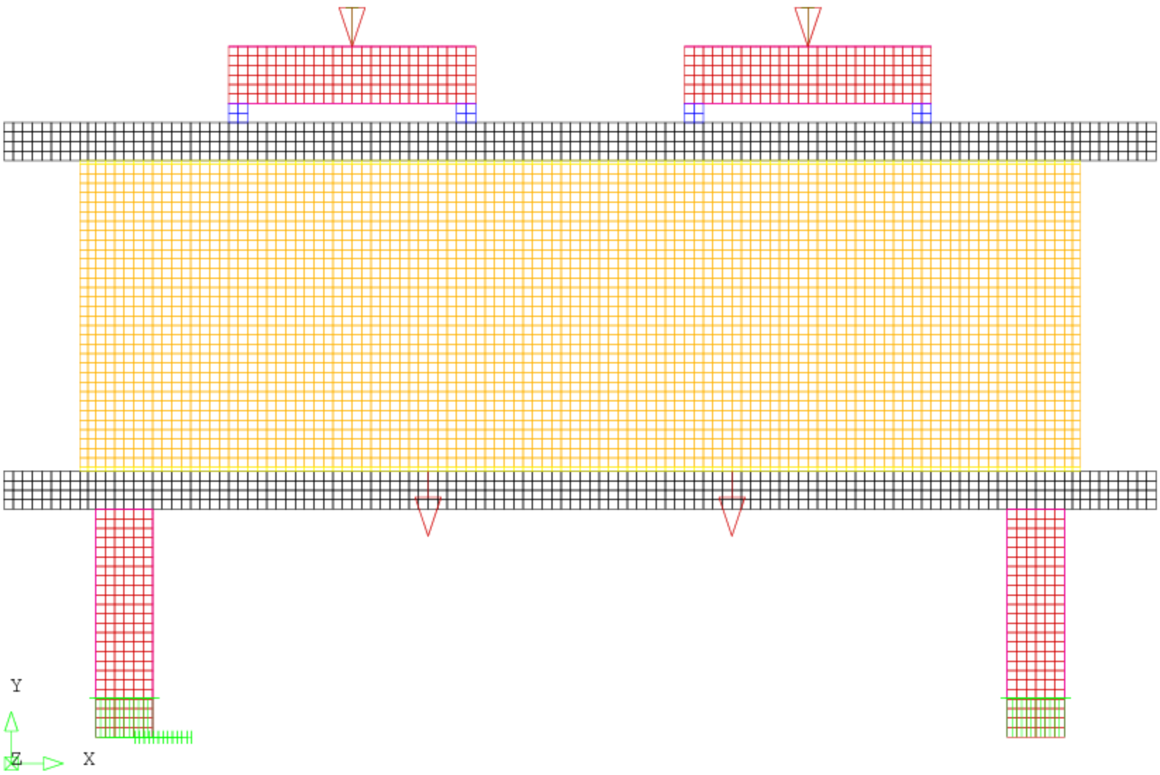

Figure 9.3: Mesh of the structure used for computational input.

Table 9.1: Geometric values of the casus.

Symbol	Representation	Geometry		Elements	Division	Integration
a	Steel HE150A web	*t*	6 mm	CQ16M	25×25 mm	2×2 - point Gauss
b_l	Concrete lower beam	*t*	270 mm	CQ16M	25×25 mm	2×2 - point Gauss
b_u	Concrete upper beam	*t*	220 mm	CQ16M	25×25 mm	2×2 - point Gauss
c	Masonry wall	*t*	100 mm	CQ16M	25×25 mm	2×2 - point Gauss
d	Rubber hinge	*t*	100 mm	CQ16M	25×25 mm	2×2 - point Gauss
e	Mortar kicker joint	*t*	100 mm	CL12I	25 mm	2 - point Gauss
f	Steel plate	*A*	150 × 30 mm	L6BEN	12,5 mm	2 - point Gauss
g	Steel HE150A flange	*A*	150 × 9 mm	L6BEN	12,5 mm	2 - point Gauss
h	Masonry wall (edge)	*t*	100 mm	CQ16M	21×25 mm	2×2 - point Gauss

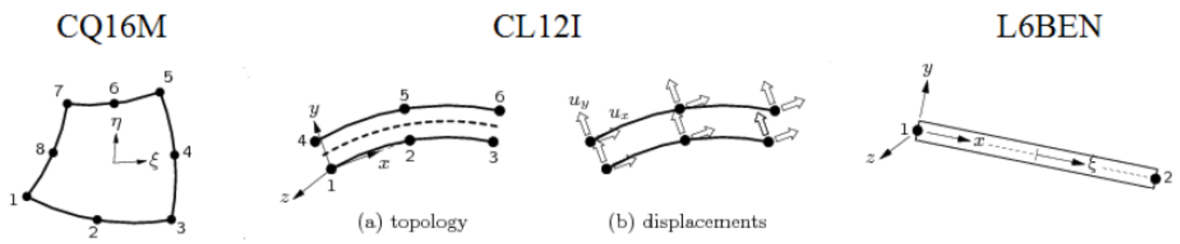

Figure 9.4: Mesh of the structure used for computational input. [5]

Table 9.2: Material properties of the casus.

Components	Parameter	Symbol	Value	Dimension
Concrete beams (plane stress elements)	Modulus of Elasticity	$E_{concrete}$	25.400,00	N/mm^2
	Poisson's ratio	$\nu_{concrete}$	0,20	-
	Density	$\rho_{concrete}$	2,40·10^{-6}	N/mm^3
Mortar kicker joints (interface elements)	Normal stiffness	k_n	100,00	N/mm^3
	Shear stiffness	k_t	41,67	N/mm^3
	Tensile strength	f_t	0,01	N/mm^2
	Softening diagram	-	Linear	-
	Fracture energy	G_f	2,5·10^{-3}	N/mm
Masonry wall (plane stress elements)	Modulus of elasticity	$E_{masonry}$	4.000,00	N/mm^2
	Poisson's ratio	$\nu_{masonry}$	0,20	-
	Density	$\rho_{masonry}$	1,80·10^{-6}	N/mm^3
	Tensile strength	f_t	0,80	N/mm^2
	Softening diagram	-	Linear	-
	Fracture energy	G_f	0,01	N/mm
	Crack bandwidth	h_f	25,00	mm
	Compressive strength	f_c	13,50	N/mm^2
	Softening diagram	-	Parabolic	-
	Crushing energy	G_c	2,00	N/mm
	Crush bandwith	h_c	1,00	mm
	Shear retention function	-	Damage	-
Rubber hinges (plane stress elements)	Modulus of elasticity	E_{rubber}	1.000,00	N/mm^2
	Poisson's ratio	ν_{rubber}	0,30	-
Steel profiles (Line & plane stress elements)	Modulus of elasticity	E_{steel}	210.000,00	N/mm^2
	Poisson's ratio	ν_{steel}	0,30	-

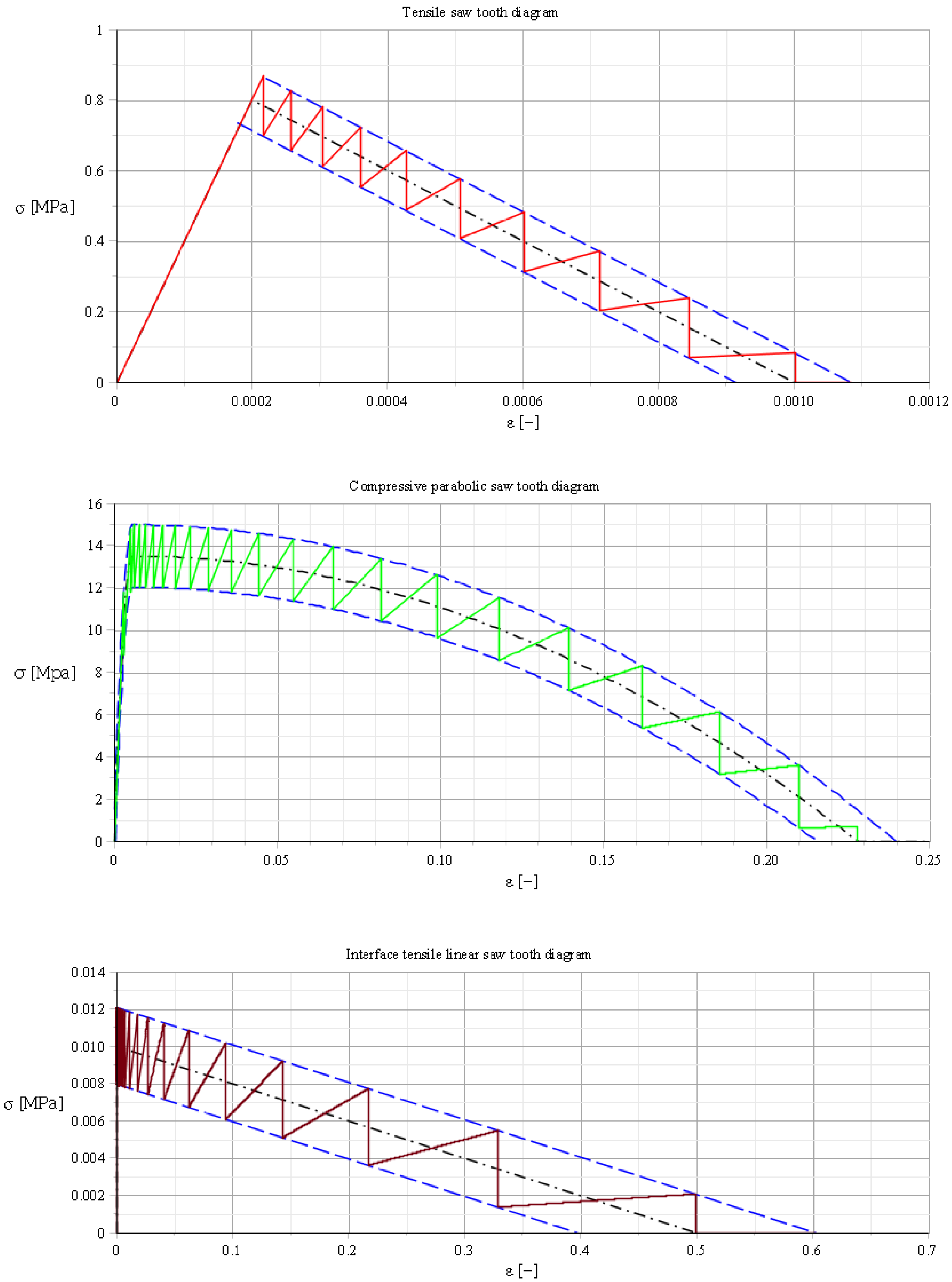

All values are presented in their absolute form

Figure 9.5: Saw tooth diagram for plane stress and interface elements using nonlinear properties.

In the deep wall-frame structure the masonry wall represents the deep wall. This deep wall is $l \times h \times t$ = 2634×800×100 mm and is interacting with the frame structure underneath of a concrete beam and steel columns. The concrete beam under the deep wall is 3034×100×270 mm, while the steel columns are HE150A-profiles with a total length of 700 mm. Between the concrete beam and the steel columns a steel plate is lain to introduce the stresses into the column and avoid peak stresses. These plates are 150×150×30 mm in dimensions. To introduce the forces from the jacks into the deep wall a system of another concrete beam, rubber hinges and steel beams are placed on top. The concrete beam on top of the deep wall is 3034×100×220 mm, the hinges are 50×50×100 mm and the steel beams are yet again HE150A-profiles, this time 650 mm large.

The masonry structure is meshed homogeneously, while in reality masonry is a heterogeneous material with units and a roster of joints. The structure has been taken from and has been meshed in its majority as the situation presented by J. Martens [3]. The major part of the structure has been divided with a 25×25 mm mesh using eight node quadrilateral isoparametric plane stress elements, CQ16M, containing a 2×2 – point Gauss integration scheme. This concerns the masonry wall, the concrete beams, the rubber hinges and the web of the steel profiles. The edge of the masonry wall and the area in its extension have been meshed with slighter smaller elements of 21×25 mm with the same kind of elements and integration scheme. The mortar kicker joints have been meshed in alignment with the masonry wall and the concrete beams using an interface element, CL12I, containing a 2 – point Gauss integration scheme. The steel plates and the flanges of the steel profiles are represented by a two node, two dimensional beam elements, L6BEN, containing a 2 – point Gauss integration scheme. While the other elements were quadratic, this element is a linear element and is thus meshed every 12,5 mm.

The structure is supported at the bottom of the lower steel profiles. One side is supported by a line of hinged supports while the other side is supported by a line of roller supports. The constraints are thus simplified to a clamped support at one column and clamped roller support on the other column. Two force loads, simulating the average floor load at a rough estimation of F = 5 kN each, are applied in the centre of the lower concrete beam. Two deformation loads, representing the addition of more storeys, are applied in the centre on top of the two steel profiles.

The load is applied in two steps, non-proportionally (constant) and proportionally (scaled), to guarantee the separation crack between the lower concrete beam and the masonry deep wall. The proportional load consists of the deformation controlled loads applied on the steel profiles at the top of the structure, which are regulated as if they were jack displacements in the laboratory. The non-proportional load consists of the two force loads attached to the lower concrete beam and of the self-weight of the two concrete beams and the masonry wall. The structure is loaded non-proportionally until the full non-proportional load is applied on the specimen. Afterwards, the proportional load is scaled till the end of the calculation.

As a side note regarding self-weight, it is brought to attention that it is not applicable as a different load type yet in SLA, while it is in NLFEA. It has to be translated to a regular non-proportional load. The self-weight is only applied on the concrete beams and the masonry wall, because they are the most important parts of the structure and deliver the most important self-weight. It has been simulated with line loads at each element height for the masonry wall and for the concrete beam as a line load at the top of the beams.

The material properties chosen for the masonry deep wall are isotropic, while masonry has an anisotropic behaviour with different characteristics in both orthotropic directions. The material properties are taken from J. Martens [3], which he took after considering experimental data from inter alia CUR-report [2]. The concrete beams, the rubber hinges and the steel profiles all behave linear elastically. Their Young's modulus and Poisson's ratio are $E_{concrete}$ = 25400 N/mm^2 and $\nu_{concrete}$ = 0,2, E_{rubber} = 1000 N/mm^2 and ν_{rubber} = 0,3 as well as E_{steel} = 210000 N/mm^2 and ν_{steel} = 0,3 respectively. The masonry wall and the mortar kicker joints display nonlinear, quasi-brittle behaviour. For the masonry wall a total strain fixed crack model is used to model smeared cracking and crushing in the deep wall, while the cracks in the joints are represented by a discrete interface cracking model. The masonry wall has an initial Young's modulus of $E_{masonry}$ = 4000 N/mm^2 and an initial Poisson's ratio of $\nu_{masonry}$ = 0,2. After reaching the maximum tensile strength of f_t = 0,8 N/mm^2, linear softening takes place to simulate cracking with a fracture energy of G_f = 0,01 N/mm. After reaching the maximum allowable strength of f_c = 13,5 N/mm^2, parabolic softening takes place to simulate crushing with a crushing energy of G_c = 2 N/mm. The shear retention function, as well as other damaged parameters, follows a damaged formulation as explained in the literature review. A crack bandwidth of h_f = 25 mm, size of the element, is used for the softening behaviour. A crush bandwidth of h_c = 1 mm is used in crushing. The normal stiffness and shear stiffness of the joints are k_n = 100 N/mm^3 and k_t = 41,67 N/mm^3 respectively. The joints can only soften in tension introducing discrete cracking after reaching its tensile strength f_t = 0,01 N/mm^2. A total energy consumption of maximum G_f = 2,5·10^{-3} N/mm will occur. Finally, with regard to the loading of the specimen, the masonry wall and the concrete beams have a density of $\rho_{masonry}$ = 1,8·10^{-6} N/mm^3 and $\rho_{concrete}$ = 2,4·10^{-6} N/mm^3.

The tensile saw tooth softening curve for continuum elements has been scrutinized in literature. The saw tooth curves for parabolic compression softening in continuum elements and for softening taking place in interface elements have not been taken into consideration in the same amount of extent. Although M. Kabos [??] implemented an improved model for parabolic compression softening for continuum elements, a definitive way is still non-existent. Therefore simplified models have been taken for the latter two, while using a simplified bandwidth of 1 mm for crushing.

9.2. Results of the casus structure

The results of both versions of the calculation are presented in this paragraph. Computational results are shown to display the process of the calculation and the structural results are discussed with graphs and figures. Both versions of SLA return the exact same results for the first 5093 steps, which will discussed prior to presenting the results for these versions separately found in later steps.

9.2.1. Results of the initial behaviour of both versions

Non-proportional loading, the force loads and the self-weight of the deep wall and the beams, is applied in the first 3888 steps of the calculation. It is not possible to apply this load fully in total in the first step. The kicker joint is progressively damaged during the course of these steps and the lower concrete beam is separated from the masonry deep wall.

From step 3889 the proportional load is applied and the non-proportional load is kept constant, if equilibrium can be satisfied, during the rest of the calculation. At step 3985 (purple) the crack in the middle starts to appear and grows in the following steps. The proportional load is scaled downwards to accommodate this failure and it can be seen that the deep wall is split in two by a vertical crack in the centre.

The compressive strut develops to a certain amount after the formation of the centre crack that it takes a more present role in the load distribution in the structure. More load can be applied and the stresses follow this compressive strut to the supports. This redistribution of the stresses through this strut at step 4325 (red) makes the load-displacement graphs go up.

More load is transferred through this compressive strut until it starts to soften in compression. Although still a significant amount of load can be carried, it is noticed that the load displacement graphs are bending downwards and the structure is losing gradually more stiffness from step 4891 (orange). The lower corners of the structure also indicate compressive difficulties.

At step 5094 both versions take different paths are discussed in the next sub-paragraphs for each, making step 5093 the last step that both versions have in common. At step 5094 the version with the decoupled saw-tooth law formulation prohibits double tensile failure in integration point 4 of element 1697, located in the middle crack, and thus skips this failure. Instead it choses integration point 3 of element 3451, located in the bottom right corner of the masonry edge wall, as the critical integration point. This double tension failure is not skipped in the coupled saw-tooth law formulation and the found critical integration point by the decoupled saw-tooth law formulation is found a step later in step 5095 by the coupled saw-tooth law formulation. This has a slight effect on the overall behaviour and it makes that the decoupled saw-tooth law formulation uses a lower amount of steps in total.

9.2.2. Results of the coupled saw-tooth law formulation

The peak load is reached at step 5214 (yellow) for the coupled saw-tooth law formulation. One of the lower corners has started to crush, damaging the compressive strut. There is an interruption in the path between the load application and the supports at the end. The load cannot be increased without experiencing failure.

The load has to decrease in order to still satisfy equilibrium and neighbouring elements in that same corner also crush. But from step 5382 there are moments that it is not possible to find equilibrium anymore with the full applied non-proportional load. It is indicated that the calculation finds an "empty load multiplier set", meaning that there is no proportional load multiplier available with which equilibrium of the structure can be satisfied. To still be able to find a solution, the initial load has also to be scaled down temporarily. At step 5441 (light green) the structure is able to reapply the full initial non-proportional load again. Then it has found equilibrium as it normally has, but with a very little loading.

This phenomena constantly happens anew and from step 6103 it is not possible anymore to fully apply the initial non-proportional load. It tries to increase to initial load multiplier and to fully apply this load again, but nowhere in the structure enough resistance is available to fulfil equilibrium. At step 6396 (green) it can be seen that a corner of one side of the structure has crushed significantly, reducing the compressive strut significantly. This damage slowly translates alongside the edge of the wall and the lower concrete beam, making a direct connection between the point of load application and support more difficult with every step.

The final step of the calculation, step 10890 (diamond), shows this progression. More of the corner will be completely crushed, unable to carry any form of stress. The force flow has to move itself around this area, also partly through the lower concrete beam, to achieve equilibrium. The damaged is localised to such an extreme extend that even with the enlarged dummy tooth the "dammem-error" as discussed in Chapter 8 occurs. The structure really is done for in this step, all related figures lead to this observation.

It is also noted that the coupled saw-tooth law tries to switch damage state during the analysis. An integration point subjected to compressive softening continues in cracking using the damage history of the first, as explained in Chapter 8. This moment is returned by the calculation at step 6473 and this happens at integration point 4 of element 3264, which is located in the bottom right corner of the masonry deep wall next to element 3451.

Although the calculation took 10890 steps, it is clear that the structure already could be considered as failed. The SLA calculation continues until all integration points are damaged. A maximum stiffness of 73 kN/mm is reached by the structure, but at step 10890 only 2,2 kN/mm remains, which is only 3% left of the maximum stiffness. At step 6396, when the structure cannot and in later steps will not be able to fully apply the initial load, the stiffness has dropped significantly to 29,4 kN/mm, a remainder of 40%. With the fact that the structure lost more than 50% of its stiffness and with the fact that after this huge drops are observed in stiffness, it can be said that the structure had already failed before around step 6000.

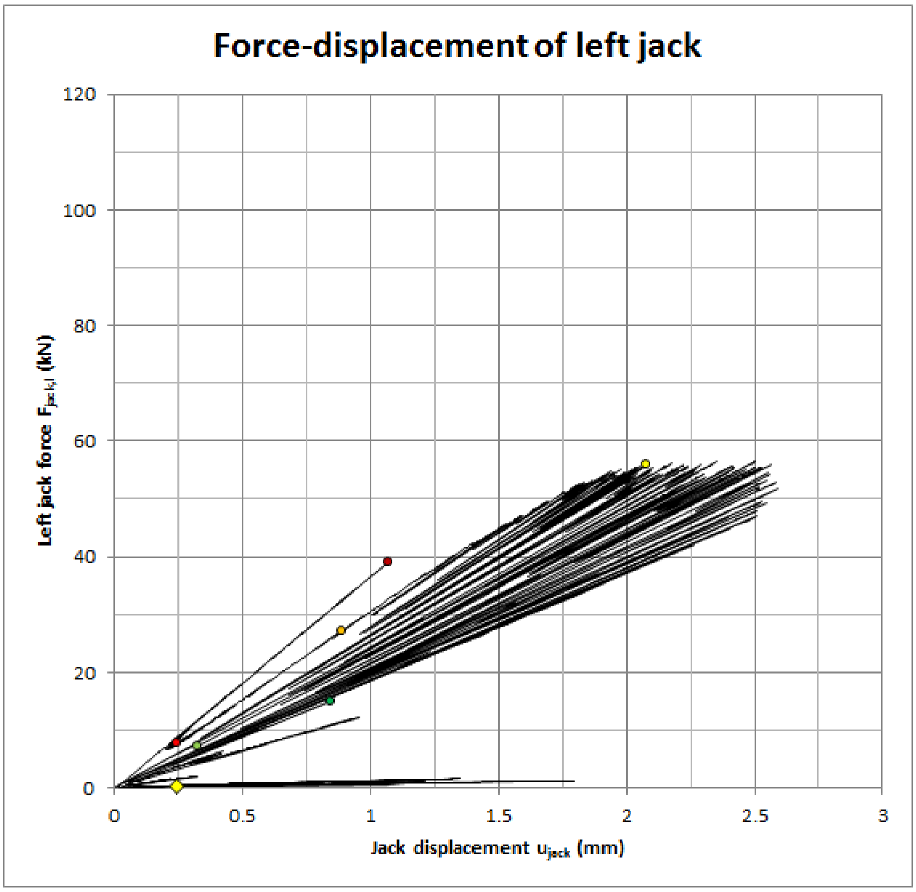

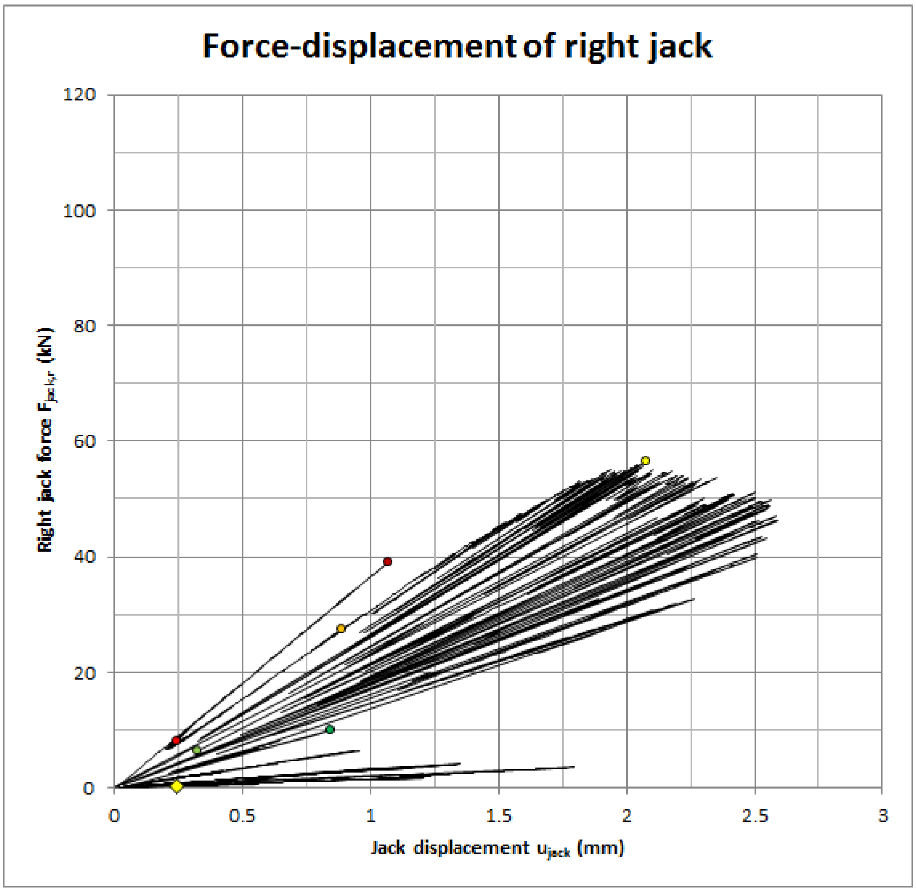

Figure 9.6: Force-displacement graphs of left and right jack for the coupled saw-tooth law formulation.

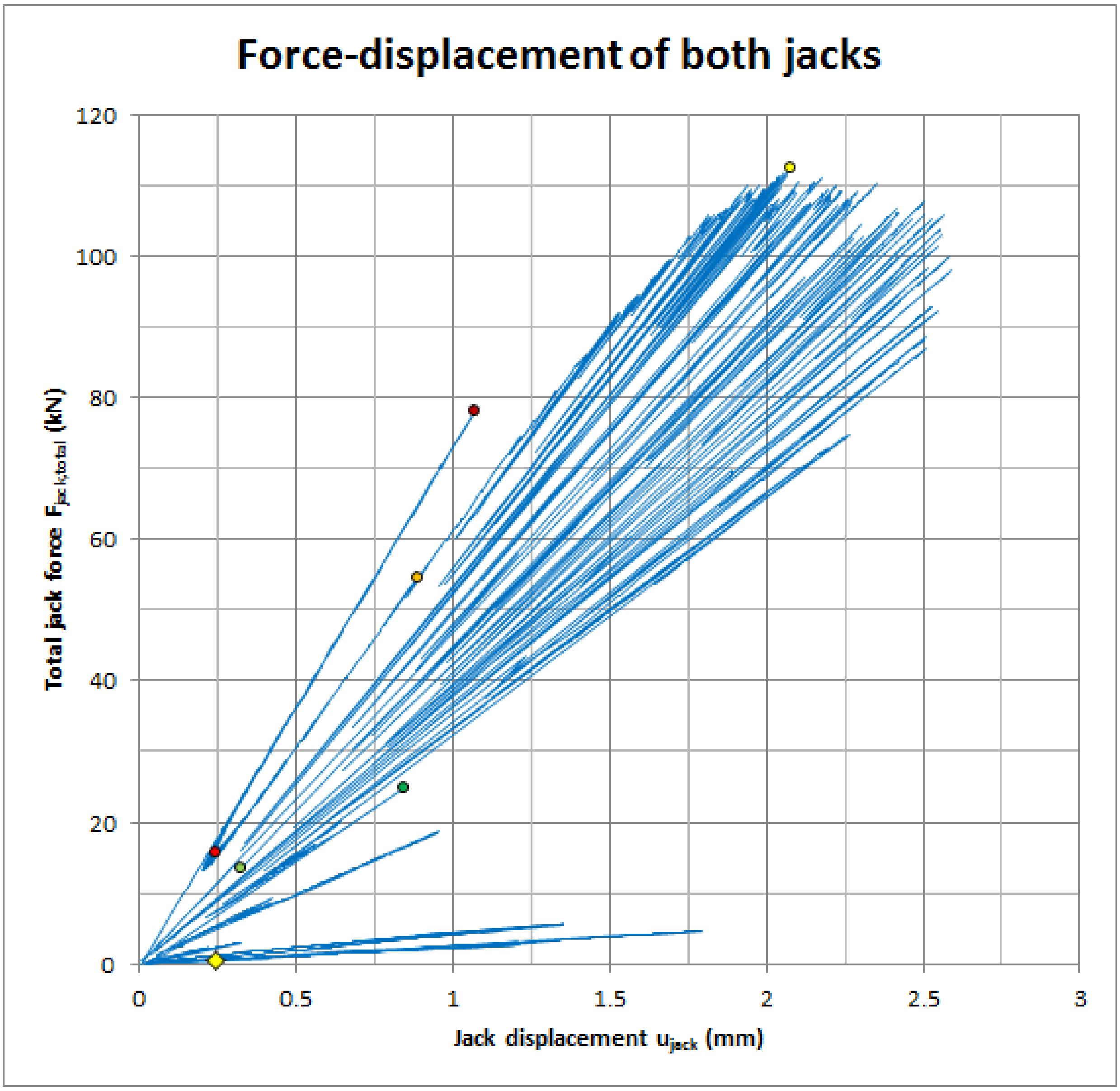

Figure 9.7: Force-displacement graph for both jacks together for the coupled saw-tooth law formulation.

Table 9.3: Force-displacement table for both jacks together for the coupled saw-tooth law formulation.

Step		u_{jack} (mm)	$F_{jack,total}$ (kN)
3985	●	1,07	78,08
4325	●	0,24	15,76
4891	●	0,89	54,44
5214	●	2,08	112,51
5441	●	0,33	13,53
6396	●	0,84	24,77
10890	♦	0,24	0,53

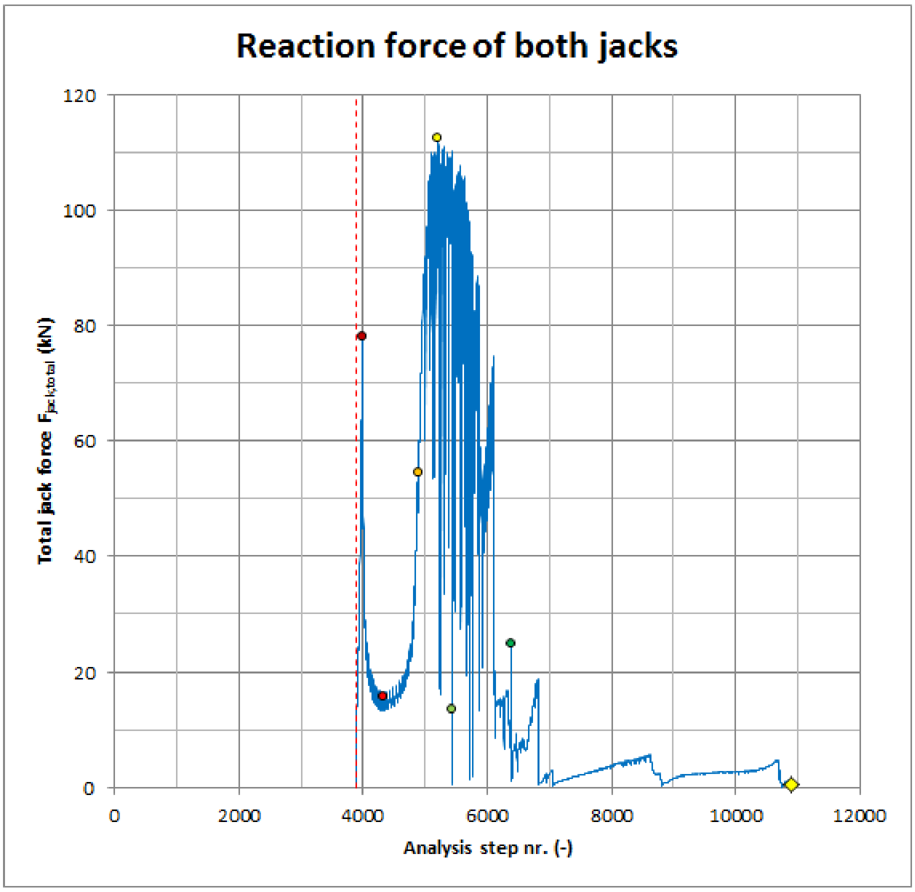

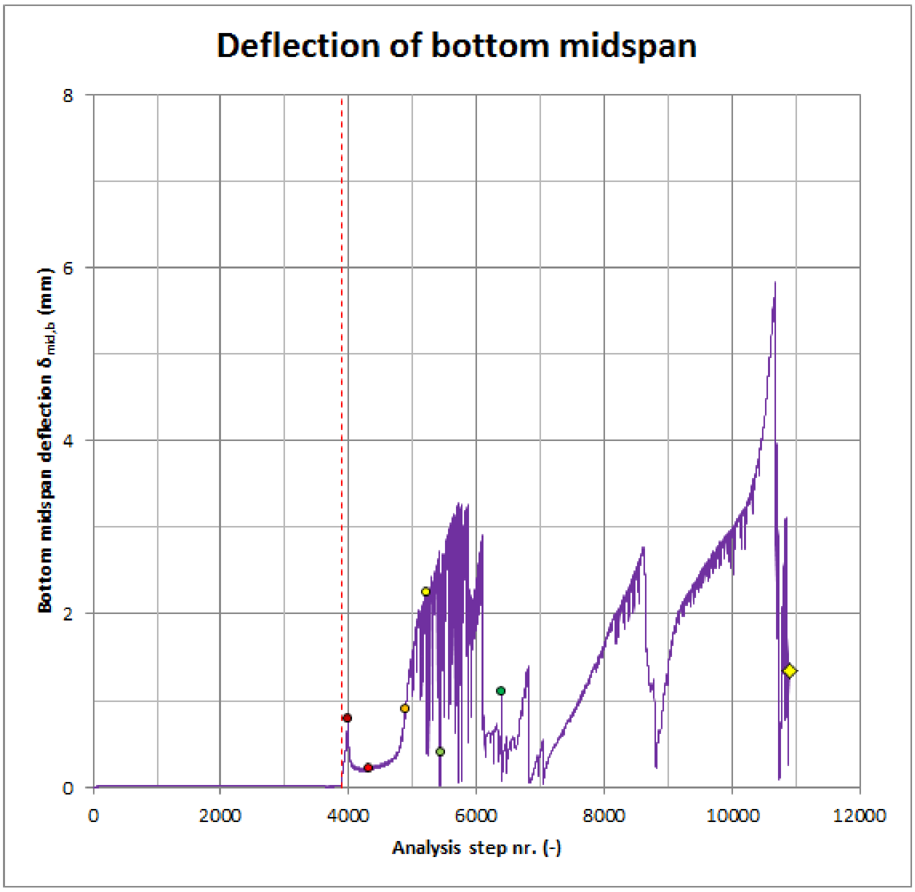

Figure 9.8: Progression of total reaction force and midspan deflection for the coupled saw-tooth law formulation.

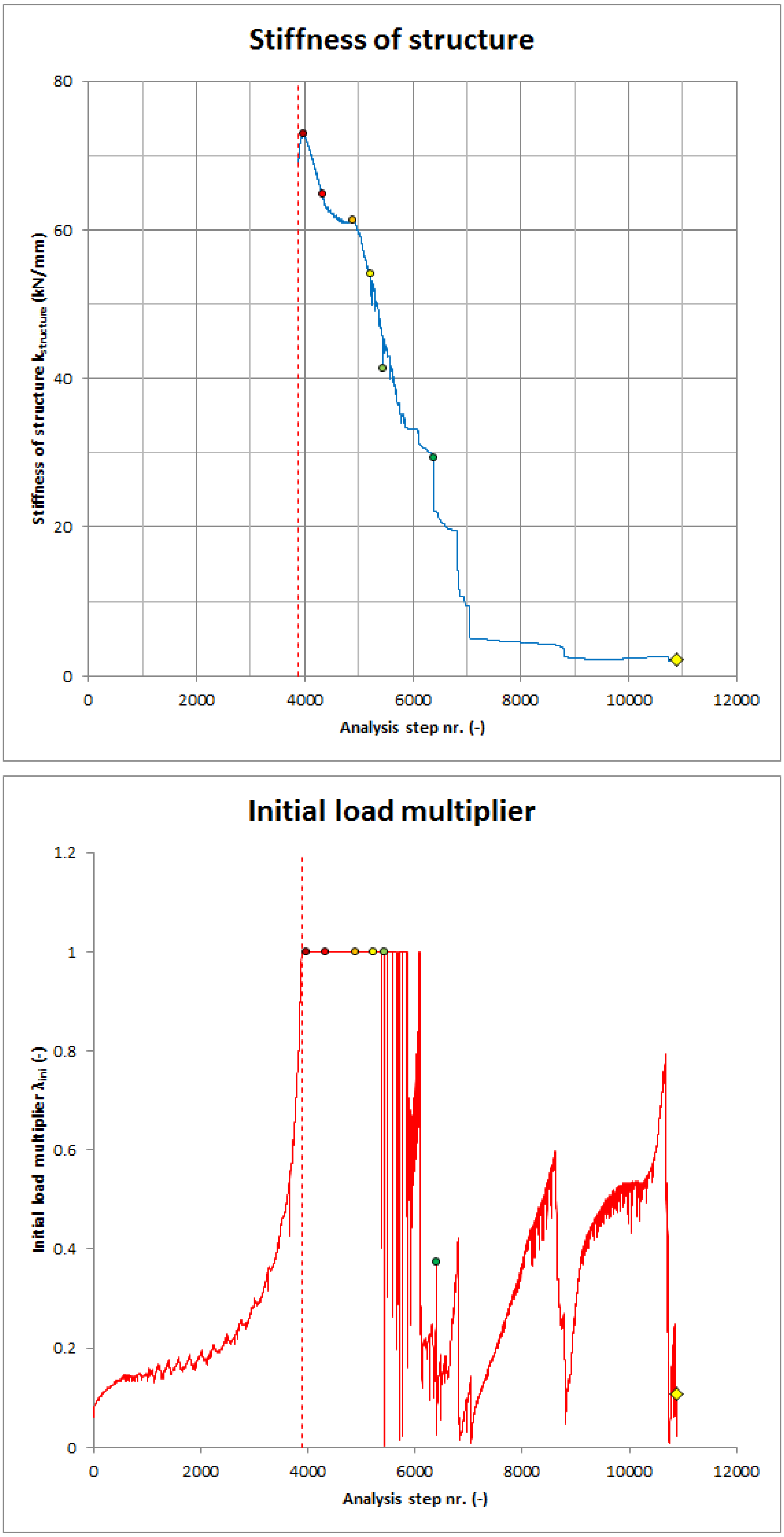

Figure 9.9: Path of the structure stiffness and the initial load multiplier for the coupled saw-tooth law formulation.

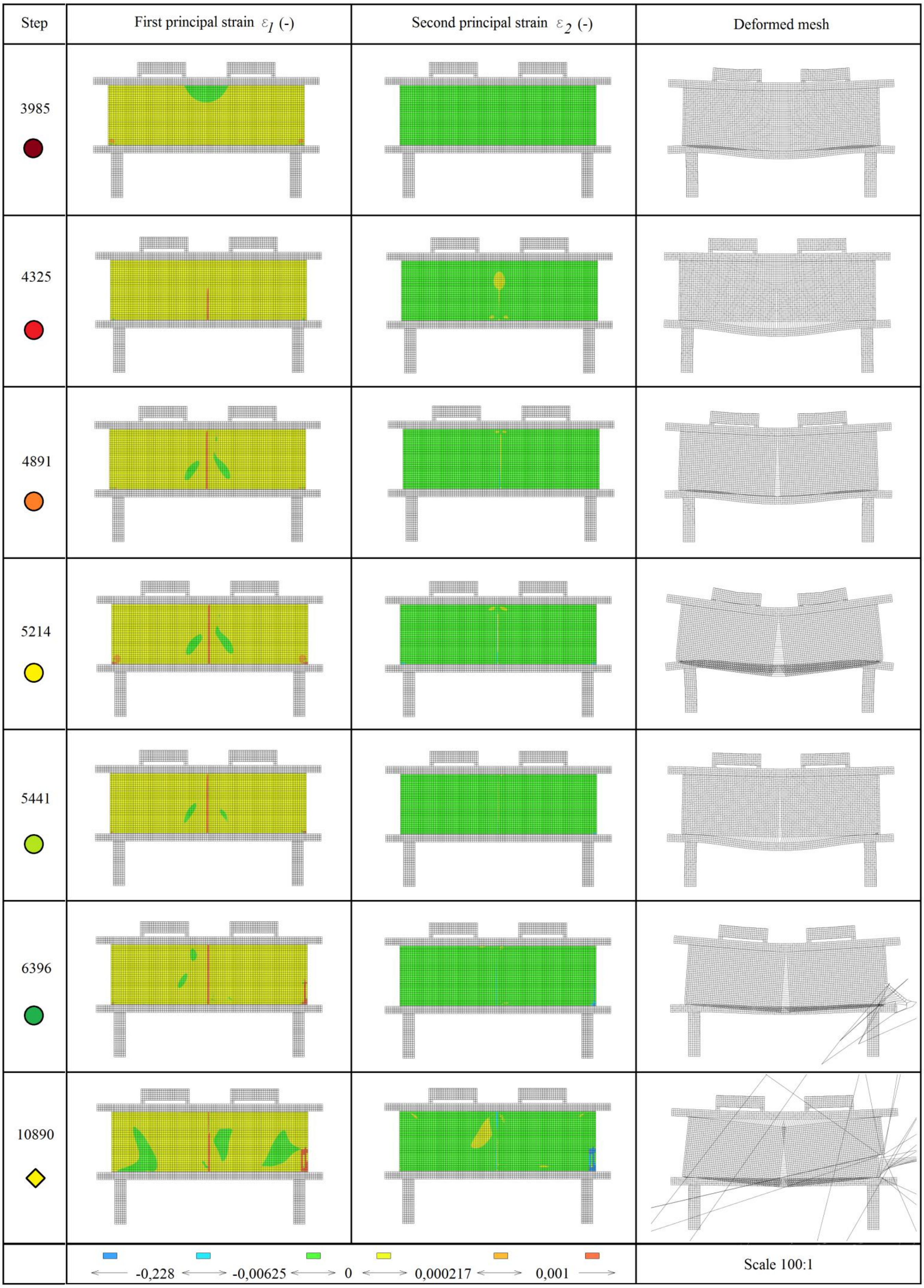

Figure 9.10: Principal strains and deformed mesh of the casus for the coupled saw-tooth law formulation.

9.2.3. Results of the decoupled saw-tooth law formulation

The peak load is reached at step 5192 (yellow) for the decoupled saw-tooth law formulation. Due to the skipping behaviour the peak load is reached earlier than with the coupled saw-tooth law formulation. Also in this case the one of the lower corners of the deep wall has started to crush.

Elements in the vicinity of that corner are crushing, forcing the load on the structure to decrease. But at step 5343 and further on there may be no solution to satisfy equilibrium with the full applied non-proportional load. The calculation returns the message that no load multiplier can be found. At step 5358 the structure is able to reapply the full initial non-proportional load again. The problem occurs multiple instances and although it seems to get stable again, equilibrium is not satisfied anymore with the full initial load from step 14443.

At step 6841(green) one lower corner of the deep wall is clearly damaged in compression. This damage slowly translates alongside the edge of the wall and the lower concrete beam, expanding in a quarter circle-like pattern. Direct force flow between the point of load application and support is hindered and a pass around the damaged area is sought for the stresses.

At step 10890, which is the last step returned by the coupled saw-tooth law formulation, the damage can be clearly seen to have expanded in that corner. The quarter circle of crushed elements is located exactly on top of the steel column. Transmission of forces have to go through the concrete beam, for the force flow through this damaged area is negligible.

The final step of the calculation for the decoupled saw-tooth law formulation is step 25557. More of the corner is completely crushed, unable to carry any form of stress. The force flow has to move itself around this area, it has to go through the concrete beam. The damaged is localised to such an extreme extend that the calculation is aborted due to the an error, see Chapter 8. The fact that that the concrete beams behave linear elastically is the reason the structure could have been damaged to this extent. The structure has failed.

Although the calculation took 25557 (diamond) steps, it is clear that the structure already could be considered as failed. A maximum stiffness of 73 kN/mm is reached by the structure, but at step 25557 no stiffness is left. At step 6716, when the structure has a difficult time to reapply the full initial load, the stiffness has dropped significantly to 31 kN/mm, a remainder of 42%. With the fact that the structure lost more than 50% of its stiffness and with the fact that after this huge drops are observed in stiffness, it can be said that the structure had already failed before around step 6500.

Step 5436 (light green) is a noteworthy step for its negative output. In this step both jacks are pushed downwards, but one returns an upward reaction force, while the other a downward reaction force. In this step almost no proportional force is applied at all and it is comparable with step 5441 of the coupled saw-tooth law formulation. It is the moment when the first integration point is completely crushed.

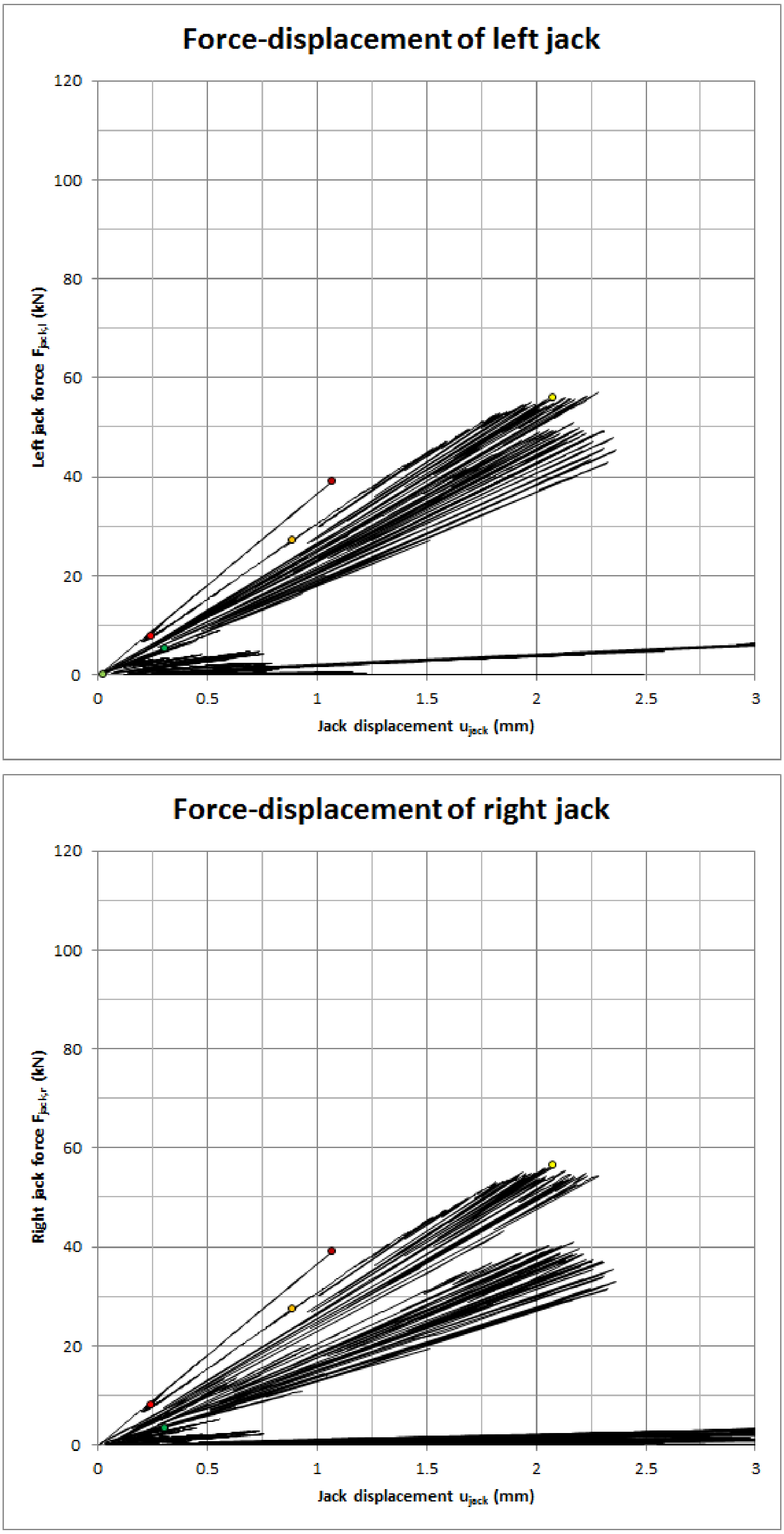

Figure 9.11: Force-displacement graphs of left and right jack for the decoupled saw-tooth law formulation.

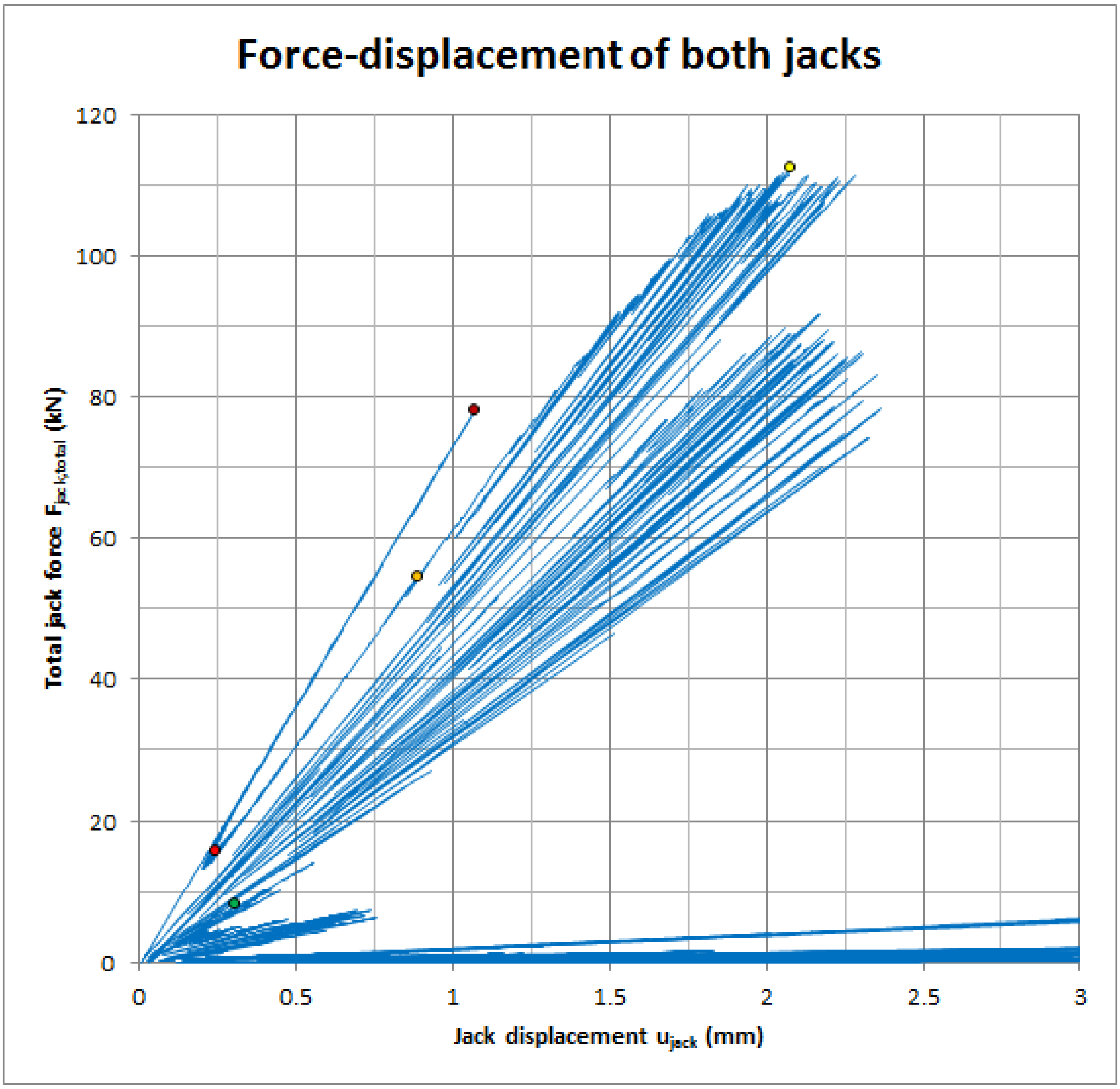

Figure 9.12: Force-displacement graph for both jacks together for the decoupled saw-tooth law formulation.

Table 9.4: Force-displacement table for both jacks together for the decoupled saw-tooth law formulation.

Step		u_{jack} (mm)	$F_{jack,total}$ (kN)
3985	●	1,07	78,08
4325	●	0,24	15,76
4891	●	0,89	54,44
5192	●	2,08	112,51
5436	●	0,02	-0,48
6841	●	0,31	8,37
25557	♦	0,62	-0,05

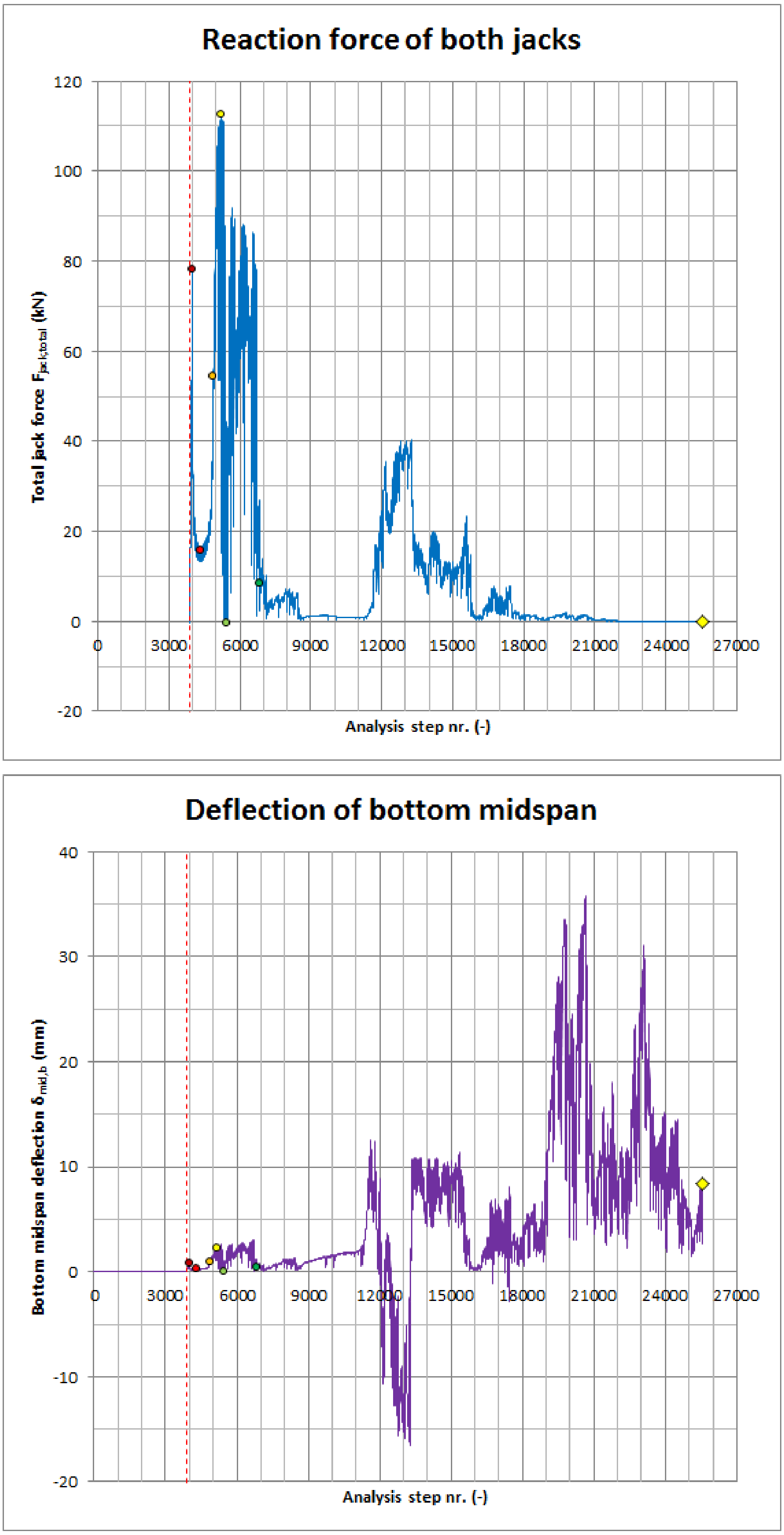

Figure 9.13: Progression of total reaction force and midspan deflection for the decoupled saw-tooth law formulation.

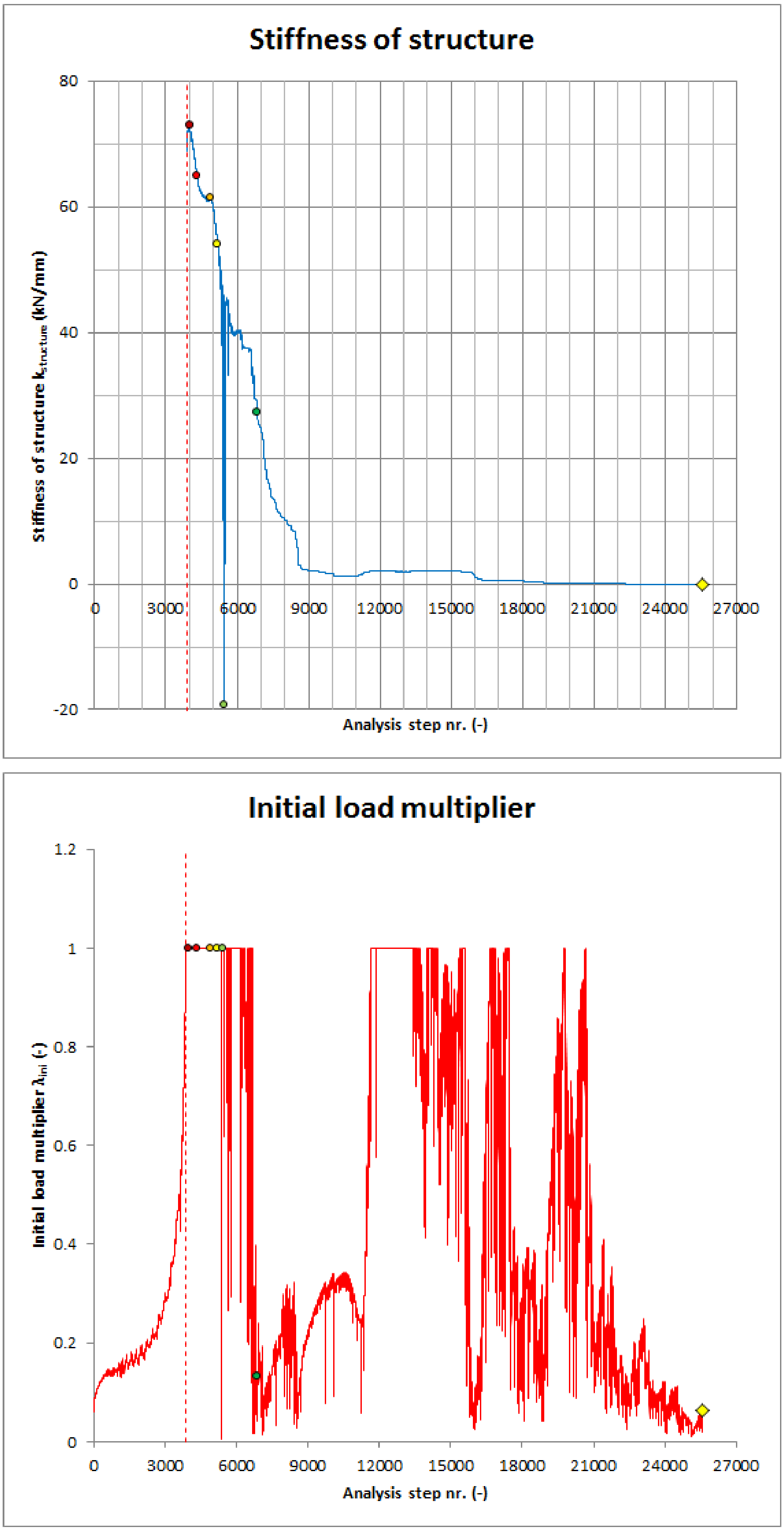

Figure 9.14: Path of the structure stiffness and the initial load multiplier for the decoupled saw-tooth law formulation.

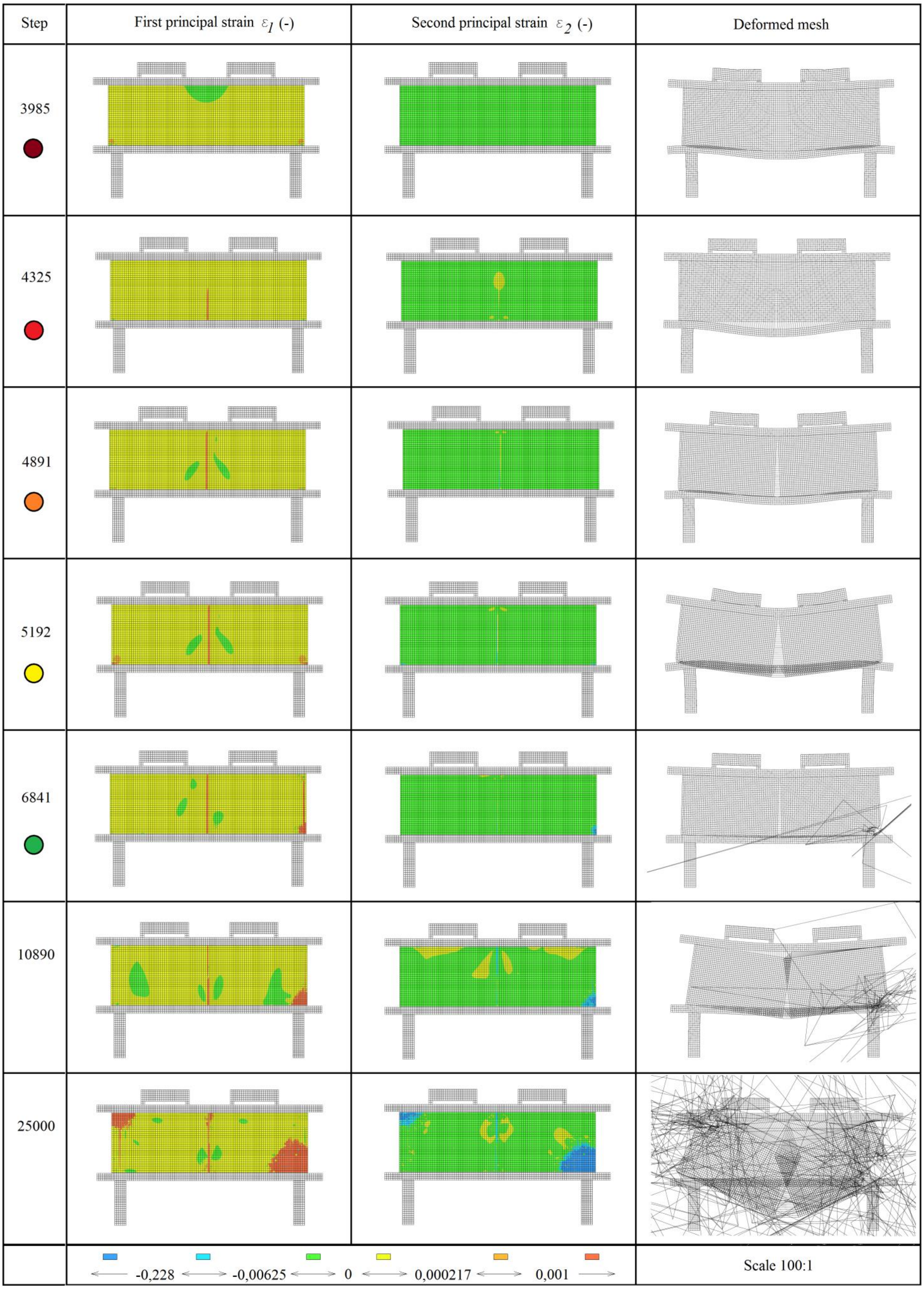

Figure 9.15: Principal strains and deformed mesh of the casus for the decoupled saw-tooth law formulation.

9.2.4. Energy consumption

The fracture and crushing energy implemented in the system has to be found back in the results. As an example the force-displacement diagram of the total jack forces plotted against the jack displacement for the coupled saw-tooth law formulation has been presented anew in figure 9.16. In this figure also the energy consumed by the middle crack and crushing corner has been represented by the approximated red triangular area and the approximated green area respectively. The consumed energy per area G is equal to the work W, figure 9.17, of the force-displacement graph divided by the area of the structure on which the work acts on A, figure 9.18.

The fracture energy used by the middle crack should be G_f = 0,01 N/mm. The estimated area covered by the red triangle in figure 9.16 is equal to $W_f \approx$ 400 Nmm. The cracked area in that part of the structure has an area of $A_f \approx$ 42500 mm^2. So the retrieved fracture energy is $G_f \approx$ 0,009 N/mm, which is roughly the same as the energy implemented.

The crush energy used by the corner should be G_c = 2,0 N/mm. The approximated area covered by the green triangle in figure 9.16 is equal to $W_c \approx$ 68400 Nmm. The crushed area in that part of the structure has an area of $A_c \approx$ 32500 mm^2. So the consumed crushing energy is $G_c \approx$ 2,1 N/mm, which closely resembles the implemented energy.

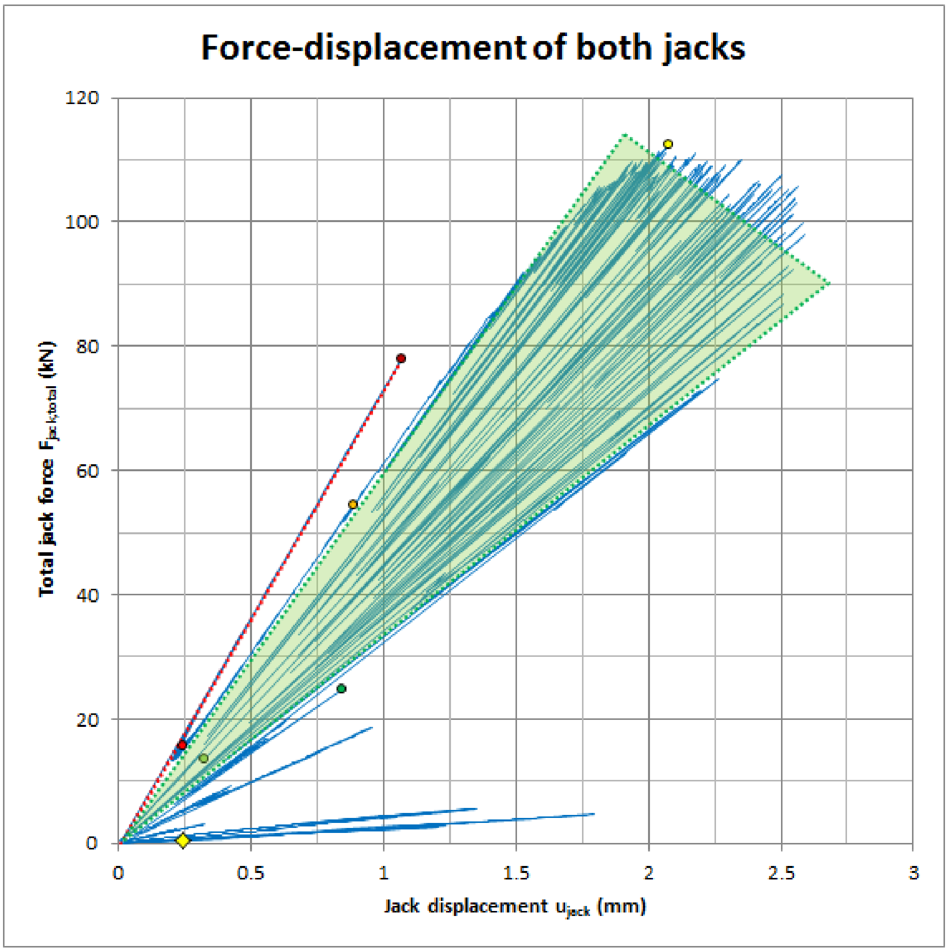

Figure 9.16: Check of cracking and crushing energy consumed for the coupled saw-tooth law formulation.

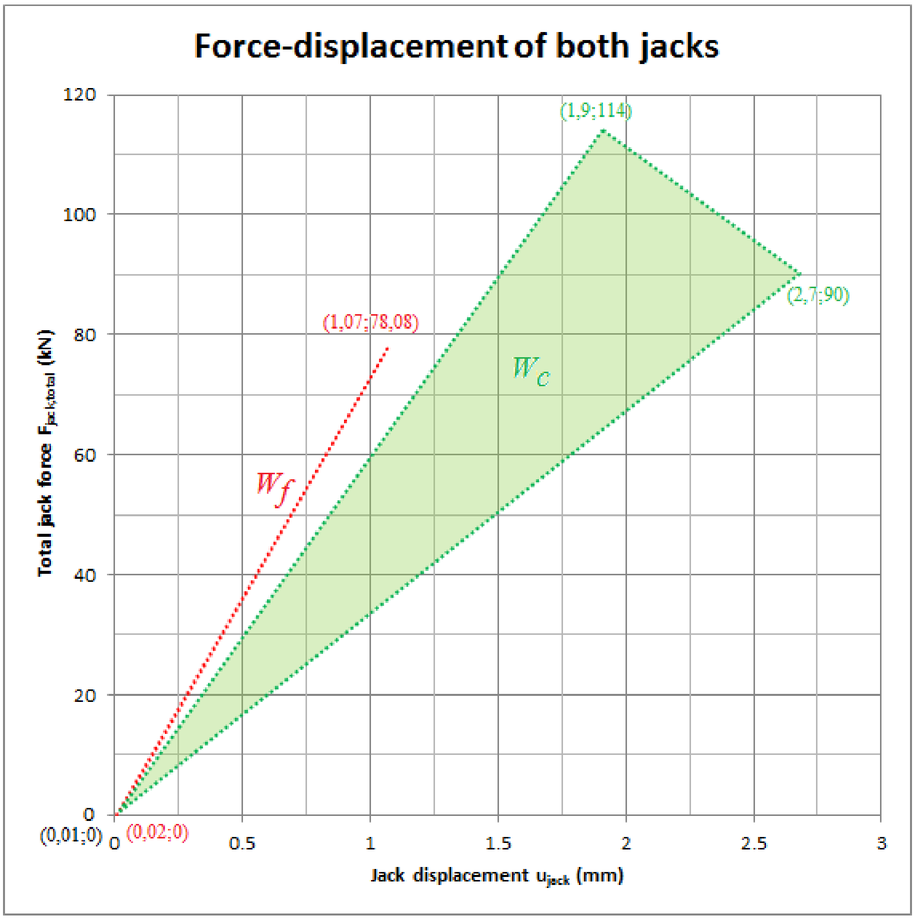

Figure 9.17: The shaded area with coordination used to check the consumed energy.

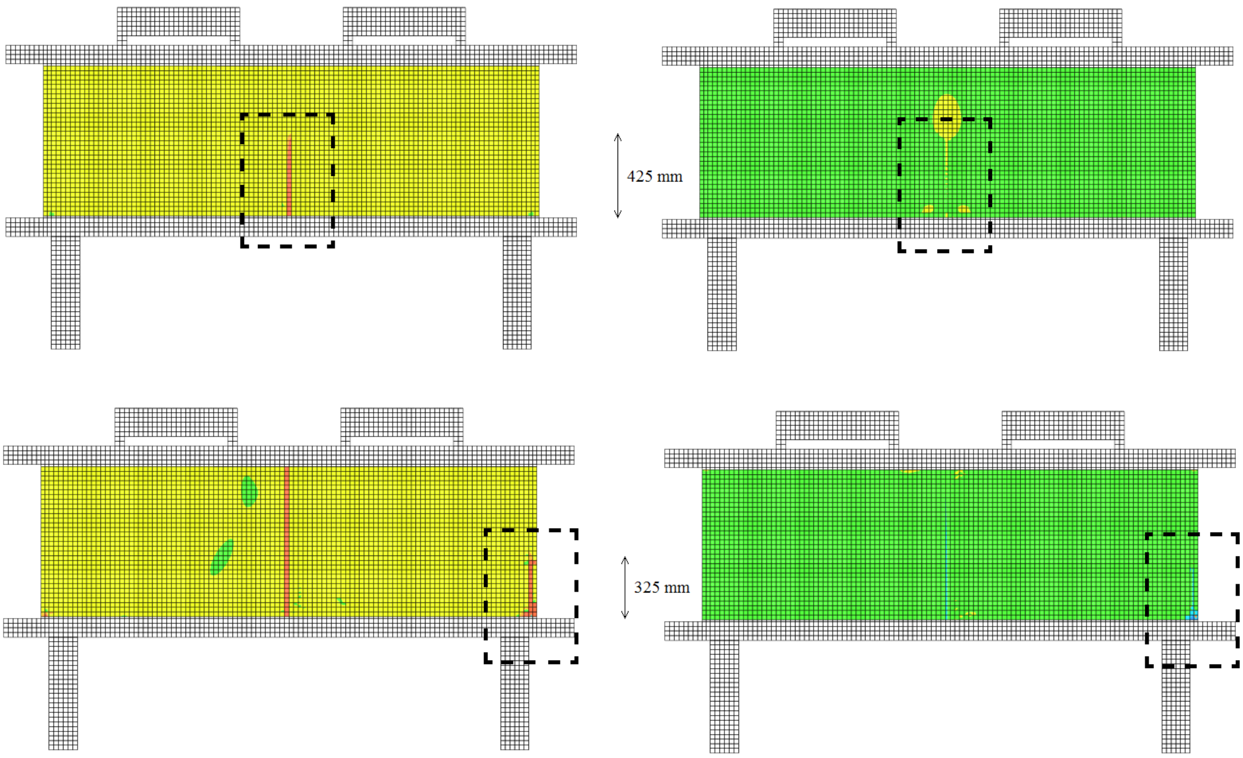

Figure 9.18: Cracked (top) and crushed (bottom) height taken into consideration for the energy consumption.

9.3. The results compared

Both versions are compared in this paragraph. While the versions show similar results, they are not the same and differences can be pointed out. A few inconsistencies between the two versions are discussed and their influences presented for the versions.

9.3.1. Crushing propagation and forming of the compressive strut

Both versions of the SLA show similar results. At first sight the version with the decoupled saw-tooth law formulation seems to only extent the amount of steps performed with regard to the other version. The decoupled saw-tooth law version allows more steps for in this version the mechanism of a compressive strut is forced in the structure, making the propagation of the crushing zone through the wall be more consistent. The coupled saw-tooth law formulation does not force this behaviour in the structure, making it more susceptible to the localizations becoming present during the analysis. The crushed zone in the lower corner of the masonry deep wall while using the decoupled saw-tooth law formulation develops as predicted, forcing the force flow to go around this damaged area and more and more through the lower concrete beam to reach the support at the steel column. The difference of the two versions for compressive crushing propagation is shown in figure 9.19.

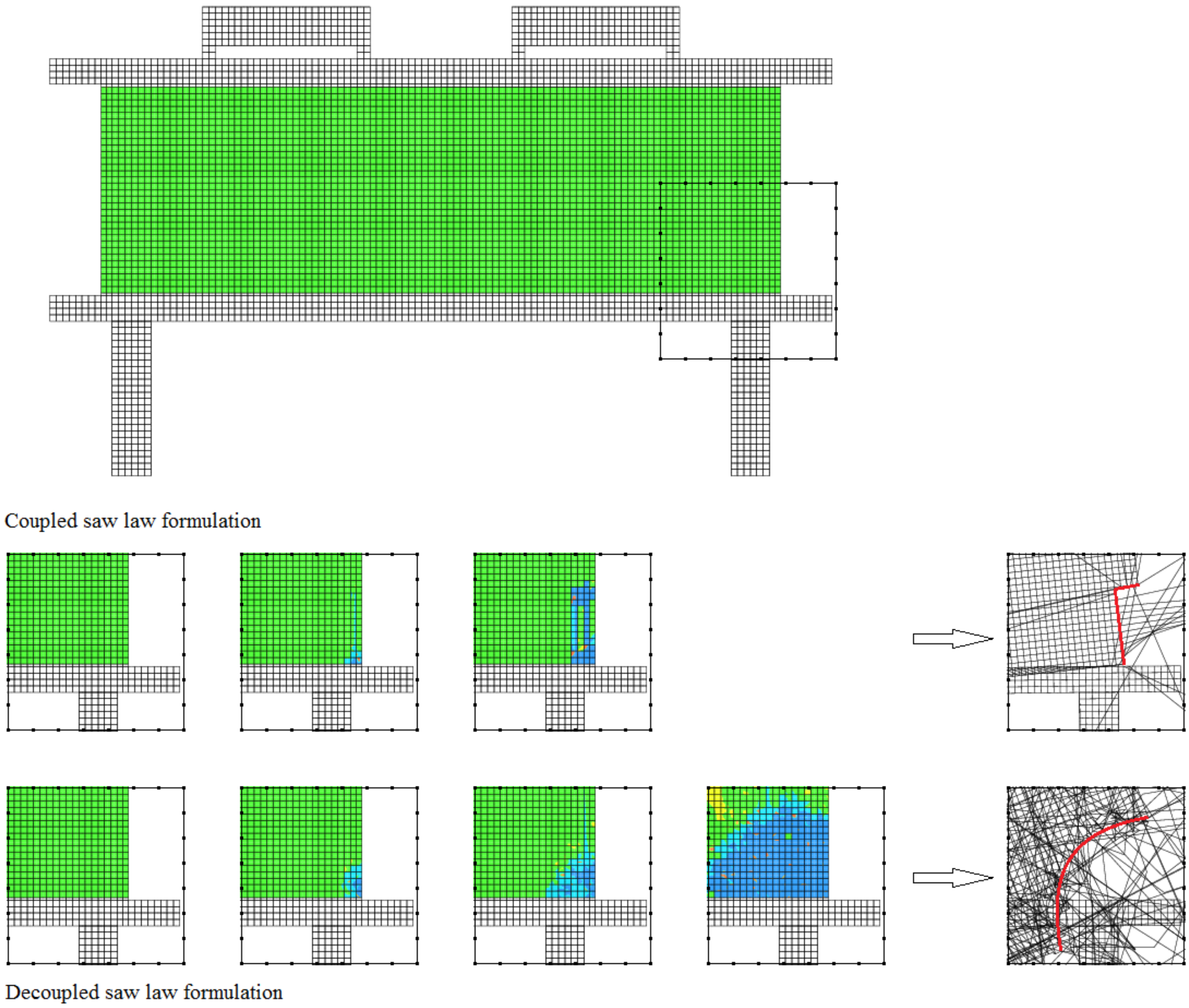

Figure 9.19: Corner crushing compared for both versions.

9.3.2. Structure stiffness and the many data points

As stated beforehand, the decoupled saw-tooth law is able to return more analysis steps than the coupled saw-tooth law formulation due to the forced strut mechanism forming in the structure. However, it is also stated that at first sight it looks like the decoupled saw-tooth law is an extension of the coupled saw-tooth law. This together means, that when the coupled saw-tooth law formulation is aborted prematurely, the results of the decoupled saw-tooth law that are still returned after this step are of little significance. The results can be used to clearly show the difference in crushing behaviour, but that is all there is.

After the coupled saw-tooth law has prematurely aborted, meaning not all integration points have been completely damaged by the SLA routine, the stiffness of the structure has reduced to an roughly estimated 2 kN/mm for both versions. This is only 2,75% of the maximum stiffness the structure could offer. The decoupled saw-tooth law continues the calculation, further reducing this stiffness to a remainder of 0 kN/mm, see figure 9.20. Although more results were obtained by the decoupled saw-tooth law formulation, they are of no further use.

The construction is far beyond its service point and has already failed when only 2,75% of the structure stiffness is left. However, the procedure will keep selecting new critical integration points if there are still not complete damaged integration points available. Normally such a situation will give rise to divergence of difficulties with finding convergence in NLFEA, retrieving less data points then actually existing and indicating possible structure failure. In SLA the user has to conclude for himself from what point the structure can be considered fatally damaged by taking the results into consideration and excluding the remainder of subsequent results.

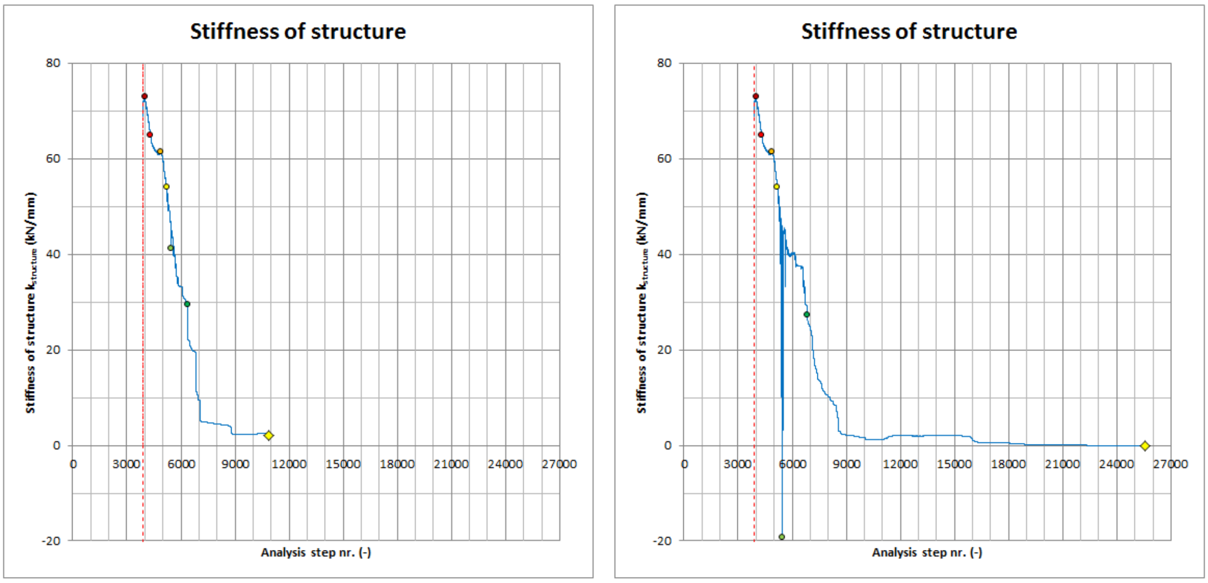

Figure 9.20: Structure stiffness compared for both versions.

9.3.3. A reversed situation.

In the version of the decoupled saw-tooth law formulation a negative value for the stiffness can be clearly seen. This situation is absent for the version with the coupled saw-tooth law formulation, although a situation similar is present. The situation is indicated by the light green dot in the graphs and indicates the first moment an integration point is completely crushed in the lower corner of the masonry deep wall. These sensitive situations rise anew later, indicated by the negative deflection at midspan at figure 9.13.

Multiple integration points are loaded heavily, but only one integration point is seen as critical. In this case it is seen as completely damaged for the next step, forces can no longer flow through this point of the compressive strut. Redistribution of stresses takes place in the next step and therefore the neighbouring (critical) integration point has to sustain the load it already was subjected too as well carrying the load of the previous critical integration point. A huge drop is therefore witnessed in all the graphs. Its effect is even that big that temporarily the total reaction force at the jacks has become negative.

At this particular moment, shown in figure 9.21, almost no internal force flow is present in the structure, expect for the lower right corner. A very localized behaviour is occurring in the structure to find equilibrium and that is the only spottable deformation aside from the deformation provided by the non-proportional load (constant load), see figure 9.22.

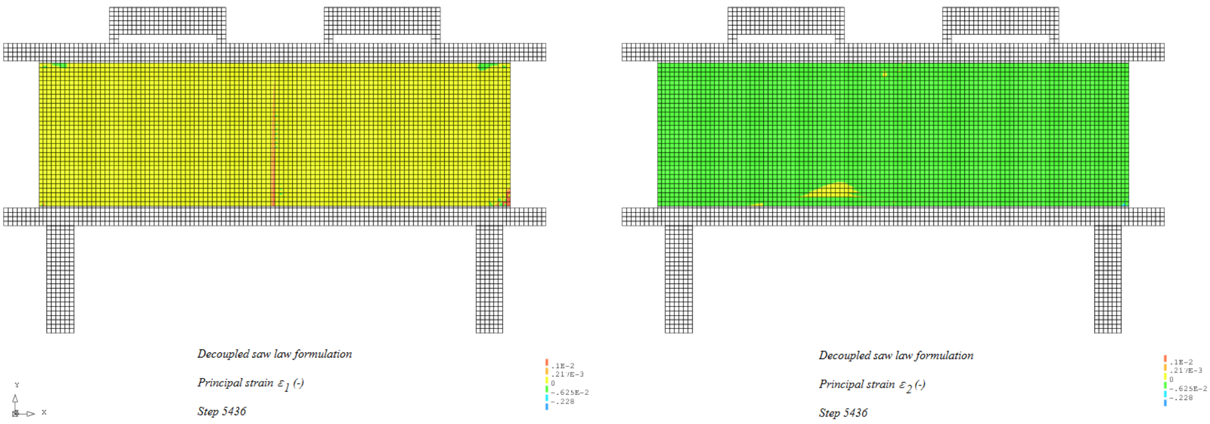

Figure 9.21: Principal strains at the discussed moment.

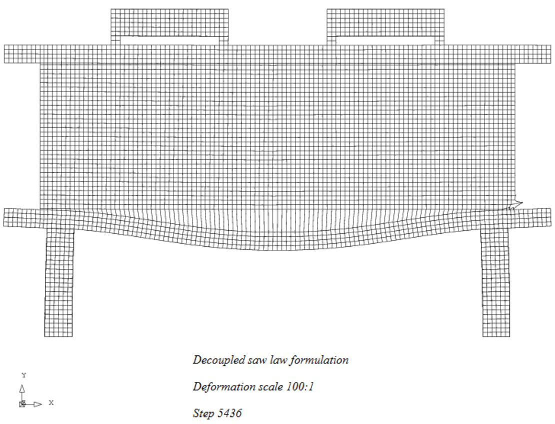

Figure 9.22: Deformation at the discussed moment.

10. Laboratory and numerical validation

For this numerical analysis with sequentially linear analysis a deep wall-frame structure has been used as the casus, where the deep wall was of masonry. Prior to this research this casus has been tested in the laboratory by R. Sterrenburg in Eindhoven University of Technology in Eindhoven [4] and also numerically tested with nonlinear analysis by J. Martens in Delft University of Technology in Delft. After comparing the results obtained concerning the casus in this thesis it is shown that the SLA can also perform quantitatively very well. As concluding remarks, overall comments on the validation of analysis are made.

10.1. Laboratory results and validation

In 2007 laboratory research has been performed by R. Sterrenburg for his Master thesis project. The goal was to determine the force flow in a deep wall of masonry. To reach this goal the researcher the casus of a masonry deep wall on a frame structure, the laboratory experimental setup is shown in figure 10.1. His obtained results of importance for the validation are presented first in subparagraph 10.1.1. and the validation takes place in subparagraph 10.1.2.

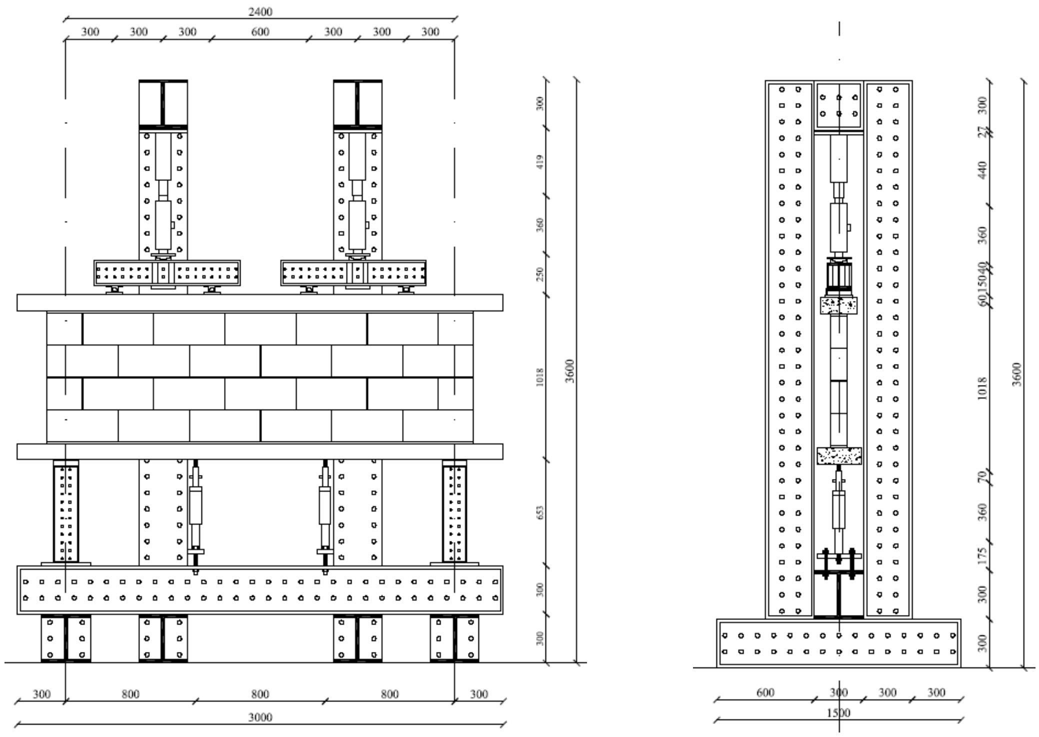

Figure 10.1: The structure used as casus. [4]

10.1.1. Laboratory results

The author of the laboratory experiments presents his findings in paragraph 3.2 of his work. In his work he made two series of test walls, series A and B, to exclude coincidences. The comparison is made with series A primarily, however, because the tested situation is most equal to the casus used for the sequentially linear analysis.

During the experiments the author observed several failure mechanisms, which he distinguishes in three different phases. The first phase is dedicated to the separation of the lower concrete beam with the masonry deep wall, thus cracking of the kicker joint. The second phase represents the appearance of the crack in the middle of the deep wall. Finally, the third and last phase starts when the sides of the structure start to tend to crack diagonally from the supports to where the load is applied. The phases with their respective applied force load is shown in table 10.1 and the crack patterns are shown in figure 10.2.

Table 10.1: The distinguished crack phases during the experiment. [4]

Phase	Test series A	Test series B
Separation crack	40 kN	40 kN
Vertical crack in middle	100 kN	100 kN
Diagonal cracks	230 kN	255 kN

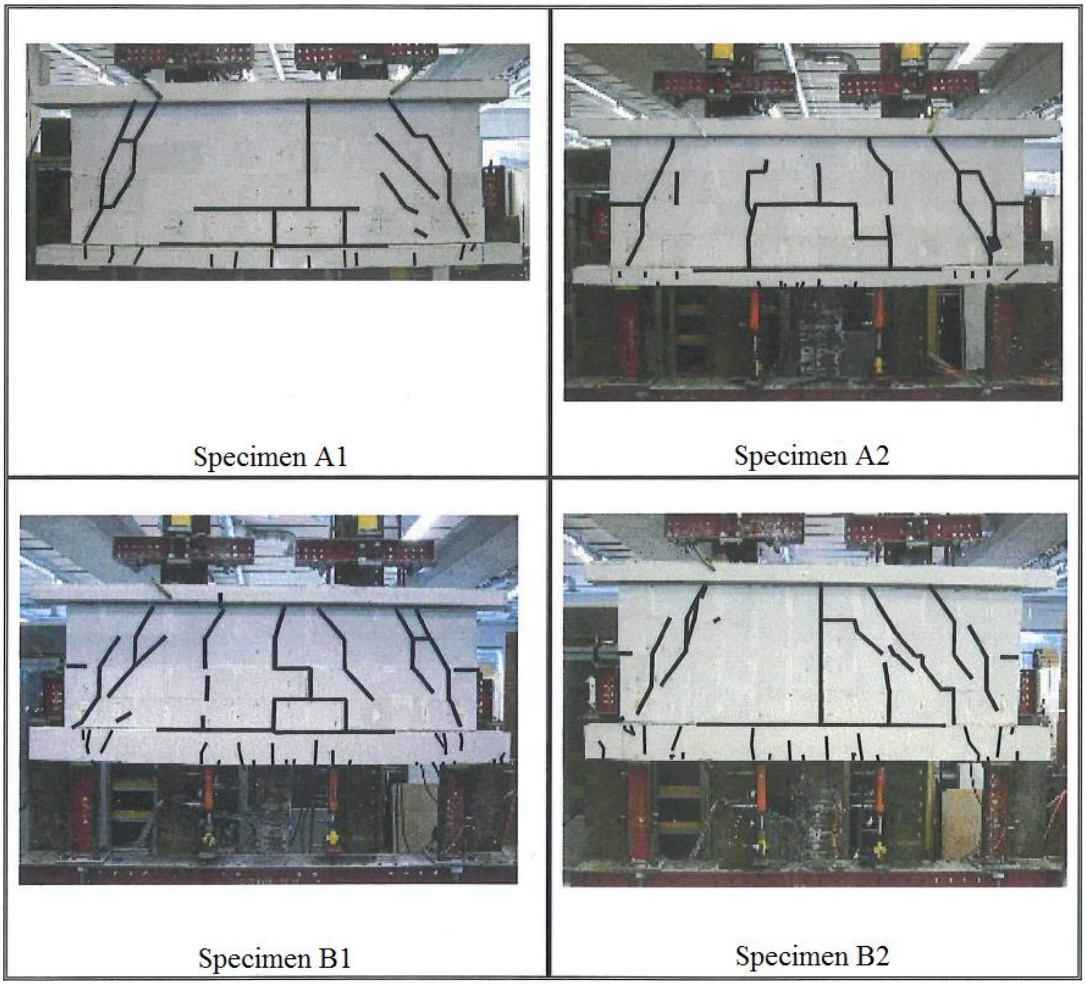

Figure 10.2: The observed crack patterns during the experiment. [4]

10.1.2. Laboratory validation

The three phases are discussed separately starting with the separation crack of the kicker joint. In this validation the focus lies on the crack patterns and the found failure mechanisms. The numerical calculation done in Chapter 9 uses a simplified model of this representation, meaning that in-depth results, like rotations of the supports, give no added value if compared quantitatively. However, global results, like crack patterns (figure 10.2) and their accompanying applied load at the moment (table 10.1), are extracted from those and can be validated qualitatively and quantitatively. Also, force-displacement graphs of the laboratory experiments were averaged over multiple points, resulting in different style of diagrams as presented in Chapter 9 and will add to the already extracted data no value.

During the laboratory analysis in the first phase the constant (non-proportional) load is applied in alternating steps with the load that is scaled (proportional load). When the constant load at the lower concrete beam is fully applied, there is already a scaled load of $F_2 = F_1$ applied in the laboratory experiment. For the numerical experiment done with the sequentially linear analysis this load is $F_2 = 0$ kN, for the scaled load is not applied yet. Different loading histories, figure 10.3, mean different results for the separation crack. However, in both experiments the crack appears in the same manner.

The vertical crack in the middle of the masonry deep wall is also spotted in the both experiments. This happens at $F_{laboratory} = 100$ kN and at around $F_{SLA} = 73$ kN, as can be seen for the latter in Chapter 9. The used concrete beams in the laboratory experiments had a much higher stiffness than the beams used in the sequentially linear analysis. This difference, together with the difference in loading history, influence the results quantitatively. However, the force retrieved by SLA is in the same order of magnitude qualitatively as the laboratory experiment.

The last phase is different for the numerical analysis. Instead of the occurrence of diagonal cracking, the structure crushes in a corner as a third phase for the sequentially linear analysis. This difference is due to the crack model chosen for the masonry deep wall in the numerical experiments. This fact is also discussed in the other paragraphs.

However, the crushing phase has not been distinguished by the author of the laboratory experiments, while it is certainly present as a last and final step. As explained in Chapter 7, although the region is cracked from support to load application, compression is still carried in that strut. Eventually, the corners have to crush and the structure would fail. The experiments in the laboratory were not carried out this far, because huge deflections of at least 10 mm in midspan were achieved. The damaged deep walls of both experiments, and the difference in the last phase, are shown in figure 10.4.

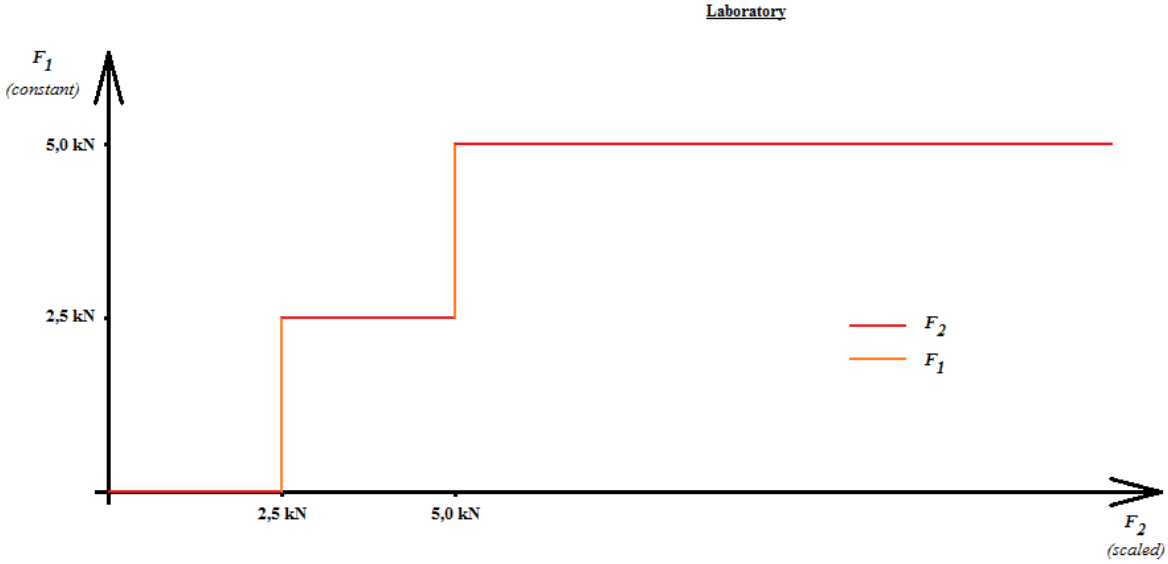

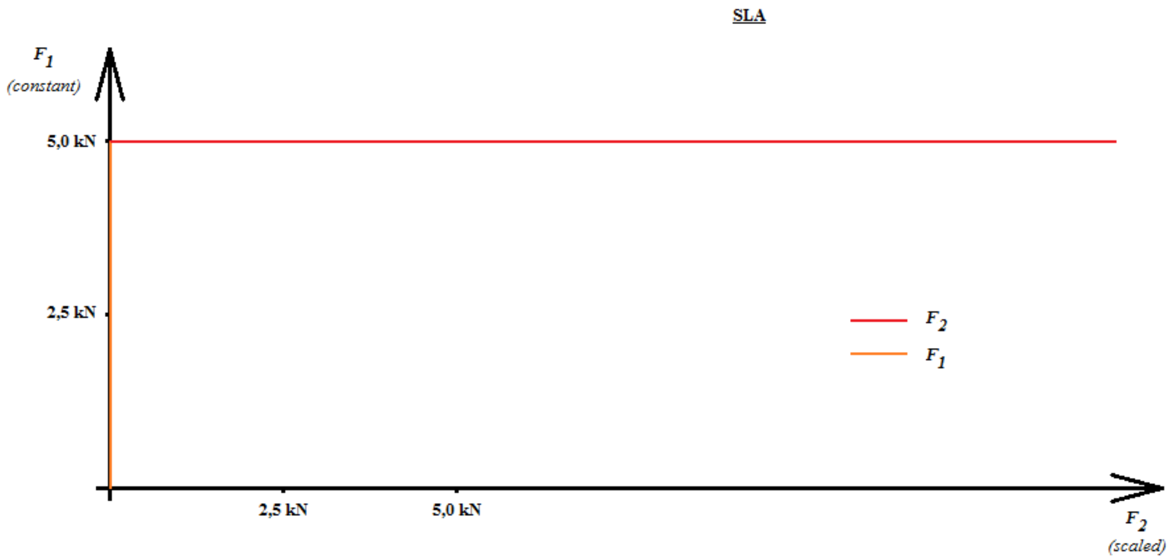

Figure 10.3: Loading history during the laboratory experiments and the SLA analysis.

Table 10.2: The distinguished crack phases during the experiment and the SLA.

Phase	Test series A	SLA
Separation crack	40 kN	0 kN
Vertical crack in middle	100 kN	73 kN
Diagonal cracks	230 kN	- kN
Crushing corner (peak load)	- kN	114 kN

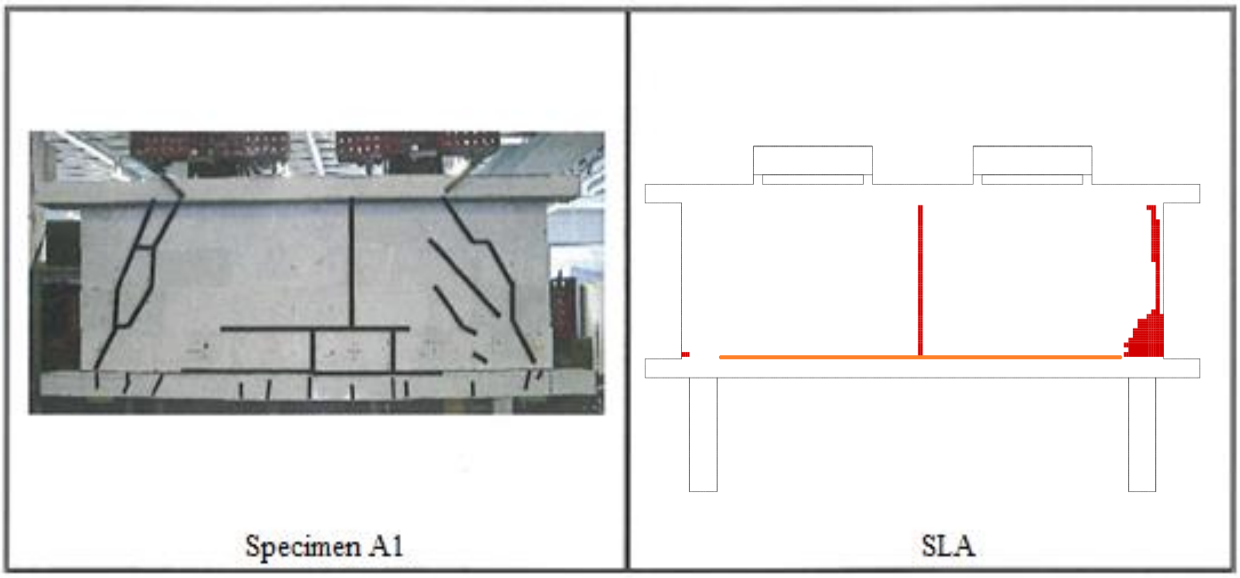

Figure 10.4: Damaged structure in the laboratory experiment and the SLA analysis.

10.2. NLFEA results and validation

In 2008 numerical research has been presented by J. Martens for his Master thesis project. The aim of the computational investigation has been to obtain failure loads for calcium silicate element walls supported by a framework . The researcher implemented the casus of a masonry deep wall on a frame structure in a nonlinear finite element analysis and is shown in figure 10.5. His obtained results of importance for the validation are presented first in subparagraph 10.1.1. and the validation takes place in subparagraph 10.1.2.

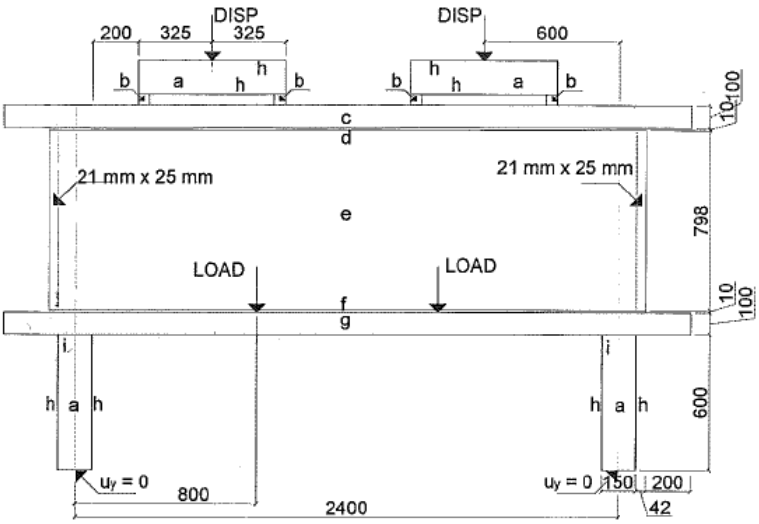

Symbol	Representing	Elements
a	Steel (web)	CQ16M
b	Hinge	CQ16M
c	Concrete beam	CQ16M
d	Joint	CL12I
e	Masonry	CQ16M
f	Joint	CL12I
g	Concrete beam	CQ16M
h	Steel (flange)	L6BEN
i	Steel (plate)	L6BEN

CQ16M = plane stress element
CL12I = interface element
L6BEN = bending element

Dimensions in mm

Figure 10.5: The model implementation in NLFEA. [3]

10.2.1. NLFEA results

The author of the nonlinear finite element analysis experiments presents his findings in Chapter 6 of his work for a homogeneous mesh with self-weight. He also presents results for a heterogeneous mesh, but this kind of mesh is not used during the sequentially linear analysis and is thus left aside.

During the experiments the author observed several failure mechanisms, which he distinguishes in four different phases of which three are the same with the phases determined in the laboratory experiments. The first phase is dedicated to the separation of the lower concrete beam with the masonry deep wall, thus cracking of the kicker joint. The second phase represents reclosure of this said separation. The third phase is the appearance of the crack in the middle of the deep wall. Finally, the fourth and last phase starts when the sides of the structure start to tend to crack diagonally from the supports to where the load is applied. The phases with their respective applied force load is shown in table 10.2 and the crack patterns are shown in figure 10.4.

Table 10.3: Loads at certain stages. [3]

Stage		Applied load F_{NLFEA} (kN)
End	stage 1	0,05
Start	stage 2	5,0
End	stage 2	27,0
Start	stage 3	31,9
End	stage 3	135,0
Start	stage 4	129,0
End	stage 4	157,0

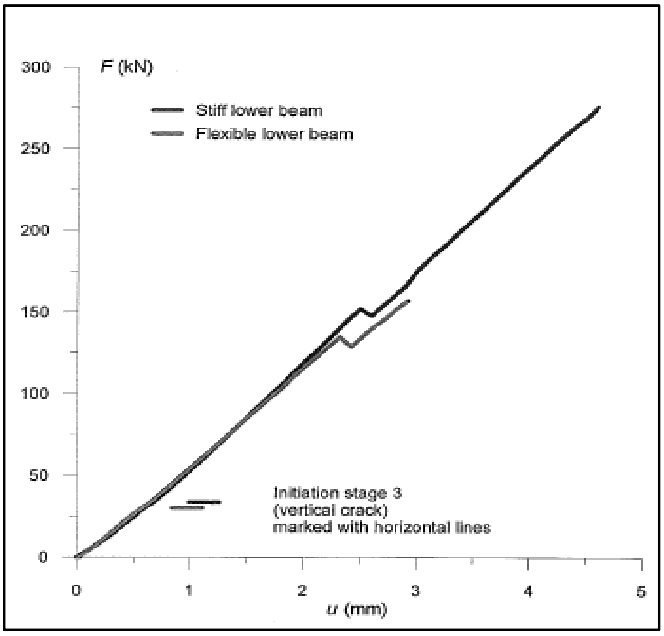

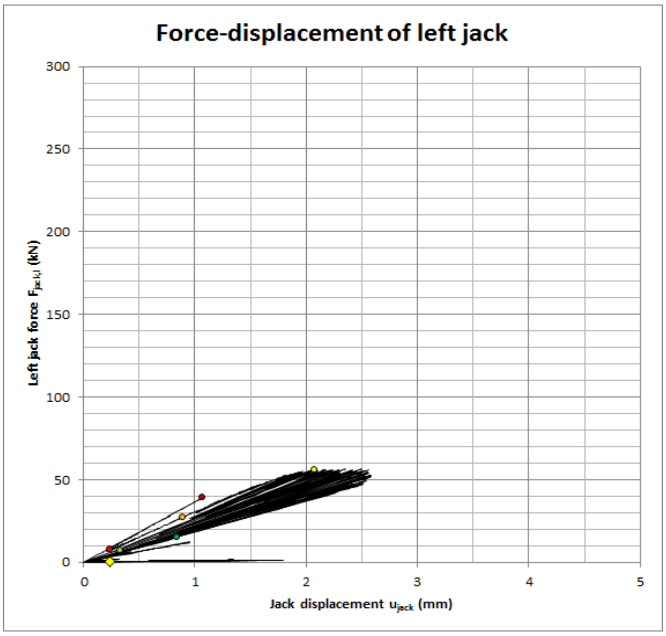

Figure 10.6: The force-displacement graph of NLFEA (left) and a force displacement graph of SLA (right). The model with the flexible lower beam is of importance for the validation. [3]

10.2.2. NLFEA validation

Again the phases are discussed separately first. In this validation focus lies on both comparing the results qualitatively as well as quantitatively. Both are results for numerical analysis and both use a simplified model for the masonry deep wall. It may thus be expected that the results should be in the same order of magnitude.

The separation crack are found by both models at a load of F = 0 kN. The crack exists solely due to the first loading type, which is applied on the lower concrete beam. The scaled loading of which is applied on top of the structure has not been applied yet, meaning that only the full constant load at the lower beam is present in this state. The nonlinear analysis concludes that this state ends at a scaled load of F_{NLFEA} = 0,05 which is negligible and in the sequentially linear analysis it is considered zero.

The second phase is not present in the results of the sequentially linear analysis. The lower concrete beam deflects upwards, closing the crack that appeared in the kicker joint. This is not possible if the constant load is still applied on the lower concrete beam. This means that the constant loading has not been taken into account into the second phase of the nonlinear analysis. If this was intentional or an mistake is unknown, but in the configuration as used for this thesis this should not happen at all.

The third phase, the appearance of the middle crack, starts around F_{NLFEA} = 31,9 kN. This moment happens in this research around F_{SLA} = 78,08. This makes the force found in this research double the force of the one found in the nonlinear analysis, $F_{SLA} \approx 2 \cdot F_{NLFEA}$. If a look is taken into the report of J. Martens, it is found that the tensile strength used by the author is twice as low in comparison with the one used in this work, in other words $f_{t,NLFEA}$ = 0,4 N/mm^2 and $f_{t,SLA}$ = 0,8 N/mm^2. With this difference in mind the results can be considered the same. For comparison the force-displacement graph of one jack is shown in figure 10.6.

Like in the laboratory experiments, the last phase of the nonlinear analysis is not present in the sequentially linear analysis. Diagonal cracks appear from the supports of the structure to the point of load application in NLFEA, but this is not the case in SLA. This is due to the crack model chosen in both analysis. The NLFEA uses a total strain rotating crack model, while the SLA uses a total strain fixed crack model. The total strain fixed crack model is the only model that is now usable in the SLA-procedure, but it is the cause for the absence of these diagonal cracks. The diagonal cracks and the crushing of the corner are two mechanisms which lie closely together, but if the crack directions are prevented from rotating the diagonal cracks are hindered growing and the crushing is thus the governing failure mechanism.

The crushing of the corner itself is unobserved in the nonlinear analysis of J. Martens. The calculation aborts in his analysis. The convergence criteria are increased, meaning they are made more tolerant, to find equilibrium, but after some successful steps convergence is not met anymore and the calculation goes wrong, probably due to the discussed limitations of NLFEA as discussed in Chapter 3. After this point crushing should occur, but the analysis type is seemingly not robust enough.

10.3. Final remarks

The peak load cannot be validated due to a different failure mechanism in the masonry deep wall after the appearance of the middle crack and due to stopping the experiments, one because of too high deformations and the other because of non-convergence. Because the diagonal cracks are appearing in the masonry deep wall in the laboratory and nonlinear analysis experiment, redistribution of stresses is possible anew in the structure. This makes it possible for these tests to increase their loading even further. In the sequentially linear analysis the crack directions are not allowed to rotate, thus restraining these crack formation. Crushing occurs earlier in comparison to the experiments resulting in a lower peak load.

In figure 10.5. the difference in appearance of failure mechanisms are presented. The reason for this difference is already discussed and it is a consequence of choice of modelling rather than that the sequentially linear framework is not working properly. Due to the modelling choice the failure of the compressive strut will happen earlier in crack formation in the case of the predecessors [3,4] than in crush formation. Nevertheless, both are part of the same tension-compression failure. If the NLFEA calculation is performed with the same total strain crack model as SLA, then the diagonal cracks are also not present and the structure will start with the crushing of the lower corners. The important thing is that the tension-compression failure has been fully represented, which is the case.

Qualitatively and quantitatively the results are much alike and differences can be explained on a global level. The same failure mechanisms tend to happen in SLA. In comparison to NLFEA, it even seems SLA is able to fully follow the behaviour of the masonry deep wall up till negligible stiffness. It is robust enough to fully encompass the quasi-brittle behaviour characteristic to masonry.

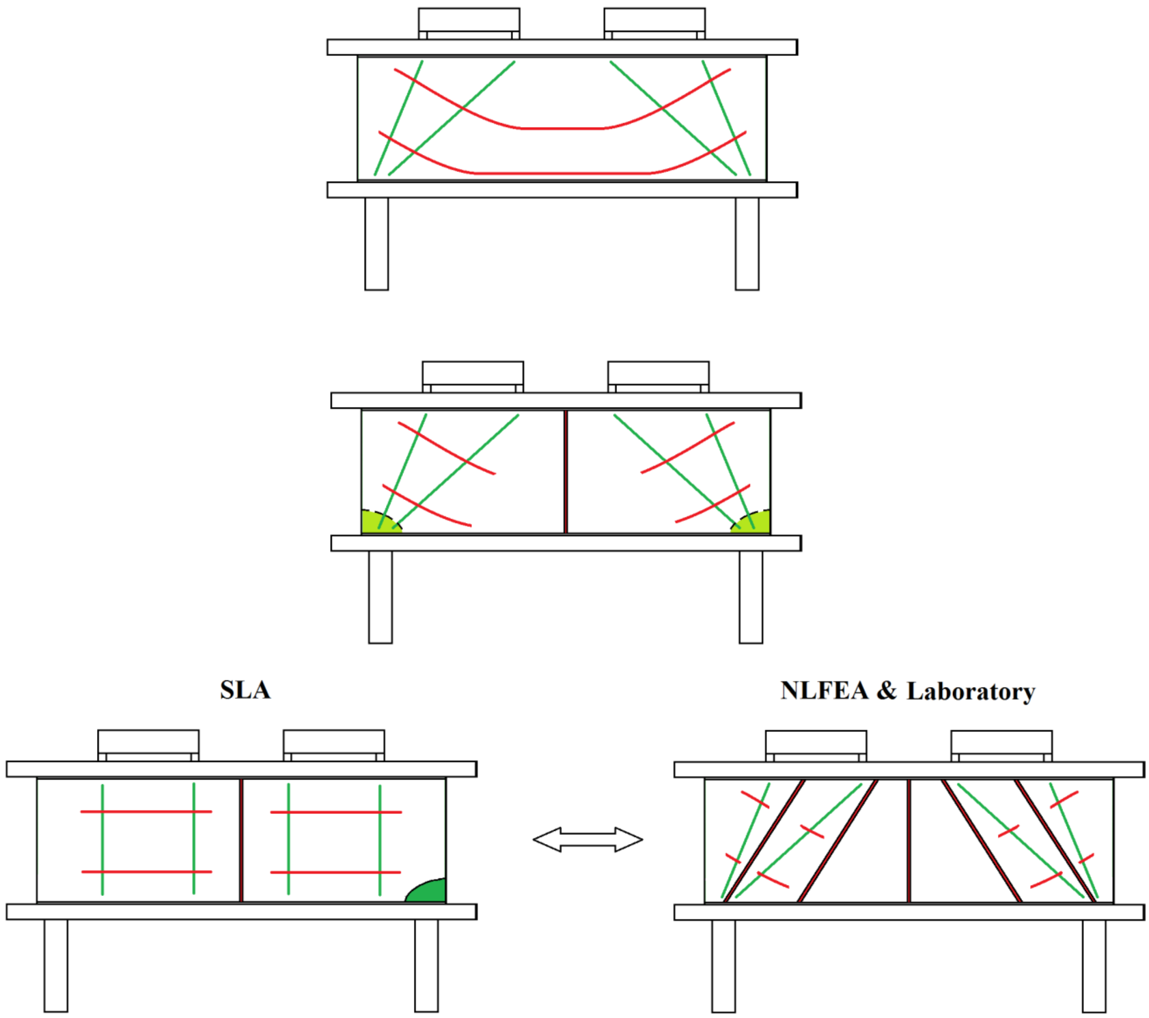

Figure 10.5: Global representation of the directions of principal stresses during the analysis. The SLA crushes to indicate that tension-compression failure takes place, while the NLFEA and laboratory let the structure generate diagonal cracks. This difference is made by the fact that SLA uses a total strain fixed crack model, while NLFEA uses a total strain rotating crack model.

TAIL

Conclusions and recommendations

11. Conclusions

This chapter provides a summary of conclusions that can be made after performing the body of the report. Conclusions about the head of the report is still considered part of the background theory and therefore the reader is for that case redirected to the references. In paragraph 11.1, the statements will concern primarily Chapter 7 and Chapter 8 and will encompass the use and limitations of the numerical methods discussed. In paragraph 11.2 the conclusions will concern Chapter 9 and Chapter 10 and are about the deep wall-frame study. Finally, the main question made in Chapter 1 is answered in paragraph 11.3.

11.1. Evaluating the numerical methods

- Standard nonlinear finite element analysis is insufficiently robust to assess the safety of structures existing out of quasi-brittle materials with respect to certain aspects, such as tension-compression failure, due to the rise of primarily and inter alia a negative tangent stiffness during the analysis making the system of equation become ill-conditioned and resulting in convergence difficulties and divergence.

- The sequentially linear analysis method is an alternative solution procedure to the nonlinear finite element analysis for these situations, for it models structures through an event-by-event strategy of imposing damage increments to, most importantly, guarantee a positive tangent stiffness during the whole analysis and thus bypassing limitations as found in nonlinear finite element analysis.

- The sequentially linear framework is still in development and has to be complemented to be considered a fully functional numerical model, but the present sequentially linear framework is tested as well as verified and functions accordingly with respect to the desired mechanisms, such as biaxial tension-shear failure in a single element and shear-compression failure in a wall.

11.2. Results and validation

- The deep wall-frame study made in order to validate tension-compression failure is performed successfully, meaning the calculation was stable and returned the full mechanical behaviour of the structure, until the structure reaches a point where failure is obviously inescapable, the moment where SLA is not able to apply the full initial load anymore, and after discussing the output, the results have been shown to be trustworthy.

- The results are in line qualitatively and quantitatively with the laboratory experiments and with the numerical experiments performed with nonlinear finite element analysis, taking the differences found into account, which were present due to choice of modelling and material properties.

11.3. Answering the main question

With the conclusions presented in both previous paragraphs it is now possible to answer the main question as found in Chapter 1. The same main question is formulated below anew for the complete picture in this paragraph.

To what extent can the sequentially linear analysis method improve the numerical robustness and show stable post-peak behaviour with respect to combined tension/compression failure and be applied successfully to for example a masonry deep wall supported on a frame?

Without further ado the answer to this main question is answered positively and shown below. With it, the thesis research has come to an end.

The sequentially linear analysis method improves the numerical robustness considerably in comparison to standard nonlinear finite element analysis to such an extent that post-peak behaviour of combined tension/compression failure can be successfully presented for quasi-brittle materials returning results past the complete failure of structures and can be applied successfully to for example a masonry deep wall supported on a frame up until the initial constant load cannot be fully applied anymore in order to find equilibrium.

12. Recommendations

In this chapter recommendations are made.

- It is recommended to continue research in this field and keep augmenting and improving the analysis type for it has been shown in this research and other research, which is partly found in the references, that the sequentially linear analysis is a strong alternative for quasi-brittle materials to nonlinear finite element analysis.

- It is recommended to improve the sequentially analysis by implementing four damage indicators and a status indicator for each integration point to facilitate a basis for crack closure-reopening, as discussed in subparagraph 8.1.4.

- It is recommended to validate other types of failures found in structures consisting of quasi-brittle materials.

- It is recommended to improve the complexity of the finite element model implemented to obtain more realistic results instead of the now used simplifications to only get a qualitative basis for validation.

References

1. DeJong, M.J., Hendriks, M.A.N., Rots, J.G., *Sequentially linear analysis of fracture under non-proportional loading*, Engineering Fracture Mechanics, 2008, 75:5042-5056.
2. Rots, J.G. (editor), *Structural Masonry: An experimental/numerical basis for practical design rules*, CUR-report 171, A. A. Balkema, Rotterdam, 1997.
3. Martens, J. *Computational modelling of calcium silicate walls: finite element analysis of wall-beam systems*, Master thesis, Delft University of Technology, Delft, The Netherlands, 2008.
4. Sterrenburg, R. *Hoge wandliggers in kalkzandsteen*, Master thesis, Eindhoven University of Technology, Eindhoven, The Netherlands, 2008. (Dutch)
5. DIANA (2011), DIANA Finite Element Analysis: User's Manual. TNO DIANA BV, Delft, Release 9.4.4, 2011.
6. Wells, G.N., *The Finite Element Method: An Introduction*, Introduction to the finite element method, University of Cambridge and Delft university of Technology, 2011.
7. De Borst, R. and Sluys, L.J., *Computational Methods in Non-linear Solid Mechanics*, Computational Methods in Non-linear Solid Mechanics, Delft University of Technology, 2010.
8. Rots, J.G., Hendriks, M.A.N., *An introduction to nonlinear analysis*, Computational Modelling of Structures, Delft University of Technology, 2011.
9. Lourenço, P.B., *Computational strategies for masonry structures*, PhD thesis, Delft University of Technology, Delft, The Netherlands, 1996.
10. Ganz, H.R., Thürlimann, B., *Tests on masonry walls under normal and shear loading*, Report No. 7502-4, Institute of Structural Engineering, ETH Zurich, Zurich, Switzerland, 1984. (German)
11. Rots, J.G., Invernizzi, S., Belleti, B., Hendriks, M.A.N., *Circumventing bifurcations in structural softening*, Computational Modelling Workshop on Concrete, Masonry and on Fiber-reinforced Composites, June 17-18, 2009, Delft, The Netherlands.
12. Rots, J.G., *Computational modelling of concrete fracture*, Dissertation, Delft University of Technology, 132 pp.
13. Rots, J.G., Invernizzi S., *Regularized sequentially linear saw-tooth softening model.* Intern. Journal for Numerical and Analystical Methods in Geomechanics, 2004, 28:821-856.
14. Rots, J.G., Belleti B., Invernizzi S. *Robust modelling of RC structures with an "event-by-event" strategy,* Engineering Fracture Mechanics, 2008, 75:590-614.
15. Slobbe, A.T., Hendriks, M.A.N., Rots, J.G. *Sequentially linear analysis of shear critical reinforced concrete beams without shear reinforcement*, Finite Elements in Analysis and Design, 2012, 50:108-124.
16. Rots, J.G., Belletti, B., Invernizzi, S. *On the shape of saw-tooth softening curves for sequentially linear analysis*, Computational modelling of concrete structures, Proceeding of EURO-C 2006, Taylor and Francis group, 2006:431-442.

17. Schlangen E., van Mier J.G.M. *Experimental and numerical analysis of micro-mechanisms of fracture of cement-based composites*. Cement and Concrete Composites, 1992, 14:105-118.
18. Beranek W.J., Hobbelman G.J., *2D and 3D-Modelling of concrete as an assemblage of spheres: revaluation of the failure criterion*. In Fracture Mechanics of Concrete Structures, Wittman F.H. (ed.), Proceeding of FRAMCOS-2, 1995:965-978.
19. Giardina, G., van de Graaf, A.V., Hendriks, M.A.N., Rots, J.G., Marini, A., *Numerical analysis of a masonry façade subject to tunnelling-induced settlements*, Engineering structures, 2013, 54:234-247.
20. CEB-FIB Model Code 1990. Bulletin No. 213/214 (1993), Comité Intern. du Beton.
21. Van de Graaf, A.V., *SLA Users Manual*, Version 0.2.00, 2009.
22. Kabos, M. *Modeling shear-compression failure of concrete beams with sequentially linear analysis*, Master Thesis, Delft University of Technology, Delft, The Netherlands, 2013.
23. Van Noort, J.R., *Computational modelling of masonry structures*, Master Thesis, Delft University of Technology, Delft, The Netherlands, 2013.
24. Vermeltfoort, A.T., *Invloed kimvoegdikte op druksterkte van kalkzandsteenmuren*, Cement, 2007, 2007:75-78.
25. Van der Pluijm, R., *Material properties of Masonry and its Components Under Tension and Shear*, Proceeding of 6th Canadian Masonry Symposium, Canada, 1992, 675-686.
26. Groot, C.J.W.P., *Effects of Water on Mortar-Brick Bond*, PhD thesis, Delft University of Technology, Delft, The Netherlands, 1993.
27. Binda, L., Fontana, A., Frigerio, G., *Mechanical Behaviour of Brick Masonries derived from Unit and Mortar Characteristics*, Proceeding of 8th Intern. Brick and Block Masonry Conference, Elsevier Applied Science, London, England, 1988, 205-216.
28. Rots, J.G., *Computer Simulation of Masonry Fracture: Continuum and Discontinuum Models*, Proceeding of the Intern. Symposium on Computational Methods in Structural Masonry, University College of Swansea, Swansea, England, 1991, 93-103.
29. Andreas, U., *Failure Criteria for Masonry Panels under In-Plane Loading*, Structural Engineering, 1996, 122:37-46.
30. Lishak, V.I., Yagust, V.I., Yankelevsky, D.Z., *2-D Orthotropic failure criteria for masonry*, Journal Engineering Structures, 2012, 36:360-371.
31. Page, A.W., *The biaxial compressive strength of brick masonry*, Proceeding Institute Civil Engineering, 1981, 71(2):893-906.
32. Page, A.W., *The strength of brick masonry under biaxial compression-tension*, Intern. Journal Masonry Constructions, 1983, 3(1):26-31.
33. Nelissen, L.J.M., *Biaxial testing of normal concrete*, HERON, Vol. 18, 3-90.
34. Rots, J.G., Blauwendraad, J., *Crack models for concrete: Discrete or Smeared? Fixed, Multi-directional or rotating?*, HERON, Vol. 34, 1989.
35. Lourenço, P.B., Rots, J.G. and Blauwendraad, J. *Two approaches for the analysis of masonry structures: micro and macro-modeling*. HERON, Vol. 40, No. 4, 1995, 313-340.

Appendices

Appendix A: Standard single element tests

To understand the to be used SLA model an element will be subjected to standard stress states. The results from the finite element program are compared with expected outcomes and differences and/or peculiarities are discussed. Limitations and potentials of the model are thus highlighted at element level. A look will also be taken into the influence of rotated axes, multiple integration points, the use of quadratic elements and the influence of Poisson's ratio. For information about elements and other DIANA specific topics, reference is made to the DIANA-manual [5].

A.1. Basic tests

A linear element with one integration point will be subjected to standard tests. The element will be modelled in tension, combined tension-tension, combined tension-compression, shear, combined shear-tension and combined shear-tension-compression loading and uses a total strain based fixed crack model. All models in these tests have a poisson's ratio of $\nu = 0$. All loading is proportional (scaled). The element and the saw-tooth curves for linear tension and linear compression softening are both showed below in figures A.1, A.2, A.3 and table A.1, while the tests are shown in figure A.4. The idea of this paragraph is that the saw-tooth curves for softening used as input to model the stress states should also be gained as output.

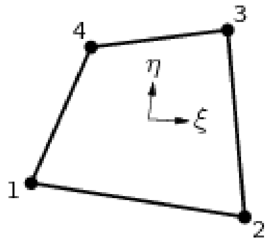

Figure A.1: Element Q8MEM.

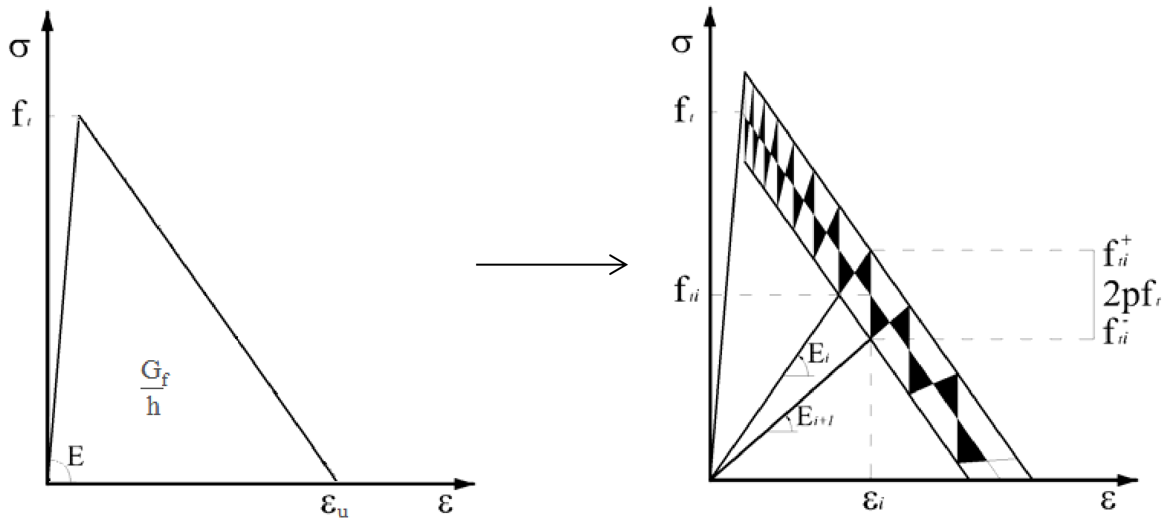

Figure A.2: Graphical theory of the saw tooth curve representation.

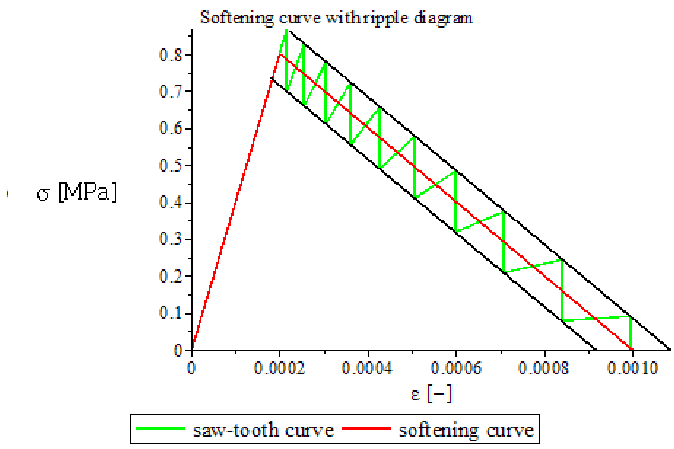

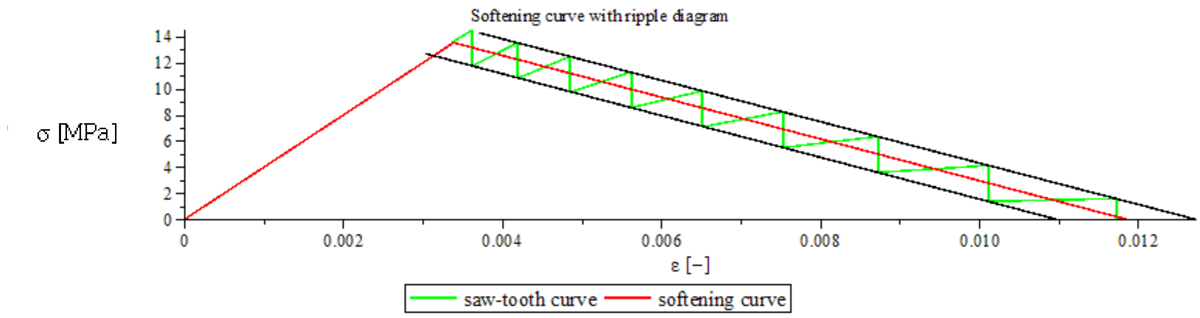

Figure A.3: Tension ripple diagram and compression ripple diagram used for the tests.

Table A.1: Input values of the ripple diagrams.

Input tension	
ε_i (10^{-4})	$f_{t,i}^{+}$ (N/mm^2)
2,17	0,867
2,57	0,827
3,04	0,780
3,60	0,724
4,27	0,658
5,05	0,579
5,99	0,486
7,09	0,375
8,40	0,245
9,94	0,090
9,94	0,000

Input compression	
ε_i (10^{-4})	$f_{t,i}^{+}$ (N/mm^2)
-36,2	-14,5
-42,0	-13,6
-48,6	-12,5
-56,3	-11,3
-65,2	-9,88
-75,5	-8,23
-87,4	-6,33
-101	-4,13
-117	-1,58
-117	0,000

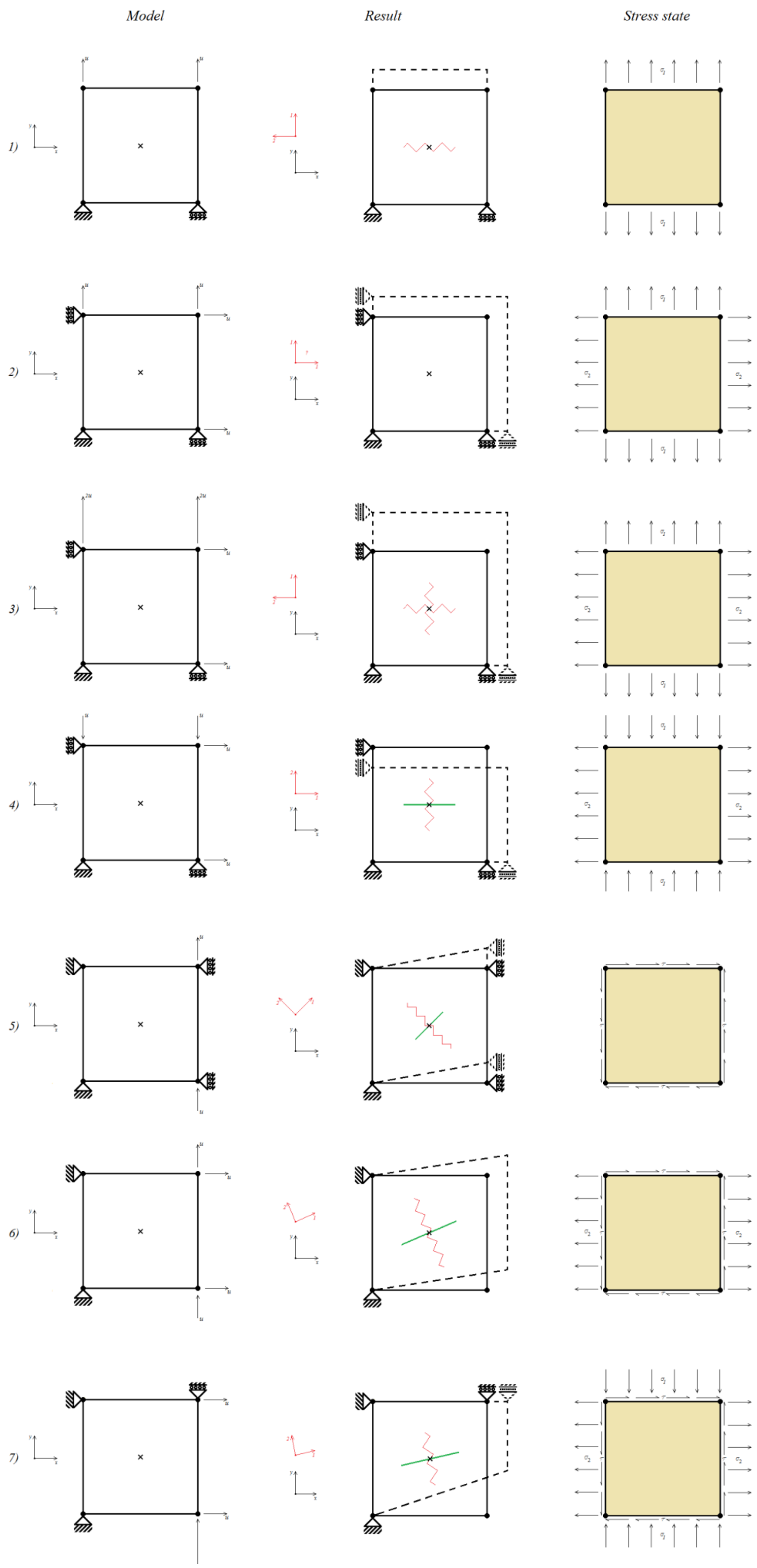

Figure A.4: Basic tests performed.

A.1.1. Tension

The procedure to verify the numerical model with regard to these standard stress states is described below for the element in tension. The used configuration for this test is presented in figure A.5. Herein the model, displacements and stress state are presented. The results can be found in the table A.2 and figure A.6. Take note that in this case σ_{yy} and ε_{yy} are equal to σ_1 and ε_1 respectively, for the principal axes collide with the standard global axes.

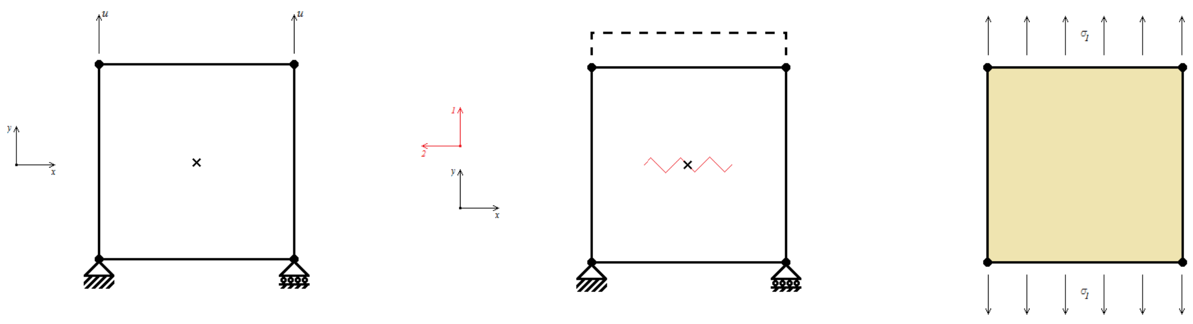

Figure A.5: Model, displacements and stress state of the tension test.

Table A.2: Tabular results of the tension test.

Input		Output						
ε_i (10^{-4})	$f_{t,i}^{+}$ (N/mm^2)	*Step*	u $(10^{-3}$ mm$)$	F $(10^2$ N$)$	ε_1 (10^{-4})	σ_1 (N/mm^2)	$\varepsilon_{k,nn}$ (10^{-4})	$\sigma_{k,nn}$ (N/mm^2)
2,17	0,867	1	5,42	1,08	2,17	0,867	0	0,867
2,57	0,827	2	6,43	1,03	2,57	0,827	0,52	0,827
3,04	0,780	3	7,60	0,98	3,04	0,780	1,09	0,780
3,60	0,724	4	9,00	0,91	3,60	0,724	1,79	0,724
4,27	0,658	5	10,70	0,82	4,27	0,658	2,63	0,658
5,05	0,579	6	12,60	0,72	5,05	0,579	3,60	0,579
5,99	0,486	7	15,00	0,61	5,99	0,486	4,78	0,486
7,09	0,375	8	17,70	0,47	7,09	0,375	6,15	0,375
8,40	0,245	9	21,00	0,31	8,40	0,245	7,79	0,245
9,94	0,090	10	24,90	0,11	9,94	0,090	9,72	0,090

In the obtained results the linear tension softening behaviour of the plane stress elements can be found. This linear tension softening behaviour is exactly the same as the input provided for the analysis. The total strains are equal to the displacement divided by the element length and the total stress is equal to the force (only one reaction force is presented) divided by the element area.

The crack strains are determined in comparison to the elastic branch of the material with the initial stiffness at the same stress level. Figure A.7 explains the concept for this particular situation.

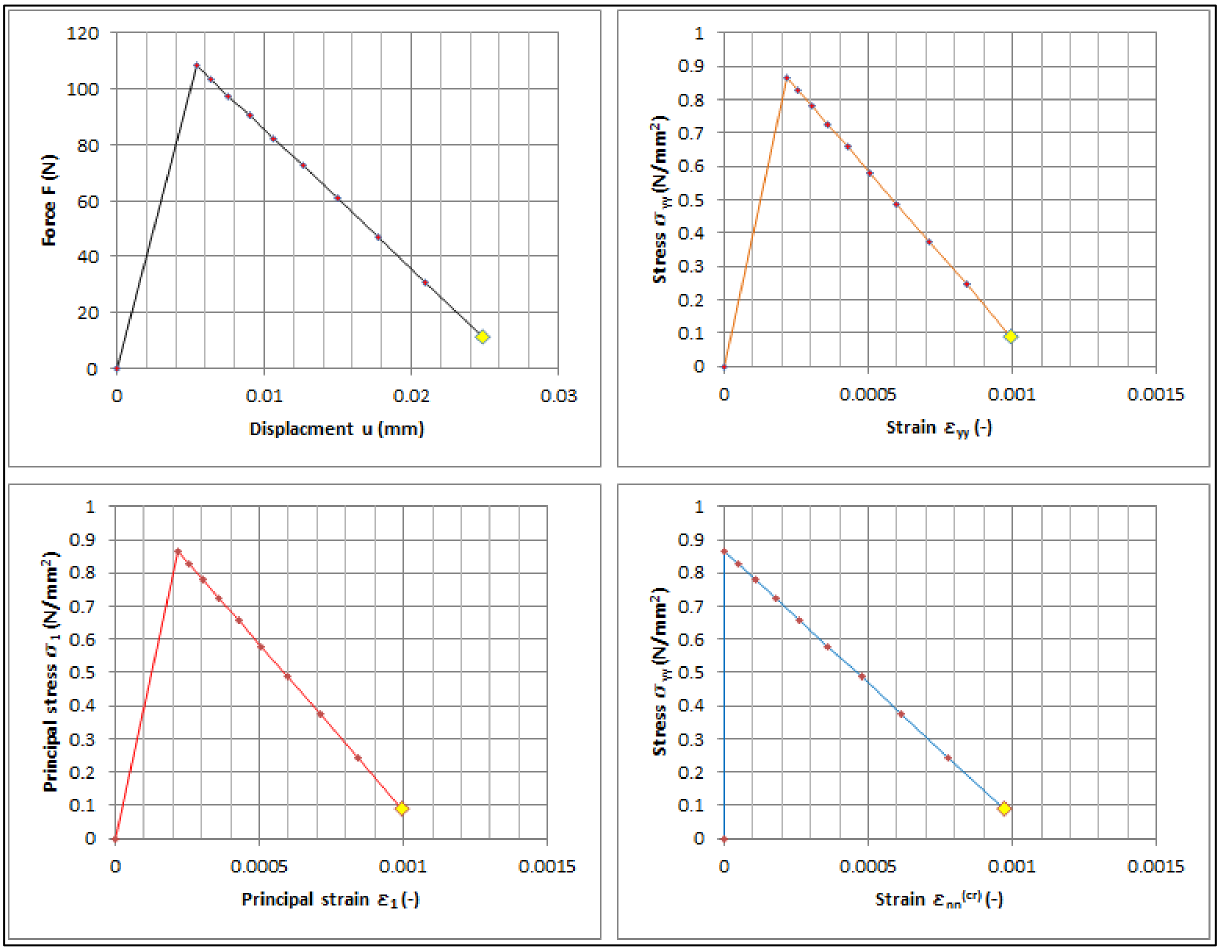

Figure A.6: Graphical results of the tension test.

$$\varepsilon_{nn}^{(cr)} = \varepsilon_{nn}^{(tot)} - \varepsilon_{nn}^{(el)} = \varepsilon_{nn}^{(tot)} - \frac{\sigma_{nn}}{E_0}$$

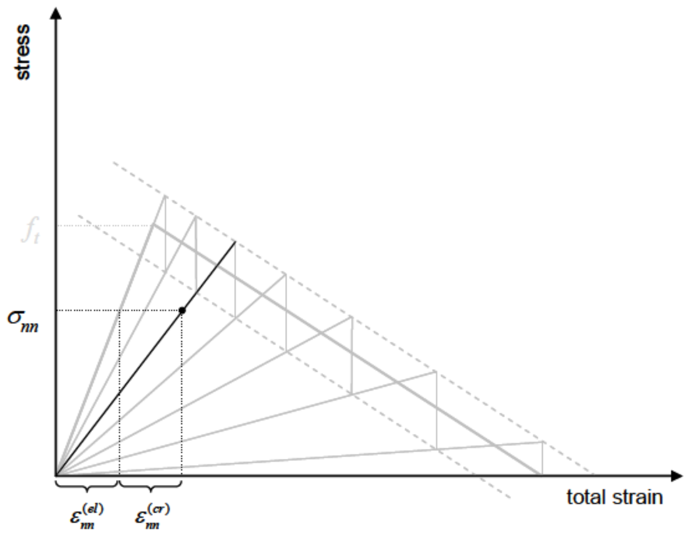

Figure A.7: Definition of the crack strains.

A peculiarity is that the last given input is needed or the last tooth of the saw-curve diagram is not present in the result. So an extra fake tooth is always needed giving a “dummy branch” as stated in *sawdch.f* of the sourcecode.

When only compression is applied to the element with a respective compressive softening curve the same conclusion can be drawn, the output is equal to the input. Keep in mind that the given output results are all due to $(1+p)f_t$ and not f_t solely. The results must be scaled to obtain the actual results, for the presented results are slightly overestimating the reality, which is the base softening diagram.

A.1.2. Tension-tension

The crack model used allows orthogonal cracking. With a double tension test a look will be taken if this goes well. The used model, obtained results and stress state is shown below in figure A.8.

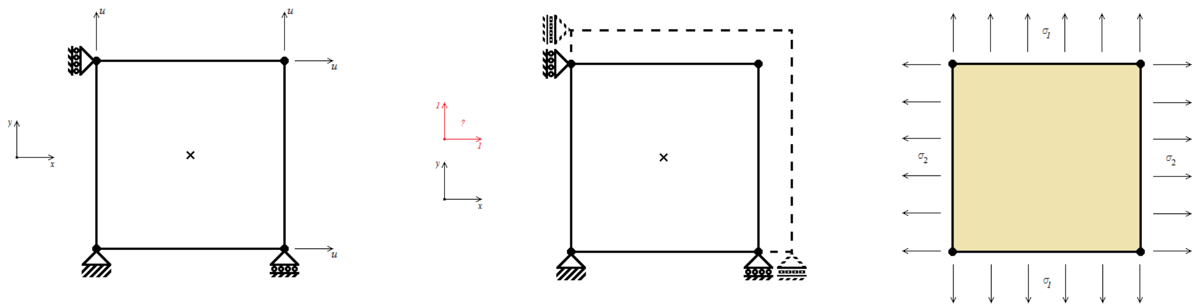

Figure A.8: Model, displacements and stress state of the unsuccessful tension-tension test.

As seen in the figure, displacement are found. However, this is only for the first step, afterwards the computation stops. The problem is the choice of the principal directions. Both directions (*x* and *y*) crack at exactly the same time. Both directions will return the same critical load multiplier and so both directions are the first principal direction. This results in the error remark that possibly all integration points are damaged. Sadly, simultaneous cracking of both directions is thus not available, which is not surprising for SLA is governed by event-by-event steps. This situation actually creates two events simultaneously, which means SLA is not suitable for this situation. So the figure below, figure A.9, is an alternative to test the situation.

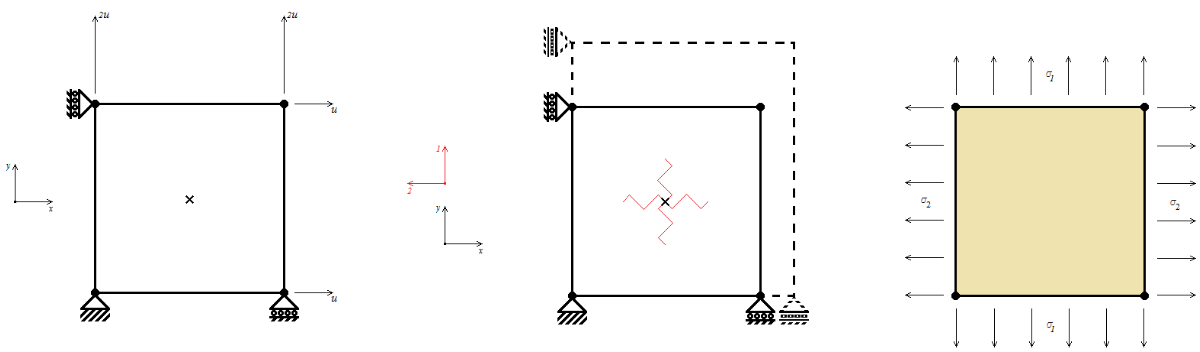

Figure A.9: Model displacements and stress state of the alternative tension-tension test.

Again there is only extension, so there were no shear stresses to be found in the results as expected. Furthermore, the principal axes were aligned with the direction of the local axes, so σ_1 and σ_2 are σ_{yy} and σ_{xx} respectively. Both directions were cracked for the coupled saw-tooth law formulation and show the corresponding softening behaviour as implemented. When one direction reaches f_t^+, the other directions is located on a secant branch. This can be seen in the graphs in figure A.10 too.

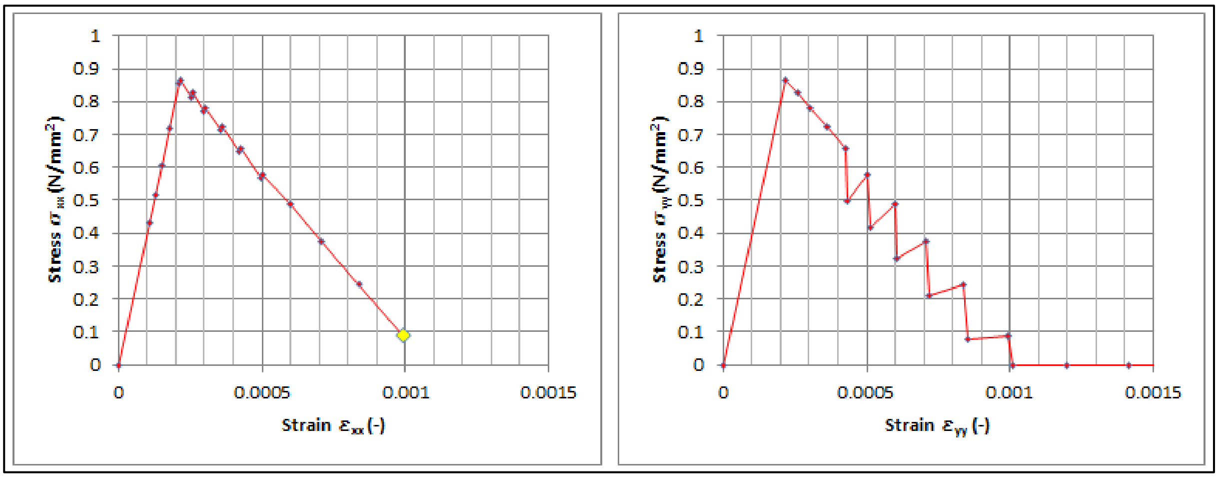

Figure A.10: Graphical results of the tension-tension test for the coupled saw-tooth law formulation.

The decoupled saw-tooth law formulation does not allow failure of the same type in both orthogonal directions. This version forces a compressive strut, which means that if the first direction fails in tension, the second direction must fail in compression. If the element fails the same way in the second direction as in the first direction, than the integration point will behave linear elastically in the second direction. This means unrealistic high stresses can be reached due to this implementation. This result is shown in figure A.11 and this phenomena is discussed in Chapter 8.

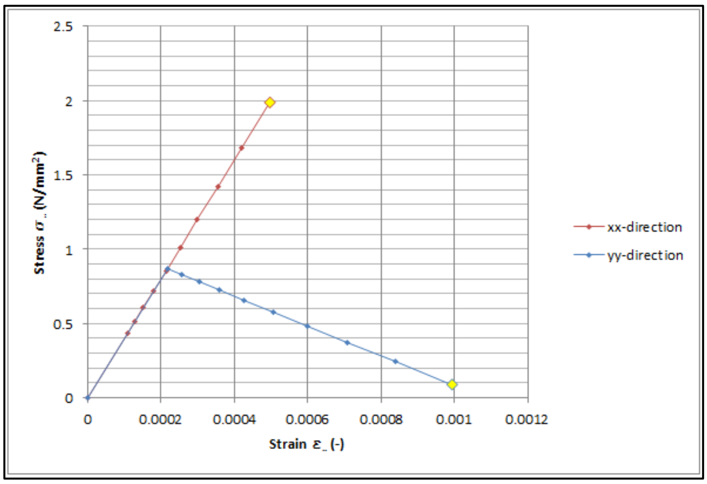

Figure A.11: Graphical results of the tension-tension test for the decoupled saw-tooth law formulation.

A.1.3. Tension-compression

Both cracking and crushing can occur at the same time, again orthogonally. The model, displacements and stress state is found in figure A.12. No distinction between the two SLA versions are made in this test as is made in the tension-tension test. Both versions allow this type of combined failure. Results are found in figure A.13 and table A.3. Nothing out of the ordinary is retrieved.

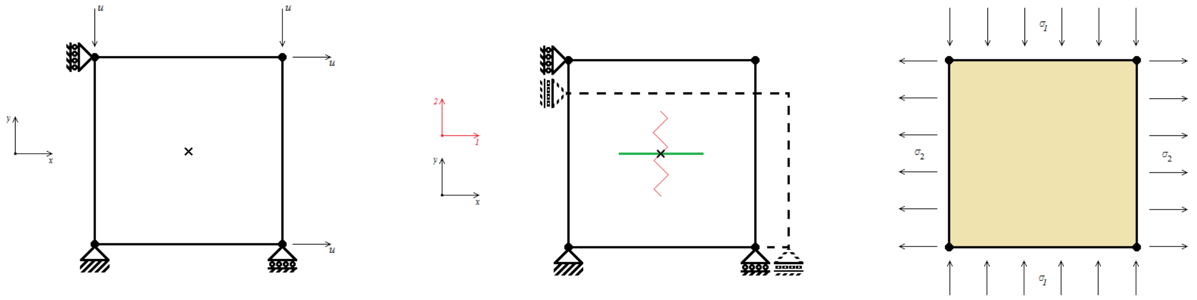

Figure A.12: Model, displacements and stress state of the tension-compression test.

The results do not go straight down after reaching the last damage increment in tension in the first principal direction. This was also noticed in the results of the tension-tension test for the coupled saw-tooth law formulation. The user should imagine it going straight down first, because the next point in the graph is partly determined by the strain increment needed in the other graph to reach it maximum upper tensile strength. The stress of the first principal direction (σ_{yy}) reduces closely to zero due to the dummy branch. The strain increments in this graph is now due to the strain increments needed for the second principal direction to reach f_t^+. These strain increments are the same, but twice as much, for there was applied twice as much displacement in that direction. Finally the calculations comes to an end for there are no critical integration points left to be damaged.

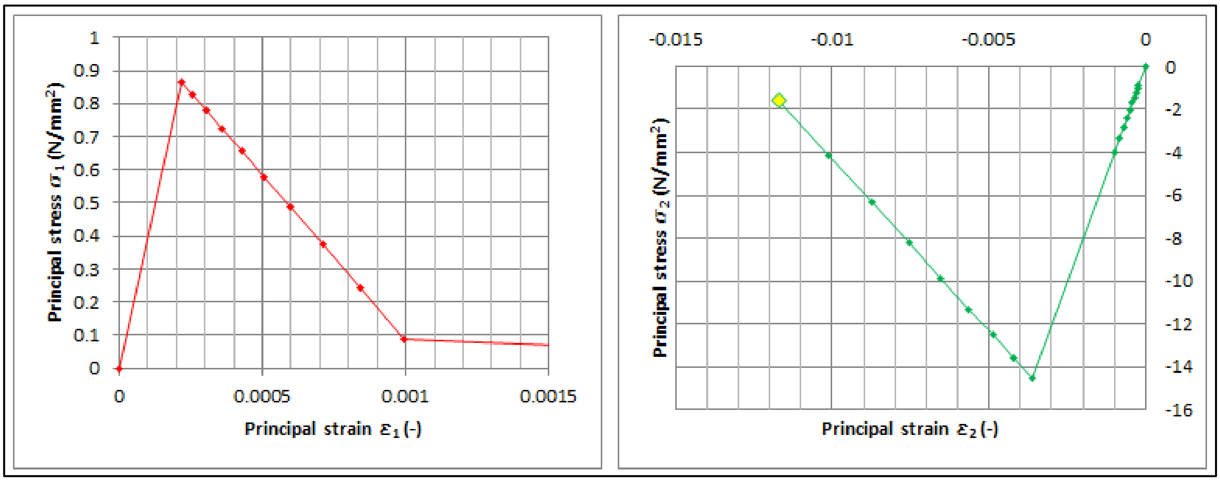

Figure A.13: Graphical results of the tension-compression test.

Table A.3: Tabular results of the tension-compression test.

Input tension		Input compression	
ε_i (10^{-4})	$f_{t,i}^{+}$ (N/mm^2)	ε_i (10^{-4})	$f_{t,i}^{+}$ (N/mm^2)
2,17	0,867		
2,57	0,827		
3,04	0,780		
3,60	0,724		
4,27	0,658		
5,05	0,579		
5,99	0,486		
7,09	0,375		
8,40	0,245		
9,94	0,090		
9,94	0,000	-36,2	-14,5
		-42,0	-13,6
		-48,6	-12,5
		-56,3	-11,3
		-65,2	-9,88
		-75,5	-8,23
		-87,4	-6,33
		-101	-4,13
		-117	-1,58
		-117	0,000

	Output				
Step	ε_1 (10^{-4})	σ_1 (N/mm^2)		ε_2 (10^{-4})	σ_2 (N/mm^2)
1	2,17	0.867		-2,17	-0.867
2	2,57	0.827		-2,57	-1.078
3	3,04	0.78		-3,04	-1.325
4	3,60	0.724		-3,60	-1.619
5	4,27	0.658		-4,27	-1.971
6	5,05	0.579		-5,05	-2.38
7	5,99	0.486		-5,99	-2.873
8	7,09	0.375		-7,09	-3.451
9	8,40	0.245		-8,40	-4.139
10	9,94	0.09		-9,94	-4.947
11	36,20	0		-36,20	-14.5
12	42,00	0		-42,00	-13.6
13	48,60	0		-48,60	-12.5
14	56,30	0		-56,30	-11.3
15	65,20	0		-65,20	-9.88
16	75,50	0		-75,50	-8.23
17	87,40	0		-87,40	-6.33
18	101,00	0		-101,00	-4.13
19	117,00	0		-117,00	-1.58
20	-	-		-	-

A.1.4. Shear

Shear should result in only γ_{xy}, ε_1 and ε_2, while ε_{xx} and ε_{yy} are not present in the element. The model, displacements and stress state of the shear test is shown in figure A.14. Results are found in figure A.15.

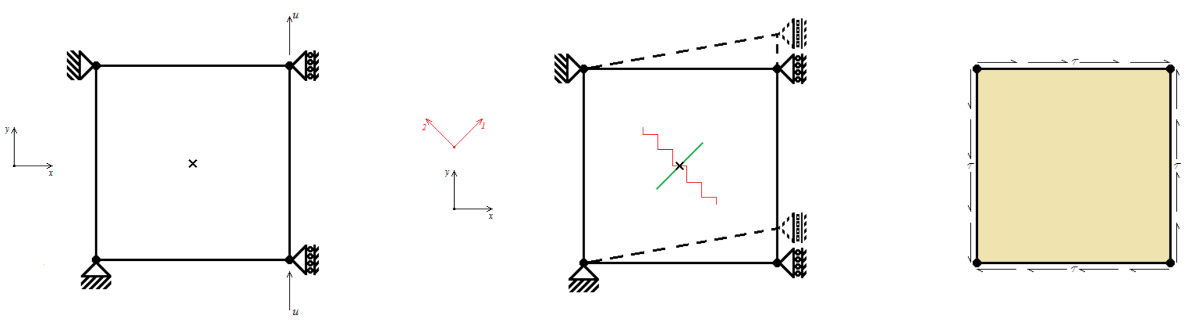

Figure A.14: Model, displacements and stress state of the shear test.

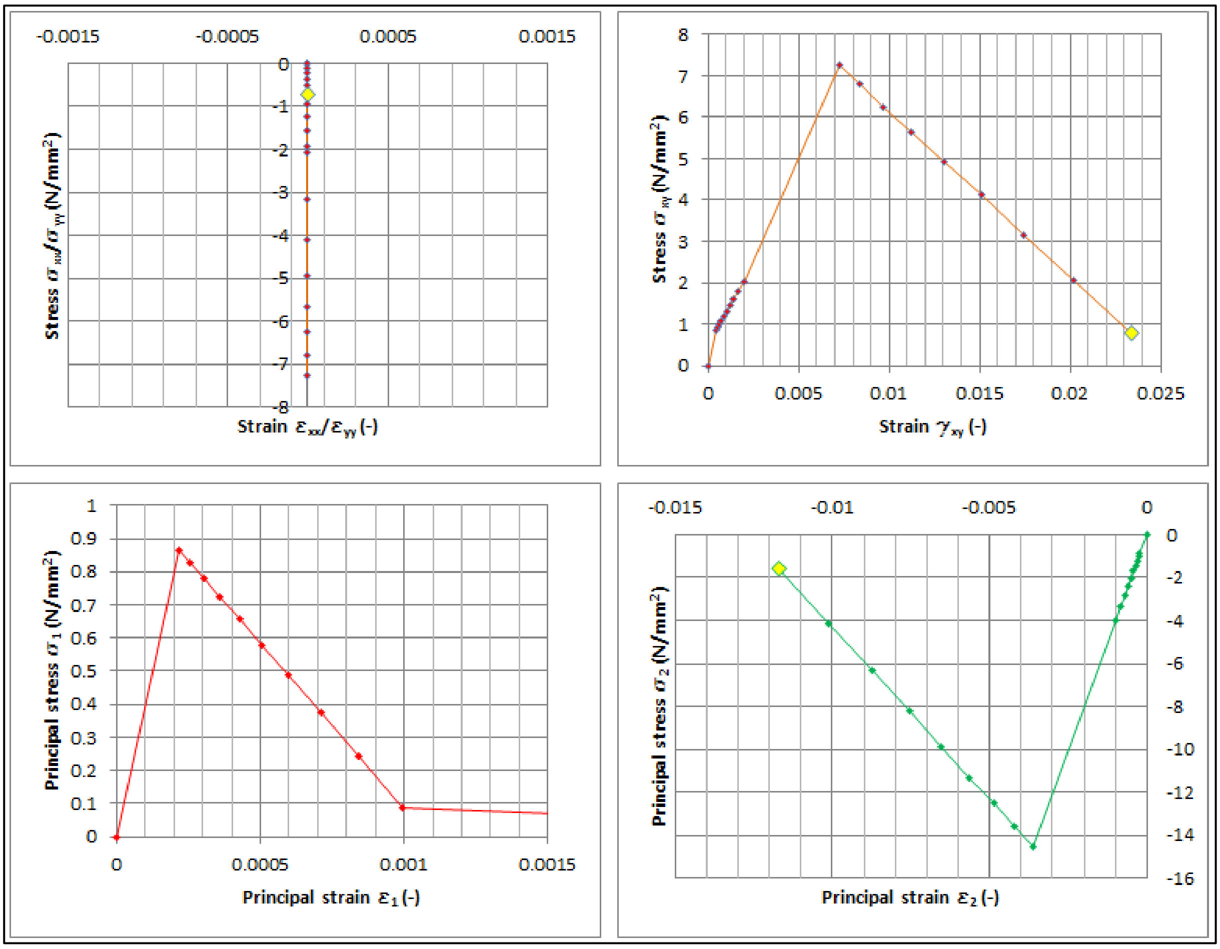

Figure A.15: Graphical results of the shear test.

What can be concluded is that the shear and principal strains are indeed the only strains present over the whole computation. However, after the first step the local stresses σ_{xx} and σ_{yy} are showing up, without their strain counterparts being present at all. Below the stresses are plotted for a few key steps using the circle of Mohr in figure A.16.

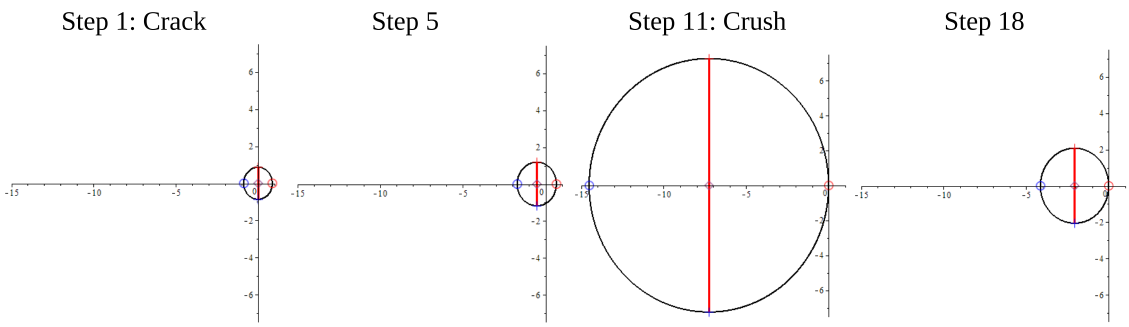

Figure A.16: Circle of Mohr for stresses for some key steps.

When the element still behaves linearly, the following isotropic constitutive law is used:

$$\begin{bmatrix} \sigma_{xx} \\ \sigma_{yy} \\ \sigma_{xy} \end{bmatrix} = \frac{E_0}{1-\nu_0^2} \begin{bmatrix} 1 & \nu_0 & 0 \\ \nu_0 & 1 & 0 \\ 0 & 0 & \frac{1-\nu_0}{2} \end{bmatrix} \begin{bmatrix} \varepsilon_{xx} \\ \varepsilon_{yy} \\ \gamma_{xy} \end{bmatrix} \tag{A.1}$$

However, when the element is cracked, the switch is made to the following orthotropic relationship:

$$\begin{bmatrix}\sigma_{nn}\\ \sigma_{tt}\\ \sigma_{nt}\end{bmatrix} = \begin{bmatrix}\dfrac{E_n}{1-\nu_{nt}\nu_{tn}} & \dfrac{\nu_{nt}E_n}{1-\nu_{nt}\nu_{tn}} & 0\\ \dfrac{\nu_{tn}E_t}{1-\nu_{nt}\nu_{tn}} & 1\dfrac{E_t}{1-\nu_{nt}\nu_{tn}} & 0\\ 0 & 0 & G_{red}\end{bmatrix}\begin{bmatrix}\varepsilon_{nn}\\ \varepsilon_{tt}\\ \gamma_{nt}\end{bmatrix} \tag{A.2}$$

Normally, the principal directions are determined using a transformation matrix. The stresses in the global directions can thus be determined using the inverse of the transformation matrix. Applying the theory results in the stresses σ_{xx}, σ_{yy} and σ_{xy} as presented as output.

The strains are calculated as the difference between the relative displacement and the total length of the element. In the global directions only relative displacements in the shear directions were possible, so the strains ε_{xx} and ε_{yy} remain zero throughout the analysis.

This is the reason why there are stresses in *x*- and *y*-direction, while there are no strains. This is post-peak behaviour only. The Mohr-circle of the global strains does expand and shrinks as expected, while the stresses are a product of the transformation of the stresses, which make their Mohr-circle shift. The procedure applied is shown below. So the law "$\sigma = E \cdot \varepsilon$" only holds in the normal and tangential directions, which in this case are σ_1 and σ_2, for a fixed model is used.

$$\begin{bmatrix}u_x\\ u_y\end{bmatrix} \xrightarrow[\textit{Kinematic}]{} \begin{bmatrix}\varepsilon_{xx}\\ \varepsilon_{yy}\\ \gamma_{xy}\end{bmatrix} \xrightarrow[T]{} \begin{bmatrix}\varepsilon_1\\ \varepsilon_2\end{bmatrix} \xrightarrow[\textit{Constitutive}]{} \begin{bmatrix}\sigma_1\\ \sigma_2\end{bmatrix} \xrightarrow[T]{} \begin{bmatrix}\sigma_{xx}\\ \sigma_{yy}\\ \sigma_{xy}\end{bmatrix} \xrightarrow[\textit{Equilibrium}]{} \begin{bmatrix}F_x\\ F_y\end{bmatrix}$$

Figure A.17: Transformation procedure.

A.1.5. Shear-tension

This gives no further unexpected results. Before the first step no vertical stresses are to be expected, for the material is still undamaged and behaves linear elastically, but they are after present after crack initiation. Below is given as usual the model, but also the received results for the last step, the expected results for that same step (which are the same) and the overall results in graphs.

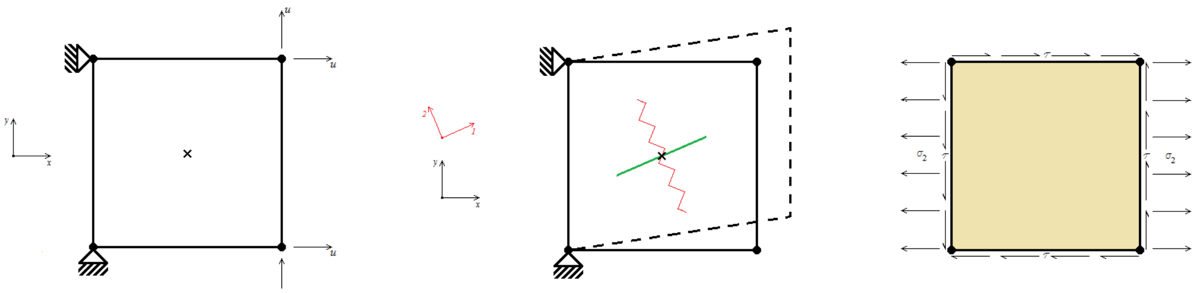

Figure A.18: Model, displacements and stress state of the shear-tension test.

For one step the obtained results are verified by hand calculations. The results of this step is shown in figure A.19 and are obtained from the output file returned by the calculation. The hand calculation is done using Maple and is presented in figure A.20. The hand calculation coincides with the results given by the numerical analysis, which means no further delving is necessary. The results of the computation is presented graphically in figure A.21, including all steps.

```
young:          1.006E-03  1.350E+02
DAMIND:         10         -8
SCLFAC=         1.412E+00

Elmnr  Intpt      EXX        EYY        EZZ        GXY        GYZ        GZX
    1      1   5.649E-02  0.000E+00  0.000E+00  5.649E-02  0.000E+00  0.000E+00

Elmnr  Intpt       E1         E2         E3
    1      1   6.819E-02 -1.170E-02  0.000E+00

Elmnr  Intpt       S1         S2         S3
    1      1   6.860E-05 -1.580E+00  0.000E+00

Elmnr  Intpt      SXX        SYY        SZZ        SXY        SYZ        SZX
    1      1  -2.313E-01 -1.349E+00  0.000E+00  5.586E-01  0.000E+00  0.000E+00
```

Figure A.19: Results for a single step of the shear-tension test.

$> \varepsilon_{xx} := 5.649 \cdot 10^{-2};\ \varepsilon_{yy} := 0;\ \gamma_{xy} := 5.649 \cdot 10^{-2};\ \theta := 0.3926990817:$

$$\varepsilon_{xx} := 0.05649000000$$
$$\varepsilon_{yy} := 0$$
$$\gamma_{xy} := 0.05649000000 \qquad (1)$$

$> T := \begin{bmatrix} \cos^2(\theta) & \sin^2(\theta) & \sin(\theta)\cdot\cos(\theta) \\ \sin^2(\theta) & \cos^2(\theta) & -\sin(\theta)\cdot\cos(\theta) \\ -2\cdot\sin(\theta)\cdot\cos(\theta) & 2\cdot\sin(\theta)\cdot\cos(\theta) & \cos^2(\theta)-\sin^2(\theta) \end{bmatrix} : \varepsilon[g] := \begin{bmatrix} \varepsilon_{xx} \\ \varepsilon_{yy} \\ \gamma_{xy} \end{bmatrix}:$

$> \varepsilon[p] := T \cdot \varepsilon[g];$

$$\varepsilon_p := \begin{bmatrix} 0.06818946206 \\ -0.01169946206 \\ 0. \end{bmatrix} \qquad (2)$$

$> E[t] := 1.35 \cdot 10^2 : E[n] := 0 : \sigma_1 := E[n]\cdot\varepsilon[p](1);\ \sigma_2 := E[t]\cdot\varepsilon[p](2);$

$$\sigma_1 := 0.$$
$$\sigma_2 := -1.579427378 \qquad (3)$$

$> T := inverse\left(\begin{bmatrix} \cos^2(\theta) & \sin^2(\theta) & 2\cdot\sin(\theta)\cdot\cos(\theta) \\ \sin^2(\theta) & \cos^2(\theta) & -2\cdot\sin(\theta)\cdot\cos(\theta) \\ -\sin(\theta)\cdot\cos(\theta) & \sin(\theta)\cdot\cos(\theta) & \cos^2(\theta)-\sin^2(\theta) \end{bmatrix}\right) : \sigma[p] := \begin{bmatrix} \sigma_1 \\ \sigma_2 \\ 0 \end{bmatrix}:$

$> \sigma[g] := T \cdot \sigma[p];$

$$\sigma_g := \begin{bmatrix} -0.231301784300000 \\ -1.34812559400000 \\ 0.558411904700000 \end{bmatrix} \qquad (4)$$

Figure A.20: Hand calculation performed to verify the results obtained in A.19.

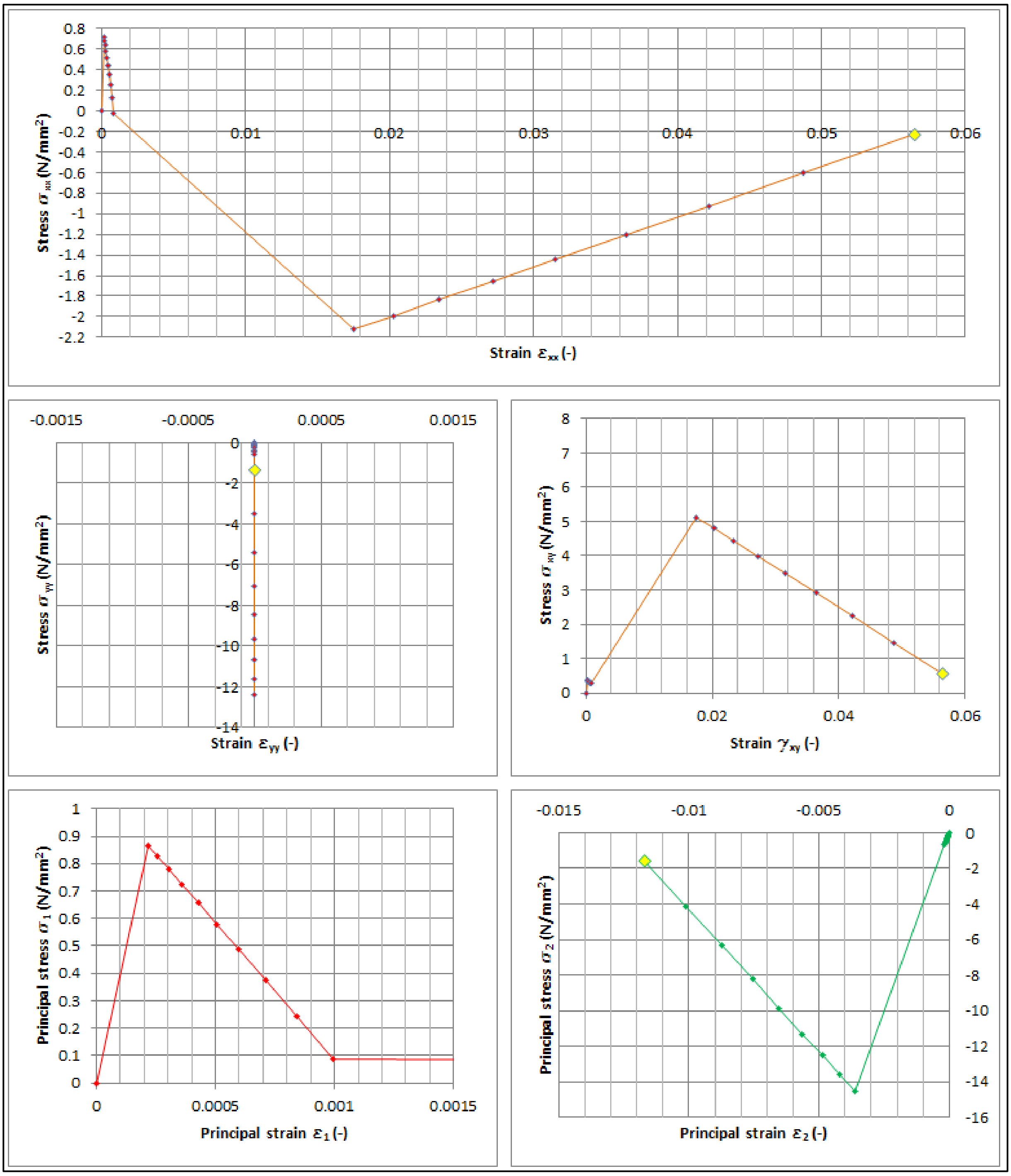

Figure A.21: Graphical results of the shear-tension test.

A.1.6. Shear-tension-compression

The element is subjected to all loading configurations. The same theory as in A.1.5 can be applied to obtain the results. The strains are a result of relative displacements and total length of the element, resulting in $\varepsilon_{xx} = \varepsilon_{yy} = \gamma_{xy}$ and $\varepsilon_1 = \varepsilon_2$. Results are shown below, but no further peculiarities seem to occur. Input and output is shown in figure A.22 and A.23.

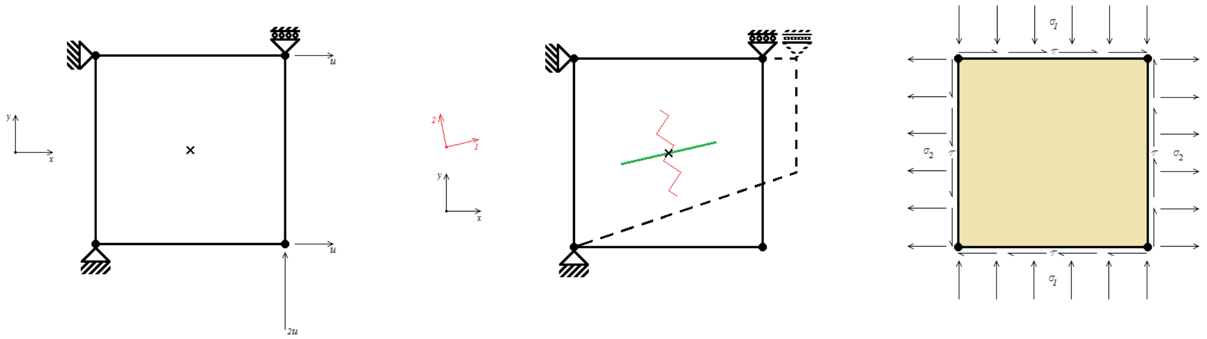

Figure A.22: Model, displacements and stress state of the shear-tension-compression test.

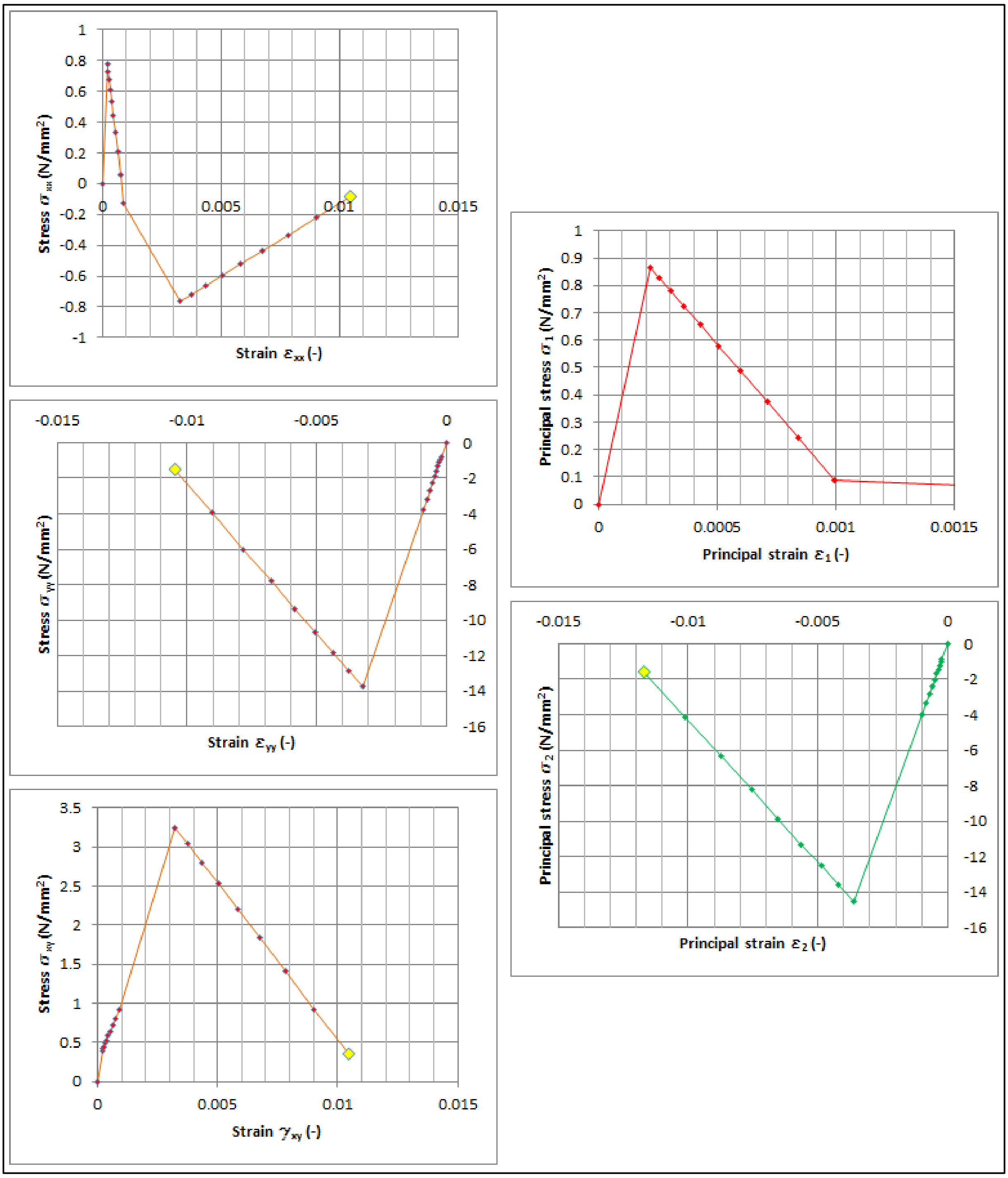

Figure A.23: Graphical results of the shear-tension-compression test.

A.2. Rotated axes

In the basic tests the local axes of the element and the global axes coincided. Here a look will be taken into the situation where this is not the case. The local axes can be changed in two different ways. The first options is to rotate the element as a whole and to put it under an angle of α degrees. The second options is overriding the local axes with a newly defined axes.

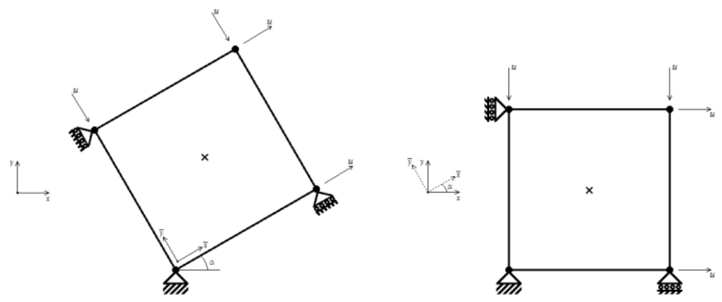

Figure A.24: Rotated element (left) and rotated local axes (right).

The test should give insight into the way results, like stresses, are transformed from one coordinate system to another coordinate system. In this test both ways of coordinate rotation, figure A.24, result in correct transformation of the stresses. The output is checked and transformed with hand calculations concluding that the transformation procedures are correctly implemented in the code.

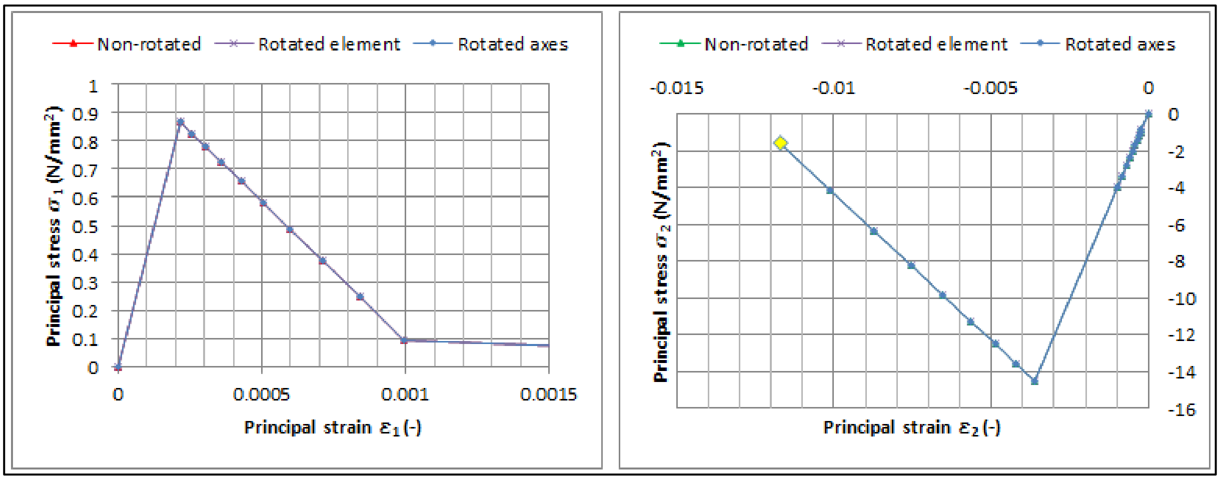

Figure A.25: Graphical results of the rotation test concerning principal directions.

In figure A.25 three lines are plotted while only one graph is visible in both the left and right diagram. All the graphs overlap each other, meaning that all return the same principal stresses. It does not matter if the axes or the element are rotated, because the results for the principal directions always will be the same. The principal directions are independent from the other axes.

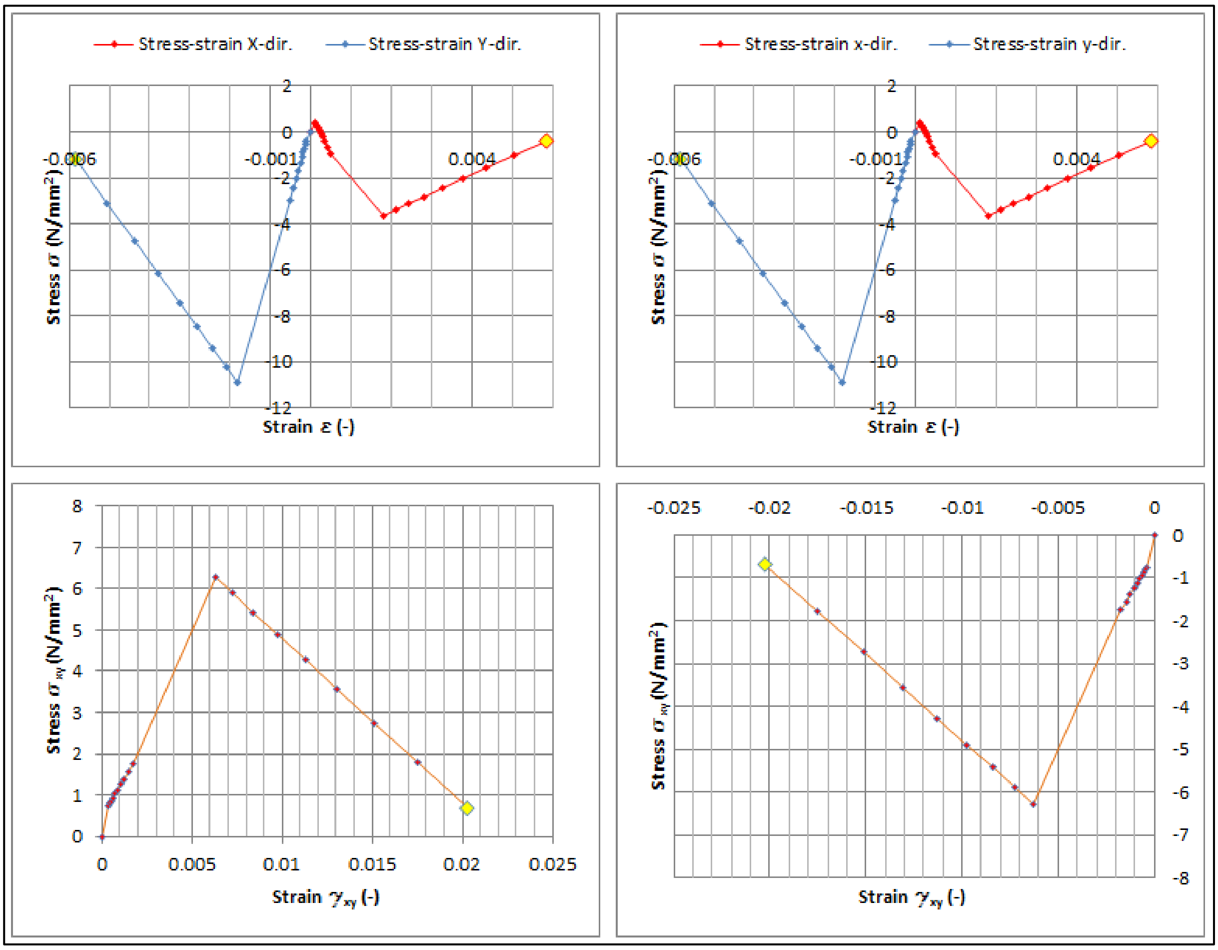

Figure A.26: Graphical results of the rotation test concerning non-principal directions with results for the rotated element (left) and results for the rotated local axes (right).

The stresses in global directions for the model with the rotated element are the same as the stresses in local directions for the model with the rotated axes. Both directions are under the same angle with respect to the principal directions. Vice versa, the directions are in the same direction as the principal directions and will yield the same results as the principal directions. The shear behaviour of both models in absolute value are the same. This is presented in figure A.26.

A.3. Multiple integration points

The same linear element can contain multiple integration points. This returns still the input as the output. The displacement is described linearly in *x*- and *y*-direction, therefore all the cracks must be in the same directions and afterwards all the integration points are crushed orthogonally to the crack direction. As will be seen in the next section, this linear description of the displacement field is important for the results to return correct output.

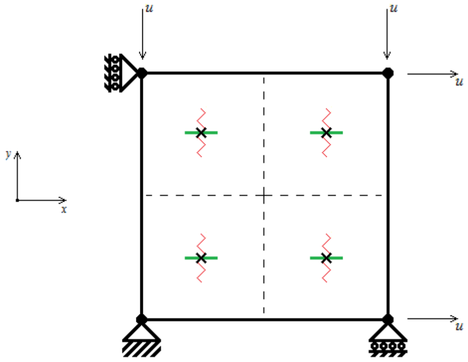

Figure A.27: Model for the multiple integration points test.

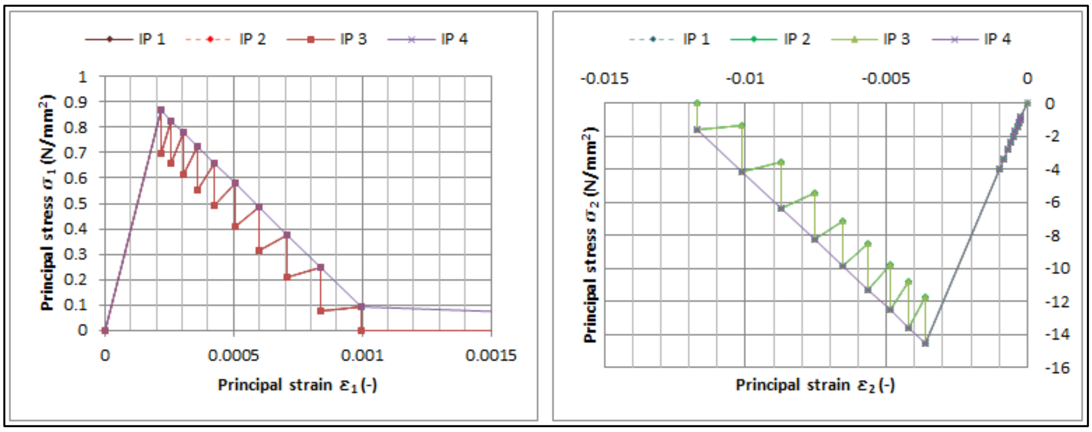

Figure A.28: Graphical results of the multiple integration points test.

All integration points follow the ripple diagram. If another integration point is currently the critical integration point, then the other points will be scaled with regards to the critical integration point and are found on their specific Secant branch. This causes visually the characteristic ripple behaviour of SLA.

A.4. Quadratic element.

A quadratic element will be subjected to both a tension and compression loading. This will result in cracking in the one direction and crushing in the other direction of the material. As shown in figure A.29 the element used has four integration points, like the linear element from section A.3.

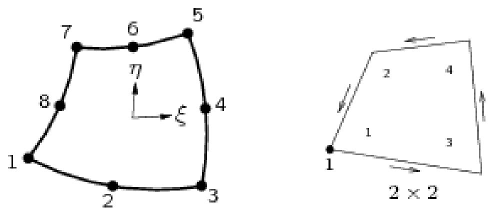

Figure A.29: Element CQ16M and the used integration scheme.

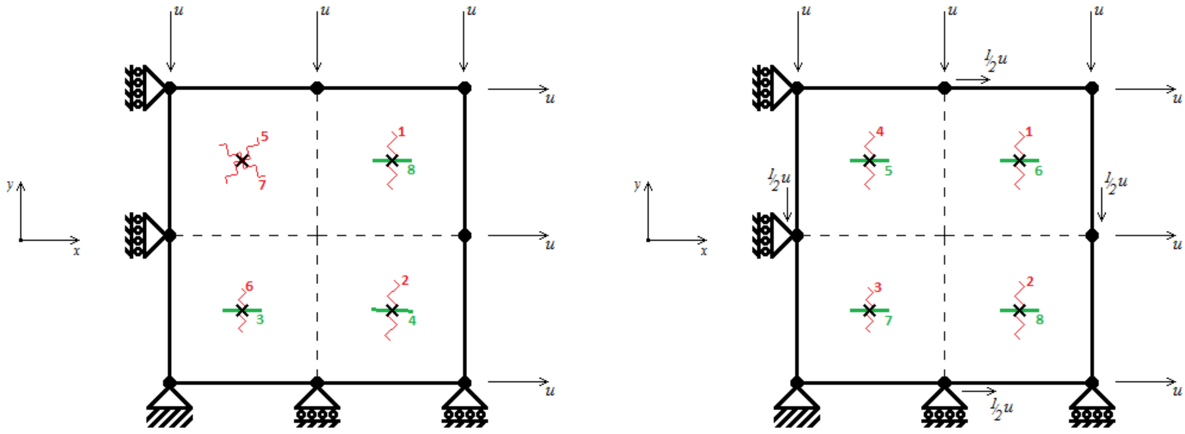

Figure A.30: Model for the quadratic element test with not all boundaries containing prescribed displacements (left) and all boundaries containing prescribed displacements (right).

In the left figure not all degrees of freedom are described with imposed deformations, while in the right figure this is the case. The correct results were retrieved with the right figure, for the centre nodes of the bottom and left side were not equally displaced as the centre nodes from the top and right side respectively. Thus $u_{x,2} \neq u_{x,6} \neq ½\cdot u_{x,3}$. Due to the loose behaviour of the nodes, unwanted results are obtained, as shown in figure 3.32. Particularly strange are integration point 1 and 2.

The displacement field for quadratic elements is not linear anymore, but quadratic. This means that indeed $u_{x,2} \neq u_{x,6} \neq ½·u_{x,3}$ can be possible, resulting in the undesired results. However, nonlinear analysis also uses quadratic elements and the question arises if the same situation arises with that computational method.

The left model is thus also used in NLFEA to see if the same happens in this analysis type or if it is a strange phenomenon of the SLA. It does not happen in the nonlinear analysis and it assumes $u_{x,2} = u_{x,6} = ½·u_{x,3}$. These results are due to the traits of both analysis types.

As stated in section 2, nonlinear analysis shows the crack apparition spontaneous and simultaneous. So integration point 3 and 4 both reach their maximum tensile strength at the same time and this means they crack at the same time. This simultaneous cracking makes sure the computation goes symmetric.

In the SLA, however, only one integration point is allowed to crack in every step. This is the critical integration point and will be the only integration point that will crack. Now the problem is not symmetric anymore, for integration point 4 is cracked, while 3 is not. In the next step integration point 3 is cracked, but the crack direction is under a slight angle to comply with the already cracked integration point 4. This changing from a symmetric to a asymmetric problem is the reason different results are obtained in SLA as shown in figure A.31.

Although the results were undesired in the model where not all the nodes had a prescribed displacement, it was the correct response. The results from the nonlinear analysis were desired, but were actually bifurcated results. The symmetry is forced by prescribing the middle nodes with displacements too and the results can also be found for each integration point in figure A.31. The difference between the nonlinear analysis and the sequentially linear analysis is found in figure A.32.

Yet another side-note has to be made. Although it might not be clearly visible, but the principal stresses of the left model slightly exceeds the maximum allowable stress f_{ti}^{+}. The crack is fixed and the f_{ti}^{+} is compared with the stress normal to the crack $\sigma_{k,nn}$ and not σ_1. However, the principal directions are allowed to rotate. This means that there will be shear in the crack $\sigma_{k,nt}$ which will result in a higher principal stress being present in the structure than theoretically is allowed, as can be shown with the circle of Mohr. This is a limitation of the fixed crack model. This is portrayed in figure A. 33.

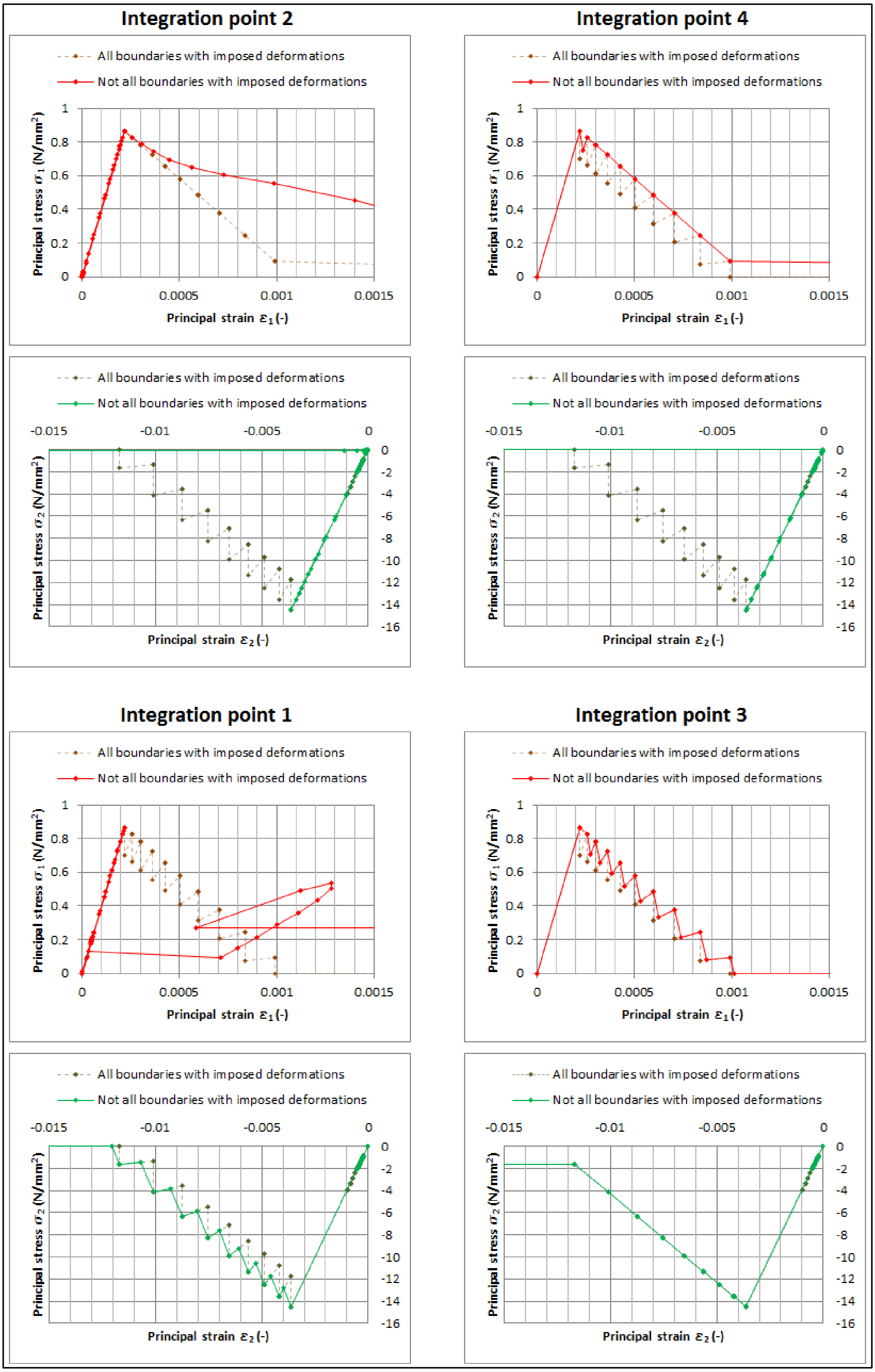

Figure A.31: Graphical results of the quadratic element test.

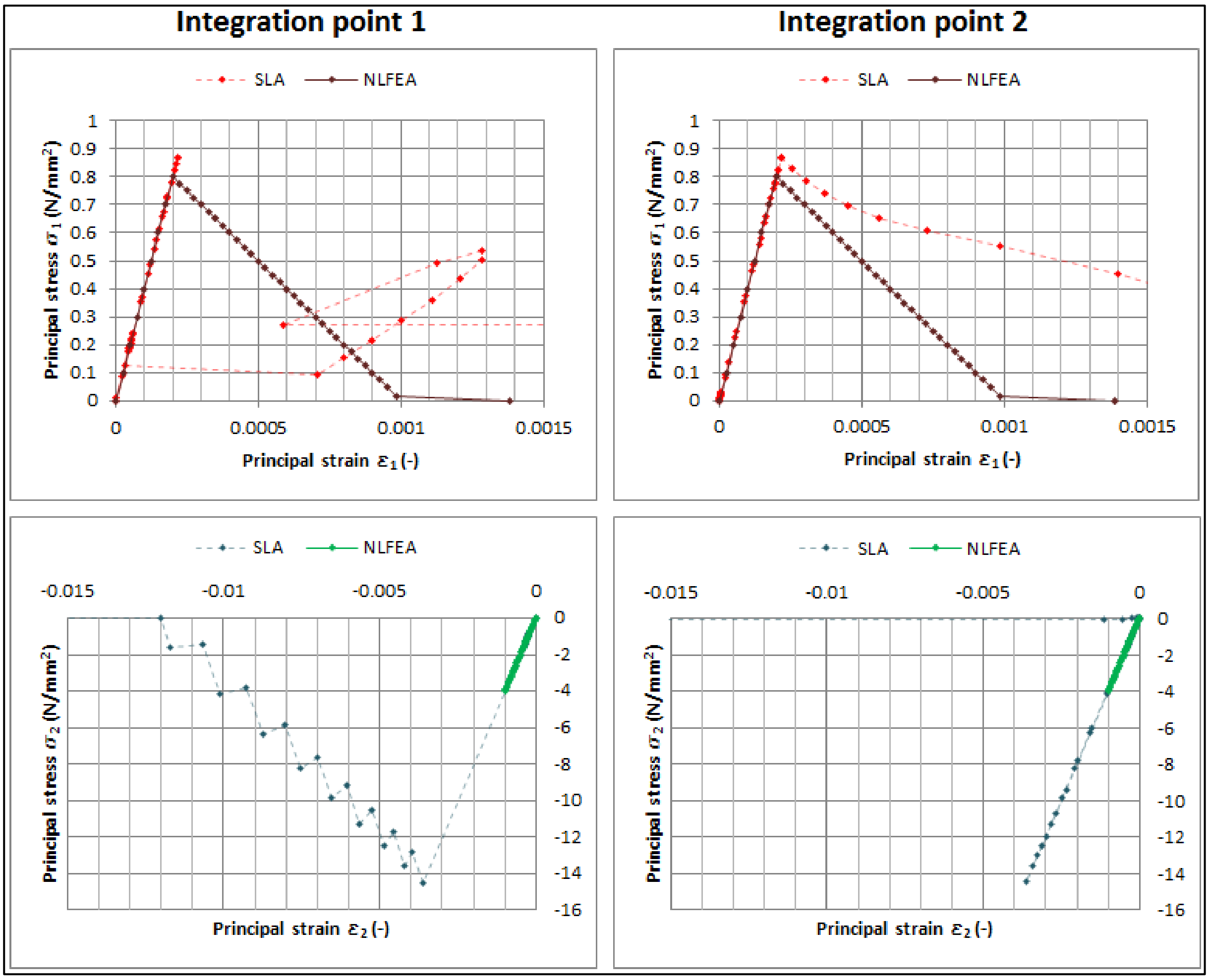

Figure A.32: Comparison NLFEA and SLA with not all boundaries containing prescribed displacements.

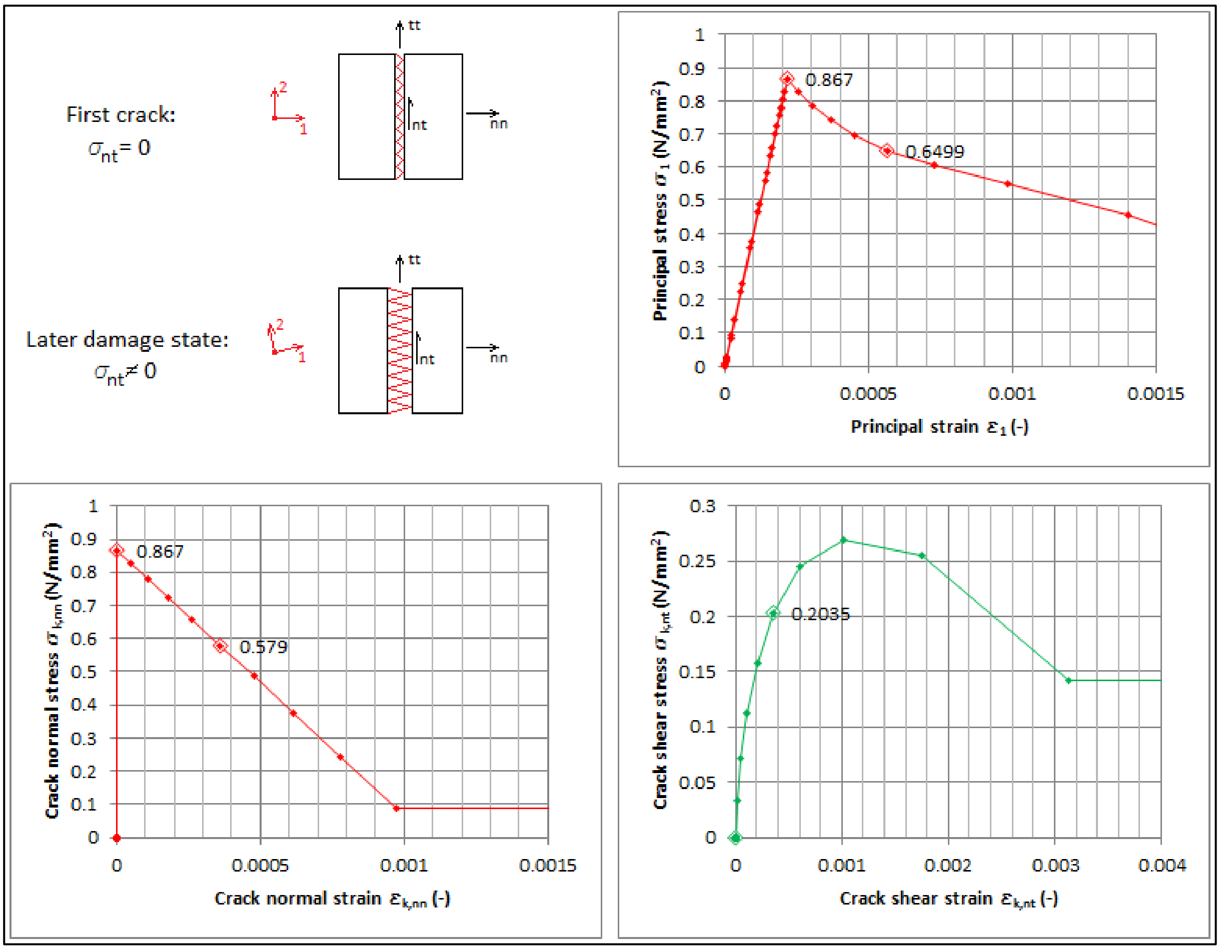

Figure A.33: Explanation of the exceeding of the maximum material strength in an integration point.

A.5. Influence of Poisson's ratio.

The same linear element will now be subjected to tension and compression. The same tension softening and compression softening is used, but now a Poisson's ratio of v = 0.2 is added to the material properties of the element. Before, the ripple diagram implemented was retrieved in the output results. Now these results, with respect to the strains, are larger. The situation is presented in figure A.34, while tabular and graphical results are presented in table A.4 and figure A.35 respectively.

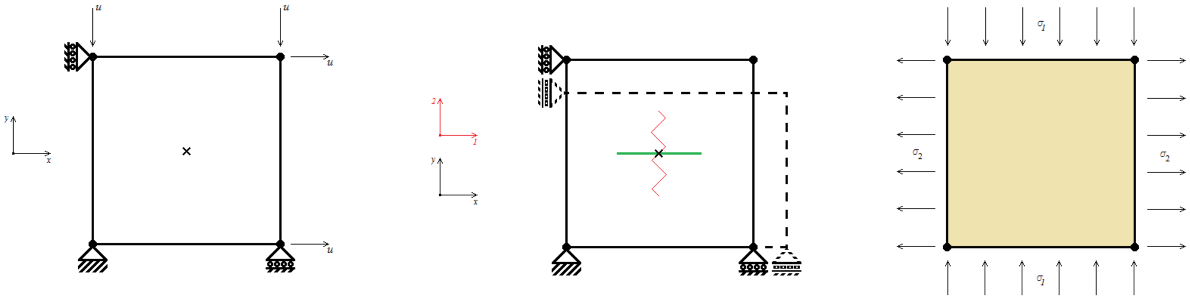

Figure A.34: Model, displacements and stress state of the test with v = 0,2.

Table A.4: Tabular results of the tension-compression test with v = 0,2.

Input tension		**Input compression**	
ε_i (10^{-4})	$f_{t,i}^{+}$ (N/mm^2)	ε_i (10^{-4})	$f_{t,i}^{+}$ (N/mm^2)
2,17	0,867		
2,57	0,827		
3,04	0,780		
3,60	0,724		
4,27	0,658		
5,05	0,579		
5,99	0,486		
7,09	0,375		
8,40	0,245		
9,94	0,090		
9,94	0,000	-36,2	-14,5
		-42,0	-13,6
		-48,6	-12,5
		-56,3	-11,3
		-65,2	-9,88
		-75,5	-8,23
		-87,4	-6,33
		-101	-4,13
		-117	-1,58
		-117	0,000

	Output				
Step	ε_1 (10^{-4})	σ_1 (N/mm^2)		ε_2 (10^{-4})	σ_2 (N/mm^2)
1	2,60	0.867		-2,60	-0.867
2	3,11	0.827		-3,11	-1.078
3	3,70	0.78		-3,70	-1.325
4	4,41	0.724		-4,41	-1.619
5	5,26	0.658		-5,26	-1.971
6	6,24	0.579		-6,24	-2.38
7	7,43	0.486		-7,43	-2.873
8	8,82	0.375		-8,82	-3.451
9	10,47	0.245		-10,47	-4.139
10	12,41	0.09		-12,41	-4.947
11	36,25	0		-36,25	-14.5
12	42,00	0		-42,00	-13.6
13	48,60	0		-48,60	-12.5
14	56,30	0		-56,30	-11.3
15	65,20	0		-65,20	-9.88
16	75,50	0		-75,50	-8.23
17	87,40	0		-87,40	-6.33
18	101,00	0		-101,00	-4.13
19	117,00	0		-117,00	-1.58
20	-	-		-	-

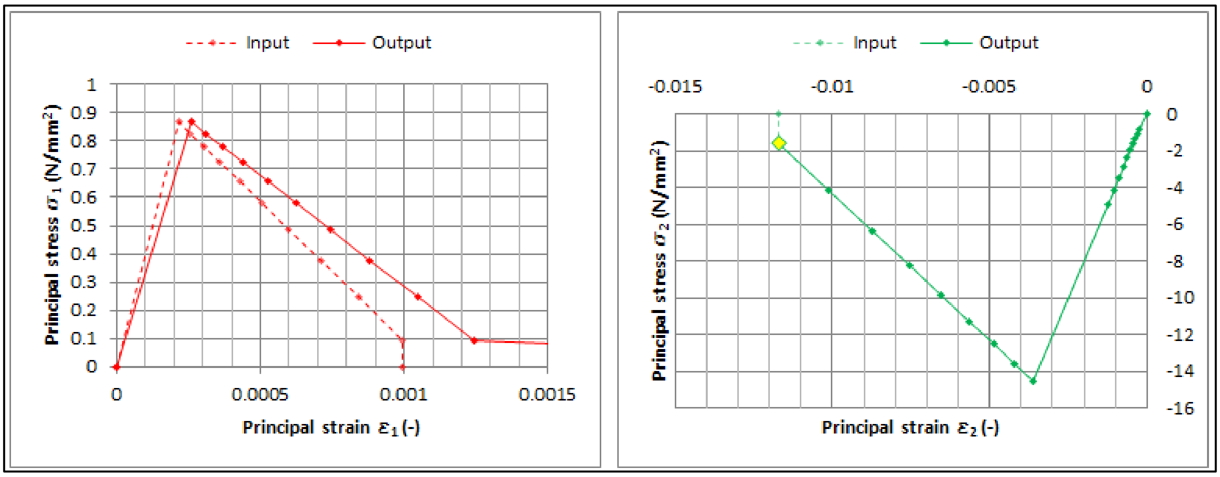

Figure A.35: Graphical results of the influence of Poisson's ratio.

The stresses are returned exactly the same, but the tensile strains are not equal to the strains of the ripple diagram implemented. This is due Poisson's ratio. When the stresses are implemented in the orthotropic constitutive law the strains received are indeed larger than the strains implemented. When $\nu = 0$, then the strains returned are equal to the strains implemented, because the constitutive matrix is decoupled. When the material is fully cracked, the interaction between the two orthogonal directions is completely reduced to zero. The tensile stresses are not present anymore in the first principle direction, for it failed. This reduces the constitutive matrix to a 2×2-matrix, for the first column and row can be removed from the system. Poisson's ratio has then no further effect for the second principal direction, as can be seen in the results. The compressive strains are the same as the strains implemented.

Poisson's ratio seemingly effects the origin of the secant branch obtained from the output, meaning they do not cross the origin anymore. This is clearly visible in a double compression test as shown in figure A.36 and A.37. The test used a linear softening diagram for compression it was run twice, one with a Poisson's ratio of $\nu = 0{,}0$ and the other with a Poisson's ratio of $\nu = 0{,}2$. The actual Young's Modulus obtained from the results is still the same as the input, but like in figure 8.13, Poisson's ratio constantly shifts the points in the graph a bit more in every step.

This shifting is visible and can be easily shown with the results found in figure A.35. The explanation is presented in figure A.38 presenting one shifted curve. In this figure it is visible that with each step the curve shifts a bit to the right. Only one point of these shifted curves is taken into consideration each step for the formation of the complete curve representing the output. This means that the output is a combination of points from multiple shifted curves, making it look like the Secant branches are different. But each point has still the correct Secant branch in its own shifted curve.

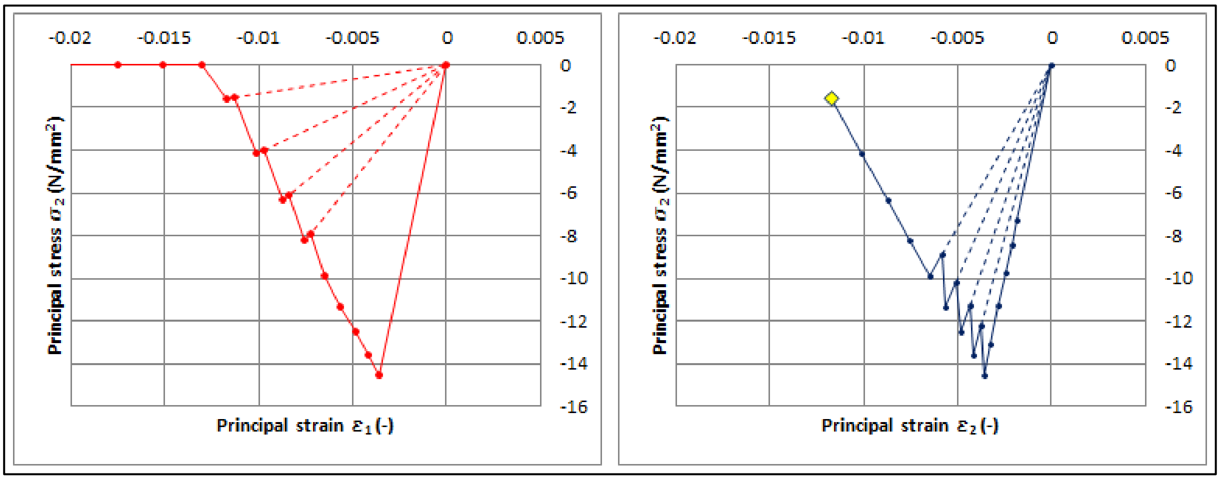

Figure A.36: Results of double compression test with v = 0,0.

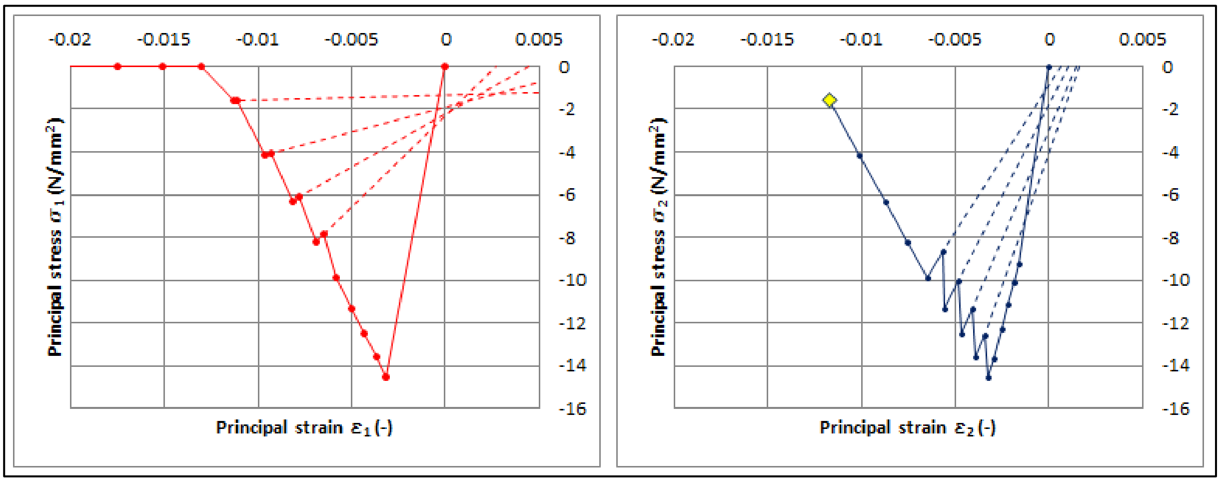

Figure A.37: Results of double compression test with v = 0,2.

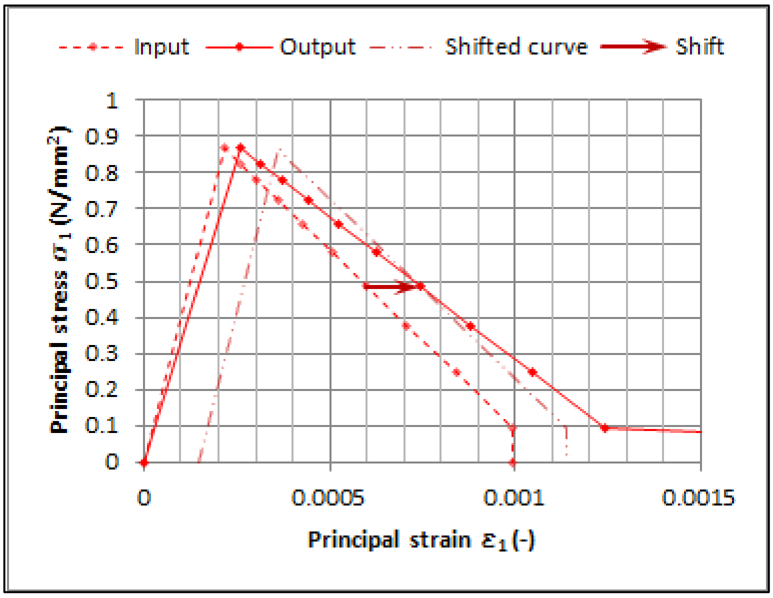

Figure A.38: Constant shifting of the graph.

A.6. Non-proportional loading

Non-proportional loading is a loading scheme recently added in SLA code to represent forces working on the structure which are present, but not dependent on the applied proportional loading. These loads remain the same magnitude throughout the analysis, like self-weight. These loads have to be implemented manually mimicked and replaced by the standard loading at the moment however, for the loading types as self-weight are not available yet in the code.

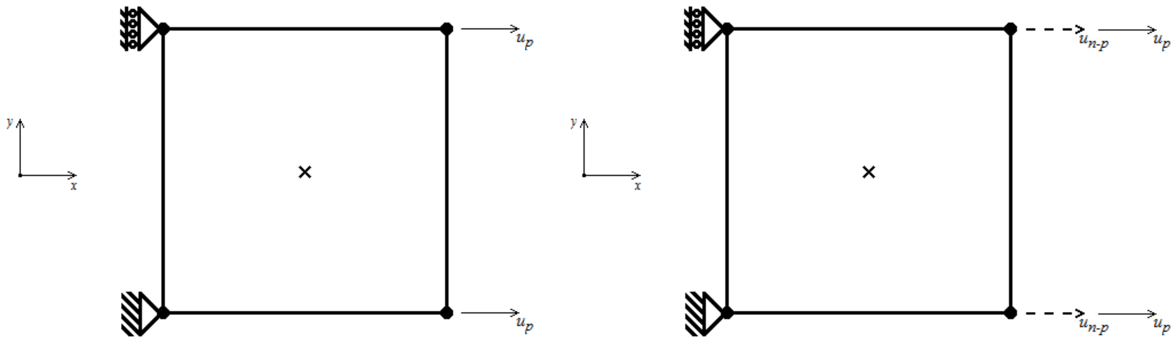

Figure A.39: Proportional loading only (left) and combined proportional and non-proportional loading (right).

A small test has been carried out and pictured in figure A.39 to check if the implementation of non-proportional loading goes well, figure A.40. The results indicate this loading scheme is correctly taken into account. When the non-proportional load does not generate significant stresses causing the integration point to reach its maximum allowable stress in the first Secant branch, then the load is applied in one step. And when the non-proportional load creates bigger stresses than allowed, it will be dealt with proportionally until the full load can be applied. After this the reduced material properties will be taken into the proportional loading phase and the calculation continues until the element is completely damaged.

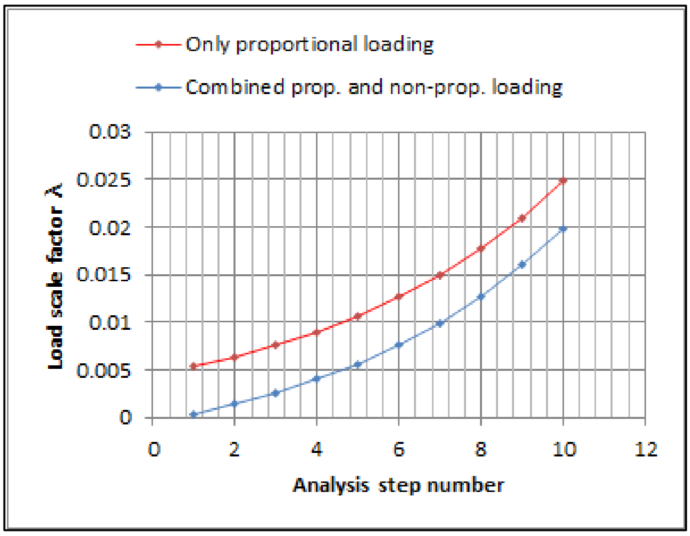

Figure A.40: Graphical results of the non-proportional loading test. The non-proportional load can be fully applied in the first step of the analysis.

However, this combination of loading does not work the same as phased analysis as used in NLFEA. Although two “phases” are used to put on the loading, it is not possible to apply more than those two phases and the two phases are always applied in the same order. The load is either assigned to the proportional (load case 1) or non-proportional load class (all other load cases) and all the loads are applied simultaneously during the active part of their loading class. It is thus not possible to let one direction to be fully proportionally be cracked by proportional loading after having applied a non-proportional load, beforehand another direction is loaded in the same way. The addition of non-proportional loading adds a second phase to the analysis, but must not be confused with phased analysis. It works accordingly, but if multiple phases are used during the experiment, it is also needed to make multiple models.

The non-proportional load (constant) and the proportional load (scaled) in figure A.39 are applied in the same direction, facilitating the same failure. If the proportional load is in reversed direction of the non-proportional load, like in figure A.41, then both versions of the SLA used in this research behave differently. As discussed in Chapter 8, the coupled saw-tooth law formulation continues the damage in reversed direction with the damage history of the first direction, while the decoupled saw-tooth law formulation does not allow reversing of failure in an integration point, making the material behave linear elastically. These results are shown in figure A.42 and it is pointed out both treat this phenomena, crack closure-reopening, incorrectly and it still has to complemented to make it function properly.

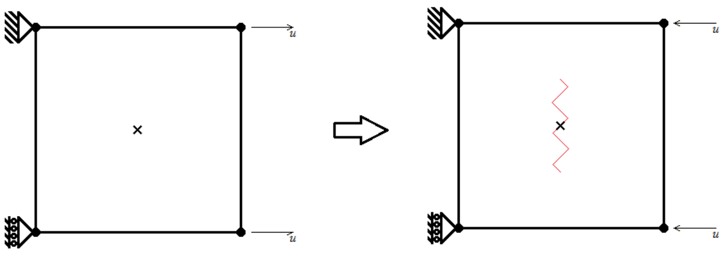

Figure A.41: Setup for verifying the behaviour of switching from cracking behaviour to crushing behaviour.

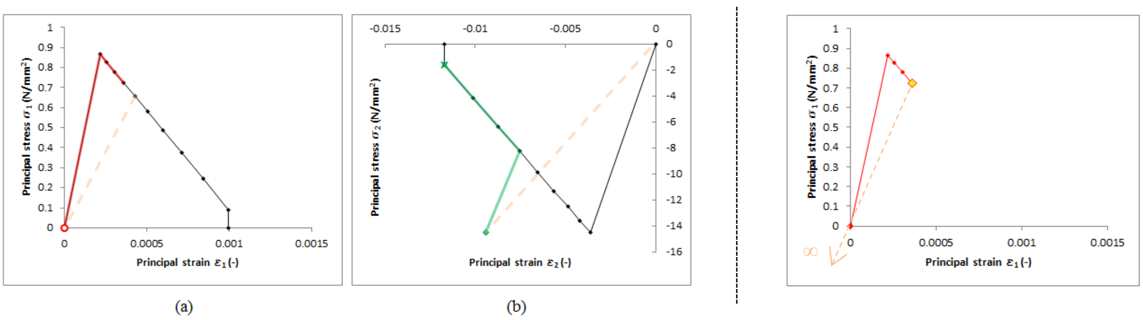

Figure A.42: Cracking until step 4 (a) after which it crushes starting from step 5 (b) for the coupled saw-tooth law formulation (left) and linear elastic behaviour after applying the proportional load in opposite direction for the decoupled saw-tooth law formulation (right).

Appendix B: Mesh study

A suitable mesh has to be chosen to model the structure. Therefore a compact mesh study has been performed to determine an adequate mesh to use for the deep wall-frame study. Several quadratic and linear meshes have been compared with quadrilaterals and has been lain next to a nonlinear finite element analysis counterpart. All meshes have their advantages and disadvantages.

All meshes shown in figure B.1 were tested chronologically as shown below in their order. The only nonlinearity in these meshes is found in the wall. The rectangular plane stress elements contained linear tension softening only, no crushing was applied yet. All other elements behaved linearly. Even the interface elements did not show nonlinear properties.

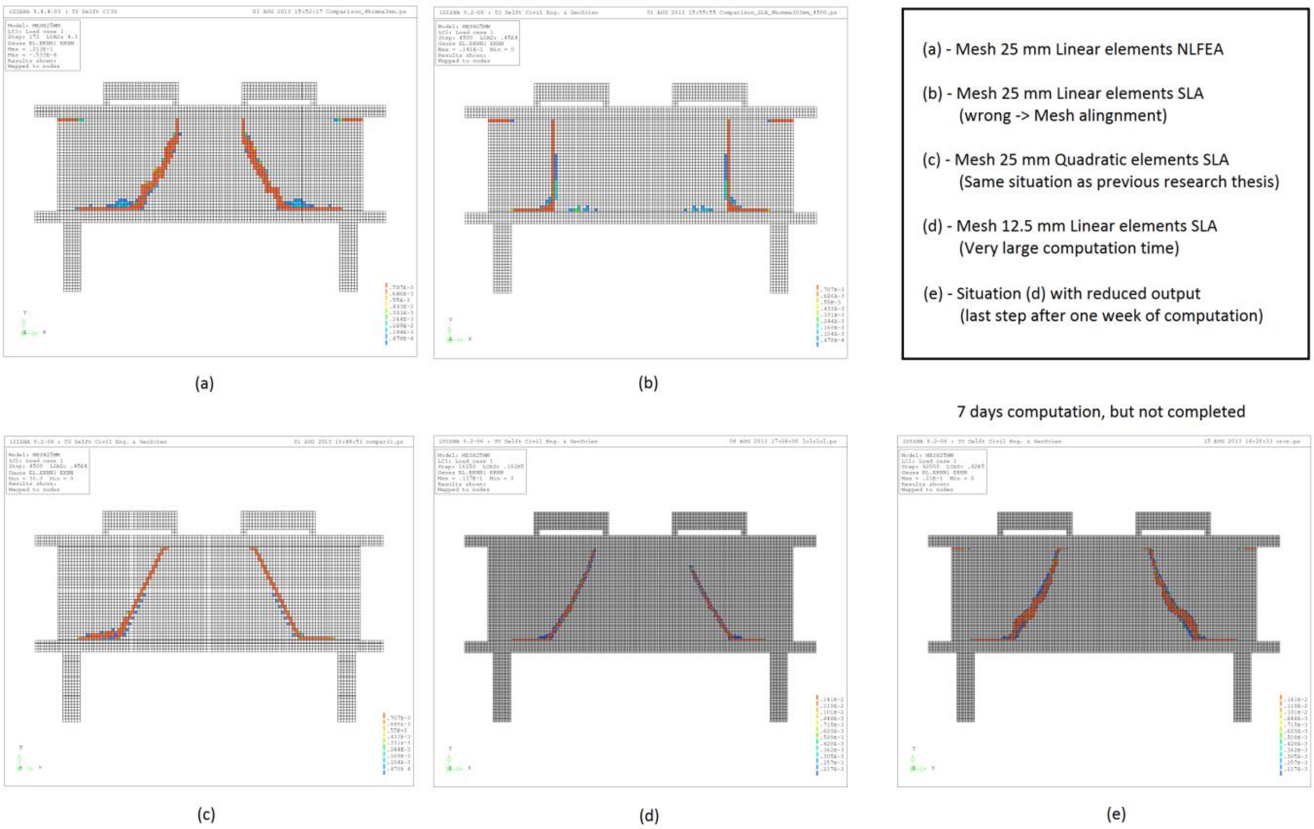

Figure B.1: All tested meshes.

B.1. A NLFEA with a mesh of 25 mm linear elements

For comparison the mesh structure has been modelled first nonlinearly with the same mesh size as can been found in the report of J. Martens [3]. This mesh size is the starting position as it seemed to work good enough for the latter mentioned author. All other sequentially linear meshes have to show equal results to be able to defend their choices.

In figure 2.2 the results are shown of different steps. The beam and wall cannot separate and the crack in the middle will not occur, for the interface element behaves linearly in these calculations. Expected are two diagonal cracks and large compressive strains at the supports. All of these can be seen in figure 2.2, meaning that the NLFEA does not show unexpected results. At the end the structure is supposed to fail due to compression. This is not possible, for the compressive softening is not taken into the calculation. Extreme results are thus obtained ending in divergence and abortion of the numerical process.

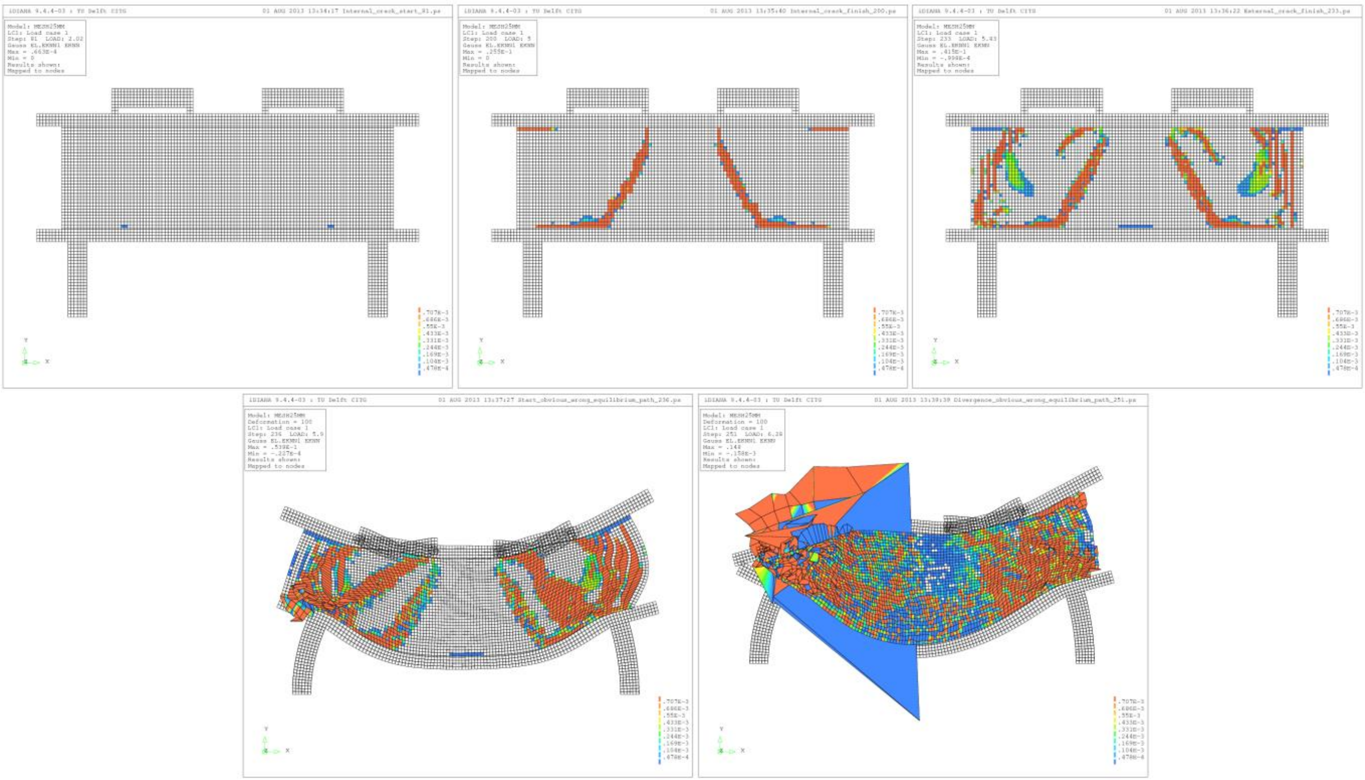

Figure B.2: Results of NLFEA with linear quadrilateral plane stress elements of 25 mm.

B.2. A SLA with a mesh of 25 mm linear elements

Out of appendix A and out of the previous paragraph it can be concluded that it is plausible to use a mesh of linear quadrilateral elements with a mesh division of 25 mm. However, looking at the results, mesh alignment clearly is the reason why the behaviour of the structure is not presented correctly. This mesh cannot be used in further calculations.

It seems the overall behaviour is known, but due to mesh alignment it has difficulties to follow this behaviour. Looking at the left side of the structure, the expected crack is the diagonal band in the centre, while the outer two are ‘failed attempts’ due to mesh alignment. The mesh alignment might be overcome by the use of a randomly generated triangular mesh, as is done in another paper [1] for the combined shear and tension test.

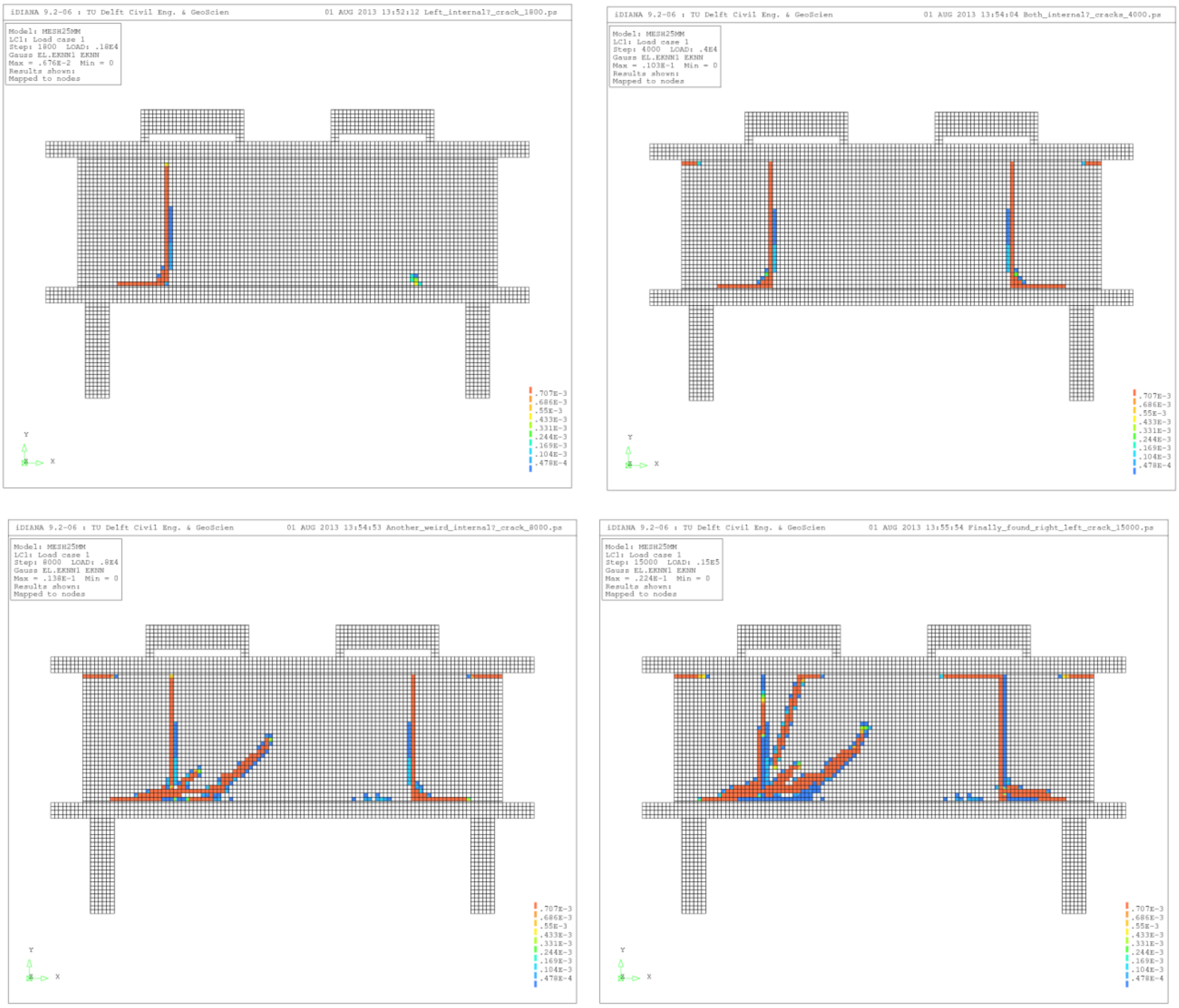

Figure B.3: Results of SLA with linear quadrilateral plane stress elements of 25 mm.

B.3. A SLA with a mesh of 25 mm quadratic elements

A mesh of linear elements did not work fully, therefore a look has been taken into a mesh of quadratic elements. In Chapter 7 quadratic elements have been used with an older version of SLA to show the potential of SLA. A quadratic mesh worked well in that situation and therefore it is taken again into account for the search of an acceptable mesh.

At first sight, the quadratic mesh shows the desired results. The quadratic mesh, however, shows two peculiarities. The first one, visible in figure B.4, is discussed here, while the other one, the premature abortion due to extreme strain localization, can be found in Chapter 8. Looking at the deformed mesh, it seems like SLA shows unstable NLFEA behaviour. This is not true. The “loose” nodes do not have any stiffness surrounding them. The integration points around them are completely damaged. The nodes cannot be hold in place and thus can go anywhere they want numerically. If it were the lattice model, these nodes would have been removed from the mesh. They do not contribute anymore to the behaviour of the structure.

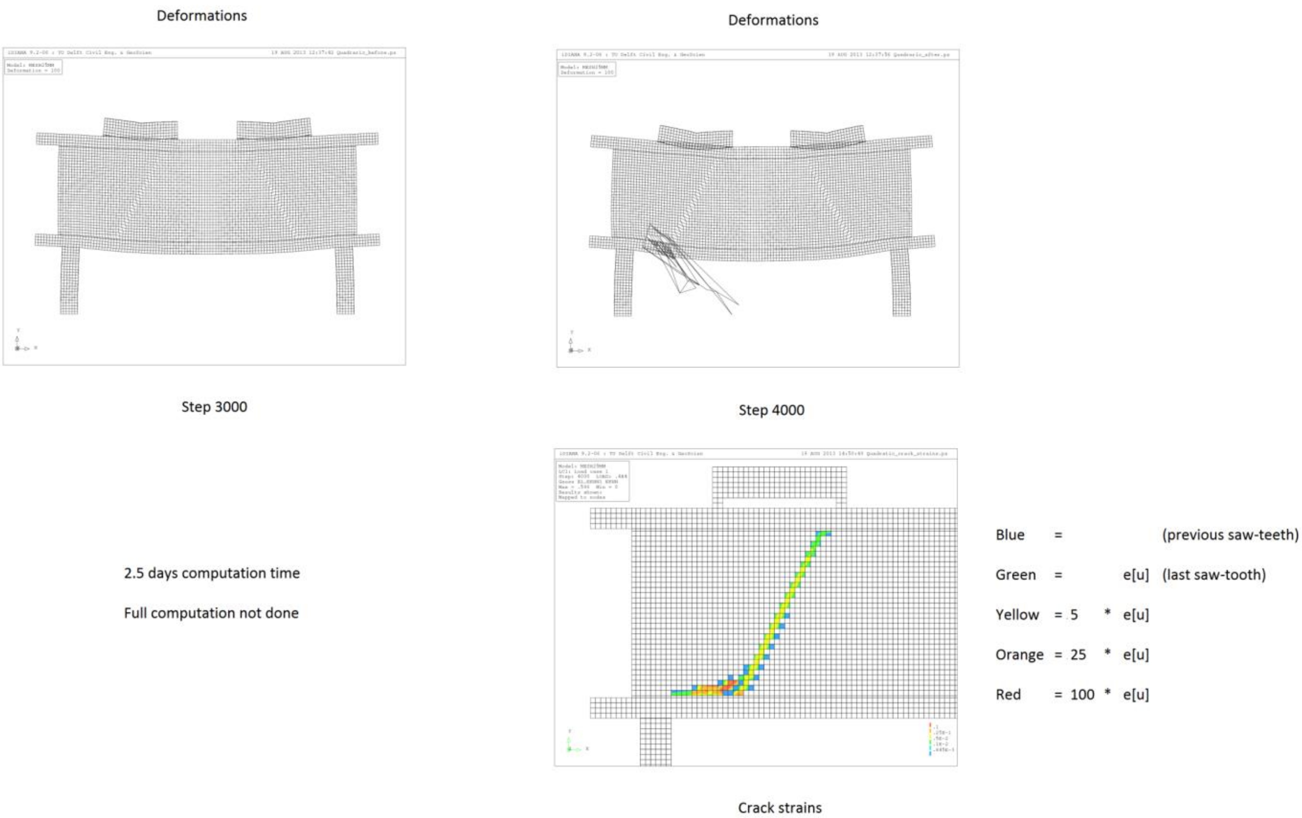

Figure B.4: Results of SLA with quadratic quadrilateral plane stress elements of 25 mm.

B.4. A SLA with a mesh of 12.5 mm linear elements

The quadratic mesh showed desirable results. Quadratic elements contain mid-nodes. Mesh size wise four linear elements fit in one quadratic element. The idea is to refine the linear mesh of paragraph B.2. to obtain desirable results like the quadratic mesh.

This is the case, but it costs a lot of computational effort. The result in figure B.5 is obtained after 7 days of computing at a local Linux server of the TUD. Only one pair of diagonal cracks is obtained. This is without the addition of the nonlinear properties of the interface and crushing of the elements of the wall. If the whole structure needs to be fully modelled expectation is that the server will have to run this calculation for at least one month.

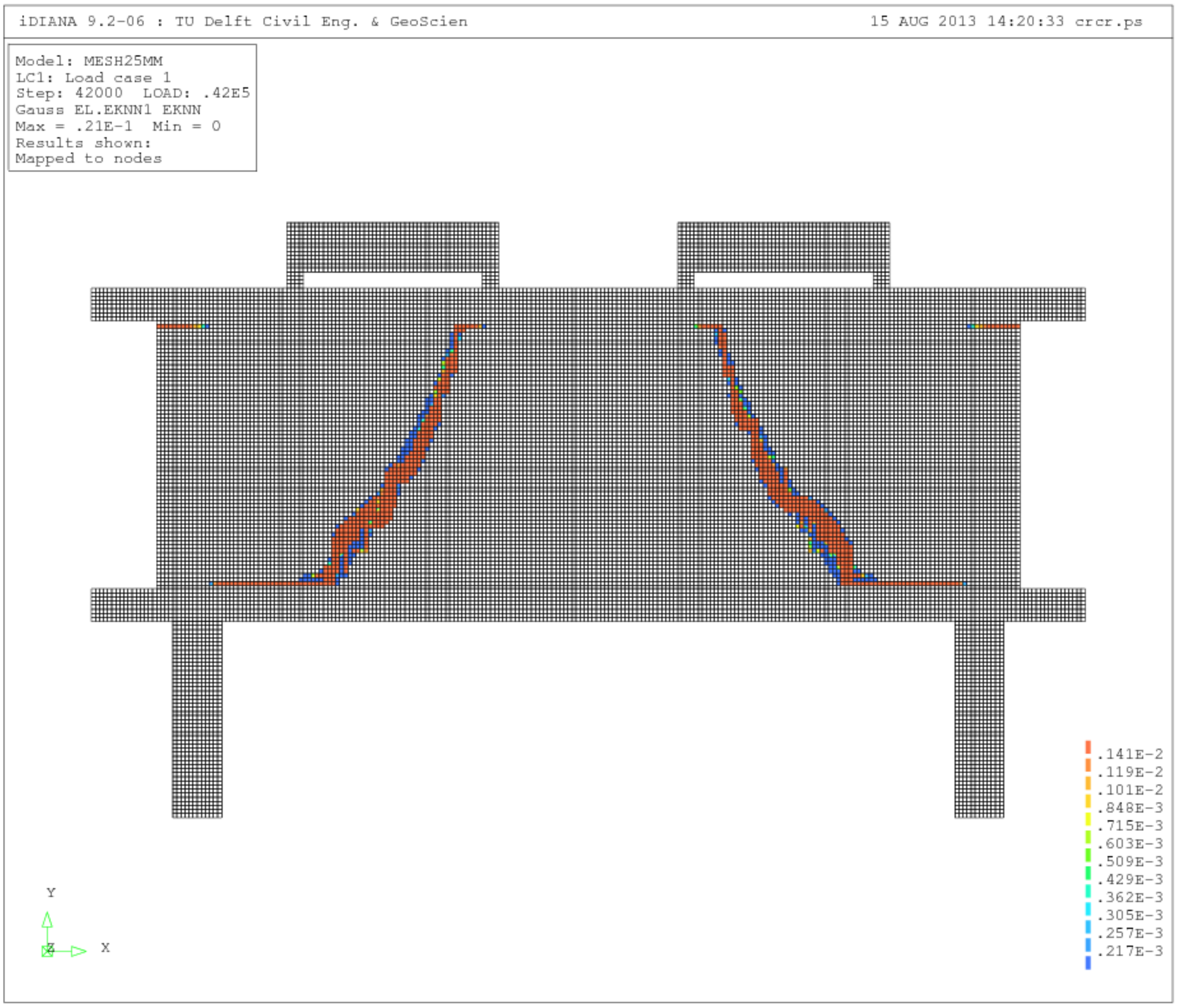

Figure B.5: Results of SLA with linear quadrilateral plane stress elements of 12,5 mm.

B.5. Mesh choice

The mesh containing linear quadrilateral elements of 25 mm could return understandable results. The results itself, however, were not desired for mesh alignment was present in this model. The crack bands followed the mesh boundaries of the elements. The overall behaviour of the structure was still the same as that of the nonlinear finite element analysis, but the results deviated too much to be used as a valid mesh.

The mesh containing quadratic quadrilateral elements of 25 mm seemed to return the desired results. Results were in the same order of magnitude as the nonlinear finite element analysis, presenting the same crack appearance and growth. The computational effort needed to get this far is also not unfavourable.

The mesh containing linear quadrilateral elements of 12,5 mm also showed the desired results. Mesh alignment was not present and crack bands as obtained in the nonlinear finite element analysis were gained. However, this mesh included a lot of integration points and this expresses itself in a huge computation time for the calculation. It is expected that the calculation has to run at least a month to get a full view of the full structural behaviour.

A choice has thus been made to use the mesh containing quadratic quadrilateral elements of 25 mm. It showed the desired results and an acceptable computational effort. This mesh basis has been used in Chapter 9 to perform the deep wall-frame study.

Appendix C: Deep wall-frame representation

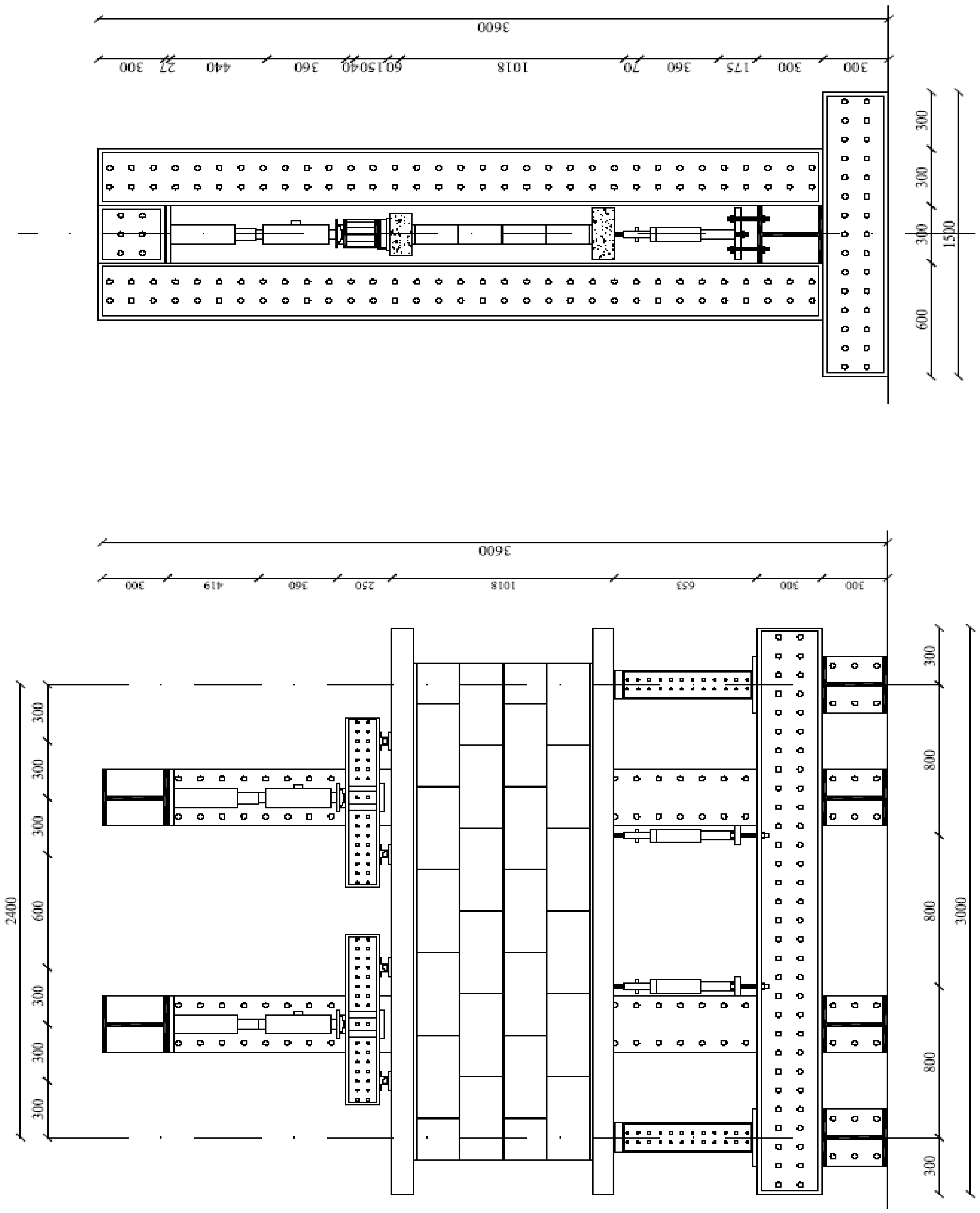

Figure C.1: The structure used as casus in the laboratory seen from the side (top) and front (bottom). [4]

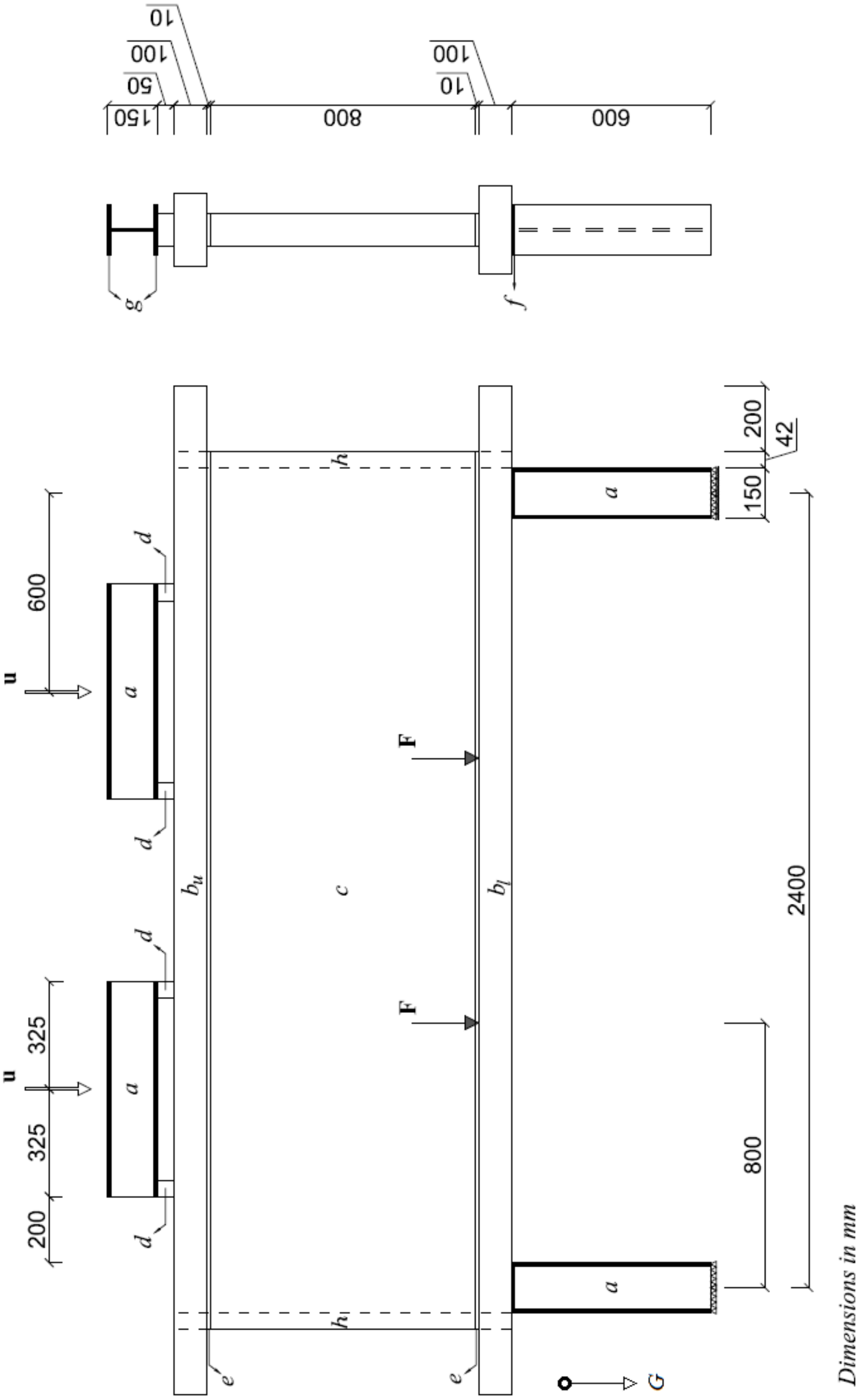

Figure C.2: Geometry of the casus used for computational input.

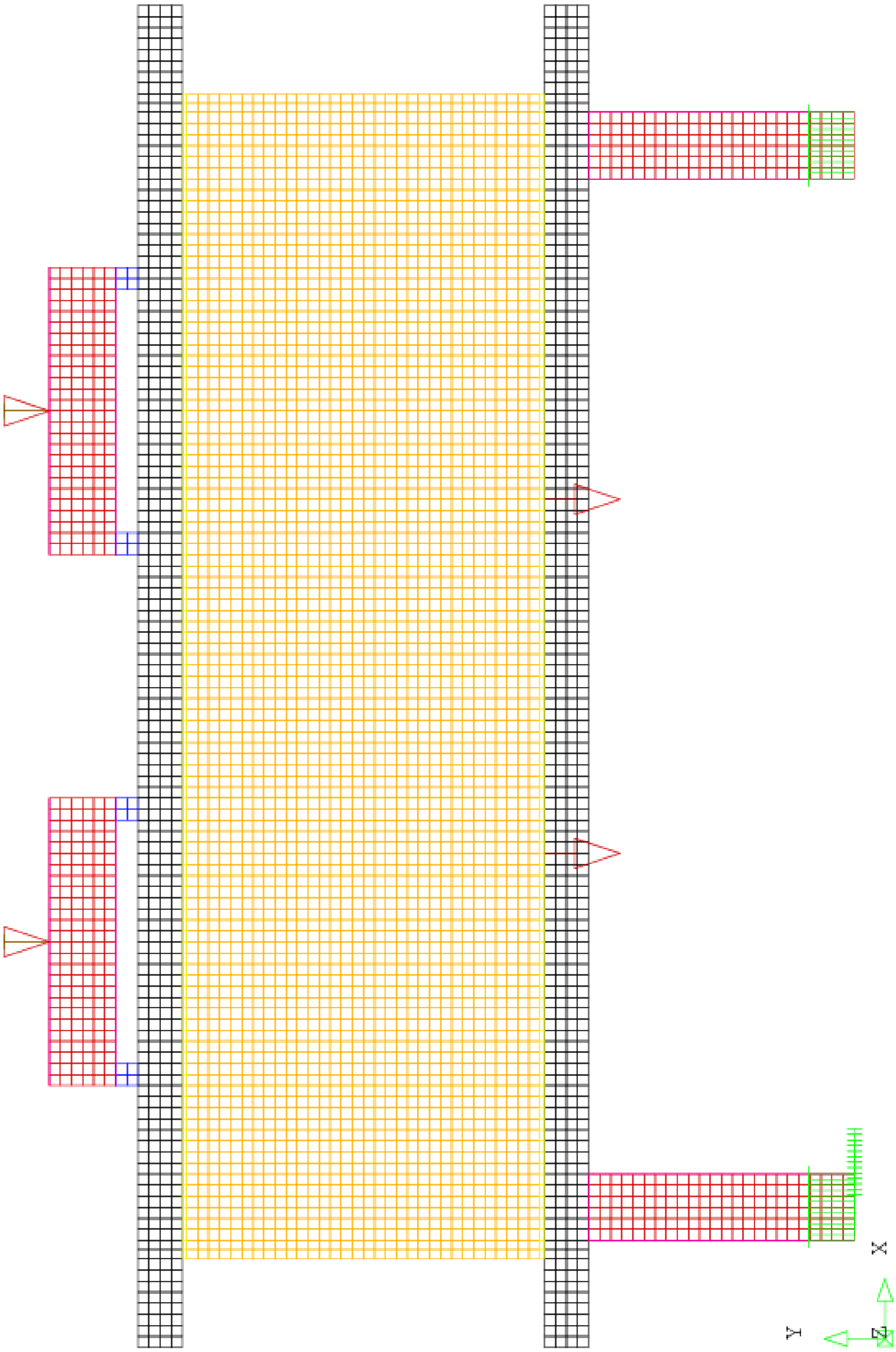

Figure C.3: Geometry of the casus used for computational input.

Table C.1: Geometric values of the casus.

Symbol	Representation	Geometry		Elements	Division	Integration
a	Steel HE150A web	*t*	6 mm	CQ16M	25×25 mm	2×2 - point Gauss
b_l	Concrete lower beam	*t*	270 mm	CQ16M	25×25 mm	2×2 - point Gauss
b_u	Concrete upper beam	*t*	220 mm	CQ16M	25×25 mm	2×2 - point Gauss
c	Masonry wall	*t*	100 mm	CQ16M	25×25 mm	2×2 - point Gauss
d	Rubber hinge	*t*	100 mm	CQ16M	25×25 mm	2×2 - point Gauss
e	Mortar kicker joint	*t*	100 mm	CL12I	25 mm	2 - point Gauss
f	Steel plate	*A*	150 × 30 mm	L6BEN	12,5 mm	2 - point Gauss
g	Steel HE150A flange	*A*	150 × 9 mm	L6BEN	12,5 mm	2 - point Gauss
h	Masonry wall (edge)	*t*	100 mm	CQ16M	21×25 mm	2×2 - point Gauss

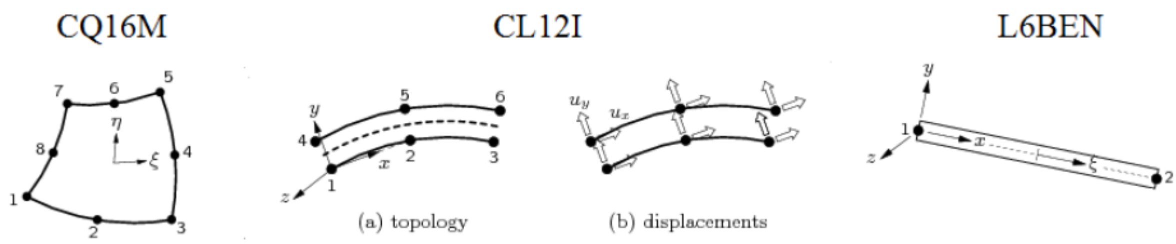

Figure C.4: Mesh of the structure used for computational input. [5]

Table 9.2: Material properties of the casus.

Components	Parameter	Symbol	Value	Dimension
Concrete beams (plane stress elements)	Modulus of Elasticity	$E_{concrete}$	25.400,00	N/mm^2
	Poisson's ratio	$\nu_{concrete}$	0,20	-
	Density	$\rho_{concrete}$	$2{,}40 \cdot 10^{-6}$	N/mm^3
Mortar kicker joints (interface elements)	Normal stiffness	k_n	100,00	N/mm^3
	Shear stiffness	k_t	41,67	N/mm^3
	Tensile strength	f_t	0,01	N/mm^2
	Softening diagram	-	Linear	-
	Fracture energy	G_f	$2{,}5 \cdot 10^{-3}$	N/mm
Masonry wall (plane stress elements)	Modulus of elasticity	$E_{masonry}$	4.000,00	N/mm^2
	Poisson's ratio	$\nu_{masonry}$	0,20	-
	Density	$\rho_{masonry}$	$1{,}80 \cdot 10^{-6}$	N/mm^3
	Tensile strength	f_t	0,80	N/mm^2
	Softening diagram	-	Linear	-
	Fracture energy	G_f	0,01	N/mm
	Crack bandwidth	h_f	25,00	mm
	Compressive strength	f_c	13,50	N/mm^2
	Softening diagram	-	Parabolic	-
	Crushing energy	G_c	2,00	N/mm
	Crush bandwith	h_c	1,00	mm
	Shear retention function	-	Damage	-
Rubber hinges (plane stress elements)	Modulus of elasticity	E_{rubber}	1.000,00	N/mm^2
	Poisson's ratio	ν_{rubber}	0,30	-
Steel profiles (Line & plane stress elements)	Modulus of elasticity	E_{steel}	210.000,00	N/mm^2
	Poisson's ratio	ν_{steel}	0,30	-

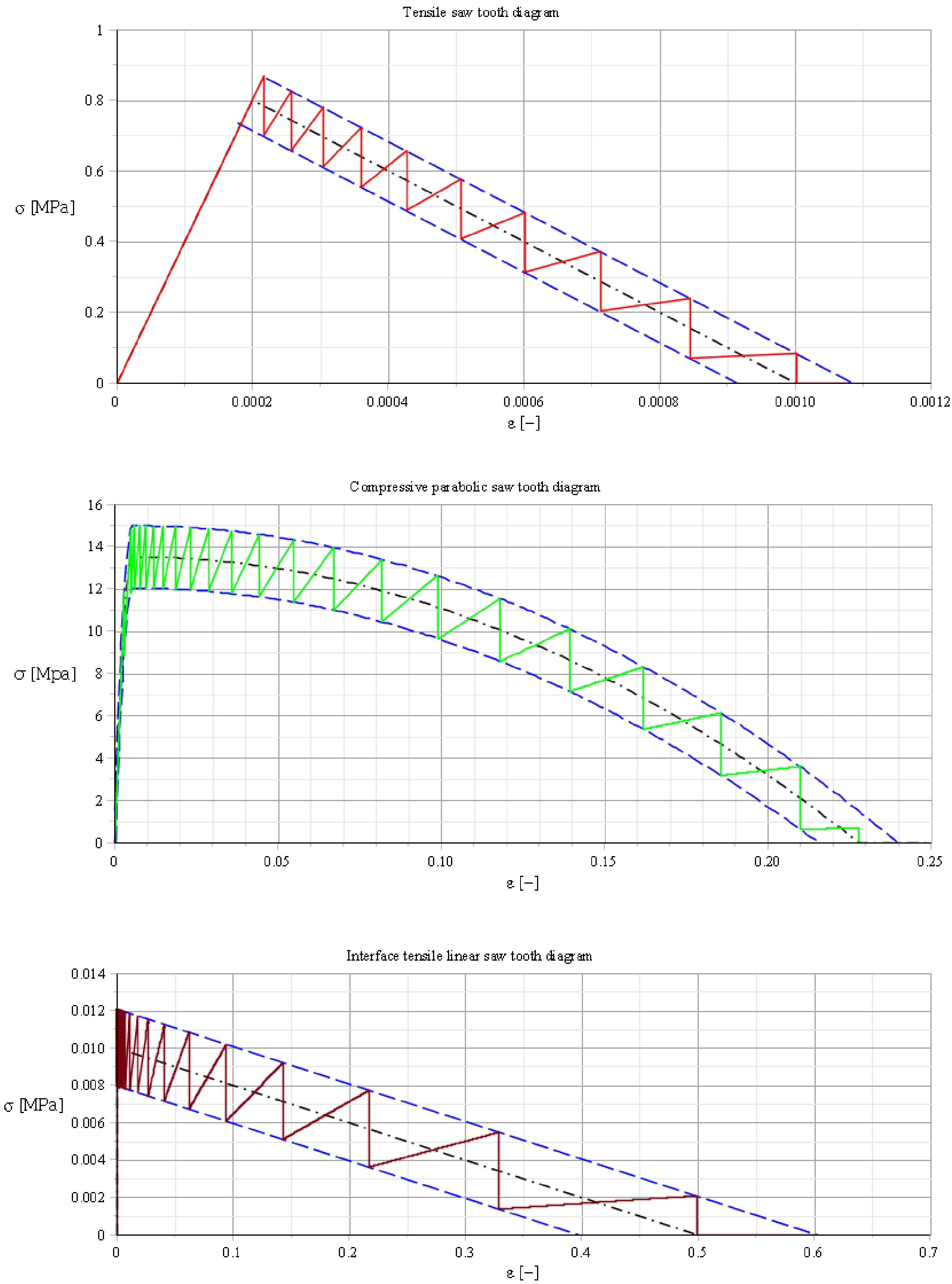

All values are presented in their absolute form

Figure C.5: Saw tooth diagram for plane stress and interface elements using nonlinear properties.